Dissertation zur Erlangung des Doktorgrades der Fakultät Chemie und Pharmazie der Ludwig-Maximilians-Universität München

Development and application of flow experiments for quantitative studies on nanoparticle binding to biological surfaces

Ellen Broda

aus

Mannheim, Deutschland

2016

Erklärung

Diese Dissertation wurde im Sinne von §7 der Promotionsordnung vom 28. November 2011 von Herrn Prof. Dr. Christoph Bräuchle betreut.

Eidesstattliche Versicherung

Diese Dissertation wurde eigenständig und ohne unerlaubte Hilfe erarbeitet.

München, den 12.04.2016

Ellen Broda

Dissertation eingereicht am	14.04.2016
1. Gutachter	Prof. Dr. Christoph Bräuchle
2. Gutachter	Prof. Dr. Ernst Wagner
Mündliche Prüfung am	07.06.2016

Summary

The increasing focus on treating cancer with personalized medicine is accompanied by the development and improvement of targeting strategies. The growing knowledge about the aberrant nature of tumors and their microenvironment can be exploited to facilitate the delivery of therapeutics to the tumor and specifically address their binding to tumor cells. Nanocarriers promote the accumulation of medicinal cargo in tumor tissues. Specific attachment to target cells can be achieved by linking targeting ligands to the delivery systems. These targeting moieties recognize specific receptors which are exposed on the surface of target cells in high numbers. Experiments *in vitro* to assess the specific binding capacity of receptor targeted delivery devices are usually performed as cell culture assays under static conditions. In these approaches, diffusion and gravitational sedimentation of the nanocarriers determine the amount of particles arriving on the cells und thus influence the results.

In this thesis, a microfluidic technique in combination with fluorescence microscopy was developed for quantification of cellular binding of nanoparticles providing reduced sedimentation and constant particle concentration. With this method, we were able to assess the potential of two peptide ligands to serve as targeting ligands.

First of all, model nanoparticles were synthesized which mimic the surface characteristics of therapeutic delivery systems, simultaneously meeting the requirements for quantitative analysis such as sufficient colloidal stability, good detectability and reproducibility. Successful surface modification of latex beads was verified by characterization with several methods including zeta potential measurements and dynamic light scattering. The shielding with polyethylene glycol revealed beads with reduced surface charge, increased solubility and decrease aggregation tendency. The equipment with short peptide ligands resulted in a positive surface potential. As a second step, a flow setup was developed and optimized. The experiments were designed such that a continuous flow of particles was passed over a cell monolayer and adhered particles were detected by fluorescence microscopy. For quantification, the particles were counted on individual cells. This procedure enabled in addition the monitoring of particle aggregation and cell integrity. Third, beads with ligand were compared with internal control beads. With this method, particle binding was quantified under the same experimental conditions diminishing heterogeneity of results.

Finally, binding studies were performed to quantify the effect of two short peptide ligands. The transferrin receptor is expressed at high levels in several malignant cells and brain capillaries, representing a suitable target for the delivery of therapeutics to diseased tissues and the brain. The peptide B6 was found to specifically bind to this receptor and was coupled onto the model particles. Likewise, the c-Met binding peptide cMBP2 which specifically addresses the c-Met/hepatocyte growth factor receptor was linked to the particles. This receptor is normally not activated in normal tissue, but promotes progression and invasive growth in some cancer cell lines. Quantitative adhesion studies of both types of particles were performed with several adequate internal control particles acting as electrostatic and specificity controls. The results showed that both peptides, B6 and cMBP2 promote binding to target cells. Furthermore, the findings suggest that the peptide B6 improved cellular adhesion of the beads by nonspecific interactions such as electrostatic interactions whereas the peptide cMBP2 enhanced binding of the beads in a specific manner only when

its amino acid sequence was in the correct order. Moreover, B6 particles showed high binding capacities to non-target endothelial cells while cMBP2 particles did not. Consequently, cMBP2 was assessed as potential targeting ligand while B6 was disqualified due to its presumably unspecific binding behavior.

The main administration route of nanocarriers is intravenously. Before a targeted delivery system can attach to receptors on target cells *in vivo*, it encounters blood components, cells lining the vessel walls and the tumor microenvironment. Adhesion of nanocarriers to these nonspecific binding sites can cause toxic effect. Therefore, it is not only important to assess the specificity of delivery systems, but also approximate their unspecific adsorption to normal tissues, organs and biomolecules. By extension of the flow setup to a system with four parallel channels, the binding of actual therapeutic delivery devices was screened to quantify their specific and nonspecific binding on four different surfaces. In two flow channels, cell were seeded, e.g. target cells and endothelial cells (which usually line the vessel walls). The other two flow channels were coated for instance with artificial extracellular matrix gel or collagen, both parts of the tumor microenvironment, and with serum which is contained in blood. Preliminary experiments were performed using polyplexes, non-viral gene vectors composed of nucleic acids complexed with polycationic carriers. They revealed for example that linear polyethylene imine (LPEI) as a carrier polymer mediated binding of the polyplexes to cells and coatings regardless if equipped with the peptide ligand GE11 or not. The number of attached polyplexes varied most on endothelial HMEC-1 cells suggesting a high sensitivity or heterogeneity of this cell line. Furthermore, when the serum content in the cell medium was increased towards levels present in humans, polyplex adhesion on all surfaces was reduced. Polyplexes composed of STP polymer as carrier and modified with the peptide ligand cRGD showed low binding to matrix gel and collagen at high serum levels which is desirable for *in vivo* applications. In conclusion, the flow experiments in combination with fluorescence microscopy and quantitative analysis represent powerful tools for the selection of appropriate targeting ligands and suitable actual delivery devices.

Contents

1 Introduction

The slogan of the German Cancer Congress 2016 pronounced "four Ps": prevention, precision, participation and personalization [1]. Especially, future cancer therapeutics will be more oriented on the individual patient. With about 500.000 newly diagnosed cancer patients alone in Germany, estimates of 14 million new cases worldwide and 8.2 million cancer related deaths in 2012 [2], personalized cancer treatment represents a huge challenge. Moreover, more than one hundred types of cancer exist and already tumor cells of single populations exhibit heterogeneous phenotypes including their metastatic potential and survival prognosis of therapy [3]. Diagnostic and therapeutic approaches are required which assess multiple parameters in high throughput and for personalization of medicine preferentially single-cell analysis should be performed to detect and treat specifically the diseased cells. The development of nanocarriers enables the accumulation of imaging and therapeutic agents in tumor tissue. For specific attachment to target cells, ligands, such as small molecules, protein, peptides and antibodies, are attached on the delivery systems to address receptors on target cells which are exposed specifically on diseased cell lines or in very high numbers. Studying the efficiency of such nanocarriers is conventionally performed first in cell culture experiments *in vitro*, followed by *in vivo* approaches with animal models before the transfer into the clinic. In recent years, a variety of additional nanotechnological techniques were invented to model tumors *in vitro* or adapt important experimental features for the characterization of nanocarrier efficiency. For example, microfluidics are used to simulate the delivery of nanotherapeutics to tumor vasculature or whole tumor models on a chip [4] were designed to assess the binding and uptake of them *in vitro*. Cell culture models experience a new dimension by modeling 3D environments as for instance hydrogel-based mimicry of the tumor microenvironment [5]. Thus, the assessment of nanocarrier efficiency can be performed by in various *in vitro* models and a combination thereof is required as each model adapts different aspects of the reality and increased complexity often is accompanied by technological effort and raising costs.

The aims of this thesis include the development of reliable and reproducible experiments for quantitative binding studies of receptor targeted nanocarriers to assess the effect of a targeting ligand and to provide information about the nonspecific binding behavior to relevant surfaces. Therefore flow experiments were introduced and optimized with which the potential of two peptides on model nanoparticles, mimicking the surface characteristics of therapeutic delivery devices, was assessed to serve as a targeting ligand. And second, the flow system was extended to quantify the adhesion of non-viral gene vectors on four different surfaces in parallel to estimate their specific and nonspecific binding behavior.

This thesis is divided into eight chapters. The introduction is followed by two chapters describing the biological and technical background of this work. In **chapter 2**, nanocarriers for drug and gene delivery are described concerning their design and function as well as their biodistribution and

clearance in vivo. The most important part of this chapter is the description of tumor targeting including the basics of the tumor microenvironment, passive targeting approaches and active targeting with the description of receptors addressed by nanocarriers used in this work. A final section explains the fundamentals of cellular uptake of nanocarriers and their intracellular distribution. In **chapter 3**, the basics of fluorescence and applied microscopy methods to investigate the binding of nanocarriers are explained.

Four chapters depict the results of this thesis. In **chapter 4**, the synthesis, characterization and cellular uptake of model nanoparticles (beads) which mimic the surface characteristics of therapeutical particles are illustrated. Most important parts of this chapter include the conception of the particles (introducing part), the characterization of their zeta potential and measurement of their hydrodynamic diameter (subsection 4.2.2), and the summary (section 4.4). **Chapter 5** documents the development and optimization of flow experiments with internal control for the assessment of cellular binding of nanoparticles. Apart from the introduction and illustration of the conceptional design (section 5.1), the description of the internal control (section 5.3) provide useful information for an easier understanding of the results presented in the subsequent chapter. In **chapter 6**, the binding studies of receptor targeted beads are elucidated. After providing a rationale for transferrin receptor and c-Met/hepatocyte growth factor receptor targeting, cellular adhesion of beads equipped with the peptide ligand B6 are described in section 6.1. The binding studies of B6 beads under flow conditions are depicted in the subsection 6.1.1. Additional information of experiments investigating the specificity of cellular adhesion of B6 beads under static conditions is described in the sections below with the exception of subsection 6.1.2.6 which depicts the binding to non-target endothelial cells under flow conditions. Furthermore, the specific binding capacity of the peptide cMBP2 attached to model beads was studied under flow conditions and showed promising results (section 6.2). In the summary of this chapter, detailed conclusions about the binding behavior the peptides B6 and cMBP2 on model nanoparticles are drawn. In **chapter 7**, the proof of principle is shown how flow experiments can be extended to investigate specific and nonspecific interactions of actual therapeutic delivery systems with multiple surfaces. Most interesting parts of this chapter include the introductory part and the first three paragraphs of section 7.1 and the description of experiments screening the binding of polyplexes on four different surfaces under flow conditions investigating various aspects (section 7.3). Additional information is given in the section above which describes the selection of suitable polyplexes for flow experiments and quantitative analysis. The conclusion provides a perspective of the screening experiments and motivation for future directions of the quantitative screening approach.

Chapter 8 contains the information about experimental materials and methods.

2 Nanocarriers for drug and gene delivery

Nanocarriers are nano-sized transporters which are designed to detect, image and treat specific sites in a living system. For imaging, radio-nucleic contrast agents can be encapsulated and super-paramagnetic nanoparticles can visualize tissues or organs in which they accumulate [6]. Furthermore, diseased cells can be addressed using specific molecules coated on the nanoparticles. The encapsulation of agents is not only used for diagnostics, but also an important strategy for therapy. Improvements of nanoparticle-based transport of therapeutics compared to directly administered free drugs include the trans-membrane delivery of molecules which are poorly water-soluble [7], prolonged blood circulation times in the body [8] and reduction of systemic side-effects [6]. Furthermore, nanocarriers offer the possibilities of highly localized release of their therapeutic cargo [9], and the simultaneous observation thereof and of the therapeutic feedback [10].

In this chapter, nanoparticle-based drug and gene delivery systems are introduced. Their interaction with biological materials will be described and the specific attachment to target cells will be elucidated in more detail. Finally, their cellular fate will be explained.

2.1 Delivery systems

Drug and gene delivery systems are nanocarriers that transport their therapeutic cargo in the human body to specific tissues and subsequently to the target site in the addressed cells. They reduce or prevent degeneration of the payload, enhance biodistribution of the medicine and control the release of cargo [11]. Delivery devices are mainly administered intravenously, but the application can also be oral, intramuscular, subcutaneous, transmucosal, transdermal and pulmonary [12].

The design options of delivery devices show a huge variety in shape, size and composition (Fig. 2.1). Mostly spherical particles are fabricated, but also rod-like, cylindrical, ellipsoidal and disk-like particles have been produced [13]. Especially the size has an enormous impact on the half-life, clearance, accumulation and cellular uptake of the nanocarriers and ranges from few nanometers up to several hundred nanometers. Delivery systems are composed of a multitude of materials comprising organic molecules like lipids and polymers, inorganic constituents like metals and metal oxides, or viruses [14]. For cancer therapy nano-transporters have been developed including quantum dots [15], gold nanoparticles [16], mesoporous silica nanoparticles [17], hydrogel-based systems [18], carbon nanotubes [19], dendrimers [20], solid-liquid particles [21], polymeric particles [22], liposomes [23], drug-conjugates [24] and genetically modified viruses [25]. The composition of the nanocarriers and their surface groups determine their physical properties, such as the colloidal stability, surface charge and hydrophobicity. These characteristics can be shielded or modified by surface coatings to either enhance their blood circulation time or direct them to specific tissues. The

latter approach can be achieved by attaching targeting ligands to the delivery systems such as small molecules [26], proteins [27], peptides [28], antibodies [29] or antibody fragments [30], nanobodies [31] and aptamers [32] (see also section 2.2.3).

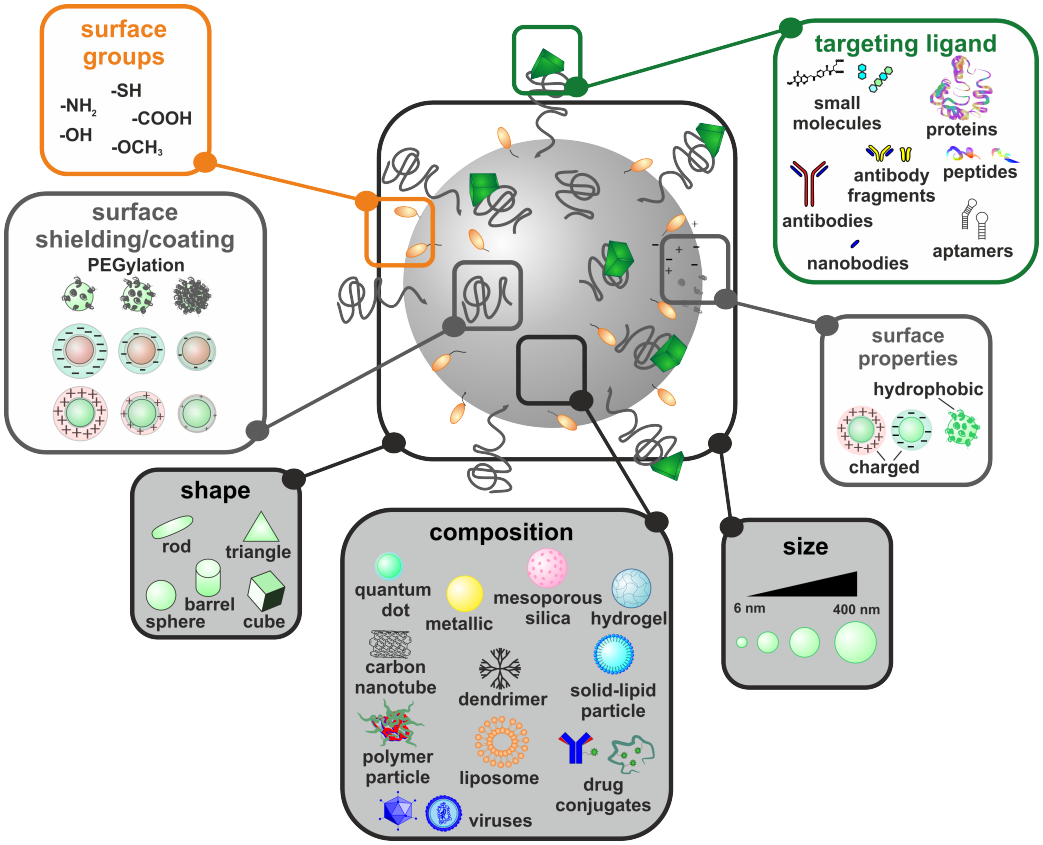

Figure 2.1: Nanocarriers. Delivery systems vary in composition, shape and size. Their surface groups can be modified by shielding with water-soluble polymers or lipid layers and coated with targeting ligands. These modifications determine their surface properties.

The configuration of nanocarriers has to be chosen carefully considering several challenges they will face upon administration. First, they have to provide a prolonged half-life and be prevented from systemic clearance. Second, they should be biocompatible, which means exhibiting low interaction with non-target tissues, organs and blood components which would result in toxic, immunogenic, thromogenic and carcinogenic responses [33]. Third, they should accumulate within the target tissue, bind specifically to target cells and be internalized effectively. Forth, they should be transported intracellular to the target compartment and last, the cargo should be able to act at the target site. Depending on the transported cargo, the nanocarriers can be categorized into drug and gene delivery devices.

2.1.1 Drug delivery devices

Since the first attempts of nanoparticle-base drug delivery sixty years ago, the field greatly advanced and the first products are on the market [34]. Mostly hydrophobic drugs are encapsulated in hydrophobic or amphiphilic carriers [35] such as doxorubicin, docetaxel, methotrexate or paclitaxel. Also hydrophilic drugs are transported in nanoparticles, for example transtuzumab or gemcitabine. One of the main challenges is the accumulation of the drugs in the carrier or, in other words the loading capacity of the transport vehicles. During transportation in the vascular system, it is important that the drugs remain within the nanoparticle and that the carrier provides a sufficient stability. After overcoming the obstacles of specific cellular binding, uptake, escape into the cytosol and translocation to the target site, the drugs have to be released from the delivery device. There are two methods for controlled release: either the disposal of the drugs is sustained for a controllable period of time [36] or it is triggered by a stimulus at the target site [37]. The first approach involves either the diffusion of the drugs from an insoluble polymer shell or matrix, or the erosion of the particle. The release can be triggered by varying pH values, enzymatic, thermosensitive or photo-activated reactions.

Transported cytostatic drugs encapsulated in nanocarriers can be classified according to their mode of action [38]. There are alkylation reagents which transfer alkyl groups to nucleic acids and proteins. Antimetabolites are inhibitors which compete with the natural substrate for the active site of essential enzymes or receptors, e.g. folic acid antagonists, pyrimidine or purin analogues. Cytotoxic antibiotics can affect the function and synthesis of nucleic acids. Spindle poisons include vinca alkaloids which bind to tubulin, thus inhibiting mitosis and taxoids which act inversely by promoting the assembly of microtubules, thus compromising disassembly. Topoisomerase inhibitors cleave, unwind and rejoin DNA structures, and platinum agents like cisplatin cross-link DNA strands, thus producing DNA adducts [39].

So far, most approved drug delivery systems are liposomes, but also include also polymeric nanoparticles and protein conjugates. They are used for the treatment of a variety of cancers including (metastatic) breast cancer [40, 41], Kaposi's sarcoma [42], ovarian cancer [41], lung cancer [43] and leukemia [44]. The number of launched clinical trials of nanoparticles for cancer therapy tripled in the past decade [14] and next-generation particles with targeting ligands for improved selectivity and stimuli-responsive characteristics for increased efficiency [45] are in pre-clinical evaluation.

2.1.2 Gene delivery vectors

In contrast to drug delivery devices, gene delivery systems transport therapeutic nucleic acids, mainly double-stranded DNA [46], small interfering RNA (siRNA) [47] and micro RNA (miRNA) [48]. They either correct dysfunction of gene expression, introduce novel desired functions or disable undesirable functions. Furthermore, they prevent the digestion of naked nucleic acids by naturally occurring nucleases [49]. Gene delivery devices can be categorized in viral and non-viral vectors.

Viral vectors are genetically modified natural viruses. Commonly adeno-associated viral (AAV) and lentiviral (LV) vectors are used for gene delivery. AAV delivery systems remain episomal, i.e. the DNA is not integrated in the genome of the transduced cell and hence are used for short-term gene expression or in terminally differentiated cells [25]. An AAV vector (alipogene tiparvovec, Glybera) which substitutes a gene encoding for lipoprotein lipase was the first gene therapeutic product approved by the European commission in 2012 [50]. Several years before, in 2004, an AAV vector for recombinant AD-p53 gene therapy for head and neck squamous cell carcinoma became commercially available in China [51]. LV delivery systems are retroviral vectors which integrate their genetic material stably into the genome of the host cell and thus are used for modification of stem cells or dividing cells [25]. Viral vectors represent the most efficient delivery systems as they are optimized by nature to infect host cells and transfer their genetic information. However, they bear the risk of high immunogenicity. Their cargo capacity is limited and the costs of production and analytics are high.

Non-viral vectors are suitable alternatives exhibiting lower immunogenicity, reduced toxicity and a high loading capacity for genetic material despite their low transfection capability [52]. These artificial delivery systems are formed by condensation of nucleic acids and cationic lipids (e.g. lipoplexes) [53] and/or polymers (e.g. polyplexes) [54] via electrostatic attraction of the negatively charged phosphate backbone of the DNA or RNA and the positive charge of the polycationic carrier. Especially polymers are advantageous offering high versatility, reproducibility and the possibility of precise production and identification. Polycationic carriers include polyamino acids like poly-L-lysine (PLL) [55], protein derivatives [56], carbohydrates [57], polyethylene glycol (PEI) [58], dendrimers [59], copolymers [60], chitosan [61] and cyclodextrin (CD) [62]. In physiological medium, the non-viral vectors remain usually positively charged which promotes the interaction with negatively charged cell surfaces. Another benefit of the positive charge is the capability of escaping from endosomal vesicles after cell internalization (see section 2.3). On the other hand, the positive charge is disadvantageous because it increases unspecific binding, promotes higher toxicity and faster removal under *in vivo* conditions. With the development of new building blocks like succinyl tetraethylene pentamine (Stp) units, polyplexes with less surface charge can be generated which in addition allow for precise analysis of structure-relationship activity [63].

First reported about twenty years ago [64], PEI is nowadays one of the golden standards of transfection reagents [52] and meanwhile has been investigated in clinical studies for cancer therapy and anti-HIV vaccination [54]. There are two variants, linear PEI (LPEI) and branched (BPEI). The linear version is more flexible and facilitates intranuclear delivery in non-dividing cells in contrast to BPEI which transfects only dividing cells in or before mitosis [65, 66]. For the transfection of specific cells, targeting ligands can be attached to the polymer chains which promote their binding to respective receptors on target cells (see section 2.2.3). Depending on the complexed nucleic acid, polyplexes can have hydrodynamic diameters of a few nanometers (single siRNA-polymer [67] or single pDNA-polymer [68]) up to hundreds of nanometers (e.g. large nucleic acids with many polymers [69]). In biological media, polyplexes can be partially or completely dissolved

by electrolytes, proteins or cellular surfaces [70]. Furthermore, they posses a high tendency to self-aggregate. The colloidal stability can be increased by advanced packing techniques such as cross-linking of polymer chains or introduction of hydrophobic moieties, and surface shielding [54]. On the other hand, the nucleic acids need to intracellularly dissociate from the carrier at the target site. For pDNA delivery, the plasmid has to enter the nucleus which occurs mainly by active transport as only nucleic acids below 250 bp can passively cross the nuclear membrane through the nuclear pore complex. A nuclear localization sequence (NLS) can be integrated into the nucleic acid delivered by the polyplex, promoting active nuclear import via binding to nuclear proteins [71].

Clinical trials using polyplexes investigate the treatment of patients with melanoma [72], bladder cancer [73], ovarian cancer [74] and solid tumors [75] amongst some others.

2.1.3 Biodistribution and clearance

In aqueous media, nanoparticles are stabilized by an electrical double layer formed by counter-ions and co-ions. In biological media, serum components interact with the particle surface via electrostatic, electrodynamic and steric interactions and are adsorbed to form a so called corona [76]. Often, it is referred to as protein corona as the main components are proteins, containing a smaller number of lipids and sugars [77]. This layer can be categorized into a hard and a soft corona. The hard corona is the part of biomolecules which is tightly adsorbed on the particle surface whereas the soft corona is a dynamic layer. The composition may vary upon time and especially in the human body in different extra- and intracellular compartments.

Upon entering the blood flow, nanoparticles are covered with opsonins which comprise complement proteins, immunoglobolins (IgG and IgM), albumins, fibronectins, fibrinogens, apolipoproteins and laminin [78]. This opsonization results in an increased detection by phagocytes. These cells posses phagocytic, Fc and complement receptors which usually recognize conserved motifs of pathogens and opsonins [79]. Consequently, opsonized objects larger than 10 nm including nanoparticles and viruses are internalized by the phagocytes mainly in a receptor-mediated manner [80]. Within the cells, enzymatic degradation decomposes the pathogens and nanoparticles, or the nanomaterial is accumulated if it is non-degradable, e.g. heavy metals [81]. Especially, the liver, the spleen and the bone marrow contain many phagocytic cells like macrophages, e.g. Kupffer cells and monocytes. Apart form the clearance of nanoparticles by the mononuclear phagocytic system (MPS), particles larger than 150 nm are removed by physical filtration in the spleen or liver [82], and particles smaller than 6-8 nm are excreted by glomerular filtration in the kidney [83]. This renal clearance depends strongly on the size of the nanoparticles, but also the surface charge can have an impact on this process, because it can promote adsorption of serum proteins which increases the hydrodynamic diameter of the particle [84]. In principle, charged particles are more prone to be cleared from the blood flow due to opsonization, especially when containing a positive surface charge [85].

To prevent rapid clearance *in vivo*, delivery systems are coated with water-soluble polymers such as polyethylene glycol (PEG), polyethylene oxide (PEO), dextran, and polyacrylic acid (PAA) [86].

This prolongs their blood circulation time and improves their biodistribution, which means in particular their increased accumulation in tumor tissue compared to other organs (see section 2.2.2).

PEG is a well established, flexible and highly water-soluble polymer [87] which is an essential component of most delivery devices as it shields the surface to 1) prevent the interaction of intrinsically toxic materials with the biological environment, 2) diminish unspecific binding with the biological environment, and 3) reduce opsonization. The PEG sheath however impairs also association of delivery systems with tumor or other target cells and can have a negative impact on the escape of the nanoparticles from cellular internalized vesicles (PEG dilemma). Furthermore, PEGylation does not completely shield nanocarriers from unspecific interactions, immunological effects can also be induced like complement activation, adsorption of immunoglobulins or anti-PEG-antibodies [88]. In addition, the extent of shielding and interaction with biological molecules depends on the length and density of PEG chains on the particle surface. The amount of PEG in combination with the particle dimensions determine the conformation, which can be densely arranged as a brush resulting in high colloidal stability and low protein adsorption or can be loosely coiled in a "mushroom-like" conformation yielding higher protein adsorption [89]. For each carrier system the amount of PEGylation has to be adjusted to obtain an optimal balance between shielding and attraction to target cells.

2.2 Tumor targeting

Tumors are usually removed by surgery or treated with radiation and chemotherapy or a combination thereof. The latter approach implies the administration of cytostatic drugs, which constrain cell devision and growth. Cancer cells are the main addressers, but healthy cells can also be affected. A convenient approach to reduce the undesired unspecific binding and to enhance the concentration is presented by encapsulation of such drugs or other therapeutic cargo in nanocarriers. To deliver the transport systems specifically to the diseased tissues and cells, two different approaches are pursued: passive and active targeting. The first approach is based on the aberrant tumor microenvironment whereas the second method exploits the abnormal characteristics of the tumor cells themselves. In this section, first the tumor microenvironment is described leading to a better understanding of passive tumor targeting. Finally, active targeting will be described primarily focusing on details useful for a better comprehension of the results of this thesis.

2.2.1 Tumor microenvironment

Tissues, in which cancer cells grow, experience molecular, cellular and physical changes, for example in gene expression, cellular proliferation, apoptosis and invasion [90]. This induces the emergence of a tumor microenvironment in the interstitial space (stroma) surrounding the tumor bed (parenchyma) and the vasculature (Fig. 2.2). The composition of this abnormal tissue differs across cancer types. An ubiquitous characteristic is a disorganized and leaky vasculature. The fast proliferation of tumor cells in a limited area induces mechanical forces in the tumor which lead to cell compression and to deformation of the vascular system. The blood vessels in tumors vary

highly in diameter, density and spreading [91]. As the growing tumor mass is poorly vascularized, new blood vessels are formed in avascular regions by extension of existing vessels (angiogenesis) [92] to enable the supply with nutrients. By this process, the vessels are perforated which promotes low blood flow and excessive fluid efflux from the vasculature into the interstitium (extravasation) [93]. Additionally, poor vascularization causes deprived oxygen supply (hypoxia) in some regions of the tumor [94]. Hypoxia is an additional promoter of angiogenesis and activates growth factors like vascular endothelial growth factor (VEGF) or platelet-derived growth factor (PDGF) [95]. Another consequence is a more acidic extracellular environment around hypoxic cancer cells arising from an enhanced rate of glycolysis [96].

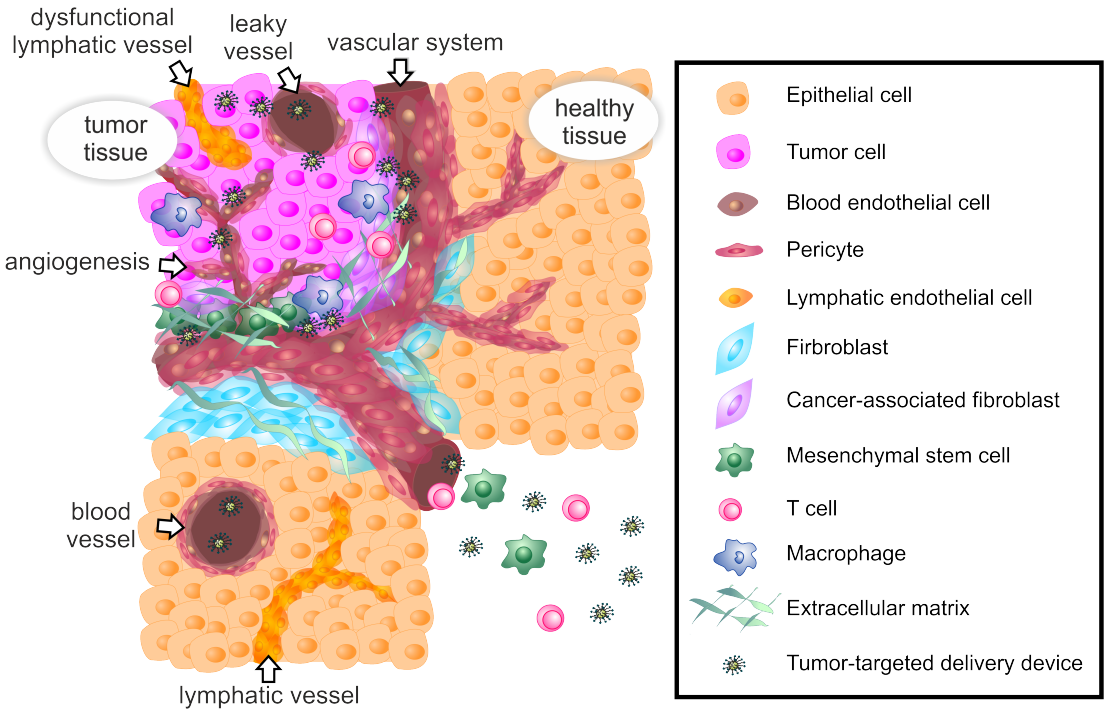

Figure 2.2: Healthy tissue and tumor microenvironment. In normal tissue, the integrity is promoted by stromal cells which provide growth factors and structural support. Fibroblasts remodel the extracellular matrix permanently to overcome mechanical stress within the connective tissue. Blood endothelial cells and pericytes maintain the integrity of blood vessels and enable the supply of nutrients to the tissue. The lymphatic system drains interstitial fluid. In tumor tissue, the blood vessels are leaky with many perforations. New angiogenic vessels are formed. The extracellular matrix is denser and contains more collagen fibers and macrophages, cancer-associated fibroblasts (CAFs) are activated and circulating mesenchymal stem cells are recruited. In the tumor microenvironment the interstitial fluid pressure (IFP) is increased due to dysfunctional lymphatic vessels. Furthermore, chemokines and cytokines attract activated T cells. The figure is inspired by Turley *et al.* [97].

Additionally, the tumor microenvironment is composed of stromal cell types like blood endothelial cells, lymphatic endothelial cells, mesenchymal stem cells (MSCs), cancer-associated fibroblasts (CAFs) and pericytes. Stromal cells, especially MSCs and CAFs support the survival of cancer cells by secretion of essential growth factors like hepatocyte growth factor (HGF) and fibroblast growth factor (FGF) [98]. T cells which are activated by chemokine gradients and adhesion molecules

infiltrate the tumor microenvironment [97]. However, inhibitory cells and molecules compromise their survival and hinder the propagation of their activation and effect.

Tumor growth increases the stromal cell-related production of extracellular matrix (ECM) components and influences their organization [90]. Usually, the matrix is formed by collagens, glycoproteins, proteoglycans, elastin and hyaluronan which are important for the regulation of cell proliferation, differentiation, survival and homeostasis in collaboration with enzymes and growth factors [99]. The basement membrane matrix is dense and comprises less porous structures like collagen type IV, fibronectin and laminins whereas the matrix of the interstitium provides the elastic strength of tissues [100]. In tumors, the modified ECM is connected to stromal cells such as fibroblasts, pericytes, endothelial and immune cells [101] and can be disordered throughout large, aggressive tumors [102]. The mechanical stress exerted by a denser ECM and hyperperfusion through leaky blood vessels in combination with a dysfunctional lymphatic system produce an increased interstitial fluid pressure (IFP) in the tumor interstitium [103]. The pressure gradients are not adequately maintained across the walls of tumor vessels resulting in diminished extravasation of drug molecules and their influx into the tumor bed [104]. In addition, also the ECM and stromal cells hinder the entrance of chemotherapeutics by creating a physical barrier [105].

With the increasing knowledge about the tumor microenvironment, therapeutic strategies emerge exploiting the discrepancies of normal and tumor tissue. This approach is pursued for instance by passive tumor targeting. By active targeting of tumor vasculature and angiogenesis [106], the nutrient supply of solid tumors is cut off, hence providing an additional promising approach for cancer treatment. In the recent years, researchers have focused more and more on addressing the tumor microenvironment itself to prevent tumor progression and treatment of drug resistance [91, 107].

2.2.2 Passive targeting

Nanoparticles in the blood circulation cannot enter the blood vessels through tight junctions between endothelial cells due to their size. Only nanoparticles with a size below 6-12 nm are able to penetrate normal tissue [108]. Usually, they are either repelled from the vessel walls or bind to endothelial cells, which form the inner part of the vessels, in an unspecific manner before they are cleared from the body (see section 2.1.3). The situation is different in tumor tissue. Through leaky tumor vasculature, nanoparticles can escape into the interstitial space surrounding the tumor bed. Normally, the nanoparticles would traverse the epithelial tissue and would be drained by the lymphatic system. However, in the tumor the lymph system is dysfunctional, preventing the outflow of nanoparticles through this pathway and enabling the retention of nanoparticles in the tumor region [109]. This concept is termed the enhanced permeability and retention (EPR) effect [35, 110].

Extensive angiogenesis and hypervascularization promote the EPR effect by increasing the amount of nanoparticles in the tumor vasculature. Furthermore, the size of the fenestrations (holes in the vessel walls) determines the entry of nanoparticles. Typically, these openings in the tumor vessels

have maximal diameters between 100-800 nm [111], but also larger perforations in the range of 1200-2000 nm have been observed [112]. Subsequently, nanoparticles with a hydrodynamic diameter up to 800 nm are able to penetrate the tumor vasculature, but also smaller cut-off sizes have been reported, for example 400 nm for the extravasation of liposomes of different sizes [113]. The efficiency of the EPR effect consequently depends on the tumor type.

The movement of nanoparticles into and within the tumor interstitium is mainly mediated by diffusion and inversely correlated with their size. Very small nanoparticles diffuse faster and their retention is lower. The optimal size range for nanoparticles to be accumulated by the EPR effect is between 30-200 nm [114]. Apart from the size, the shape of the nanoparticles influences their passive targeting efficiency. Spherical particles mainly exhibit a laminar flow profile, thus only particles close to the surface exit through the gaps in the vessel walls [115]. On the contrary, rod- and bar-like particles tumble more during flow providing further possibilities for passive targeting [116, 117]. In addition, the surface characteristics of a particle influence if it is cleared from the body or accumulated within a targeted or non-targeted tissue.

To date, nanocarriers approved for clinical use rely on passive targeting [34] which enhances their enrichment and the concentration of therapeutics in the tumor region. Furthermore, the biodistribution and biocompatibility are improved and the blood circulation time is prolonged. Further promising delivery systems are under clinical development [34]. However, no specific cells are addressed. The selective binding to target cells is pursued by active targeting.

2.2.3 Active targeting

Reaching the close proximity to cells, nanocarriers can interact with molecules on the cell surface and depending on their nature bind to them. The plasma membrane forming the cell border consists of lipids (phospholipids, glycolipids and sterols) and proteins (integrated in the membrane like ion channels, proton pumps and receptors, anchored by lipids or peripheral). Additionally, membrane-bound glycolipids and proteoglycans form a carbohydrate layer, the glycocalyx. Arriving nanoparticles consequently are confronted with a heterogeneous negatively charged surface with many potential interaction sites. The composition of surface molecules on cancerous cells is different to the one on normal cells. For example, the glycosylation pattern is changed [118] and many specific surface receptors are overexpressed [119]. This differences can be exploited to chose molecular markers or targets for diagnostics and therapy. By attaching targeting ligands on nanocarriers, complementary overexpressed receptors can be addressed. With this approach two aims are pursued: to deliver the transport particles to specific cells while sparing normal cells. Once bound to a receptor, the nanocarriers are internalized predominately by receptor-mediated uptake.

Overexpressed receptors which are targeted in preclinical cancer models include G-protein coupled receptors (GPCRs) like bombesin [120] (present on a variety of cancer types including lung, prostate, breast, ovarian and many more), or endothelin receptors [121] (in melanoma tissues), integrins [122] (on activated endothelial and tumor cells), folate receptors [123] (in most tissues),

transferrin receptors [27] (present on breast, ovarian and brain cancers), epidermal growth factor receptors [124] (on lung, breast, bladder and ovarian cells), fibroblast growth factor receptors [125] (in breast, prostate, bladder and gastric cancer), sigma receptors [126] (in non-small lung carcinoma, prostate cancer, melanoma and breast cancer) and others [119] (Fig. 2.3). The angiogenic tumor vasculature can be addressed by targeting [127] of vascular endothelial growth factor (VEGF) receptor, platelet derived growth factor (PDGF) receptor or integrins [128].

Targeting moieties can be natural and artificial ligands. They include small molecules like vitamins (e.g. folic acid or biotin) or bisphosphonates, proteins like transferrin or lactoferrin, growth factors, antibodies, antibody fragments, nanobodies, peptides, saccharides or polysaccharides and aptamers composed of single-stranded DNA or RNA [129]. The efficiency of delivery systems equipped with ligands depends on many factors, for example the affinity, density, accessibility and multivalency of the targeting ligands on the carrier, the concentration of competing endogenous natural ligands in the medium and the size of the particles [54].

There are ongoing discussions about the active targeting approach. For instance, the nanoparticles equipped with ligand may be deposited on tumor cells next to leaky blood vessels, thus compromising their diffusion, penetration and equal distribution in the tumor tissue [130]. The improvement of the accumulation efficiency of delivery devices in tumors by active targeting strategies is still under debate [131] and is believed to be caused by variations in surface characteristics of particles, non-uniformity of tumor models and different targeting ligands [132]. In this thesis we describe experiments which provide an improved comparability by introduction of an internal control or parallelization of potential binding sites, and quantitative assessment. In addition, we investigated control particles with similar surface characteristics to provide appropriate conditions for reliable comparisons. There are some remaining challenges of active targeting approaches and personalized nanomedicine like heterogeneous cell populations arising from genetic, epigenetic or microenvironmental influences [133].

Four different peptide ligands and vitamin B9 were used in this thesis for adhesion studies of receptor targeted nanocarriers. The complementary receptors will be shortly described in the following.

Transferrin receptor targeting

The transferrin receptor (TfR, CD71) is a homodimeric transmembrane receptor with a molecular weight of 190 kDa [134] (Fig. 2.3). Two identical glycosylated subunits of ca. 95 kDa are connected via two disulfide bonds to form the dimer [135]. The monomers contain a large globular extracellular C-terminal domain with the transferrin (Tf) binding site, a hydrophobic transmembrane connection and a short N-terminal cytoplasmic domain [136]. The extracellular domain can be divided in a helical, an apical and a protease-like domain. Two types of transferrin receptors have been discovered so far. While TfR1 is ubiquitously expressed in most proliferating cells, TfR2 is mostly present in tissues where iron metabolism is regulated such as liver and small intestine [137, 138]. The TfR2 subtype has a lower affinity for transferrin and its expression is not correlated with iron levels in contrast to the expression of TfR1 which is inversely correlated with the iron

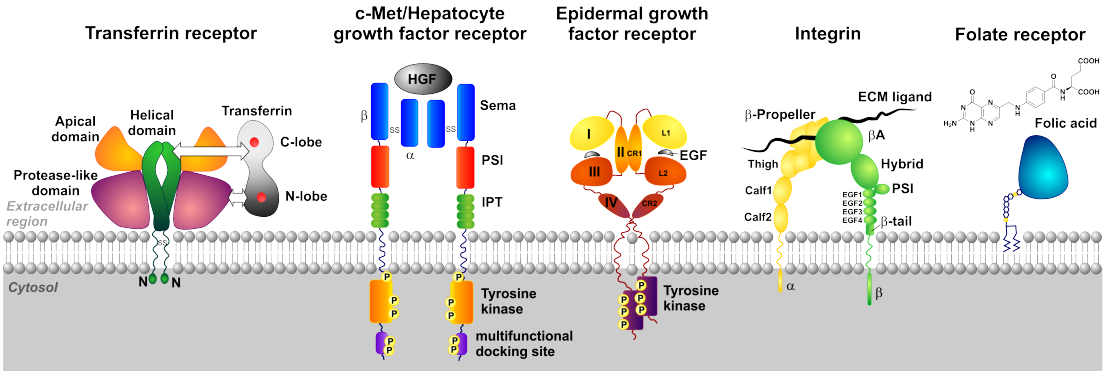

Figure 2.3: Receptors activated by their natural ligands. The transferrin receptor homodimer interacts with diferric transferrin, the c-Met/hepatocyte growth factor receptor (HGFR) homodimer is activated by HGF binding, the asymmetrical epidermal growth factor receptor (EGFR) homodimer is phosphorylated by EGF binding, the integrin α/β heterodimer is illustrated in its active form binding an extracellular matrix (ECM) ligand and the folate receptor (FR) with its natural ligand folic acid are depicted. Abbreviations: HGF, hepatocyte growth factor/scatter factor; PSI, plexin, semaphorin and integrin (domain); IPT, Ig-like, plexins, transcription factors; EGF, epidermal growth factor; sema, sempahorin; ECM, extracellular matrix.

concentration. Both receptor subtypes show 45-66 % similarity in the extracellular domain [139].

The physiological function of the TfR involves the controlled import of transferrin-bound iron which is required for several cellular processes such as DNA synthesis, metabolism and proliferation [140]. Transferrin is a glycoprotein of 78 kDa which reversibly binds iron with very high affinity ($K_d = 10^{-22}$ M at pH 7.4) at the binding sites in the N-lobe and the C-lobe [141]. Only ferric iron (Fe^{3+}) has a high affinity to transferrin and binds to the apo-transferrin present in its open conformation [142]. This induces a conformational change and results in the closed conformation of the holo-transferrin upon binding of a second ferric iron. Ferric iron is almost insoluble in aqueous neutral media and thus is chelated or complexed to proteins or macromolecules [143].

The transferrin receptor homodimer can bind two transferrins which implies the transportation of up to four iron molecules. Transferrin binds to the TfR fast via interaction of the C-lobe with the helical domain of the receptor, or slow by the interaction of the N-lobe with the protease-like domain. The latter process occurs with high affinity in the nanomolar range [144]. Upon binding of Tf to the TfR, the ligand-bound receptor is internalized in a temperature and energy-dependent manner via clathrin-mediated endocytosis [134]. The trafficking of endosomes containing the Tf/TfR proceeds via two pathways: either fast recycling back to the surface or transportation to the endocytic recycling compartment (ERC) [144]. These processes can take place either via static or dynamic endosomes which differ in their maturation kinetics. Most TfR are recycled back to the membrane (85-95 %) [145]. The entire recycling process requires only 10 min on average, but also faster recycling in the range of 4-5 min has been reported [146, 147]. The import of protons pumped by a V-ATPase into the endosome acidifies the vesicle [134]. At a pH of approximately 5.3, two lysine residues of Tf are protonated triggering the release of ferric iron from the Tf/TfR complex [148]. A divalent cation transporter transfers the iron into the cytosol accompanied by reduction of ferric to ferrous iron (Fe^{2+}) via an oxidoreductase.

TfR is expressed in non-proliferating cells at a low level including vascular endothelial cells of brain capillaries, hepatocytes, kupffer cells of the liver, pancreatic cells, breast and kidney cells [149]. Higher levels of the receptor are found on cells with higher proliferation including the basal layer of skin, the endothelium of brain capillaries and crypts of the intestinal villi. In cancer, the TfR is expressed in metastatic and drug-resistant tumors of organs including pancreas, colon, lung and bladder. Correlations of TfR expression with malignancy, aggressiveness and growth are documented as well as high turnover rates of the TfR in tumors was reported [149–151] .

TfR targeting of tumor cells or for delivery to the brain is broadly investigated using the natural ligand Tf, synthetic peptides, antibodies and antibody fragments [27, 152, 153].

Hepatocyte growth factor receptor/c-Met targeting
The c-Met/hepatocyte growth factor receptor (HGFR) is a transmembrane α/β-heterodimer with a molecular mass of 190 kDa [154] (Fig. 2.3). The extracellular part comprises three domains: a semaphorin (sema) domain which contains the whole α-subunit and part of the β-subunit, a PSI (found in plexins, semaphorins and integrins) and a immunoglobulin-plexin-transcription (IPT) domain consisting of four sub-domains [155]. A transmembrane helix connects the extracellular part to an intracellular catalytic tyrosine kinase domain flanked by distinctive juxtamembrane and C-terminal sequences functioning as multi-functional docking sites.

The natural ligand of c-Met, the hepatocyte growth factor (HGF)/scatter factor (SF) is a serine protease secreted by mesenchymal cells in an inactive state [156]. Extracellular proteases cleave the single chain to mature HGF into its active form containing an α- and a β-chain connected by a disulfide bond. HGF/SF is a pleiotropic factor (one gene influences more phenotypic traits) and cytokine (regulates growth and differentiation of cells) which promotes cell proliferation, survival, motility, scattering, differentiation and morphogenesis [157]. In multiple diseases, HGF acts protective, for example in liver cirrhosis or lung fibrosis [158, 159]. The ligand can bind at the two binding sites of c-Met/HGFR [157]. First, the IPT3 and IPT4 domains bind the N-domain of HGF/SF with high affinity, independent of the maturation state of the ligand. Second, the sema domain binds the HGF/SF with low affinity, only when the ligand is fully matured. Upon binding to c-Met, homodimerization and phosphorylation of two tyrosines in the catalytic part of the kinase domain occur. This activation triggers the phosphorylation of two other C-terminal tyrosines and the recruitment of effectors. Signaling cascades activate several processes including proliferation, cell motility, cell cycle progression, transformation, invasion, cell migration and non-adhesive growth, positive and negative feedback on c-Met [155].

The internalization of c-Met is mainly clathrin-and dynamin-dependent [160]. Often, the E3 ubiquitin ligase c-Cbl is involved in the uptake process. Trafficking of c-Met from early endosoms to perinuclear regions can occur along microtubules and protein kinase C promotion and non-receptor tyrosine phosphatase PTP1B [161]. For degradation, direct binding of c-Cbl to Met is required.

Physiologically, c-Met regulates many essential processes in cell development and function and wound healing. It is expressed in epithelial cells of organs including liver, pancreas, prostate, kidney, muscle and bone marrow, during both embryogenesis and adulthood [162]. Aberrant regulation of the proto-oncogene c-Met and its protein product results in development and progression of several types of cancer [163]. The decisive and continuous activation of c-Met can occur by several mechanisms including genetic alterations, transcriptional overexpression and ligand-depended mechanisms. The up-regulation is caused by activation of oncogenes, inactivation of suppressor genes, down-regulation of mRNAs or by hypoxia (oxygen depletion) [164]. Cancer therapies which target HGF/c-Met are mainly kinase inhibitors and antibodies. Only few nanoparticle-based strategies deliver therapeutics into c-Met expressing cells or tissue. The targeting moieties include antibodies and peptides [165, 166].

Epidermal growth factor receptor targeting

The epidermal growth factor receptor (EGFR) is a heavily N-glycosylated protein of 170 kDa [167] (Fig. 2.3). Approximately 20 % of its molecular weight are carbohydrates. The glycosylation is important for the receptor-ligand interactions. The EGFR contains an extracellular region which is divided into four domains: domain I, II, III and IV. The domains I and III exhibit a leucin-rich repeat, thus are called L1 and L2 and both contribute to ligand binding [168] with an affinity of ca. 400 nM [169]. The domains II and IV are similar to those in laminin with several disulfide bonds and are termed cysteine-rich domains (CR1 and CR2) [170]. Monomeric EGFR is autoinhibited in a tethered, closed conformation and extends to an untethered open conformation upon dimerization which is fully receptor-mediated [171]. Ligand binding stabilizes the open state. Apart form the extracellular part, the EGFR contains a hydrophobic transmembrane region and an intracellular catalytic tyrosine kinase domain and multiple tyrosine moieties.

The EGFR family consists of four receptors: EGFR (erbB-1/Her1), erbB-2 (Her2), erbB-3 (Her3) and erbB-4 (Her4). Pairing of specific monomers results in different functionality. While ligand binding is obligatory for Her3 and Her4, there is no activating ligand for Her2 [172]. In general, there are several ligands for the EGFR including epidermal growth factor (EGF), transforming growth factor alpha (TGFα), heparin-binding EGF-like growth factor, amphiregulin, epiregulin, β-cellulin, epigen and neuregulin 2β [173, 174]. The ligands are integral membrane proteins which are cleaved by metalloproteinases to yield mature ligands.

The activation of EGFR does not depend on the phosphorylation of the activation loop [175]. The receptor is rather activated by the formation of an asymmetric dimer where the C-terminal lobes of two kinase domains interact with each other. Ligand binding recruits two monomers resulting in dimerization and subsequent activation of the kinase domains. Several ligands induce dimerization and heterodimerization with related receptors which results in receptor autophosphorylation of approximately 10 tyrosine residues [176]. The phyosphorylated tyrosins are binding sites for several cytosolic proteins with Src homology 2 (SH2) domains or phosphotyrosine binding motifs. The recruitment of multiple downstream effectors results in the activation of signaling cascades which for example stimulate proliferation and cell survival [177]. Phosphorylation of Tyr974 induces

endocytosis and activation of Tyr1045 triggers EGFR ubiquitination and proteosomal degradation [178, 179]. EGF binding promotes internalization to lysosomes while signaling is sustained until the receptor is degraded. In contrast, TGFα dissociates from the receptor in the endocytic recycling compartment. The main route of EGFR internalization is clathrin-mediated endocytosis, followed by fusion with early endosomes and sorting compartments from where the receptor is recycled back to the surface or to multivesicular bodies (MVB) from where it can follow the pathway to lysosomal degradation [180]. EGFR is constitutively endocytosed and recycled back to the surface with a half-life of 30 min in the absence of ligand. The receptors remain on the cell surface most of the time (80-90 %) [181].

EGFR normally regulates cell proliferation, survival and differentiation. In cancers, receptors are overexpressed and continuous signaling is activated for instance caused by mutations or hypoxic tumor microenvironment which can promote increased EGFR mRNA translation. In many types of cancer, EGFR is overexpressed including head and neck, breast, renal, non small cell lung, colon, ovarina, glioma, pancreatic and bladder cancer [182]. The malignant states influence cell motility, proliferation, angiogenesis and reduced apoptosis. Cancer therapies target the function of the kinase domain with tyrosine kinase inhibitors like erlotinib (Tarceva) or monoclonal antibodies, e.g. cetuximab (Erbitux) [183]. Furthermore, EGFR targeting is performed using antisense oligonucleotides, antibody based immunoconjugates, peptides, affibodies and nanobodies are used apart from small molecule kinase inhibitors and monoclonal antibodies [124].

Integrin targeting
Integrins are integral membrane proteins which link the extracellular matrix (ECM) to the cytoskeleton [184] or bind other adhesion receptors on neighboring cells (see Fig. 2.3). They are heterodimers of an α- and a β-subunit [185]. At least 24 heterodimers exist which are combinations of 18 α- and 8 β-subunits. The subunits usually consist of 750-1000 amino acids and their domains are connected by flexible linkers. They are integrated into the membrane via a single helix and posses a short unstructured cytoplasmic tail. The α-subunit consists of four or five extracellular domains including a seven-bladed β-propeller, a thigh and two calf domains (and half of the subunits contain a α-I domain). Within the β-propeller are at least three or four Ca^{2+}-binding sites which influence ligand adhesion upon Ca^{2+} binding. The β-subunit has seven domains: a βI-domain, a hybrid domain, a plexin-semaphorin-integrin (PSI) domain, four cysteine-rich epidermal growth factor (EGF) modules and a β-tail domain. In an inactivated state, the integrin heterodimers are in a bent conformation with low ligand affinity which is also present in a primed, extended conformation with closed head-piece. In the active state, the conformation is extended presenting an open head-piece and high ligand affinity [186].

The combination of the heterodimeric integrins implicates the binding of one or more ligands. The integrin $\alpha v\beta 3$ binds for instance vitronectin, fibronectin, von Willebrand factor (vWF), tenascin, osteopontin, fibrillin, fibrinogen and thrombospondin [119].

The αv and $\alpha v\beta$n integrins are highly expressed in activated endothelial cells and tumor cells while

they are not present in resting endothelial cells or most adult epithelia. The expression of integrins αvβ3, αvβ5, α5β1, α6β4, α4β1 and αvβ6 is correlated with disease progression in numerous tumor types and thus investigated most in cancer studies [187]. The expression and exposure of various integrins at the cell surface determines to which ligand or cells they bind and thus the survival in a particular microenvironment. Their functions involve physiological processes like development, maintenance and repair of tissues as well as pathological processes including proliferation, differentiation, the sprouting ability of endothelial cells during angiogenesis, invasiveness of tumor cells and cell migration [188, 189]. The regulation of their functions is achieved by ligand engagement, binding of intracellular proteins and endocytic uptake and trafficking [190]. The internalization of integrins occurs via various endocytic pathways including clathrin- or caveolin-mediated mechanisms and is highly dependent on the combination of the heterodimer, cell type, stimuli and matrix [191]. Usually, integrins have a long half-life, are mainly recycled back to the plasma membrane and barely degraded [190].

The targeting of integrins involves both the tumor cells and the supporting vasculature [192]. Mainly αvβ3 integrins are addressed by various ligands including peptides, peptidomimetics and non-peptide ligands which simulate the RGD (arginine-glycine-aspartic acid) sequence of several ECM proteins [122].

Folate receptor targeting
The folate receptor (FR) is a cysteine-rich glycosyl phosphatidylinositol (GPI) anchored gylcoprotein which binds folate with high affinity ($K_d \approx 0.1$ nM) [193] (see Fig. 2.3). Folate receptor α has a globular structure which is stabilized by eight disulfid bonds and incorporates a deep binding pocket for folate with conserved residues in all receptor subtypes (α,β,γ,δ) [194].

The natural ligand, folate (vitamine B9) occurs either in its oxidized state as folic acid or in its physiologcially active reduced state as tetrahydrofolate (THF) [195]. Reduced folates have biosynthetic functions including the synthesis of DNA and RNA, metabolism of amino acids, and methylation reactions. Subsequently they are involved in the differentiation, proliferation and survival of cells [196]. Folate can be internalized by cells via three different routes: 1) proton-coupled folate transporters (PCFT) import the vitamin in acidic environments of the upper small intestine [197]. Hereditary folate malabsorption has severe consequences which occur within few month after birth, for example anemia, recurrent or chronic diarrhea and hypogammaglobulinemia [198]. 2) Reduced folate carriers (RFC) which are ubiquitously expressed are usually the main route for folate internalization at physiological pH [196]. This anion exchanger absorbs reduced folates and organic phosphates, but has very low affinity for folic acid [199]. 3) Folate receptor endocytosis internalizes folates and 5-methyl-THF, the major circulating form of folate, both exhibiting high affinities to the receptor in the range of 0.1-1 nM [200]. Folate receptor endocytosis includes a variety of uptake pathways [201]. Mainly clathrin-independent pathways are suggested for FR uptake. Only after cross-linking of the receptors, selective localization to caveolae has been reported which is followed by caveolae-mediated uptake [202]. The majority of FRα (50-75 % is located in endosomal compartments and the recycling back to the surface via the endocytic recycling compartment is slow [203].

Whereas FRα is expressed in low levels in normal cells and tissues, it is upregulated in many human cancer cells of organs including the ovary, brain, kidney, breast, colon, myeloid cells and lung [119], but mostly not elevated in sarcomas, lymphomas and cancers of pancreas, testicles, bladder, prostate and liver [200]. FRα is required to increase the concentration of folate in fast dividing cancer cells [204]. There is evidence that FR expression is correlated with advanced stages of disease [205] and overexpression is accompanied by poor prognosis for breast, colorectal, ovarian and endometrial cancers [206]. Folic acid is widely used for tumor targeting as this vitamin is small, cheap and easy to attach to nanocarriers.In addition, it is non-toxic and non-immunogenic [207, 208].

2.3 Cellular uptake, trafficking and endosomal escape

Cellular uptake

The internalization of nanocarriers into cells can occur via natural processes or can be induced by physical methods. The latter include several procedures: 1) the direct introduction of delivery systems or therapeutic cargo via microinjection [209] into the cytosol or nucleus of the cells, 2) the application of an electrical field to increase the permeability of the cell membrane (electroporation) [210], and 3) the destabilization of the plasma membrane by treatment with ultrasound (sonoporation) [211]. However, these strategies have limitations in their practical use as they require detailed knowledge of localization or compromise the cell integrity.

Small molecules which are essential for cell survival, such as sugars, ions and amino acids, cross the cell membrane through integrated pumps or ion channels. Nanocarriers and macromolecules cannot traverse this double-layered lipid barrier and are internalized by encapsulation into membrane vesicles (endocytosis). The highly regulated endocytotic pathways mediate complex physiological processes, for example signal transduction via hormones, antigen-presentation, immune control and cellular homeostasis [212]. The uptake of large particles is called "cell-eating" or phagocytosis and the upatke of fluid and solutes is termed "cell-drinking" or pinocytosis.

Phagocytosis is typically restricted to specialized mammalian cells such as macrophages, neutrophils and monocytes. These cells decompose pathogens like bacteria, or cell debris and other remnants [79] which attach to receptors presented on the cell surface, e.g. Fc receptors, complement receptors and phosphatidylserine receptors that are recognized by dead cells. The binding induces a signal transduction and the recruitment of actin. By extension of the membrane, the pathogens are enclosed and degraded by free oxygen radicals and acidic hydrolysis in the phagosomes.

Pinocytosis pathways are categorized into at least four types: 1) macropinocytosis, 2) clathrin-mediated endocytosis (CME), 3) caveolin-dependent endocytosis and 4) clathrin- and caveolin-independent endocytosis (Fig. 2.4). *Macropinocytosis* is stimulated by activation of tyrosine kinases upon growth factor binding or other stimuli [214]. Driven by changes of the actin structure, membrane ruffles are formed which protrude from the cell and collapse onto the plasma membrane

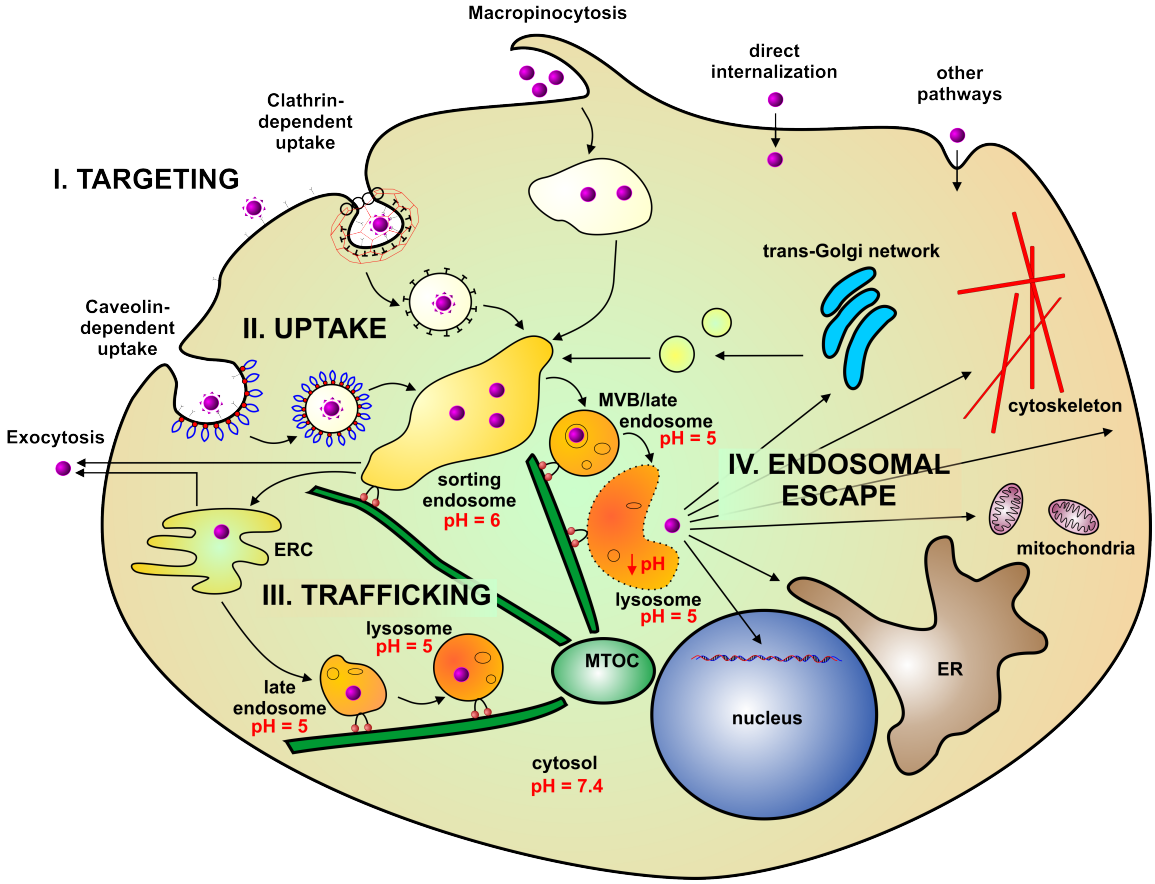

Figure 2.4: Cellular uptake and internal transport of nanoparticles. Nanoparticles internalized by various uptake pathways into endosomal vesicles are transported within the cell along cytoskeletal structures mediated by motor proteins. The nanoparticles in early endosomes can be transferred to sorting endosomes, or excreted from the cell by fusion with the plasma membrane. An alternative pathway involves the maturation into lysosomes accompanied by acidification and recruitment of degradative enzymes. The nanoparticles must escape from the endosomal vesicles to reach cytoplasmic or nuclear targets after translocation in the respective compartment and diffusion through the crowded cytoplasm. Abbreviations: ERC, endocytic recycling compartment; ER, endoplasmic reticulum; MTOC, microtubule-organizing center; MVB, multivesicular bodies. The figure is inspired by Chou *et al.* [213] and modified according to Sun *et al.* [34].

to form macropinosomes (0.5-10 μm). By these uptake pathways small and larger particles are internalized non-specifically. *Clathirin-mediated endocytosis* involves the more selective uptake of essential nutrients like cholesterol bound to low density lipoprotein (LDL)-receptor, or transferrin (Tf) bound to the Tf receptor (TfR). Furthermore, CME supports cell and serum homeostasis and controls the levels of ligand-bound surface signaling receptors by concentration and internalization thereof [215]. Coated pits are formed by polymerization of the cytosolic protein clathrin in combination with assembly proteins. These vesicles (ca. 120 nm) are pinched off by the small GTPase dynamin [216]. After disassembling of the clathrin coat, vesicles merge with early endosomes [217]. *Caveolin-mediated endocytosis* involves the enrichment and internalization of multiple signaling molecules and membrane transporters in flask-shaped lipid microdomains of cholesterol and sphingolipid-rich plasma membrane (caveolae) [218]. The hairpin-like membrane protein caveolin is integrated in these structures which binds and promotes sorting of several molecules including lipids, fatty acids and membrane proteins [219]. In combination with other proteins like cavin, which induces surface curvature, and dynamin, which promotes budding, endosomal vesicles (ca. 60 nm) are formed [220]. They merge with caveosomes or multivesicular bodies (MVBs) at neutral pH and can circumvent fusing with liposomes [221]. This uptake mechanism is in general slower than CME. *Clathrin- and caveolin-independent endocytosis* can be categorized into Arf6-dependent, fotillin-dependent, Cdc42-dependent and RhoA-dependent pathways according to their effectors [215]. Cholesterol-dependent membrane parts with specific compositions are involved in these uptake routes.

Apart from endocytotic pathways, nanocarriers can enter cells via other mechanisms including membrane fusion [222], transient induction of holes in the membrane [223, 224] or via cell-penetrating peptides [225]. These processes do not compromise the integrity of the cell membrane.

The uptake pathway by which a nanocarrier is internalized depends on its structure and physicochemical properties (size, shape, charge, hydrophobicity) and is governed by the surface modification and adsorption of biological molecules [220]. These characteristics can alter the uptake route and efficiency. Many positively charged nanoparticles are predominantly internalized by CME. An exception are for instance PEI-based polyplexes, which take several uptake pathways including caveolae-mediated endocytosis [226]. In cell culture assays, the excess of free polymer could have an impact on internalization. Negatively charged nanoparticles preferentially use caveolae-dependent endocytosis [227]. The impact of the particle size is discussed in literature, but there are no clear tendencies and it is suggested that chemical composition has a much higher influence [220]. Uptake capability and efficiency is further affected by the shape of the particles and their orientation [228]. Moreover, the cell line into which the delivery systems are transferred are crucial as they may be able or may not be able to internalize particles via specific uptake routes. Furthermore, other cell line-related factors may contribute to preferential uptake pathways.

Trafficking

Internalized nanoparticles encapsulated in membrane vesicles are transported within the cells along cytoskeletal structures (trafficking) or are secreted from the cell back into the extracellular space

(exocytosis)(Fig. 2.4). Usually, the cargo in the vesicles first arrives in early endosomes. In this organelle, the nanomaterial is sorted and can be transported via several pathways including routes to late endosomes and lysosomes for degradation, to the trans-Golgi network, or to the endocytic recycling compartment (ERC) from where receptors and other payload is returned to the plasma membrane [229]. The transport involves motor proteins carrying the vesicles along the cytoskeleton e.g. on microtubules [213]. The pH varies in different endosomal compartments, for example acidification occurs during maturation of early endosomes via late endosomes into lysosomes.

Endosomal escape
There are several strategies for nanocarriers to escape from endosomes to release their cargo at the target site where it can execute its therapeutic effect. These mechanisms include 1) pore formation in the endosomal membrane, 2) swelling and rupture due to a pH buffering effect, 3) fusion in the endosomal membrane and 4) photochemical disruption of the endosomal membrane [230].

Peptides with high affinity to lipids can insert into the lipid bilayer of the endosome and cause tension [230]. When they cluster into barrel-like or toroid-shaped structures, the tension can be reduced and pores are formed. Thus, small cargo can diffuse out of the vesicles. *Pore formation* is also one of the processes bacteria use for endosomal escape [231].

Another escape mechanism is the so termed *"proton sponge hypothesis"* which exploits the buffering capacity of certain cationic polymers or other agents which usually contain secondary and/or tertiary protonatable amine groups with pK_a values in the range of the endosomal/lysosomal pH [232]. During maturation of the endosome, membrane integrated V-ATPases pump protons into the endosomal compartment which is accompanied by the influx of chloride ions and water. Successive protonation results in continuous import of protons and increased osmotic pressure. Different theories exist to explain the release of the endosomal content [54]. One explanation is that the enhanced pressure leads to swelling of the vesicles and finally rupture of the endosome. Furthermore, the protonatable agent is believed to interact with the phospholipid membrane which causes in addition tension and permeabilization of the membrane. This processes might contribute to cargo release from the endosome.

The sheath of enveloped viruses can fuse with the lipid bilayer via single integral membrane peptides (fusogenic peptides). These molecules can undergo a conformational change via certain triggers such as pH changes, which initiates fusion in the membrane [233]. By insertion of fusogenic peptides on nanocarriers, the payload can exit the endosome by *membrane fusion*.

Photochemical internalization (PCI), the photochemically induced endosomal release strategy, is achieved by using photosensitizer which localize mainly in membranes of endosomes and lysosomes [234]. Upon excitation with light, reactive oxygen species (ROS), predominantly singlet oxygen is generated which destroys the membrane integrity. The cargo of the vesicles can escape without damage.

Several natural products derived from viruses, bacteria, plants, animals and humans as well as synthetic peptides and chemical agents are used to promote endosomal escape of nanocarriers which is one of the main hurdles of gene and drug delivery [230].

3 Fluorescence microscopy

In past decades, a huge variety of nano-sized materials have been developed involving the demand for imaging techniques of their interactions with biological systems in a non-invasive manner. In this respect, fluorescence microscopy represents a powerful tool. Many fluorescent dyes such as organic molecules, nanocrystals or fluorescent proteins have been evolved covering a large spectral range of visible light and part of the infra red (IR) and ultra violett (UV) regions. With elaborate labeling techniques it is possible to mark specific molecules in order to visualize certain cellular or extracellular regions. Using multiple colors, different parts of a specimen overlapping or intersecting each other can be imaged. So, also distinct biological processes can be observed surrounded by many others occurring simultaneously in the immediate environment [235]. With the improvement of bio-orthogonal fluorophores concerning their solubility, quantum yield and photochemical stability, an enormous variety of biological systems is imaged nowadays ranging from whole living animals, huge samples like tissues over cells and subcellular regimes down to the interaction of single large molecules in the nanoscale range. By live-cell imaging, dynamic processes were visualized in real-time, for example, studying the internalization dynamics of receptor targeted gene delivery systems [236] with single particle tracking. Applying quantitative analysis, uptake [237] and uptake kinetics [238] of nanoparticles into cells were investigated. Furthermore, mechanistic insights into the uptake pathway of receptor targeted nano therapeutics [239] or the controlled endosomal escape of delivery devices via photosensitizer activation [240] have been gained.

Widefield microscopy provides sufficient temporal resolution to measure processes in real-time, but the spatial resolution is restricted to few hundred nanometers. Besides this conventional fluorescence microscopy technique, advanced methods have emerged in the past decades [241]. An approach with improved axial resolution, thus enabling resolution in all three spatial dimensions is confocal microscopy. As the focus volume is reduced and out-of-plane fluorescence is not measured, the background is highly reduced. Though, to obtain the whole image, the sample has to be scanned which extends the acquisition time. Fortunately, fast scanning systems and advanced approaches like spinning disks for simultaneous illumination and detection of multiple points have been developed. Another approach to increase the axial resolution of a large field of view without scanning [242] can be achieved by total internal reflection microscopy (TIRFM) [243]. Various other fluorescence techniques can be combined with microscopy, including quantitative approaches like fluorescence recovery after photobleaching (FRAP) [244], Förster resonance energy transfer (FRET) [245] and co-localization. Thus, diffusion coefficients of cargo released by nanocarriers [246], receptor trafficking dynamics [247] or the fate of biodegradable drug delivery systems [248] can be studied.

Spatial resolution can be improved by multiple techniques including structured illumination microscopy (SIM) [249], near-field optical microscopy (NSOM) [250], 4Pi microscopy [251], I^5M mi-

croscopy [252] or light sheet microscopy (LSM) [253] can be applied. In addition, resolution down to few nanometers (ca.20 nm) can be achieved by super-resolution microscopy, whose development was awarded with the Nobel prize in chemistry 2014 [254]. These methods include the raster scanning microscopy approach with stimulated emission depletion (STED) and the localization-based techniques like photoactivated localization microscopy (PALM) [255], fluorescence photoactivation localization microscopy [256] or stochastic optical reconstruction microscopy (STORM) [257]. These methods require high labeling densities, photoswichable or phototunable dyes, often high laser powers and are restricted in acquisition time. These requirements can induce non-physiological behavior and phototoxicity.

Depending on the research question and subsequent the addressed problem, the most adequate fluorescence methods and evaluation tools should be chosen. In this work, widefield microscopy was used to study the cellular adhesion of nanoparticles and spinning disk microscopy was employed for characterization of nanoparticles as well as to explore their specific attachment to receptors. In this chapter, these microscopy methods will be introduced, with respect to their spatial resolution after description of the principles of fluorescence and characteristics of fluorophores.

3.1 Principles of fluorescence

A molecule can be excited from its electronic ground state (S_0) into its first (S_1) or higher excited states (S_{1+x}) by the absorption of light if its energy is at least the difference of the two states. The excitation energy E is inversely proportional to the wavelength λ of the excitation light:

$$E = \frac{h \cdot c}{\lambda} = h \cdot \nu \tag{3.1.1}$$

where h is the Plank's constant, c the speed of light in vacuum and ν is the excitation frequency. Excitation and emission processes are depicted in a Jablonski diagram in Fig. 3.1 [258]. A fluorophore in its ground state can absorb one or more photons within femtoseconds (blue arrows). The probability of absorbing a photon is given by its molar extinction coefficient ε. It is excited more likely when the electric field of the excitation laser light is polarized parallel to the molecule's dipole moment [259]. During excitation with an energy of at least the difference between the first excited and ground state (S1-S_0), usually vibrational changes occur as well according to the Franck-Condon principle. The molecule does not stay long in its excited state and returns to its ground state by radiative and non-radiative transitions. First, energy is transferred to surrounding molecules by direct interactions during vibrational relaxation (purple arrows). Within the same time range, internal conversions occur by isoenergetic transition from vibrational modes of an excited state to high vibrational levels of a lower excited electronic state (gray arrow). Then, from the vibrational ground state of an excited singlet state (S_1), fluorescence is emitted when the molecule relaxes back to the electronic ground state (S_0) by radiating a photon (green arrow). This process takes place in the range of nanoseconds. The cycle is repeated until the molecule photobleaches. Good fluorophores have a high quantum yield which represents the ratio of emitted to absorbed light. A maximum value of 1 is obtained when all absorbed photons are emitted. Another pathway for an excited

fluorophore to return to the ground state is to undergo a spin-forbidden transition to the triplet state (T_1), the so-called intersystem crossing (red dotted arrow). As another forbidden transition is required to return to the ground state (S_0), it can remain in the triplet state for microseconds. Returning back to the ground state by emitting a photon is called phosphorescence (orange arrow). Long-lived triplet states are disadvantageous for good fluorophores as they prevent the molecule to cycle through absorption and fluorescence emission. In addition, the lifetime of the fluorophore is extended which represents the time it spends in the excited state before emitting a photon.

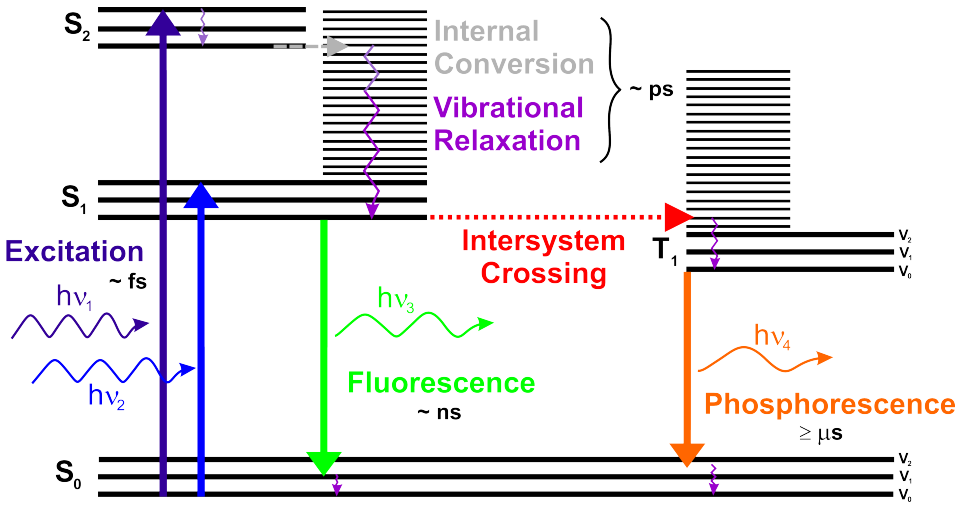

Figure 3.1: Jablonski diagram. The energy states of a molecule are shown. By light absorption, the molecule is excited from its electronic ground state, S_0, to an excited singlet state, S_1, S_2,etc. within fs (blue). By non-radiative transitions, the molecule relaxes to electronic states of lower energy within ps, including vibrational relaxations (purple arrows) to the vibrational ground state, V_0, internal conversion (gray arrow) to higher vibrational states of a lower electronic excited state and intersystem crossing red arrow), the isoenergetic forbidden transition to a triplet state, T_1, by spin conversion. Radiative transitions back to the ground state occur as fluorescence (green arrow) within ns or as phosphorescence (orange arrow) within μs. Schematic adapted from Lichtman *et al.* [258].

In Fig. 3.2, the absorption and emission spectra of ATTO 488 are shown. The absorption spectrum (blue line) illustrates the wavelengths at which the dye can be excited. Photons are absorbed more likely at the absorption maximum. The fluorescence emission spectrum (green line) usually has a mirror symmetry. The emission maximum is offset to longer wavelengths with respect to the absorption spectrum, the so termed "Stokes shift". This displacement occurs due to energy losses during non-radiative de-excitation processes such as vibrational relaxation and internal conversion.

3.2 Fluorophores

Typical fluorescent molecules usually have conjugated double bonds or aromatic systems delocalized electrons. The more rigid and the more extended a π-electron system is, the lower is the distance between energetic levels. This means, light with less energy, i.e. longer wavelength, is

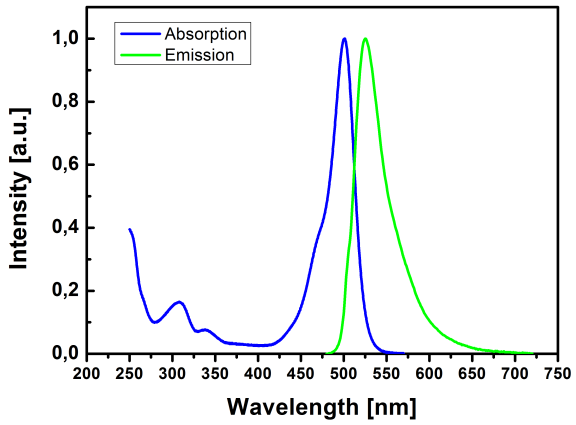

Figure 3.2: Absorption and fluorescence emission spectra of ATTO 488. The absorption spectrum (blue) and the emission spectrum (green) have mirror symmetry and are separated by the Stokes shift. Values taken from [260].

required to excite the molecule. Moreover, a high photostability is advantageous meaning the resistance against irreversible damage caused by light exposure. Apart from bleaching, the fluorescence can be diminished by quenching processes, like excited state reactions, the transfer of energy to a close-by molecule, the formation of a complex with another molecule, or the collision with molecules which promote non-radiative de-excitation [261], such as oxygen or iodide.

To link a fluorophore to biological samples, a variety of methods is available including covalent coupling chemistry, adsorption processes, intercalation of molecules, gene expression of fluorescent proteins tags and immunostaining. In Fig. 3.3, the chemical structures of the fluorophores used in this work are depicted as way of example. To visualize the nuclei of cells the DNA can be stained by 4',6-diamidino-2-phenylindole (DAPI) which intercalates into A-T rich regions of double-stranded DNA. The fluorescence emission maximum of DAPI is around 461 nm. This dye also interacts with RNA, but the fluorescence signal is much lower. The xanthene dyes ATTO 488, Alexa Fluor 488 and FITC, and the indocarbocyanine dyes Cy5 and Alexa Fluor 647 are typical organic dyes. They are usually coupled covalently to functional groups of biological probes or nanoparticles via reactive groups. Fluorophores are linked to amino groups for example with reactive esters, carboxylates, isothiocyanates and sulfonyl halogenides. Thioles can be labeled via maleimide or iodocaetamide chemistry. Biocompatible and specific attachment of fluorophores to alkynes or azides is achieved by click chemistry. Differently, the green fluorescent protein (GFP) discovered in the jellyfish *Aequorea Victoria* can be tagged on many proteins via genetically engineering [262]. The fusion protein is preferentially attached at the C- or N- terminus of a protein where it does not influence its function. In the center of the β-barrel structure of GFP, the amino acids serine65, tyrosin66 and glycine67 are post-transcriptionally modified to yield the chromophore of the fluorescent protein [263]. The absorption maxima of GFP are at 395 nm and 475 nm.

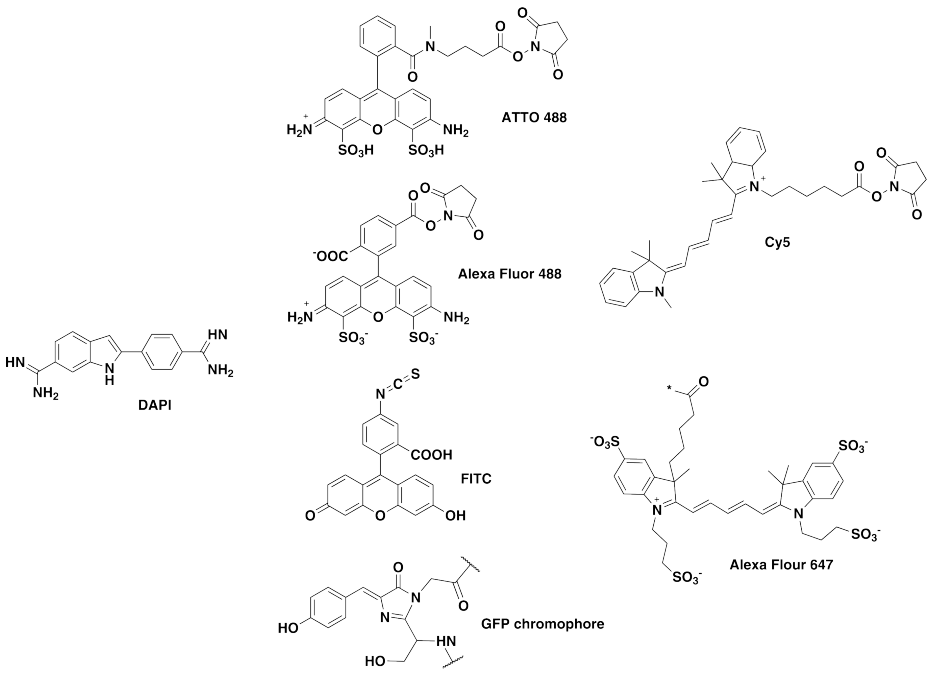

Figure 3.3: Fluorophores. Chemical structures of the fluorophores used in this work are depicted. The dye 4',6-diamidino-2-phenylindole (DAPI) was excited with a 405 nm laser, the xanthene dyes ATTO 488-NHS, Alexa Fluor 488-NHS and fluorescein isothiocyanate (FITC), as well as the chromophore of the green fluorescent protein (GFP) consisting of post-translational modified Ser65Tyr66Gly67 can be excited with a 488 nm laser and the indocarbocyanines Cy5-NHS and Alexa Fluor 647-carboxy with a 633 or 639 nm laser.

3.3 Widefield and spinning disk microscopy

The fundamentals of modern light microscopy are based on the diffraction of light by the specimen and the objective lens which limit the resolution of an image [264]. The image of a point emitter is described by its point spread function (PSF). In the lateral plane, this diffraction image consists of concentric bright and dark circles alternating with gradually weaker intensity. Two emitters can be resolved when the central bright disk, the so termed Airy disk, of the one spot is located at least in the first minimum of the second spot or further apart (Rayleigh criterion). The lateral resolution, i.e. the radius of the Airy disk r is defined by the wavelength λ of the emitted light and the numerical aperture (NA) of the objective:

$$r = 0.61 \cdot \frac{\lambda}{NA} = 0.61 \cdot \frac{\lambda}{n \cdot sin\alpha} \tag{3.3.1}$$

where n is the refractive index of the medium between objective and cover slip and α the half angle of the aperture. This resolution applies to conventional widefield microscopy in the lateral plane. In axial direction however, the sample should be imaged in the focus plane, otherwise it will appear blurred. Depending on the type of the objective, air, water or oil are between the lens and the cover glass.

In Fig. 3.4 A, a typical light pathway of an epi-fluorescent widefield microscope is depicted. From a

light source, a beam is focused on the back focal plane of a condenser illuminating the sample on a cover slip. A convenient light source is a laser as it provides intense, coherent and monochromatic light. If several laser lines are used in a microscope, an accusto optical tunable filter (AOTF) can be integrated in the light pathway to enable selection of the desired wavelength. When a radio frequency is applied to such a piezo crystal, a diffraction grating is created and diffracts light of only a narrow band of frequencies. By varying the amplitude of the sound wave, not only the range of selected wavelengths can be tuned, but also the intensities. In an epi-fluorescent microscope, the condenser is also the objective lens which magnifies the sample and collects the emitted fluorescent light. Thus, only the small amount of reflected excitation light has to be separated from the emission light. A dichroic mirror separates the emission from the excitation light by reflecting a certain range of wavelengths while transmitting others. Implementing bandpass filters in the emission pathway narrows down the range of wavelengths arriving at the camera. The fluorescence is typically detected by charged coupled devices (CCD) cameras. Improvement of sensitivity and thus the number of images recorded before a probe photobleches is achieved by electron multiplying CCD (EMCCD) cameras using impact ionization for increased EM gain.

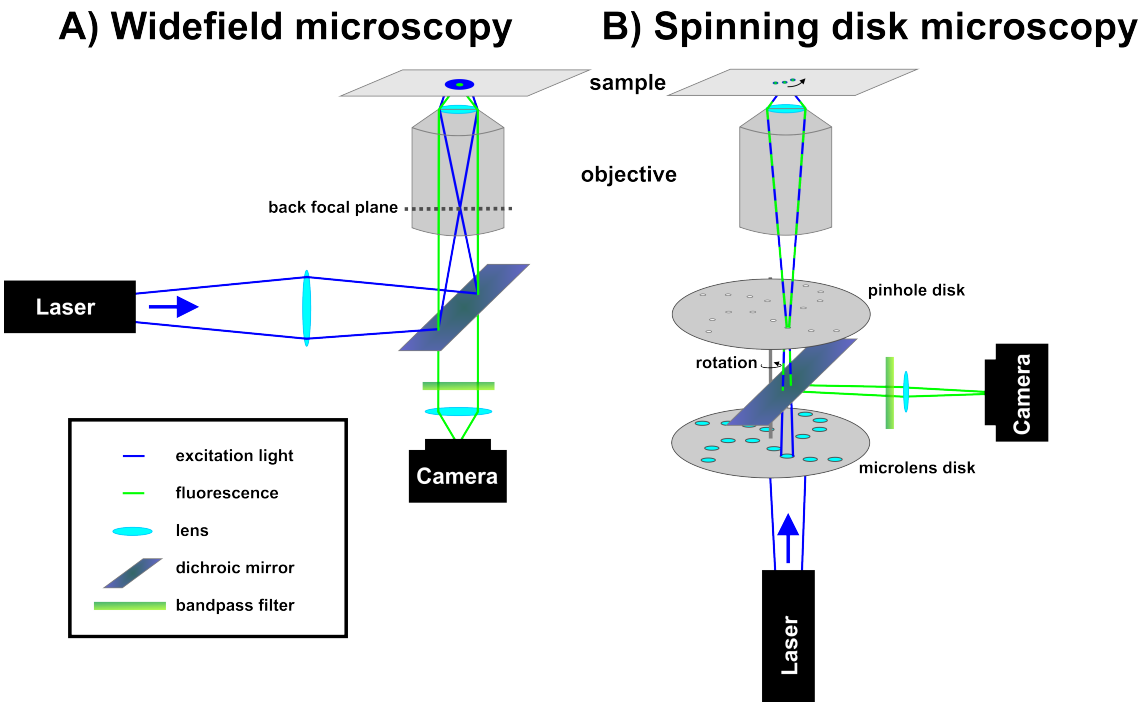

Figure 3.4: Principles of widefield and spinning disk microscopy. In a widefield microscope the excitation light is focused on the back focal plane of the objective and illuminates the sample after passing the objective with a wide beam. In an epi-fluorescent mode, the fluorescence emission is collected by the objective, separated from the excitation light by a dichroic mirror and directed onto a CCD camera after passing an emission filter. In a confocal spinning disk microscope, the laser light is directed through a spinning disk unit. Using Yokogawa technology, mikrolenses on a first rotating disk focus the excitation light onto pinholes on a second disk. Thus, only a small confocal volume of the sample is excited with light after passing the objective. The fluorescence is collected by the objective and again passed though the rotating pinhole disk, separated from the excitation light by a dichroic mirror and recorded by a camera after passing a pinhole and emission filter. With this method the sample can be resolved with increased axial resolution.

Resolving a fluorescent probe in the axial direction is enabled by confocal microscopy. This technique uses the implementation of a pinhole into the light pathway restricting the excitation and/or emission volume of the sample. This means that only the focal plane is illuminated and/or the fluorescence of the focal plane detected while out-of-focus signal does not pass through the pinhole. The signal-to-noise ratio is improved and hence the contrast is increased. However, only small regions of the sample are probed and raster scanning has to be applied to obtain the whole image. This procedure takes time and restricts the temporal resolution.

The scanning speed can be drastically reduced by insertion of a Nipkow disk into the conjugated image plane [265]. This spinning disk with multiple perforations allows for parallel point-illumination and detection of the specimen. Though, a high percentage of the illumination light does not reach the sample and is reflected which can cause background signal. An advanced system represents the Yokogawa spinning disk unit (see Fig. 3.4 B). A second disk with 20 000 microlenses is used to focus the illumination beam on the pinhole disk mounted on the same axis. Hence, the excitation light arriving at the probe is one order of magnitude increased. Emitted light is passed through the pinhole disk and reflected by a dichroic mirror between the two disks. The axial resolution of a spinning disk microscope with a pinhole disk depends on the refractive index n of the medium between objective and cover glass, the wavelength λ and the numerical aperture NA:

$$r = 0.67 \cdot \frac{\lambda}{n - \sqrt{n^2 - NA^2}} = 0.67 \cdot \frac{\lambda}{n(1 - \sqrt{1 - sin^2\alpha})} \tag{3.3.2}$$

where α is the acceptance angle of the objective. The fluorescence recorded in the axial direction should be detected at a distance of not more than half of the axial resolution [266] to avoid undersampling (Nyquist criterion). Otherwise signals with artifacts might be obtained.

4 Model nanoparticles for receptor targeting studies

With the increasing interest in nanoparticle based strategies for diagnostics[267] and therapy[14, 268], precise and reliable investigation strategies are required to be able to develop biocompatible and efficient nanosystems. To gain insights into the efficiency of nanoparticles to detect, image, target or treat diseased cells and tissue [269, 270], standard procedures include as a first step cell culture based assays, followed by experiments in animals until finally clinical trials are performed. After administration into the test system, the nanoparticles can interact with the surrounding components like proteins, ions and cells whereby a corona around the nanoparticles can be formed usually determining their fate [271]. Especially for diagnostic and therapeutic purposes, it is of great importance that the nanoparticles interact specifically with the diseased tissue and cells. Therefore, targeting ligands are coated on the nanoparticles to enhance the specific interaction with targeted receptors on the cell surface and particle uptake [272]. In our studies, we aimed to quantify the effect of such targeting ligands. To pursue this goal, model nanoparticles were developed, experiments under flow conditions with an internal control were designed and optimized (see chapter 5) and the potential of two short peptides to serve as targeting ligands was assessed (see chapter 6). In this chapter which is partially adapted from our publication in the Journal of Controlled Release [273], the synthesis and characterization of model nanoparticles as well as the uptake into cancer cells will be described. The synthesis was developed in collaboration with Dr. Ulrich Lächelt and the peptide conjugates were synthesized by Dr. Ulrich Lächelt and Stephan Morys.

Model nanoparticles were established to serve two purposes: First, to investigate the effect of targeting ligands, comparable and easy-to-synthesize nanoparticles were required which mimic the surface characteristics of common drug and gene delivery devices. Second, the model delivery system should meet the requirements for quantitative analysis. Desired characteristics of the nanoparticles are low aggregation behavior, good detectability, reproducibility and stability over several months. These goals were accomplished by synthesizing labeled, PEGylated latex beads to which ligands or control molecules were coupled.

In Fig. 4.1 a model nanoparticle is illustrated. The core is a commercially available latex (polystyrene) bead with surface amino groups which are positively charged under physiological pH value. Two different bead sizes were tested, one with 110 nm diameter and another one with 200 nm diameter. A small amount of the amino groups (5 – 10 %) was labeled with fluorescent dyes (Cy5 or ATTO 488) for detection with fluorescence microscopy. The surface was shielded with polyethylene glycol (PEG) to reduce the surface charge and the capability of the dye to interact with the cell or surrounding molecules. This method is common for many nanocarriers as PEG hinders protein

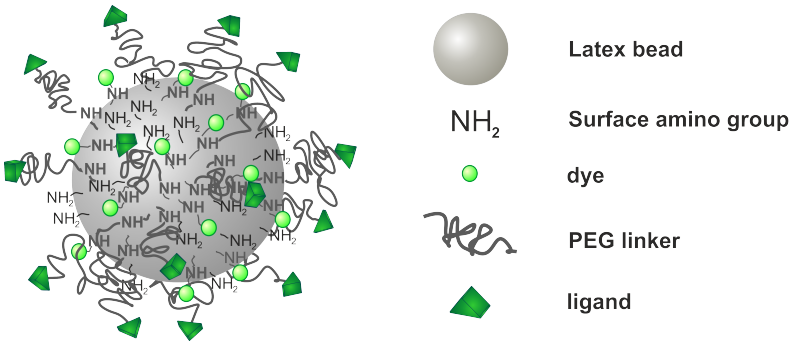

Figure 4.1: Model nanoparticle. Schematic drawing of a model bead composed of a latex core and surface amino groups labeled with a fluorescent dye. The surface charge is shielded by a PEG linker to which a ligand or control molecule is coupled.

binding, thus preventing unspecific absorption, increases hydrophilicity and enhances biocompatibility of the nanoparticles [274]. Two different sizes of PEG linkers were tested, 2 kDa and 5 kDa, for optimal shielding. Ligands were linked at the end of the PEG chains to improve specific interaction with target cells. Two short peptide ligands, B6 for transferrin receptor (TfR) targeting and cMBP2 for hepatocyte growth factor receptor (HGFR)/c-Met targeting were coupled to the beads as well as folic acid for folate receptor targeting. In addition, transferrin, the natural ligand for the TfR was coupled to the beads for comparison. In order to provide suitable control beads, also different other molecules were linked to the beads including scrambled or modified peptides, or β-mercaptoehanol. These will be described in more detail in the following chapter.

4.1 Synthesis

The synthesis of the model beads included three steps: Labeling, PEGylation and ligand attachment (see Fig.4.2). Commercially available polystyrene beads (110 nm or 200 nm diameter) with surface amino groups were labeled with fluorescent dyes (5 % Cy5 or 8 % ATTO 488 of the amino groups) via *N*-hydroxysuccinimide (NHS) ester chemistry. To confirm successful labeling, the beads were coated on a coverglass by spin coating and the fluorescence of the dyes was observed by widefield microscopy. Again using NHS ester chemistry, remaining surface amino groups were linked to NHS-PEG2/5-OPSS which contained 2 or 5 kDa PEG for surface shielding and orthopyridyldisulfide (OPSS) for conjugation with thiols. The amount of coupled NHS-PEG2/5-OPSS was estimated by the following assay. Dithiothreitol (DTT) was mixed with a small quantity of beads, 2-thiopyridone (2-TP) was cleaved from the OPSS residue on the beads and its absorption was measured at 343 nm. The assays yielded that 5-10 % of the NH_2 groups on the beads were coupled to the PEG linker. As a last step of the synthesis, ligand-cysteine, control peptide-cysteine or β-mercaptoethanol, respectively, was added to the PEGylated beads, the 2-TP leaving group was cleaved and the corresponding disulfide bridge was formed. Measurements of the zeta potentials of the differently modified beads suggested successful attachment of the ligands.

Short peptide ligands and a small molecule were used to specifically address overexpressed recep-

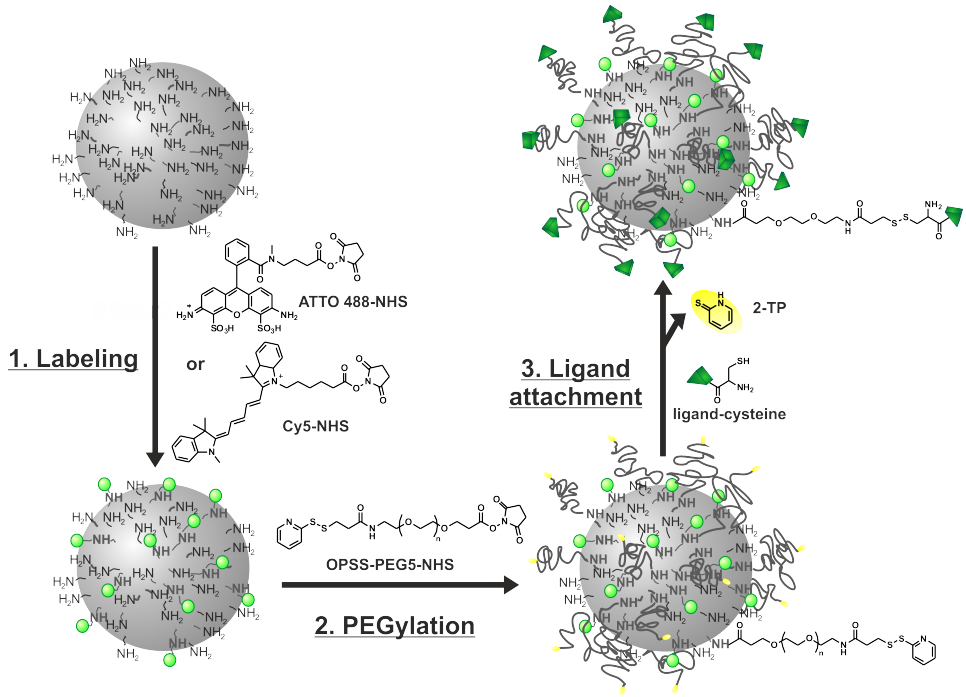

Figure 4.2: Synthesis strategy of model beads. 1. Labeling of polystyrene beads with ATTO 488- or Cy5-NHS esters, respectively. 2. PEGylation via succinate ester chemistry and 3. Ligand attachment via disulfide bridges using cysteine modified peptides or β-mercaptoethanol and cleavage of 2-thiopyridone (2-TP).

tors on the surface of target cells. For c-Met (hepatocyte growth factor receptor) targeting cMBP2 was chosen, to address the TfR, the peptide B6 was used (amino acid sequences: see Table 4.1) and for folate receptor targeting folic acid. In addition, transferrin (Tf), the natural ligand of the TfR was coupled to the beads. The synthesis was performed in two different ways. In the first procedure which is similar to the standard synthesis, Tf-iminothiolane [Tf(it)] was coupled to the PEGylated beads instead of a cysteine derivate. The second method involved a pretreatment of the PEGylated beads with DTT to reduce the OPSS group and provide a free thiol group for coupling with Tf-pyridyldithiol propionate [Tf(pdp)]. Control beads were provided by coupling β-mercaptoethanol to PEGylated beads yielding hydroxyl-terminated (OH) PEGylated beads. As these control beads exhibit a lower surface charge, additional control beads with similar electrostatic characteristics were synthesized to investigate the binding specificity of the peptides according to the correct amino acid sequence. Therefore, scrambled peptide versions (B6scr1, B6scr2 and cMBP2scr) were provided consisting of the same amino acids, but in different orders. Additionally, to exclude influences of electrostatic interactions, a modified peptide (B6mod) was used where all highly basic amino acids such as lysine and arginine were replaced by glycine.

The beads are named according to the following nomenclature: Ax-PEGy-ligand/control, where A stands for the amino groups on the surface of the beads, x is the original diameter of the bead in nm, y is the size of the PEG linker in kDa or as subscript the number of ethylene glycol units and the name of the ligand or control molecule, e.g. B6. As an example, a bead with a diameter of 200 nm, 5 kDa PEG spacer and the peptide ligand B6 is named A200-PEG5-B6.

4.2 Characterization

To study the efficiency or toxicity of nanoparticles, it is necessary to characterize well these nano systems as size, shape, surface properties and concentration influence their cellular binding and uptake [275]. Various methods were applied to characterize the synthesized beads. Fluorescence microscopy was performed to qualitatively analyze the labeling and aggregation of the beads in the different synthesis and preparation conditions and to quantitatively obtain the labeling distribution on single beads. Dynamic light scattering was applied to determine the hydrodynamic diameter of the beads. The zeta potential was measured and disclosed differences in surface modification as well as surface charge of the beads. With the determination of the light absorption of the beads at 225-231 nm, the concentration of the bead suspensions after synthesis could be approximated. Finally, the uptake of the beads into target cells was investigated under static conditions to get insights into the functionality of the ligands on the beads.

4.2.1 Fluorescence characteristics

The fluorescence of the beads depends on several factors: First, the intrinsic properties of the dye including excitation and emission maxima, quantum yield and lifetime, second the labeling degree and third the microscope adjustment like laser intensity at the objective, excitation and emission filters, exposure time and sensitivity of the detection device. While it is very important to keep all these factors constant for quantitative analysis, qualitative assessments can be done even under changing conditions. In this sub chapter, the variation of synthesis and preparation parameters of the beads will be described step by step in relation to the qualitative effect on the fluorescence images. Furthermore, the labeling distribution on single beads obtained by quantitative fluorescence measurements will be discussed.

In Fig. 4.3 A, synthesis and preparation which influence the fluorescence of the model beads are illustrated. Changing these parameters results in more or less aggregated beads which hence appear as smaller or larger fluorescent spots. Fig. 4.3 B shows beads prepared with different synthesis parameters on coverglass. Comparing beads with a diameter of 110 nm and 200 nm, the fluorescence of the larger beads seems to be more uniform whereas the smaller beads tend to be more aggregated. Regarding differently labeled beads (Cy5 and ATTO 488), the fluorescence appearance depends on the photo-physical properties of the dyes. Better surface shielding decreases the aggregation behavior of the beads. While lower shielding with a PEG spacer of 2 kDa resulted in larger fluorescent spots of beads with a diameter of 110 nm (A110), and thus higher aggregation, smaller fluorescent spots could be observed with 5 kDa PEG. The beads are less prone to aggregation with a larger PEG linker. Another important factor is the surface functionality which affects the steric configuration on the outer part of the bead, the surface charge and the hydrophilic or hydrophobic properties. Comparing hydroxylated beads (A200-PEG5-OH) with B6 beads (A200-PEG5-B6), the beads with peptide seem to have a slightly higher tendency to aggregate. This is caused by the more hydrophobic structure of the peptide containing highly basic amino acids.

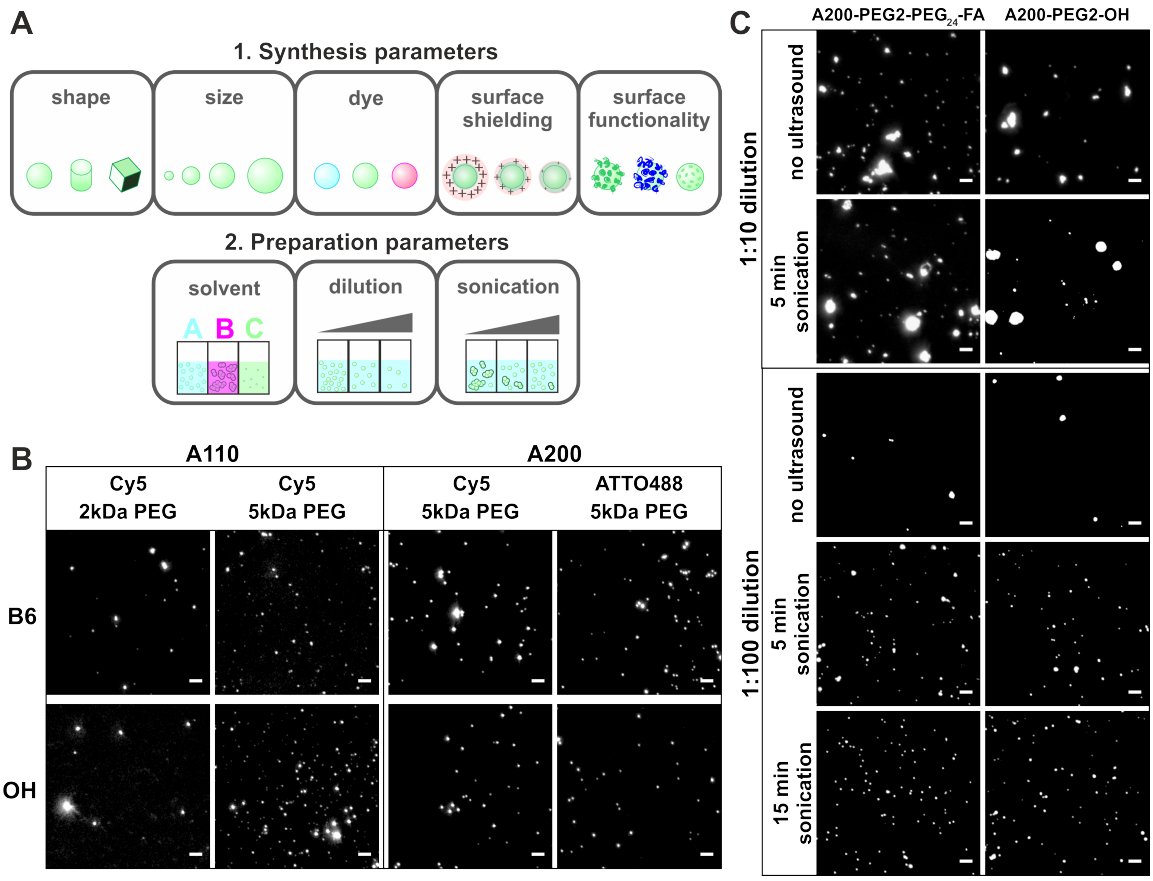

Figure 4.3: The influence of synthesis and preparation parameters on the fluorescence images of model beads. (A) Scheme of synthesis and preparation parameters which have been considered and optimized for the model beads. (B) The fluorescence of spherical model beads on coverglass (excited with 488 nm or 633 nm, 300 ms) is depicted. Several parameters were varied: size (A110 - diameter: 110 nm and A200 - diameter: 200 nm), fluorescent dyes (Cy5 and ATTO 488), surface shielding (2 kDa PEG and 5 kDa PEG linker) and surface functionalization (short peptide B6 and hydroxylated surface). (C) The fluorescence of Cy5 labeled A200-PEG2 model beads with folic acid or hydroxylated surface functionalization on coverglass (excited with 633 nm, 300 ms) is shown. The preparation parameters which were varied are the following: dilution ($1:10$ and $1:100$) and sonication (no ultrasound, 5 min and 15 min sonication). Scale bar = 5 µm.

Apart from synthesis parameters, also the preparation of the beads influences their aggregation behavior. Fig. 4.3 C illustrates the fluorescence of A200-PEG2 beads on coverglass prepared with different dilutions and sonication times. The solvent is a main factor influencing the colloidal stability of nanoparticles. Changing the polarity, the pH value or the ionic strength can contribute to aggregation of the particles. Studying therapeutic nanocarriers, it is important to remain under physiological conditions, i.e. to use appropriate buffers or cell medium. With the addition of serum, e.g. fetal bovine serum (FBS) a protein corona can be formed around the nanoparticles and also influence the aggregation tendency (in both ways). The model beads were prepared in phosphate buffered saline (PBS), pH 7.4. During washing steps, where the beads were centrifugated at high spin (13.400 rpm) aggregates formed which were disrupted by sonication (see Fig. 4.3 C). Additionally, sufficient dilution of the beads was important as the beads aggregated strongly in highly concentrated suspensions. For cellular adhesion experiments, the bead suspensions were added to

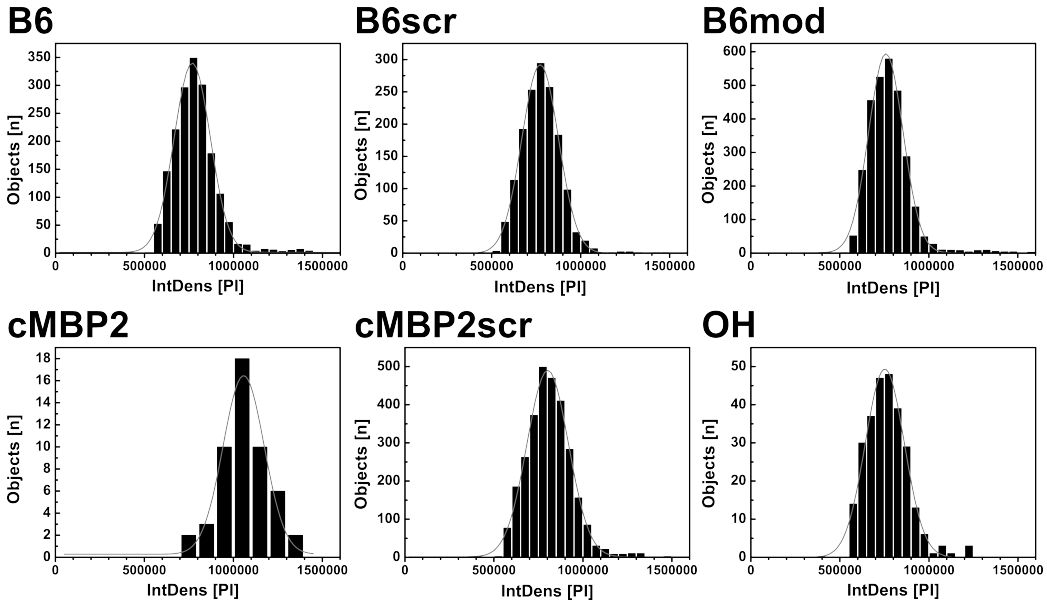

Figure 4.4: Integrated fluorescence density (IntDens) of single beads labeled with ATTO 488. The fluorescence of single beads (A200-PEG5) was measured by confocal spinning disk microscopy. The integrated fluorescence density was analyzed by Particle_in_Cell_3D (routine 4) [276] and the volume of counted objects (in number of voxels, i.e. volumetric pixels) was confined to 450-800 voxels. The histograms of the fluorescence of single beads show a Gaussian distribution.

cell medium supplemented with 10 % FBS. Generally, this further dilution was sufficient to obtain a low degree of aggregation. Experiments where large aggregates could be observed were discarded.

To obtain the labeling distribution on single beads, the integrated fluorescence density (IntDens) of the beads (A200-PEG5) was analyzed. Therefore, beads labeled with ATTO 488 were diluted (1:100) in PBS buffer, sonicated and added to cell medium supplemented with 10 % FBS. Stacks of the fluorescence of the beads sedimented on the bottom of the slides were recorded by excitation with a 488 nm laser. The image stacks were evaluated according to Torrano *et al.* [276] To obtain the fluorescence intensity of single beads, the volume of analyzed objects which correspond to single fluorescent spots was confined to 450-800 voxels. Fig. 4.4 shows the histograms of the fluorescence IntDens of single particles of different bead types fitted with a Gaussian distribution. Similar intensity value distributions were obtained for all bead types. In case of non-uniform labeling, a tailoring would have been expected. Furthermore, in case of non-resolved dimers, objects with a doubled IntDens would have been counted. This was only the case for very few objects. Thus, the preparation and detection of single beads was successful. Aggregation during synthesis, preparation, storage and experiments could not be excluded completely, however mainly single beads could be provided.

4.2.2 Zeta potential and hydrodynamic diameter

Electrophoretic and dynamic light scattering measurements were performed to characterize the zeta potential, the "electrokinetic charge" [277] and the hydrodynamic diameter, the particle diam-

eter including the solvating shell of the beads. The results are shown in Table 4.1 including the polydispersity index (PDI) and the peptide sequence of the ligands and control molecules. In the first part (I) of the table A200 beads used for binding studies in chapter 6 are listed, in the second part (II) additional A200 beads for control experiments and for testing of the folate ligand are shown and in the third section (III) parameters of A110 beads are depicted.

Zeta potential

Measurements of the zeta potential at physiological pH value showed a very high positive value for unmodified amino beads, which was drastically reduced after PEGylation (A200-PEG5-OPSS) demonstrating effective surface shielding. After addition of 2-mercaptoethanol, the resulting hydroxylated (OH) control beads exhibited a zeta potential of 9 mV. The B6 beads and the scrambled versions (B6scr1 and B6scr2) yielded enhanced positive surface charges with similar zeta potentials in the range of 24-30 mV which can be explained by the presence of four highly basic amino acids (lysines and arginine) within the amino acid sequence of the peptides. The electrostatically modified B6mod beads revealed a slightly negative zeta potential with reduced surface charge as expected. For the beads equipped with the cMBP2 peptide and the scrambled version (cMBP2scr) a zeta potential of 18-21 mV was measured which is less positive than that of B6 beads as only one arginine and one lysine with free ε-amino residue are present in the amino acid chain.

Changing the pH value from pH 7.4 to 6.8, a reduced zeta potential of the unmodified beads from 51 mV to 32 mV was measured which can be explained by more neutralized amino groups on the surface of the beads at more acidic pH. The PEGylated beads (A200-PEG-OPSS) still exhibited a low absolute value for the zeta potential, however it was positive instead of negative suggesting that the isoelectric point, i.e. the pH value where the particles are completely uncharged, is within the range of pH 6.8 and 7.4. The zeta potential of the beads with B6 ligand remained almost constant whereas beads with one tenth of the peptide B6 used during the synthesis [A200-PEG-B6(1:10)] had a zeta potential diminished by one third compared to the beads with the original amount of B6 peptide. As this zeta potential is in the same range as the one for PEGylated beads, this leads to the assumption that only very few peptides were coupled to the beads or that they were not freely accessible on the surface. For the beads with the natural ligand transferrin (A200-PEG5-Tf), a negative zeta potential was measured, as expected since the diferric Tf possesses a negative net charge. The modification of A200-PEG5 with folate coupled via three different cysteine-(PEG)-derivatives resulted in zeta potenitals of 7-10 mV suggesting low amounts of folate on the surface.

Finally, regarding the smaller latex beads with a diameter of 110 nm, the unmodified particles had a similarly high surface charge as the larger ones. Equipped with the ligand B6, the A110-PEG5 beads had a zeta potential of 13 mV which is much lower as for larger beads due to either lower surface area and/or lower amount of coupled ligands. Without ligand the surface charge was neutral and with folate on the surface it was -13 mV. Interestingly, these beads had a more negative zeta potential when a much smaller PEG spacer was used (A110-PEG2). A reasonable explanation could be a high aggregation propensity of the beads.

Table 4.1: Zeta potential, hydrodynamic diameter and PDI of differently modified aliphatic amine latex beads and amino acid sequence of peptide ligands. Parameters were obtained for beads with (I,II) 200 nm diameter used for receptor targeting studies; (I) adapted from [273], and (III) 110 nm diameter. Unmodified beads (A200/110) were PEGylated with 2 or 5 kDa PEG (A200/110-PEG2/5-OPSS) and functionalized with TfR/c-Met-targeted peptide or natural ligands (A200/110-PEG2/5-B6/cMBP2/Tf/FA), non-targeting peptide controls (A200-PEG5-B6scr1/B6scr2/B6mod/cMBP2scr) or a hydroxylated control (A200/110-PEG5-OH). Measurements were performed as triplicates. Peptide sequences are displayed in the amino acid single letter code.

Name	Zeta potential [mV]	Hydrodynamic diameter [nm]	PDI	Sequence
(I) A200 beads in water, 1 mM ***NaCl, pH 7.4***				
A200-NH_2	51±7	241±95	0.155	-
A200-PEG5-OPSS	-11±7	314±161	0.262	-
A200-PEG5-B6	30±5	313±144	0.212	(C)GHKAKGPRK
A200-PEG5-B6scr1	29±6	234±68	0.084	(C)AGKHGKRPK
A200-PEG5-B6scr2	24±14	260±102	0.153	(C)RPKAHKGKG
A200-PEG5-B6mod	-7.9±10.3	324±170	0.277	(C)GHGAGGPGG
A200-PEG5-cMBP2	21±10	236±67	0.082	KSLSRHDHIHHHK(C)
A200-PEG5-cMBP2scr	18±8	286±144	0.255	HHSIHRLHHKSDK(C)
A200-PEG5-OH	9.1±11.0	291±146	0.252	-
(II) A200 beads in water, 1 mM ***NaCl, pH 6.8***				
A200-NH_2	32±4	651±275	0.355	-
A200-PEG5-OPSS	7.0±6.4	223±57	0.091	-
A200-PEG5-B6	28±6	232±59	0.040	(C)GHKAKGPRK
A200-PEG5-B6(1:10)	10±6	255±91	0.150	(C)GHKAKGPRK
A200-PEG5-Tf(it)	-13±4	339±112	0.228	*679 amino acids*
A200-PEG5-Tf(pdp)	-13±5	250±80	0.125	*679 amino acids*
A200-PEG5-FA	7.1±7.6	250±79	0.085	-
A200-PEG5-PEG2-FA	8.3±5.5	239±59	0.018	-
A200-PEG5-PEG_{24}-FA	10±5	251±84	0.092	-
(III) A110 beads in water, 1 mM ***NaCl***				
A110-NH_2	47±5	295±226	0.241	-
A110-PEG5-B6	13±4	321±204	0.383	(C)GHKAKGPRK
A110-PEG5-OH	0.68±4.2	232±117	0.308	-
A110-PEG5-FA	-13±3	534	0.581	-
A110-PEG2-FA	-26±6	2179	0.742	-

Hydrodynamic diameter

Dynamic light scattering (DLS) measurements disclosed that the hydrodynamic diameter of the originally 200 nm polystyrene beads in water at pH 6.8-7.4 is within the range of 230-340 nm when the beads are functionalized (see Table 4.1). The polydispersity index (PDI) values which correspond to the size distribution of the nanoparticles are between 0.16-0.26 at physiological pH and 0.36 at pH 6.8 for precursor beads whereas the PDI range drops to 0.02-0.28 after modification. This implies that the precursor beads aggregated during DLS measurements especially at lower pH values as the surface charge is low which results in low stabilization while modified beads were not or only slightly aggregated. Regarding the hydrodynamic diameter of the originally 110 nm polystyrene beads in water at neutral pH value, the range is within 230-320 nm, thus similar to the A200 beads and even much larger when equipped with folate. These beads aggregated strongly which is also indicated by PDI values of 0.24-0.38 for unmodified, hydroxylated and beads equipped with B6 and 0.6-0.7 for beads with folate.

4.2.3 Light absorption

An important factor for cellular adhesion or uptake studies is the dosage of the nanoparticles. By measuring the light absorption of the different bead suspensions in bulk, we were able to estimate the concentration of the beads and amino groups on the bead surfaces.

Table 4.2: Light absorption. Mean absorption of aliphatic amine latex beads (200 nm diameter), the corresponding concentration of amino groups on the bead surface and the concentration of the beads in PBS buffer after modification; n = 5.

Name	Absorption at 230 nm	Concentration of NH_2 groups [μM]	Concentration of beads [number of beads/mL]
A200-PEG5-OPSS	0.46	1.0	$3.1 \cdot 10^{12}$
A200-PEG5-B6	0.47	1.0	$3.1 \cdot 10^{12}$
A200-PEG5-B6scr1	0.44	0.9	$2.9 \cdot 10^{12}$
A200-PEG5-B6scr2	0.43	0.9	$2.8 \cdot 10^{12}$
A200-PEG5-B6mod	0.42	0.9	$2.8 \cdot 10^{12}$
A200-PEG5-cMBP2	0.47	1.0	$3.1 \cdot 10^{12}$
A200-PEG5-cMBP2scr	0.48	1.0	$3.2 \cdot 10^{12}$
A200-PEG5-OH	0.52	1.1	$3.5 \cdot 10^{12}$

The absorption of the different synthesized beads used for binding studies was measured at 230 nm. Before, a calibration curve was generated using unmodified beads (see Appendix Fig.1) and the

attenuation coefficient ε^* (947400 $M^{-1}cm^{-1}$) was calculated using the Lambert-Beer law.The concentration of amino groups c(NH_2) was calculated according to following equation:

$$c(NH_2) = \frac{A}{\varepsilon^* \cdot l} \cdot 10^6 \cdot 200[\mu M] \tag{4.2.1}$$

where A is the absorption of the diluted beads and l the pathlength. Furthermore, the concentration of beads per mL c(beads) was derived by the subsequent equation using the manufacturer's specifications:

$$c(beads) = \frac{c(NH_2) \cdot 4.978 \cdot 10^{12}}{c_0(NH_2)} \left[\frac{beads}{mL}\right] \tag{4.2.2}$$

where $c_0(NH_2)$ = 1.58 µmol/mL is the concentration of amino groups at the beginning of the synthesis. The results are shown in Table 4.2. The concentration of amino groups was approximately 1 µM for all bead types resulting in about three billion beads per milliliter. As very similar concentrations were obtained no further adjustment was done for experiments under flow conditions.

4.3 Cellular uptake of model nanoparticles

A major goal of therapeutic nanoparticles is their uptake into specific cells where their cargo can be released or the genetic material can be modified after translocation. By equipping the nanoparticles with targeting ligands, cells are addressed which overexpress the target receptor on the surface. Testing the uptake of such nano systems on target cells gives information about the effectiveness of the ligand to enhance cellular internalization. Herein, the uptake of model beads into HuH7 cells was tested which were used for binding studies (see chapter 6). The HuH7 cells possessed both target receptors, TfR and c-Met on their surface which was tested by immunostaining (see Appendix 6 Fig. 5 and Fig. 4).

Labeled beads were incubated on HuH7 cells for 2 h under static conditions, the membrane was stained and the fluorescence was measured by spinning disk microscopy. The evaluation was performed with the macro Particle_in_Cell-3D [276]. In Fig. 4.5 A, representative 3D images of single cells containing internalized beads (magenta) or beads in the apical (yellow) or basal (orange) membrane are shown. The mean values of internalized fluorescence (IntDens) per cell and bead type are depicted in Fig. 4.5 B. Beads with the targeting ligand B6 were internalized most effectively. Cells incubated with beads coated with the scrambled versions contained three-quarters of the fluorescence of the B6 beads, whereas only very few neutral control beads showed cellular uptake. In experiments with cMBP2 or scrambled peptide, only approximately one forth of the amount of beads compared to B6 were taken up. The uptake efficiency, i. e. the percentage of internalized fluorescence in relation to the total fluorescence of the beads on the cells was calculated and is illustrated in Fig. 4.5 C. Approximately 80 % of B6, B6scr1 and cMBP2 beads were internalized within 2 hours whereas the scrambled versions B6scr2 and cMBP2scr comprised only 55-60 % within the cytosol. The neutral beads uptake was 30-40 %.

These results suggest that effective internalization depended on the charge of the beads. The

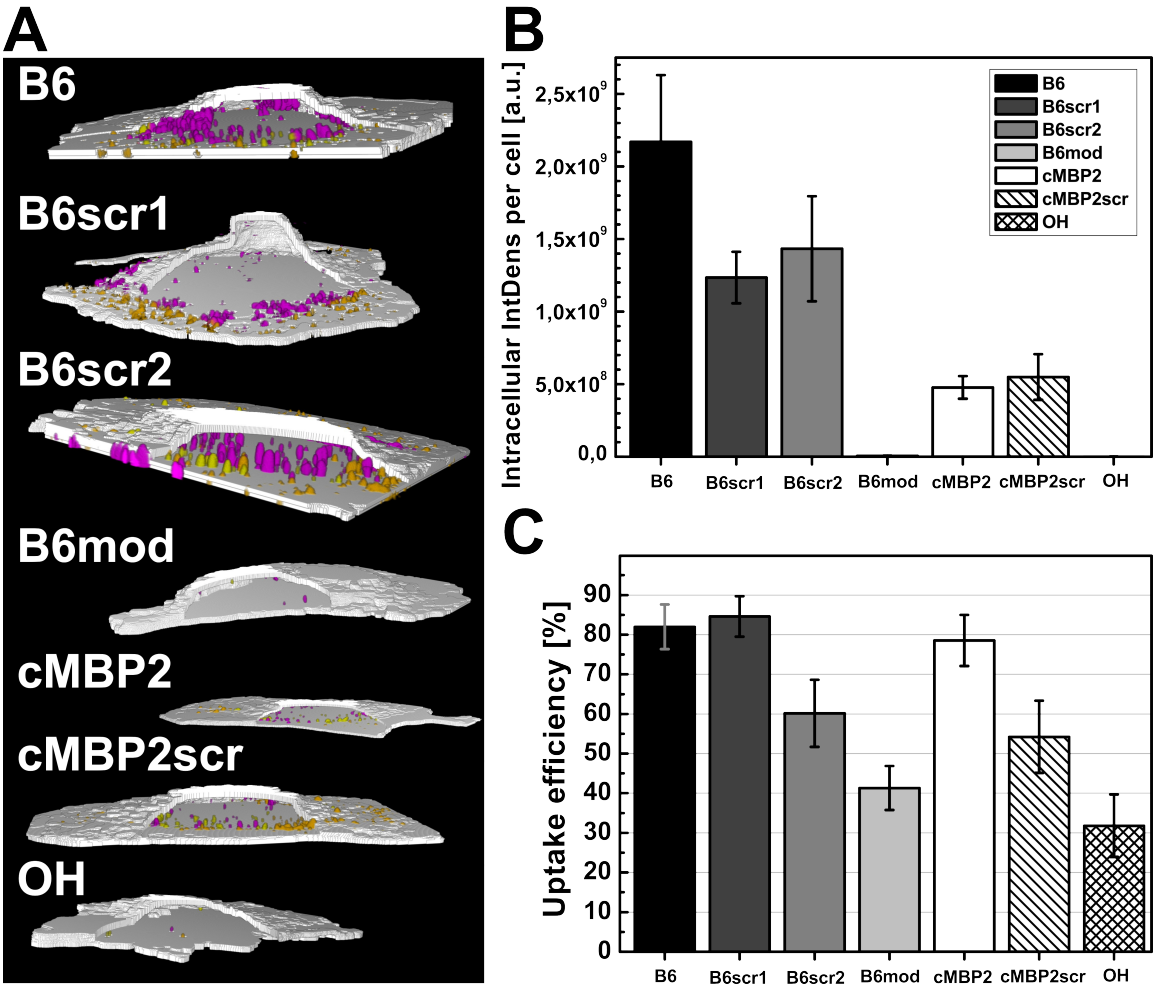

Figure 4.5: Cellular uptake of different model beads. Cy5-labeled beads were incubated on HuH7 cells for 2 h in 8 well chambers, the fluorescence was measured with spinning disk microscopy and evaluated with the macro Particle_in_Cell-3D [276] (routine 3). (A) View in 3D of single cells with different internalized beads (magenta) or with beads within the apical (yellow) or basal (orange) membrane region. (B) Mean fluorescence integrated density (IntDens) of intracellular beads within single cells. n = 12-15. (C) Mean uptake efficiency (percentage of intracellular fluorescence) of the different beads in single cells. n = 12-15.

likelihood of cellular uptake was increased for positively charged beads compared to neutral ones. Furthermore, the similar percentage of uptake for B6 and B6scr1 beads into HuH7 cells suggests similar uptake processes.

4.4 Summary and conclusion

In summary, a successful synthesis of model nanoparticles for quantification by fluorescence microscopy mimicking the surface characteristics of therapeutic nano delivery systems was developed. Using the versatile coupling strategy via disulfide bridge formation, provides the option to link various cysteine-modified targeting ligands to the model beads. Thus, there is a large range of applications. Three different ligands, the peptide B6 for TfR targeting, the peptide cMBP2 for HGFR/c-Met targeting and folate for folic acid receptor targeting were attached to the beads while in addition several control beads were provided. The hydrodynamic diameter of the originally 200 nm large beads was between 230-340 nm after modification. This size range is still small enough for nanoparticles to penetrate into tumor tissue through leaky tumor vasculature having a pore cut-off size of >200 nm [278]. An even more advantageous size would be in the range of 100 nm or smaller as cellular uptake processes are facilitated [275] and clearance via spleen or liver are avoided [279]. However, beads of 110 nm showed much higher aggregation propensity, especially when equipped with folate as targeting moiety. Much better stabilization was obtained for the larger beads (A200). Since we aimed to quantify the adhesion of the beads, low aggregation behavior was of greater importance than an optimal size for nanoparticle uptake.

The original surface charge of the amino beads at physiological pH value was very high and the zeta potential around +50 mV. An effective shielding was obtained by coating the beads with PEG. This is a common proceduce as many nanocarriers are equipped with PEG to enhance the biocompatibility and blood circulation time [280]. Optimization of PEGylation, i.e. the amount and density of PEG on the surface of the beads was achieved by using a 5 kDa PEG spacer and resulted in reduced surface charge, increased solubility and decreased aggregation tendency of the beads. Furthermore, using PEG spacers with a molecular mass of 5 kDa is shown to maximize circulation half-life and prevent opsonization, i.e. clearing from the blood system [281, 282]. The amount of PEG linkers on the bead surfaces was estimated by a small assay. 5-10 % of all amino groups were covered which corresponds to 0.08-0.15 PEG molecules per nm^2 or a distance of 4.6 nm - 9.1 nm between two PEG molecules. This means that the PEG chains were in a "mushroom"-like conformation for a low PEGylation degree (5 % PEG), in a "brush"-like conformation for a higher PEG density (10 % PEG) [283], or most likely in a conformation between these two states (calculations see Appendix 2).

To provide stable model nanoparticles with low aggregation tendency, it was important to additionally optimize the preparation procedure of the beads. First, dilution of the beads increased the colloidal stability. Second, the time of sonication during and after synthesis was adjusted such that single beads could be observed under the microscope and did not show disruption. Relatively low PDI values of 0.02-0.28 nm were measured and thus beads without or only little aggregation were used.

The measurements of the zeta potential revealed that beads with the ligand B6 and the scrambled peptide versions B6scr1 and B6scr2 exhibited high positive surface charges caused by several basic amino acids. These beads showed the best cellular uptake by HuH7 cells after 2 h. Beads equipped with the second peptide ligand, cMBP2 and the scrambled version were less positively charged due to less basic amino acids. Lower amounts of those beads were internalized by the cells. Control beads with hydroxylated surfaces or with a peptide where all basic amino acids were replaced by the neutral amino acid glycine had a lower, more neutralized zeta potential. Almost none of those beads were internalized by the HuH7 cells. This can be explained by the fact that in general, positively charged nanoparticles exhibit a high affinity to cell surfaces as they can interact with negatively charged membrane glycans. [55] Thus, they bind more likely to the surface of cells than neutral particles. Hence, a combination of adhesion and uptake was measured while in chapter 5 an experimental setup was developed to study only adhesion.

Regarding the uptake efficiency of the beads with ligand, 80 % of the cMBP2 and B6 beads were internalized, but also beads carrying the negative control peptide B6scr1. All other control beads showed less uptake in the range of 30-55 %. These results indicate that the two peptide ligands enhanced the cellular uptake and a similar affinity of B6 and B6scr1 beads to HuH7 cells can be assumed. However, staining the cell membrane of HuH7 cells for these uptake experiments proved to be difficult with several membrane dyes as the plasma membrane line could not be distinguished continuously compared to other cell lines. Best results in our experiments were obtained with wheat germ agglutenin conjugated dyes (WGA-Alexa488).

By measuring the absorption of the latex beads at 230 nm, their concentration could be estimated. Suspensions of beads which were used for binding studies (see chapter 6) contained approximately three billion beads per milliliter for all bead types. As the beads were highly diluted for flow experiments (1:4800), concentrations of all types were in the same range for all nanoparticles and thus were not adjusted.

In conclusion, a successful, optimized and reproducible synthesis and comprehensive characterization of functional model nanoparticles for quantitative adhesion studies was described. In the next chapter, the development of flow experiments will be specified which were designed to perform cellular binding studies using the model nanoparticles.

5 Development of flow experiments for cellular targeting studies

Functional targeting groups on nanoparticles are designed to improve specific recognition of and attachment to receptors which are upregulated and exposed on the surface of target cells [269, 284]. In the case of cancer therapy, therapeutic nanoparticles can address circulating tumor cells directly within the blood flow as well as tumor endothelial cells at the vessel walls. On the other hand, primary tumors are reached after extravasation of leaky blood vessels [92]. Whether the nanoparticles bind to target cells depends on the following steps: 1) the nanoparticles have to reach the proximity of the cell surface, 2) avoiding nonspecific interactions with extracellular components and non-target cells and 3) recognizing of and attaching to receptors on target cells.

As our goal was to investigate the effect of a targeting ligand on cellular binding, we needed an experimental setup to perform reliable and reproducible *in vitro* studies. Traditionally, cell culture-based assays are performed under static conditions, where nanoparticles approach the cell surface by diffusion and gravitational sedimentation, but also can agglomerate during this process [285]. To avoid this and to mimic better the physiological conditions, a microfluidic setup was used. In previous studies, the amount of cellular associated nanoparticles is either appraised qualitatively by visualization or quantified by various methods including light and electron microscopy, radioactive labeling and fluorescence spectroscopy [286]. A commonly used fluorescence technique is flow cytometry which allows for measuring large numbers of cells within a short time range resulting in good statistics [287, 288]. Nonetheless, particle localization cannot be determined. Furthermore, the obtained particle numbers are rather relative instead of absolute values without additional elaborate calibration [286]. In general, quantification techniques which are based on fluorescence intensity require many optimized conditions e.g. concerning the illumination, autofluorescence, crosstalk and potential controls [289]. Additionally, such techniques face problems like photobleaching, blinking [290] and quenching effects. Alternatively, cell-associated nanoparticles can be counted by selecting the intensity maxima of fluorescent spots. This method requires labeling and sufficient resolution of single particles in close proximity. Since we could provide single, stable, low or non-aggregating labeled model nanoparticles, this evaluation procedure was chosen and validated by a quantitative assessment based on fluorescence intensity. The model nanoparticles are PEGylated polystyrene beads (diameter: 200 nm) decorated with ligands or control molecules and described in chapter 4.

In this chapter we present the development of an experimental flow setup in combination with fluorescence microscopy. It is partially adapted from our publication in the Journal of Controlled Release [273]. We discuss the application of flow conditions on cell culture experiments. In addition,

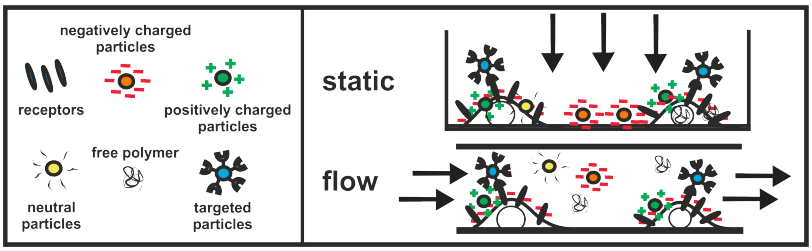

Figure 5.1: Comparison of cellular adhesion of nanoparticles under static and flow conditions. Particles diffuse in the medium and sediment to the bottom of the well where they can attach to the cell monolayer when static experiments are performed. Under flow conditions, particles pass over the cell monolayer and only particles with a certain affinity attach to the cells. Particles with low affinity are flushed away.

we describe the optimization of various experimental parameters and the choice of an appropriate quantification method. Furthermore, external and internal controls will be debated as experiments with biological samples like cells show heterogeneous results.

5.1 Cellular adhesion experiments under flow conditions

Intravenously administrated nanoparticles are transported by the blood flow from which they can extravasculate trough fenestrations of vascular tumor tissues. First, the distribution of the particles within the tumor region depends on the flow velocity of the fluid and the interstitial fluid pressure which is increased in solid tumors [291]. The diffusion of the particles within the tumor surrounding area is affected by their charge, size and shape [283]. Second, functional groups on the particle surface contribute to nonspecific interactions such as electrostatic and van der Waals interactions with extracellular matrix components. Cell culture monolayer models are not able to reconstruct the complex and heterogeneous tumor microenvironment. Nonetheless, they are a first easy model system in which cells are cultivated under controlled conditions producing consistent and reproducible results [292]. They represent with appropriate *in vivo* studies a promising approach for the pre-clinical assessment of the efficacy of novel cancer treatments in humans [293].

In Fig.5.1 the application of nanoparticles under a) conventional static cell culture conditions is compared to b) flow conditions. Three facts are important here. First, whether nanoparticles reach the proximity of the cell surface is determined by gravitational sedimentation and diffusion. Especially heavy and large particles may sediment and influence the results of cellular uptake studies [294]. Gravitational sedimentation can be avoided by using a microfluidic system which additionally contributes to a homogeneous distribution of nanoparticles in the medium [295]. Second, the charge of nanoparticles and their hydrophobicity influence their binding behavior to cells. Generally, the adhesion of positively charged nanoparticles to the negatively charged cell surface is favored [296] whereas negatively charged particles are repelled. All kinds of particles can bind to the cell surfaces under static conditions. In contrast, loosely attached particles are flushed away when shear flow is applied. Third, ligands on receptor-targeted nanoparticles can specifically attach to the corresponding receptors on the cell surfaces enhancing their binding to the cells.

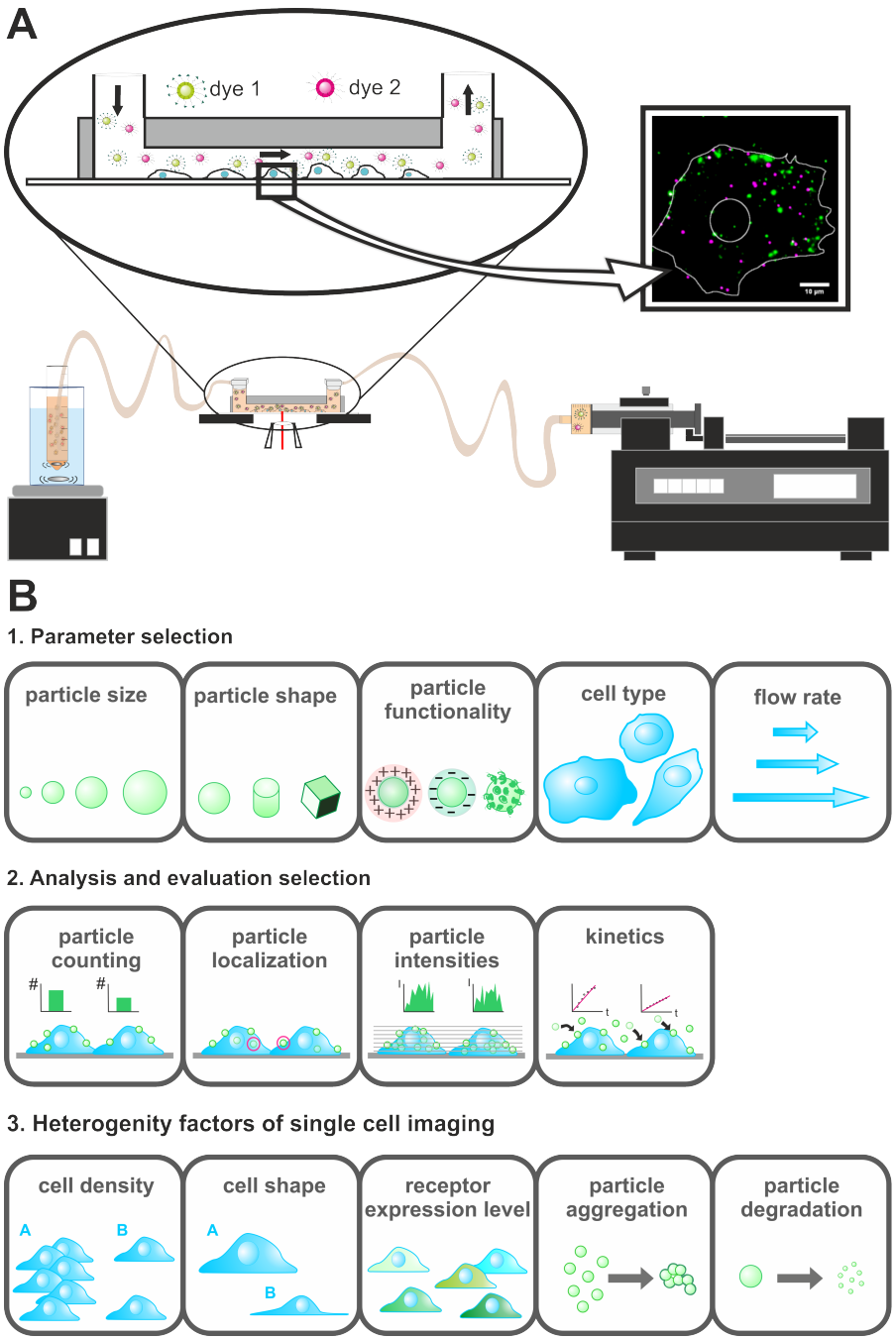

Figure 5.2: Flow system and conception of experiments with internal control. (A) Schematic drawing of the flow setup: model nanoparticles suspended in cell medium in a reservoir (left) are passed through a flow channel (middle) by the force of a syringe pump (right). The fluorescence of bound particles on a cell monolayer within the flow channel is measured by widefield microscopy. Enlargement: Competitive flow experiment is performed by streaming differently labeled beads with ligand and control particles through the flow channel. Particles attached on single cells are imaged by alternating excitation with 488 nm and 633 nm lasers. (B) Scheme of experimental parameters, read-out methods and heterogeneity factors of single cell flow experiments.

To investigate the effect of a targeting ligand on cellular binding, we decided to perform experiments under flow conditions as they offer the above mentioned advantages over static experiments. Furthermore they provide a hydrodynamic microenvirmonment for the cells which can be closer to *in vivo* conditions. For instance, tumor cells can be exposed to elevated interstitial fluid pressure [291, 297, 298]. This could be mimicked by shear flow. Another example would be to target the vascular endothelium [299] for the treatment of infectious or cardiovascular diseases.

In Fig. 5.2 A the concept of the flow system is shown. Nanoparticles were suspended homogeneously in a heated reservoir (T = 37 °C) and passed through a flow channel on a incubation stage (T = 37 °C). The syringe pump generates a laminar shear flow which is tunable. In the flow channel, model beads equipped with ligands were simultaneously perfused with differently labeled control beads over a cell monolayer. Their cellular association was observed on single cells by measuring the fluorescence of the beads. The cell membrane was discriminated by recording transmitted light images using a differential interference contrast (DIC) filter.

A number of experimental parameters influence the adhesion and uptake mechanisms of nanoparticles on and into cells such as particle size [300, 301], shape [302] and functionalization [303–305], as well as cell type [238] and shear rate [303, 304, 306]. In Fig. 5.2 B, a set of such parameters is illustrated and followed by the choice of the evaluation method(s) and factors causing heterogeneous results. By keeping all other experimental parameters constant, one by one can be investigated systematically. The measurement of adhesion or uptake of nanoparticles by sensitive fluorescence microscopy techniques has the advantage that detailed insights can be gained at the cellular level. Single nanoparticles can be localized and counted on and within cells, the total amount on single cells can be quantified and binding or uptake kinetics can be determined to give information about uptake efficiency. However, there are many factors causing heterogeneity of the results, including cell density, cell shape, receptor expression level, and particle aggregation and degradation. The choice of suitable parameters and evaluation methods will be described in detail in the following chapter. Consecutively, the processing of the heterogeneous results will be explained as well.

5.2 Optimization of flow experiments

The optimization of individual experimental settings is focused on the choice of ligands to be examined, the evaluation method, the flow rate and perfusion time. As all these factors influence each other, adjustment of multiple of them was done at a time, but they will be described individually. Two differently labeled bead types were directly compared in our flow experiments. Thus, we analyzed if the dye combination has an impact on the results.

Choice of the ligand

Two short peptide ligands, the transferrin receptor (TfR)-targeted peptide B6 and the c-Met binding peptide (cMBP2) were tested for their potential to serve as a targeting molecule. Short peptide

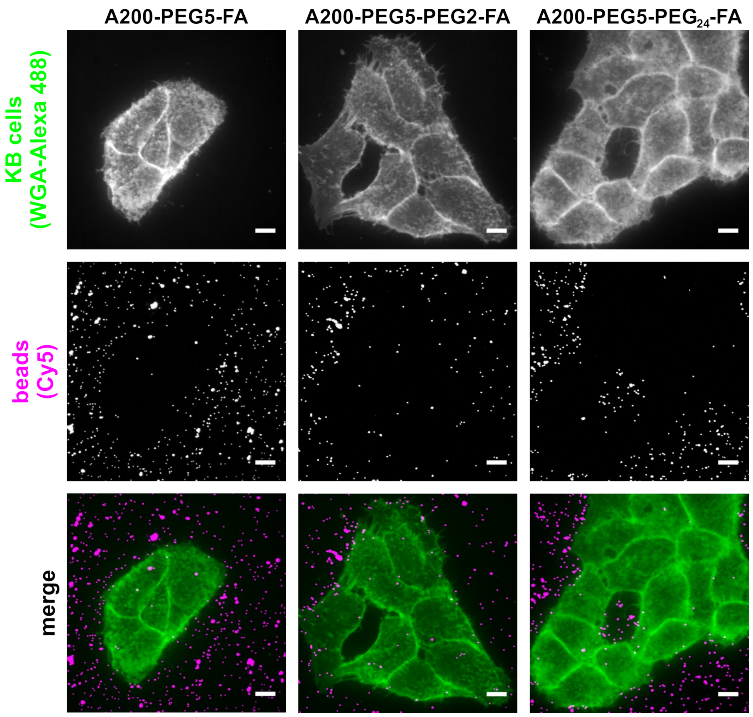

Figure 5.3: Model beads equipped with the targeting ligand folic acid (FA) bind mainly next to target cells. Cy5-labeled model beads (A200-PEG5-ligand) with three different folate ligands: I) folate (FA), II) 2 kDa PEG and folate (PEG2-FA) and III) 24 units of ethylene glycol and folate (PEG_{24}-FA) were incubated with KB cells for 45 min in folate-free medium under static conditions and fixed afterwards. The fluorescence of the beads (magenta) and of the cell membrane stained with WGA-Alexa488 (green) were measured by spinning disk microscopy. Representative z-projections of the KB cells, the beads and merged images are shown. Scale bar = 10 µm.

ligands possess several advantages such as small size, easy and cheap synthesis, good biocompatibility and low immunogenicity [307, 308] compared to large protein ligands and monoclonal antibodies. The B6 peptide (9 amino acids) was chosen by Xia *et al.* from a phage display assay to bind the human TfR [309], which is overexpressed in various human cancer cell lines and enhances their metastatic potential [310]. So far, this peptide ligand has been applied for delivery of PEG-PLA nanoparticles to the brain [311] and dual targeting approaches with polyplexes [312]. The tyrosine kinase c-Met (receptor for the hepatocyte growth factor) has gained increasing attention recently due to its role in sustaining tumor progression [164]. The epitope-mimicking cMBP2 (12 amino acids) has been selected by Kim *et al.* from a combinatorial peptide library [313] to bind c-Met and was recently tested for non-viral gene delivery applications as a potent targeting ligand [166].

Both targeting peptides were tested on HuH7 cells which overexpress the TfR and possess HGFR/c-Met on their surface. This was confirmed by immunostaining experiments analyzed by flow cytometry (see Appendix 5) and by fluorescence microscopy (see Appendix 4). Furthermore, model nanoparticles equipped with the peptide B6 or the peptide cMBP2 were efficiently internalized by HuH7 cells (within 2 h to 80 %; see chapter 4.3).

Moreover, the small molecule folic acid (vitamin B9) was coated on model beads for folic acid receptor (FR) targeting. This vitamin was used by Leamon *et al.* to deliver macromolecules into living cells by receptor-mediated endocytosis [314]. The surface receptors for folic acid are overexpressed in many human cancer cells [315, 316]. FR targeting is performed using multiple strategies, including antifolates [317], FA-conjugated drugs and nanocarriers [318], folate-based imaging [319] and immunotherapy agents [320].

To assess the functionality of the folate-equipped beads, their uptake was investigated on KB cells which overexpress the FR [321]. Since in literature the ratio of folic acid/PEG polymer was found to be crucial for the uptake of folate conjugates [322], three different folic acid conjugates with distinct amounts of PEG were tested. In detail, beads without additional PEG (A200-PEG5-FA), with a 2 kDa PEG spacer (A200-PEG5-PEG2-FA) and with an extra PEG linker of 24 ethylene gylcol units (A200-PEG5-PEG_{24}-FA) were incubated with KB cells for 45 min. In Fig. 5.3, z-projections of Cy5-labeled FA beads on KB cells are illustrated: in the first row the cell membranes of KB cells stained with WGA-Alexa 488 are shown, followed by Cy5-labeled FA beads and in the last row a merged image of both fluorescence channels is depicted. Interestingly, all three conjugates bound mainly next to the cells and not on the cells indicated by the fluorescence-free spaces in the particle images. This means that the affinity of the FA beads to the bottom of the well chamber was higher than to the target cells. Coating the well bottoms with poly-L-lysine, collagen or fibronectin before seeding the KB cells did not change the low attachment of the FA beads on the cells. Thus, these FA model beads rather decrease than increase the binding to target cells which was not expected. Consequently, they were not suitable for the cellular binding studies. To explain these findings, several aspects were considered: First, the zeta potential measurements of the FA beads showed surface charge values similar to PEGylated beads (see Table 4.1), indicating that only few ligands were accessible on the surface. On the other hand, a higher amount of ligand induced aggregation. Interactions of the aromatic system of FA with other molecules among each other or with the surface of the polystyrene beads, despite PEGylation, cannot be excluded. As in literature many divers PEGylated carrier systems were successfully used for FR targeting such as mesoporous silica nanoparticles [323], siRNA conjugates [324] or nanodiamonds [325], these nano carriers were presumably optimized for folic acid. Instead, the polystyrene PEG beads were incompatible with this ligand.

Evaluation method

Sensitive fluorescence microscopy was chosen to study cellular adhesion. So, the model nanoparticles could be localized on single cells and their aggregation status could be controlled. Two kinds of experiments were possible: measuring adhesion kinetics and quantifying the number of bound particles at a defined time point. The latter was applied as more statistics could be obtained.

Furthermore, two recording modes were possible: on the one hand measuring the integral fluorescence intensity of the nanoparticles by confocal microscopy and on the other hand recording the fluorescence by widefield microscopy followed by counting the intensity maxima of fluorescent

spots. The approach based on the integrated fluorescence intensity requires identical experimental conditions and settings including additional controls. Thus, to perform comparable experiments, calibration measurements of a standard sample is necessary accounting for the power and the performance of the cameras. Therefore, we chose to count the intensity maxima of fluorescent spots which correspond to single labeled beads or small aggregates. To validate the accuracy of the results, both procedures were compared.

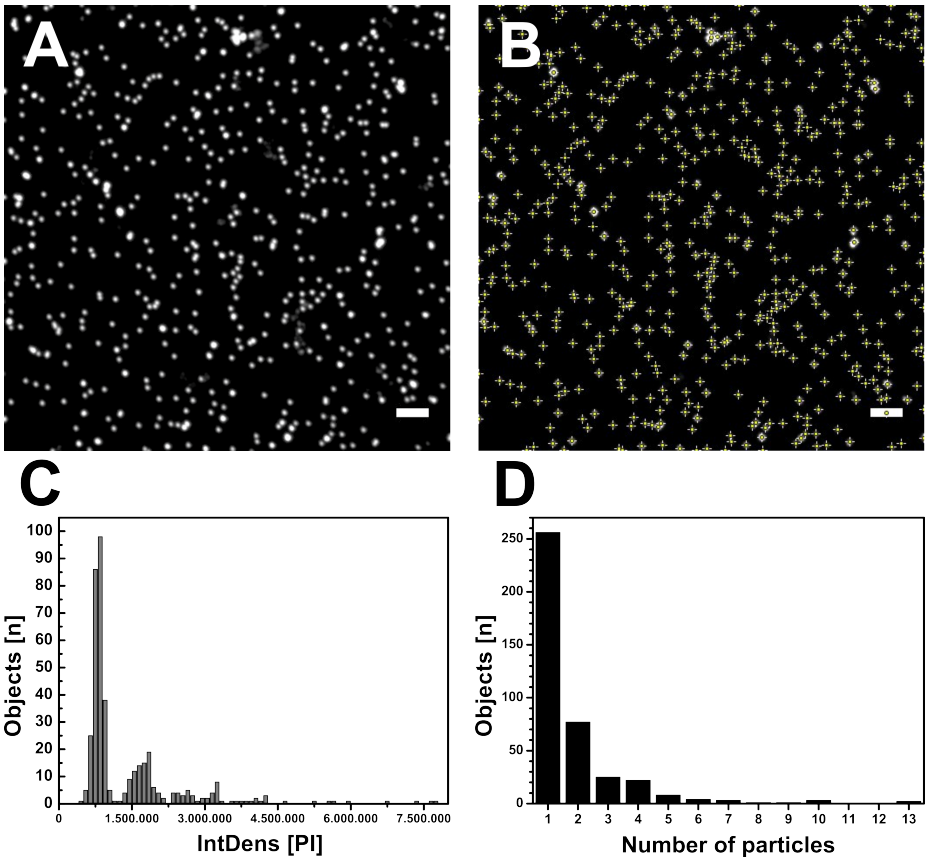

Figure 5.4: Particle analysis by counting intensity maxima of fluorescent spots and fluorescence integrated density (IntDens) based evaluation. (A) Z-projection of the fluorescence of labeled A200-PEG5-B6 beads in CO_2-independent medium and 10 % FBS measured by spinning disk microscopy. (B) Selection of intensity maxima (yellow crosses) corresponding to the counted number of beads. Scale bar = 5 µm. (C) IntDens of objects corresponding to one (first peak) or more B6 beads shown in A) analyzed by Particle_in_Cell-3D. [276] (D) Number of particles per object analyzed as in C).

Beads labeled with ATTO 488 in PBS buffer were diluted, sonicated and dispersed in CO_2 independent medium supplemented with 10 % FBS. These suspensions were then added to ibiTreat µ-slide wells. The beads sedimented on the bottom of the wells. Confocal fluorescence stack images were recorded exciting with the 488 nm laser. In Fig. 5.4 A, an exemplary z-projection of B6 beads is illustrated. By analyzing the intensity maxima with ImageJ software, 600 particles were counted (Fig. 5.4 B). Separately, the fluorescence integrated density (IntDens) of the particles was determined using the fluorescence intensity calibration routine of the macro Particle_in_Cell-3D [276].

Table 5.1: Comparison of two evaluation methods: Particle counting and procedure based on the fluorescence integrated density. Z-stacks of different types and numbers of model beads were recorded with spinning disk microscopy. Intensity maxima were counted on z-projections and are listed in the 1st column. The integrated density (IntDens) of the beads of the same image stack was determined by the macro Particle_in_Cell-3D [276] and divided by the mean IntDens of the respective bead type (see Fig.4.4), resulting in the number of particles displayed in the 2nd column. The last column shows the difference in particle numbers obtained by both methods.

Name	Counted maxima	Calculated number of particles (IntDens based)	Difference
A200-PEG5-cMBP	11	10	1 (10%)
A200-PEG5-OH	65	89	24 (27%)
A200-PEG5-B6scr	167	184	17 (9%)
A200-PEG5-cMBPscr	370	436	66 (15%)
A200-PEG5-B6	600	746	146 (20%)
A200-PEG5-B6mod	654	796	142 (22%)

In Fig. 5.4 C, the IntDens distribution of the fluorescent objects is plotted. Single particles (first peak), dimers (second peak) and more particles per fluorescent spot (object) could be determined. In total 405 objects were detected by this routine. By dividing the IntDens of the objects by the mean value of the IntDens of a single bead (see chapter 4.2.1), the number of particles per object could be calculated (Fig. 5.4 D). Using this method 746 particles were determined. In total, 20 % more beads were calculated by using the integrated density based method. This suggests that some particles were either aggregated or in such close proximity that they could not be resolved as single spots.

The comparison was performed for several bead types (see Appendix 2). In Table 5.1, the ascending number of counted intensity maxima and the calculated number of particles by the IntDens approach are compared. In the last column, the difference of the particle numbers determined by both methods is shown. The divergence ranges between 10-27 %. While just a few beads per field of view could be determined accurately by both methods, more beads per field of view involved higher discrepancy. On the other hand, a reasonable number of beads per field of view was required for significant results. The best agreement in the number of particles obtained by both methods was in the range of 167-436 beads per field of view. Hence, the number of particles can be determined most accurately within this range. The concentration of the particles and the perfusion time were adjusted such that this criterion was met.

Flow rate

The flow rate affects the exerted shear force on the cells. Shear forces influence, for example, the cytoskeletal arrangement of endothelial cells [299, 326] and can activate them. While these cells are exposed to blood flow, epithelial tumor cells of solid carcinomas are embedded in a different microenvironment. They are surrounded by extracellular matrix and a dysfunctional lymphatic

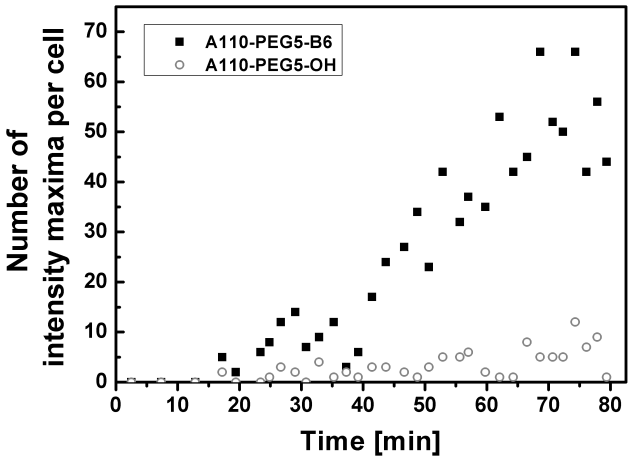

Figure 5.5: Adhesion kinetics of model beads on HuH7 cells. The adhesion of beads (diameter: 110 nm) with the peptide ligand B6 (A110-PEG5-B6, black solid squares), labeled with ATTO 488 and control beads (A110-PEG5-OH, grey open circles), labeled with Cy5 on HuH7 cells was monitored for 80 min of very low shear flow (0.13 dyn/cm^2) by widefield fluorescence microscopy. After a lag time of 12 min, beads start to bind to the cells. TfR-targeted B6 beads showed increasing attachment with time while only few control beads bound during the whole experiment.

system which causes an increased interstitial fluid pressure [279]. Thus, we did not intend to simulate blood flow conditions for cellular binding studies, but rather a shear force in the range of the hydrodynamic tumor microenvironment. In general, the main goal of applying shear flow was to provide constant concentration of particles and reduce sedimentation. Therefore, the cells were perfused only for a short time range in which they did not adapt to the flow conditions and the surface receptor status of TfR and c-Met remained constant (see Appendix 6).

The applied shear forces of 0.26 dyn/cm^2 (0.026 Pa) were relatively low, but in the range of increased interstitial fluid pressure [298]. The influence of shear flow on particle adhesion was tested by increasing the shear force by one order of magnitude (2.63 dyn/cm^2, 0.26 Pa). Attention was payed that particles were transported in a continuous laminar manner in both investigated shear conditions. Furthermore, the volume of the cell medium was kept constant for both flow rates to provide the same particle numbers. To account for that, it was necessary to direct the flow back and forth several times at the higher flow rate.

Perfusion time

The following three aspects were taken into consideration to find an eligible perfusion time, i. e. the time range where shear forces are exerted on the cell monolayer in the flow channel. First, the particles should not be internalized as they can aggregate in endosoms. This would affect the number of fluorescent spots on the cells in such a way that less particles would be counted. The uptake of the model nanoparticle started in the range of 60-80 min of incubation on HuH7 cells. Consequently, a shorter time range was considered as appropriate. Second, the final number of

beads per cell had to be considered in order to reasonably evaluate the experiment. As mentioned before, a sufficient number of particles had to be attached to single cells to yield good statistics. In addition, the fluorescence of single particles should still be resolvable and saturation of the cells should be avoided. The number of adhered beads per cell does not only depend on the perfusion time, but also on the flow rate, the particle concentration and the affinity of the particles. These factors had to be taken into account accordingly. Third, as aforementioned, the surface receptor levels should remain the same during the time of the flow experiment which means that the cells should not adapt to flow conditions during that time.

Adhesion kinetics were measured to find an appropriate time point. TfR-targeted model beads with a diameter of 110 nm (A110-PEG5-B) and hydroxylated control beads (A110-PEG5-OH) were passed over HuH7 cells for 80 min at a very low shear flow (0.13 dyn/cm^2). The fluorescence of the beads was measured by live cell imaging widefield microscopy. The number of counted beads is depicted in Fig.5.5. While only a low number of both bead types bound during the first 40 min, increasing amounts of B6 beads attached in the time range between 40 and 80 min. Thus, for this shear rate an appropriate time point would be in the range of 40-60 min, avoiding uptake and providing a sufficient number of particles for the statistics. In summary, after 40 min, the number of bound particles per cell for all used shear rates was high enough to result in sufficient statistics, but still low enough to count single particles.

Influence of the dyes

When two different particle types are directly compared, it is important to ensure that their different labeling dyes have no influence on the results. To test if the dye combination has an impact on the actual outcome, flow experiments were performed with exchanged dye combinations (Fig. 5.6).

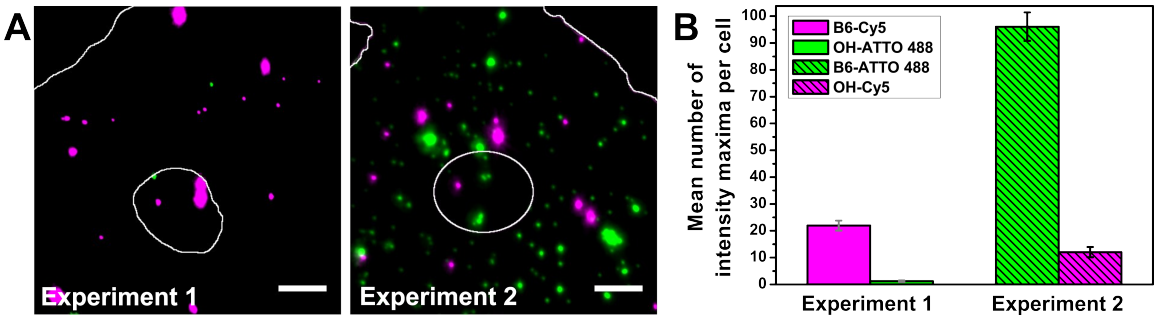

Figure 5.6: Flow experiments with exchanged dye combinations. TfR-targeted beads with peptide ligand B6 and hydroxylated control beads were incubated for 40 min on HuH7 cells under low shear conditions (0.26 dyn/cm^2). Two experiments were performed with exchanged dye combinations. (A) Representative images of B6 beads with Cy5 labeling (magenta) compared to hydroxylated control beads (ATTO 488, green) on a HuH7 cell (Experiment 1) and of B6 beads with ATTO 488 labeling (green) compared to hydroxylated beads marked with Cy5 (magenta) (Experiment 2). The plasma membrane and the nuclei are depicted by white lines. Scale bar = 10 µm. (B) Mean numbers of intensity maxima counted on single cells for Experiment 1 (solid columns) and Experiment 2 (striped columns) with exchanged dye combination. n = 19-20.

TfR-targeted B6 beads were labeled with Cy5 (magenta) and mixed in equal amounts with hydroxylated control beads (OH beads) labeled with ATTO 488 (green). The mixture was passed over a HuH7 cell monolayer at a low flow rate (0.26 dyn/cm^2) for 40 min, the cells were fixed afterwards and the fluorescence of the beads was measured by widefield microscopy adjusting the focus over single cells. The experiment was repeated with beads labeled with an exchanged dye combination, i.e. B6 beads marked with ATTO 488 and OH beads bearing Cy5. In Fig. 5.6 A, the fluorescence of the beads on representative single cells for both experiments are shown. The cell membrane and the nuclei are illustrated by white lines. The mean values of counted intensity maxima on single cell images are depicted in Fig. 5.6 B. While in Experiment 1 around 22 B6 beads (magenta) bound compared to 1.2 control beads (green) on average, 96 B6 beads (green) compared to 12 control beads (magenta) were counted in Experiment 2. Clearly, more TfR-targeted B6 beads bound to the target cells than control beads in both experiments. Nevertheless, the ratio of beads with ligand compared to control beads was different in the second experiment and the total number of bound particles was more than four times higher. In summary, the two different dyes on both particle types could be detected properly and the dye combination did not influence the major outcome. Nonetheless, the magnitude of the results was different in both experiments as well as the total amount of cellular bound particles. This finding suggests that the total number of adhered particles has an impact on the results. Therefore, additional controls or selection criteria should be introduced. In the following chapter, considerations of an external or internal control for the flow experiment will be discussed.

5.3 Internal control

Differences in the number of cellular associated nanoparticles was found in pre-experiments under flow conditions. In addition, factors were detected which cause these heterogeneous results. These parameters comprise the cell density, shape, receptor expression level as well as particle aggregation and degradation. Exemplary images of single cells are illustrated in Fig. 5.7 where different numbers of beads (upper and lower image) due to one of these factors. The fact that less particles bound to the cells at high cell density or when particles were aggregated was found as a common result. Different numbers of adhered particles were observed on cells with varying shape, i.e. height and spreading or with different target receptor expression level.

The question arises, how to account best for the impact of these factors. By comparing the adhesion of receptor-targeted to control particles on single cells, we provide an internal control. Additionally, two external controls were tested. In a first external control experiment, the beads presented in Fig. 5.6 were coated on coverglass and their fluorescence was measured. In Table 5.2 the number of beads per field of view (63.7x63.7 μm^2) is shown in the diagonal. The ratio of the number of two bead types is given by dividing the number of beads of the first row by the one of the first column. In all instances, the ratio was between 0.72-1.39 suggesting similar amounts of targeted and control particles. In a second external control experiment, the beads mixture used for flow experiments was pipetted into collagen coated image spacer chambers of 7.6 μL between two coverglasses. As

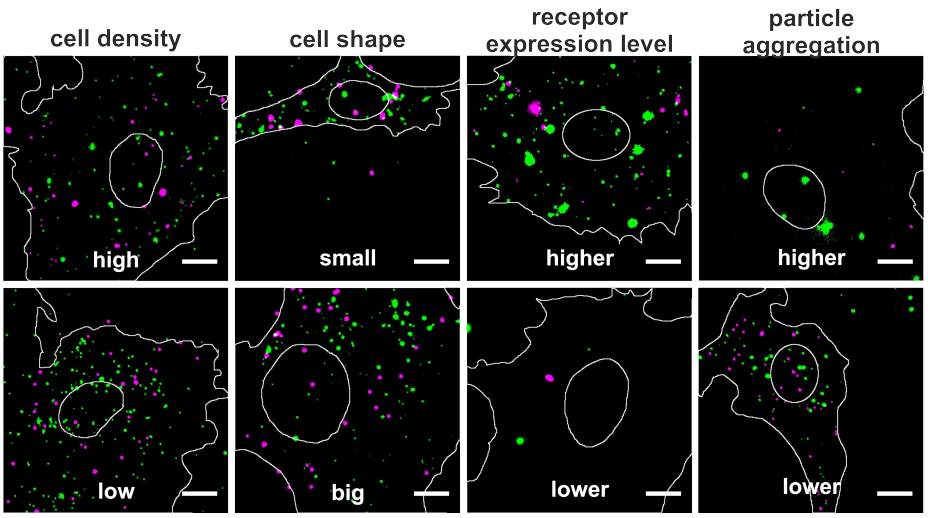

Figure 5.7: Influencing factors of single cell experiments causing heterogeneous results. Z-projections of single cells illustrating heterogenous results caused by different factors: I) *cell density:* at high confluence, the total number of adhered beads is lower than at low confluence; II) *cell shape/geometry:* in total less beads adhere to smaller cells than on bigger cells, even when the ratio of receptor-targeted to control beads is the same; III) *receptor expression level:* more receptor-targeted beads (green) bind to cells with higher receptor expression. IV) *particle aggregation:* beads can aggregate which causes reduced numbers of fluorescent spots on the cells. Scale bar = 10 μm.

before, the beads were imaged by widefield fluorescence microscopy and the number of particles was counted. Ratios were obtained in the range of 0.87-1.7 for B6 beads compared to different control beads (see Appendix 1). This shows that a factor of at most 1.7 would influence the results of the flow experiments. Beyond that, the number of beads with ligand B6 were 20-22 per field of view in the first external control experiment whereas only 16 control beads were counted in two independent samples with different dyes. This finding lead to the assumption that both particle types have different affinities to the coverglass. Consequently, the results of flow experiments could be falsified by including the factors from the external control(s). Hence, we decided to use only an internal control.

Table 5.2: External control I. Beads with ligand (A200-PEG5-B6) and control beads (A200-PEG5-OH) used for the flow experiment in Fig. 5.6, labeled with different dyes (Cy5 and ATTO 488) were coated on coverglass at 3000 rpm. The mean numbers of counted intensity maxima per field of view (63.7x63.7 μm^2) are displayed highlighted in the diagonal from the upper left to the lower right. n = 21-25. The ratio of different bead types was obtained by dividing the number of beads from the first row by the number of beads from the first column.

	B6 (Cy5)	**B6 (ATTO 488)**	**OH (Cy5)**	**OH (ATTO 488)**
B6 (Cy5)	**22.0±2.9**	0,92	0,72	0,72
B6 (ATTO 488)	1,1	**20.1±4,0**	0,78	0,79
OH (Cy5)	1,39	1,28	**15.8±2.8**	1,0
OH (ATTO 488)	1,38	1,26	0,99	**15.9±1.7**

Summing up, the same experimental conditions could be provided by simultaneously incubating the receptor-targeted model nanoparticles with control particles. Thus, the same particle concentration of both bead types was used and they were exposed to the same shear conditions, surface receptor levels and cell density. Instead of averaging over the heterogeneous number of bound beads, we decided to illustrate the heterogeneity of the results. This was achieved by the following procedure. For each cell, the number of beads with ligand was divided by the number of control beads resulting in a factor (see Fig. 5.8 A). The obtained factors were plotted in a histogram. From this distribution, the subsequent conclusions could be drawn: Factors below or equal to 1 are assigned to the fact that the ligand did not enhance particle binding, whereas factors above 1 (especially above 2) indicated an positive effect of the ligand on cellular particle binding. In Fig. 5.8 B, two factor distributions are shown. In the upper histogram, the factors of Experiment 1 are shown (Fig. 5.6). Here, Cy5-labeled B6 beads were compared to ATTO 488-labeled hydroxylated control beads. In the lower histogram, the factors of the number of ATTO 488-labeled B6 beads divided by the number of Cy5-labeled OH beads are depicted. In both cases, the factors were above 2, suggesting that the peptide B6 improved the binding of the model nanoparticles on every single cell. These experiments show the "proof of principle" of our method. The effect of a ligand on cellular binding can be approximated not only by an average value, but also the distribution on single cells can be displayed. In chapter 6, we present binding studies of TfR and c-Met-targeted model beadsusing the herein described optimized procedure.

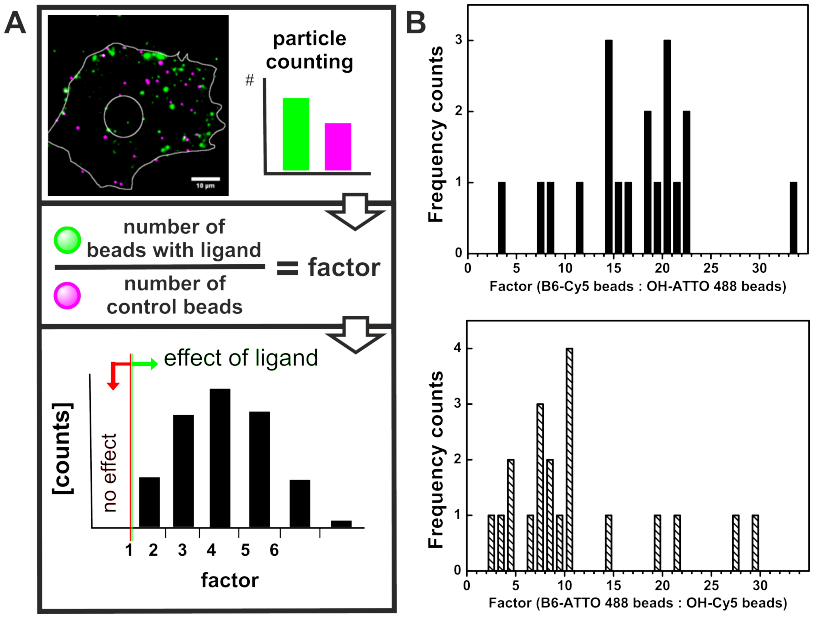

Figure 5.8: Internal control: calculation of factors and factor distribution. (A) The fluorescence of labeled beads bound onto single cells was imaged by widefield microscopy and the intensity maxima were counted. The factor of the number of beads with ligand divided by the number of control beads is calculated for each cell. Plotted in a histogram the factor distribution shows the effect of the ligand. Factors above 1 indicate enhancement of binding, factors equal or below 1 indicate no effect of the ligand. (B) The factor distributions of B6 beads compared to hydroxylated control beads on HuH7 cells after low shear flow (0.26 dyn/cm^2) are depicted for two different dye combinations: the upper histogram shows A200-PEG5-B6 (Cy5) compared to A200-PEG5-OH (ATTO 488) and the lower histogram shows A200-PEG5-B6 (ATTO 488) compared to A200-PEG5-OH (Cy5).

5.4 Summary and conclusion

In summary, we developed and optimized an experimental flow setup with internal control for quantitative adhesion studies on a single cell level. Briefly, a particle suspension is passed through a flow channel by the force of a syringe pump. A broad range of shear forces can be generated and thus, a variety of experiments can be performed with this setup. For instance, studies can be conducted to target the vascular endothelium [299, 327–329], or components of or within the blood flow such as metastatic cancer cells [303]. Also, other objectives can be pursued with the use of microfluidics. We intended to provide constant particle concentrations and to reduced sedimentation of larger particles or aggregates [300, 330]. In addition, a hydrodynamic microenvironment was introduced which can also be present around tumors [331]. Cancer cells are surrounded by disordered extracellular matrix and interstitial fluid. Due to the leakiness of the tumore tissue, the interstitial fluid pressure is elevated. This facilitates the transvascular transport of nanocarriers. Within the tumor diffusion is the predominating transport mechanism in combination with steric, hydrodynamic and electrostatic interactions between the particles and components of the extracellular matrix [279]. With our flow experiments we provide a first step in the direction of modeling the *in vivo* situation. We applied shear forces which are exerted on tumor cell surfaces exposed to elevated interstitial fluid pressure [332, 333]. Furthermore, the shear flow was increased by one order of magnitude to investigate the influence of it on cellular particle binding. Next steps towards the *in vivo* condition would be sophisticated 3D models [334–336] and animal studies [293, 337] which can mimic the complexity more realistically.

In our experiments, model nanoparticles (see chapter 4) with targeting ligand and differently labeled control beads were simultaneously passed over a cell monolayer within the flow channel. There is not a standardized norm for pre-clinical studies [270]. Indeed, the choice of experimental parameters as well as controls influence their results. We decided to perform experiments with an internal control to provide the same experimental conditions for both, receptor-targeted and control particles. So, the particles were exposed to the same cell density, the same cell environment and surface receptor levels. Thus, experimental influences on the heterogeneity of the results could be minimized. Furthermore, the internal control enabled the calculation of factors, the number of beads with ligand divided by the number of control beads. By plotting the factor distribution, the varying ratio of both particle types (with ligand and control) on single cells could be illustrated. Additionally, external control experiments were performed comparing the number of beads on cover glass or in collagen coated chambers under static conditions. As a maximum variance of factor 1.7 was observed, every factor above 2 was considered as positive targeting.

Applying sensitive fluorescence microscopy, the localization of single particles on, within or next to the cells could be determined. Furthermore, we monitored the aggregation status of the particles and the integrity of the cells. These qualitative examinations were combined with a quantitative approach in order determine the efficiency of targeting ligands.

Quantitative assessment of cellular attachment was carried out by counting the fluorescence inten-

sity maxima of labeled nanoparticles on single cells. This fast method was validated by comparison with a well established evaluation procedure based on the integrated fluorescence intensity of labeled nanoparticles (Particle_in_Cell-3D by Torrano *et. al.* [276]). The following factors were determined to influence the number of bound particles per cell: cell density and cell geometry, expression level of target receptors, particle aggregation and degradation. The number of beads per cell was optimized for reasonable evaluation. Furthermore, the time of shear flow was adjusted such that the particles were not internalized within that period and the target receptor levels did not change. Moreover, we tested if the dye combination (Cy5, λ_{max} = 649 nm and ATTO 488, λ_{max} = 501 nm) had an impact on the results when two different types of particles were compared. As the fluorescent molecules were covalently attached on the particle surface and surrounded by a PEG layer, no interaction of the dyes with the cells was expected. This was confirmed. Interestingly, the total number of particles per cell varied strongly in different experiments. Such heterogeneity of the results is known for biological experiments [338]. This diversity can originate from varying gene expression of individual cells of the same genetic clone [339]. Hence, we chose to select only experiments with a reasonable number of particles per cell for evaluation. With this criteria sufficient statistics could be achieved and misinterpretation of the results could be avoided.

In conclusion, we presented a suitable method to quantify the effect of targeting ligands on cellular adhesion of nanoparticles. It includes an optimized flow experiment, a suitable measurement technique and a reliable evaluation procedure.

6 Binding studies of receptor targeted beads

Sophisticated nano therapeutics are designed to be transported to diseased tissue, to specifically attach and be internalized into the target cells, and to be active only at the target site. There are many strategies to pursue each of these goals. While "passive targeting" enhances the accumulation of nanoparticles of a certain size range within the tumor region, "active targeting" is applied to specifically address the target. Therefore, targeting ligands are attached at the surface of the delivery devices. These ligands bind specifically to overexpressed receptors on the surface of target cells. Targeting moieties include small molecules, peptides, proteins, aptamers and antibodies or antibody fragments. Short peptide ligands are advantageous because of their low costs, long term stability, low immunogenicity, high modifiability and low influence on the physicochemical properties of the nanocarriers [340].

Here, we assessed the potential of two short peptide ligands to serve as a successful targeting ligand. First, peptide B6 which binds to the transferrin receptor (TfR) was studied. The TfR is a type II transmembrane receptor. Two identical monomers form a homodimer which is linked by two disulfide bonds. It consists of a short cytoplasmic part, a single transmembrane pass and a large extracellular domain [341, 342]. TfR mediates the uptake of transferrin-bound iron in clathrin-coated endosomal compartments. Furhter functionality involves the regulation of cell growth [343]. TfR is omnipresent on the cell surface of most normal human tissues and expressed at higher levels in malignant cells [153] as well as in brain capillaries [137]. With these properties, the TfR represents an attractive target for tumor therapy or delivery to the brain.
A second peptide, the c-Met binding peptide (cMBP2) which adheres to the hepatocyte growth factor receptor (HGFR)/c-Met was analyzed. The c-Met is a transmembrane receptor tyrosine kinase [344]. An extracellular α-domain and a transmembrane β-domain with an intracellular kinase part form a heterodimer linked by a disulfid bond [345]. HGFR/c-Met signaling is involved in invasive growth during embryogenesis and postnatal organ regeneration. It is highly regulated and usually not activated in adults except during wound healing and tissue regeneration. In cancer cells, the signaling pathway can be reactivated promoting tumor progression, invasive growth and metastasis [156]. Moreover, HGFR/c-Met is overexpressed in multiple epithelial and mesenchymal cancer cells [346]. Hence, c-Met is another reasonable candidate for cancer therapy.

In this chapter which is partially adapted from our publication in the Journal of Controlled Release [273], the effect of the peptides B6 and cMBP2 on cellular adhesion of nanoparticles is described. To quantify the impact of nanoparticle binding, flow experiments with internal control were performed (see chapter 5). Model nanoparticles (beads) that mimick the surface characteristics of therapeutic

nanocarriers (see chapter 4) were used. By comparing the number of receptor targeted beads to control beads, the effect of the ligand was approximated. We describe experiments using different beads as electrostatic and specificity controls. In the first part of this chapter, we focus on binding studies of B6 equipped beads under shear conditions. As we did not obtain the expected results with the specificity control, additional experiments were performed to gain more insights into the cellular binding behavior of model beads with the B6 ligand. In the second part of this chapter, c-Met targeting experiments under flow conditions are described. In a final summary and conclusion, we evaluated the capability of both peptides (B6 and cMBP2) to be used as effective targeting moieties.

6.1 Cellular adhesion of TfR targeted B6 beads

The peptide B6 (GHKAKGPRK) which was found to tether the TfR [309] was investigated as a potential ligand for receptor targeting. PEGylated model nanoparticles (polystyrene beads) were equipped with a ligand or control molecule. The number of B6 beads on single cells was directly compared to differently labeled hydroxylated beads (OH). As the latter beads have a reduced surface charge, these control beads were considered as an electrostatic control. In addition, B6 beads were compared to beads with a scrambled peptide (B6scr, AGKHGKRPK and RPKAHKGKG) consisting of the same amino acids, but in a different order. Apart from this specificity control, beads with a modified peptide (GHGAGGPGG) were used as a third internal control. The modification comprised the replacement of all basic amino acids by glycine to yield a neutral peptide and hence B6mod beads with a similar reduced surface charge as the OH beads.

The binding studies were performed on HuH7 cells which have high TfR expression levels shown by western blot analysis by Lu *et al.* [347]. We confirmed the results with immunostaining of TfR followed by flow cytometry analysis or fluorescence imaging (see Appendix 5 and 4).

6.1.1 Indication of the incapacity of B6 to bind as a specific targeting ligand

To assess the adhesion behavior of TfR targeted B6 beads we performed competitive binding experiments under shear conditons. The method is described in detail in chapter 5. Briefly, the binding of beads with ligand was compared to the binding of control beads on target cells. Therefore, labeled B6 beads were mixed with differently labeled control beads in equal amounts within a reservoir containing cell medium. Then, the bead suspension was passed over a cell monolayer in a flow channel for 40 min by the force of a syringe pump. Two different flow rates were used. Experiments were performed at low shear flow of $26\,s^{-1}$, corresponding to shear forces of $0.26\,dyn/cm^2$ and moderate shear flow of $263\,s^{-1}$, corresponding to shear forces of $2.63\,dyn/cm^2$. The cells were fixed afterwards and imaged by widefield microscopy.

In Fig. 6.1 A, representative images of the beads with ligand (green) and control beads (magenta) on single cells are illustrated for each type of experiment. The adjacent bars in Fig. 6.1 B show that the mean number of beads with B6 ligand bound around 5 times more than non-charged hydroxy-

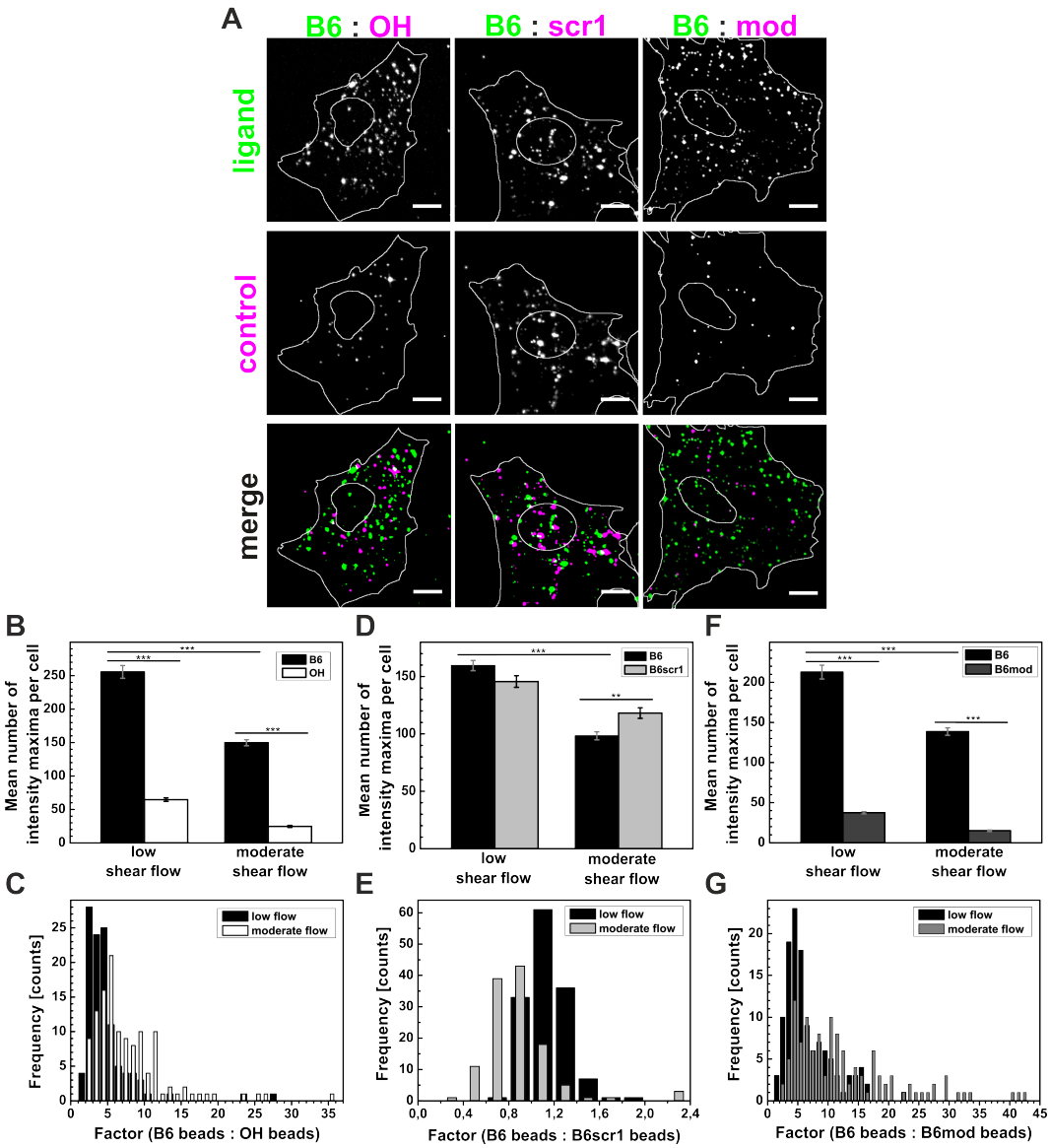

Figure 6.1: Effect of the peptide B6 on cellular binding. Adhesion of beads with ligand (B6, dye 1) and control beads (dye 2) on HuH7 cells after 40 min under low (26 s^{-1}) and moderate (263 s^{-1}) shear conditions. (A) Representative images of receptor targeted beads (with ligand: B6; green) and control beads (hydroxylated, with scrambled or modified peptide; magenta) on single cells after low shear flow. The plasma membrane and the nucleus are depicted by white lines. Scale bar = 10 µm. (B) The mean numbers of TfR targeted B6 beads (black column) and hydroxylated control beads (white column) on single cells after low (left) and moderate (right) shear flow are shown. ***p<0.0001, n =112-125. (C) The factor distributions of B6 beads compared to hydroxylated control beads after low (black) and moderate (white) shear flow are depicted. (D) The mean numbers of TfR targeted B6 beads (black column) and control beads with scrambled peptide B6scr (light grey column) on single cells after low (left) and moderate (right) shear flow are shown. ***p<0.0001, **p≤0.001; n =122-140. (E) The factor distributions of B6 beads compared to control beads with scrambled peptide B6scr after low (black) and moderate (grey) shear flow are depicted. (F) The mean numbers of TfR targeted B6 beads (black column) and control beads with modified peptide B6mod (dark grey column) on single cells after low (left) and moderate (right) shear flow are shown. ***p<0.0001; n =123-124. (G) The factor distributions of B6 beads compared to control beads with modified peptide B6mod after low (black) and moderate (grey) shear flow are depicted.

lated (OH) beads on average (electrostatic control). The number of bound beads, with and without ligand decreased by 40-50 % at 10fold higher shear forces. As expected, the number of control beads dropped even more than the number of B6 beads. This suggests that the attachment forces of the B6 peptide on the cell surface are stronger than the interactions of the hydroxylated polystyrene beads. To examine the heterogeneity of particle binding on single cells, the factor distribution of the number of B6 beads divided by the number of control beads is displayed in Fig. 6.1 C. The obtained factors ranged from 1.1 to 27 with an average value of around 4 at low shear flow and from 2.1 to 35 with an average value of 6 at moderate shear flow. By comparing the adhesion of B6 beads to the adhesion of beads with scrambled ligand (B6scr1) (specificity control), similar attachment of both bead types was detected at both shear rates (Fig. 6.1 D). The peak of the factor distributions were close to 1 in both cases, indicating similar affinity of both peptides to the HuH7 cell surface (see Fig. 6.1 E). The sequence of the B6 peptide seems not to be crucial for receptor binding, but other interactions like electrostatic attraction might play a role in the adhesion process of B6 equipped beads to HuH7 cells. Interestingly, the total mean number of beads per cell was in the range of 200-400 for all experiments and the number of bound B6 beads was reduced in the presence of B6scr1 beads. This implies that B6 and B6scr1 beads might compete for cell surface binding and that saturation of cell binding is reached. Theoretically, there should be many more transferrin binding sites (210.000 per HuH7 cell according to Tinder *et al.* [348]) and also unspecific binding sites like negatively charged surface molecules on the cell surface. These facts suggest that there could be a charge effect of already bound, positively charged beads partially repulsing newly arriving positively charged beads. As we found that the binding of B6 beads seems to be independent of the peptide's amino acid sequence, we provided supplementary control beads. Therefore, the B6 peptide was modified in such a way that all basic amino acids were replaced by glycine, a neutral amino acid. These B6mod control beads exhibited a lower surface charge than the B6 beads. They showed a similar binding pattern as the hydroxylated control beads (Fig. 6.1 F). On average, 5 times more B6 beads bound per HuH7 cell compared to B6mod beads at low shear flow. The ratio of the mean values was increased to approximately 9 when elevated shear flow was applied. This is comparable to the results obtained by comparison with hydroxylated control beads. The factor distribution of the number of B6 beads divided by the number of B6mod beads, displayed in Fig. 6.1 G, was similar as the factor distribution resulting from experiments with hydroxylated control beads. This indicates that the basic amino acids are involved in the binding process. Furthermore, our findings point to the fact that the binding of B6 beads to HuH7 cells seems to be dominated by different interactions such as electrostatic interactions of the positively charged beads with the negatively charged cell surface instead of specific receptor-ligand interaction.

In order to confirm the findings, we tested the adhesion of B6 beads on a second target cell line. Overexpression of TfR on DU145 cells was shown by Nie *et al.* [349] using flow cytometry. As before, flow experiments with internal control were performed. The binding of B6 beads was compared to the binding of hydroxylated beads and of beads with scrambled peptide (B6scr1) at low shear flow. In Fig. 6.2 A, the mean values of B6 beads (black) and control beads (hydroxylated: whiten, B6scr1: gray) are displayed. Around 5 times more B6 bound compared to hydroxylated beads. The number of attached B6scr1 beads was even more than the number of B6 beads. These

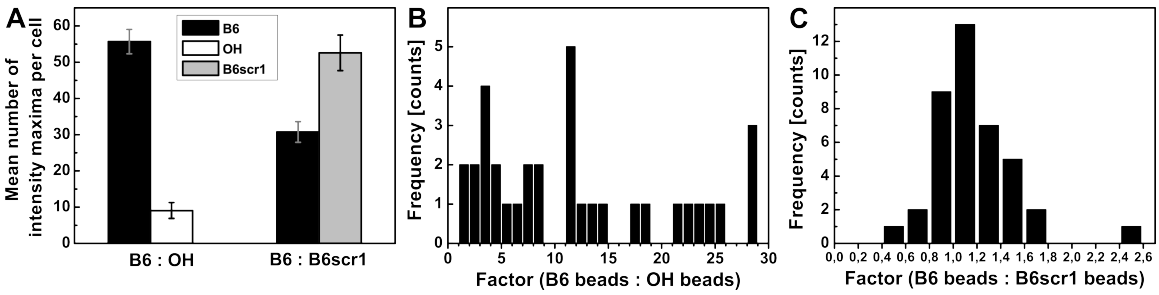

Figure 6.2: Effect of the peptide B6 on binding to TfR targeted DU145 cells. Adhsion of beads with ligand (B6, dye 1) and control beads (dye 2) on DU145 cells after 40 min under low (26 s^{-1}) shear conditions. (A) The mean numbers of TfR targeted B6 beads (black column) and hydroxylated (white column) control beads or with scrambled peptide B6scr1 (grey column) on single cells are shown. n = 40. (B) The factor distribution of B6 beads compared to hydroxylated control beads are depicted. (C) The factor distribution of B6 beads compared to control beads with scrambled peptide (B6scr1) are represented.

results were similar as observed on HuH7 cells, but the total number of adhered beads was clearly lower on DU145 cells. The factor distribution of B6 beads compared to hydroxylated beads ranged from 1 to 29 (see Fig. 6.2 B), suggesting again an positive effect of the peptide on particle binding. The factors of the comparison with scrambled peptide are depicted in Fig. 6.2 C. Both bead types bound with equal ratio to the DU145 cells. These results support the hypothesis that the binding of the B6 beads does not involve the specific interaction of the peptide with the TfR. So, do the B6 beads bind specifically to the TfR on the cells or is unspecific attraction the main binding interaction?

6.1.2 Transferrin receptor specificity and unspecific binding

The peptide B6 was found by phage display to improve the gene transfer of adenovirus to several cell lines expressing the human TfR [309]. This specificity was attributed to a certain motif of the peptide's amino acid sequence. However, our experiments could not confirm these findings. Furthermore, the binding site at the TfR was not identified. Hence, we performed additional experiments to get more insights into the binding behavior of model beads equipped with the peptide ligand B6.

6.1.2.1 Second scrambled peptide

In previous flow experiments, similar numbers of TfR targeted B6 and control beads with scrambled peptide (B6scr1) were counted on single cells. This suggests that both peptides have a similar affinity to the target cells. To test if the scrambled peptide is by chance another ligand of the TfR, a second scrambled peptide (B6scr2) was coupled onto the model beads. Additional flow experiments were performed at moderate shear flow. The number of B6 beads was compared to first, the number of B6scr1 beads and second, the number of B6scr2 beads. The mean numbers of adhered beads on single cells are shown in Fig. 6.3 A. Similar amounts of all three bead types (B6, B6scr1 and B6scr2) were determined. Beads with the second scrambled peptide (B6scr2) even showed slightly increased attachment. The factor distributions of the number of targeted compared to control beads are depcited in Fig. 6.3 B. Both distributions are similar and show a maximum

around 1. This implies that the affinities of beads with either of the scrambled peptides are almost equal. Thus, the amino acid sequence of the peptides does not play a role in the binding process to HuH7 cells. There are two possibilities: all peptides, B6, B6scr1 and B6scr2, are ligands of the TfR and bind specifically to the receptor, or they bind non-specifically to HuH7 cells due to other attraction forces such as electrostatic interactions.

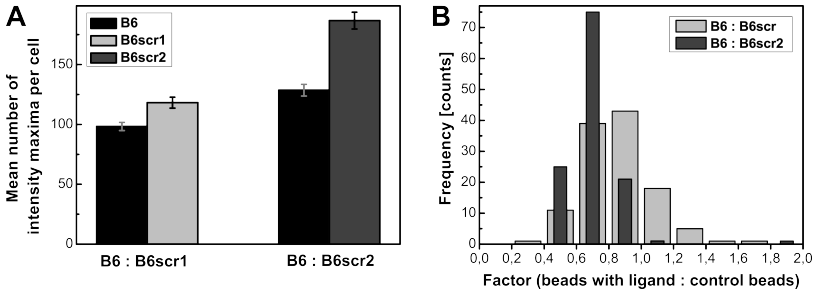

Figure 6.3: Effect of the scrambled amino acid sequence. Adhesion of beads with B6 ligand (dye 1) and with B6 scrambled peptide (dye 2) on HuH7 cells after 40 min of moderate shear flow (263 s^{-1}). (A) The mean number of beads with B6 ligand (black column) and scrambled B6 peptide (B6scr1, light grey column; B6scr2, dark grey column, second sequence) on single cells is shown. n = 122-123. (B) The factor distributions of B6 beads compared to control beads with scrambled peptide (B6scr1, light gray) or a second scrambled peptide (B6scr2, dark gray) are depicted.

6.1.2.2 Uptake

Beads coated with the peptide B6 are designed to enter the target cells via the TfR. The endocytosis of the Tf-TfR complex and its recycling is a fast process in the range of 10-20 min [146, 147]. Thus, a high accumulation of nanoparticles within the cytosol is expected entering the cells via this route. The receptor-mediated uptake of Tf is clathrin-dependent. Despite the fact that clathrin-coated pits have a diameter of 100 nm, it has been shown that Tf-coated nanoparticles (> 500 nm) can be internalized by clathrin-coated vesicles [350]. If the TfR targeted B6 beads are internalized by the same route, an enhanced uptake efficiency is expected compared to the control beads.

The cellular uptake of nanoparticles can be assessed by various methods. With confocal microscopy, it is possible to estimate if a particle is inside the cell, within the cell membrane region or outside the cell thanks to the resolution in z. In this case the membrane of the cell has to be stained and a two channel image has to be acquired. Another method to determine if the particles are internalized is to use a quencher of the fluorescence (eg. trypan blue) of the particles. After the treatment only the particles that are internalized are still fluorescent. Co-localization of particles with endosomal markers is another procedure that gives information about the particles' uptake. Furthermore, the active transport of internalized particles can be recorded by visualization of the particles' movement. This method is a very clear and easy discrimination of particles inside the cytoplasm and was used to show the uptake of the model nanoparticles. Therefore, TfR targeted beads (A200-PEG5-B6) and control beads (A200-PEG5-B6scr1/B6mod/OH) labeled with ATTO 488 were incubated with target cells (DU145) for 6 h. Movies were recorded by spinning disk microscopy where the movement of the beads was observed in one plane for approximately 1 min. In Fig. 6.4,

the fluorescence of the beads at the beginning of the measurement is shown (left) and the respective time projections (right). Transmission light images were used to mark the nuclei (dotted lines) and the cell membrane (dashed line). Clearly, more B6 and B6scr1 beads than B6mod and OH beads were internalized. Movement of actively transported beads can be observed in the time projections as directional lines. Many B6 and B6scr beads show such motion whereas less movement of B6mod and hydroxylated beads was observed. These control beads resided mainly in the perinuclear reagion. A difference in the uptake behavior of B6 and B6scr beads was not detected. These results confirm the findings of another uptake experiment where the beads were incubated with HuH7 cells for 2 h under static conditions (see chapter 4.3). In conclusion, B6 and B6scr show faster, but similar uptake into target cells whereas the control beads with less surface charge are internalized less efficient.

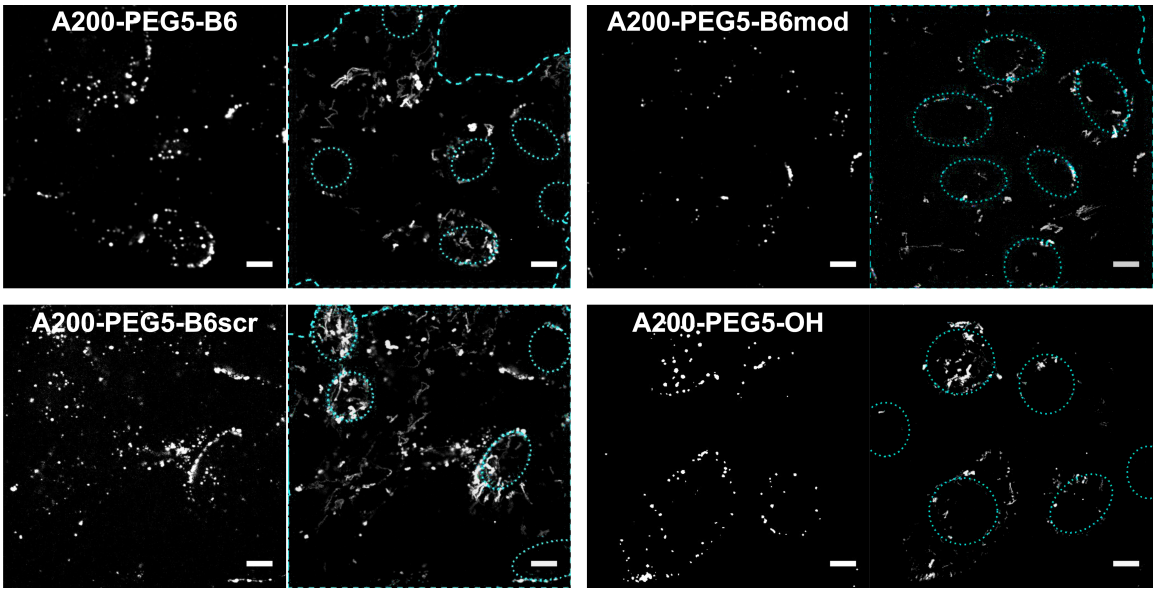

Figure 6.4: Uptake of TfR targeted B6 and control beads into DU145 cells. ATTO 488 labeled B6 beads or Cy5 labeled control beads (with scarmbled peptide B6scr, with modified peptide B6mod or hydroxylated) were incubated on DU145 cells for 6 h in 8 well chambers, the fluorophores were excited by 488 nm and 639 nm lasers and the fluorescence of one plane of several cells was measured with spinning disk microscopy for 65.37 s at 7.65 s^{-1}. The first image of the time series is shown on the left, a time projection is depicted on the right where a dashed line displays the cell borders and the dotted lines illustrate the region of the nucleus. Moving beads on the cell membrane, during membrane penetration and diffusive motion within the cell can be recognized as small lines, whereas larger lines indicate active transport of beads within the cell. Scale bar = 10 µm.

6.1.2.3 Colocalization with free ligand in endosomal compartments

As mentioned before, the receptor-mediated uptake of Tf is clathrin-dependent. Therefore, Tf can be used as marker of clathrin-dependent endocytosis. This means, that beads entering the cells via the same route should be in the same endosomal compartments as free Tf molecules. A high degree of co-localization within target cells was expected for labeled Tf and TfR targeted B6 beads. Attention was paid that the concentration of labeled Tf was low. Thus, we could exclude that free Tf competed for binding with the B6 beads. In the experiment, Alexa647 labeled Tf was

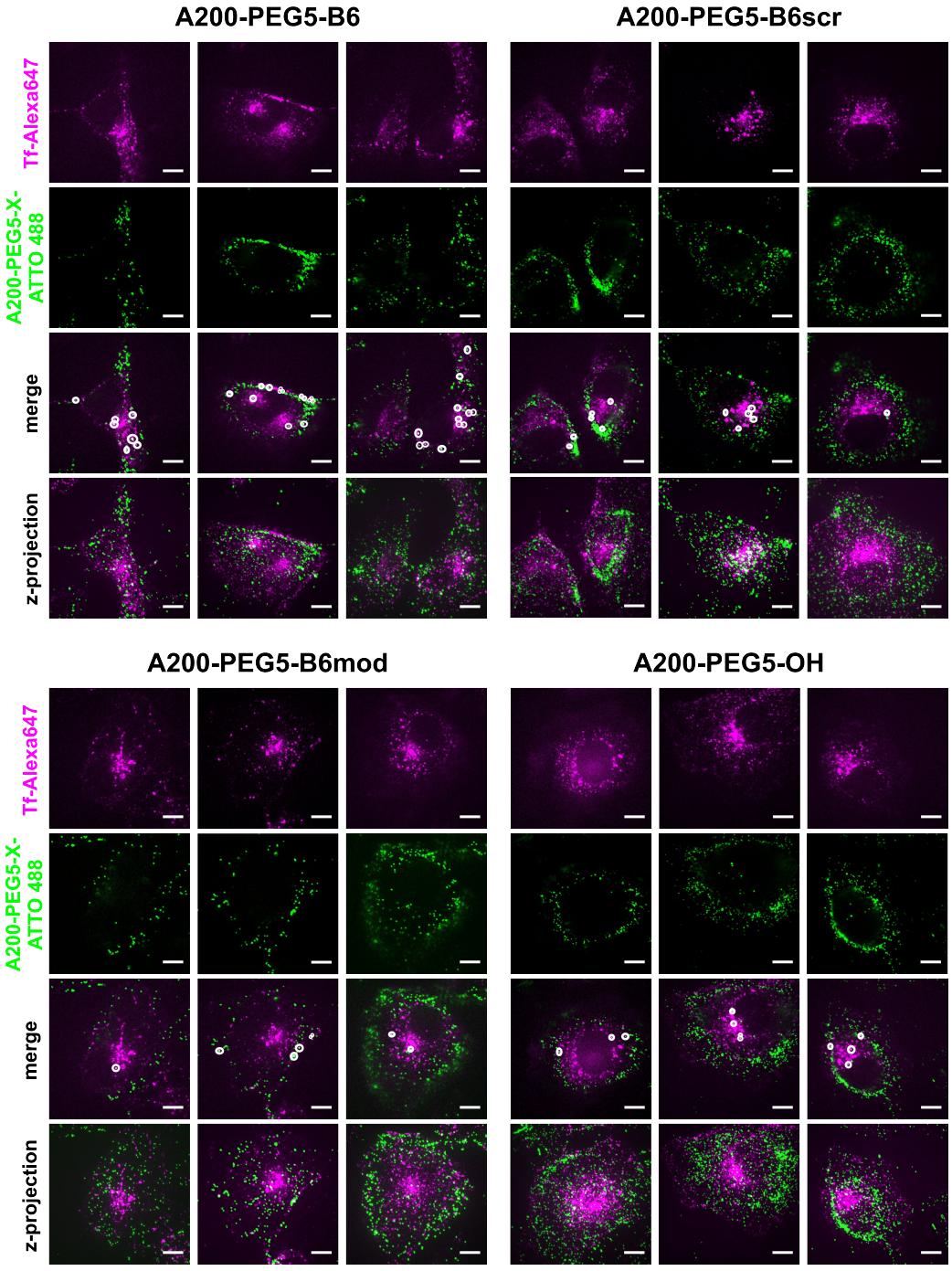

Figure 6.5: Localization of TfR targeted B6 or control beads and free transferrin on single HuH7 cells. HuH7 cells were preincubated with Tf-Alexa647 (3.3 µg/mL) for 45 min, ATTO 488-labeled beads were incubated for 1.5 h and the cells were fixated with PFA afterwards. The fluorophores were excited alternatingly with 488 nm and 639 nm lasers and cell stacks were recorded by spinning disk microscopy. In the first row the fluorescence of Tf-Alexa647 in one plane of single cells is shown, in the second row the fluorescence of A200-PEG5-x beads (x = B6, B6scr, B6mod or hydroxylated), in the third row a merged image is displayed where colocalizing spots are encircled. In the last row a z-projection over the whole cell is depicted. Predominantly there is no colocalization of Tf and the beads indicating different uptake pathways. Scale bar = 10 µm.

preincubated for 45 min and coincubated with B6 or control beads for 1.5h with HuH7 cells under static conditions. The cells were fixed and the fluorescence of Tf and the beads was investigated on single cells by spinning disk microscopy. In Fig. 6.5, representative images of the fluorescence of Tf (magenta), of the beads (A200-PEG5-B6/B6scr/B6mod/OH, green) and merged images of HuH7 cells are shown. A plan in the middle of the cells was chosen. The round, non-fluorescent areas can be assigned to the regions of the nuclei. Co-localizing fluorescent spots of Tf and beads are encircled. Additionally, z-projections of the cells are depicted. Transferrin was observed in the perinuclear region of the cells. Beads of all types were mainly located on the cell membrane. Few beads were internalized and few co-localizing spots of Tf with all kind of beads were found on all cells. By qualitative analysis, most overlapping fluorescence with the fluorescence of Tf was observed for B6 beads. No significant difference could be detected by comparison with the control beads. When incubating labeled Tf with the cells for a longer period of time (6 h), no fluorescence of the protein could be detected. Presumably, the Tf was recycled back into the cell medium during this time. Overall, a distinct conclusion cannot be drawn form these findings. A clathrin-dependent uptake of B6 beads cannot be excluded, but is very unlikely.

6.1.2.4 Colocalization with TfR-GFP

In addition to localize the TfR targeted B6 beads in clathrin-coated endosoms, we visualized them directly on cells overexpressing fluorescent receptor. Therefore, HeLa cells were transfected transiently with TfR-GFP and incubated with Cy5 labeled beads for 30 min and 2 h, respectively. As a control, Tf labeled with Alexa633 was incubated with the cells. Fluorescence image stacks over single cells were recorded by spinning disk microscopy with alternating excitation at 488 nm and 639 nm. In Fig. 6.6, representative fluorescence images of TfR and B6 beads or Tf are shown in a central cell plane. In addition, a merged image is displayed. The GFP labeled receptors were located throughout the whole cell except the nuclear region. High accumulations of TfR were found close to the nucleus and at pointed cell borders. The beads were not internalized after 30 min and partially after 2 h. Few beads showed co-localization with the receptors. In contrary, high amounts of free Tf was observed on the fluorescent receptors especially at the accumulation sites. This proves the association of Tf with the TfR. In the first place, these results suggest that no or only very few TfR targeted beads bind specifically to the receptors. However, the endogenous receptors are not labeled. Moreover, the fluorescence of the GFP labeled receptor is not resolved for single receptors. This means that there is still the possibility of specific binding which cannot be detected by this experiment.

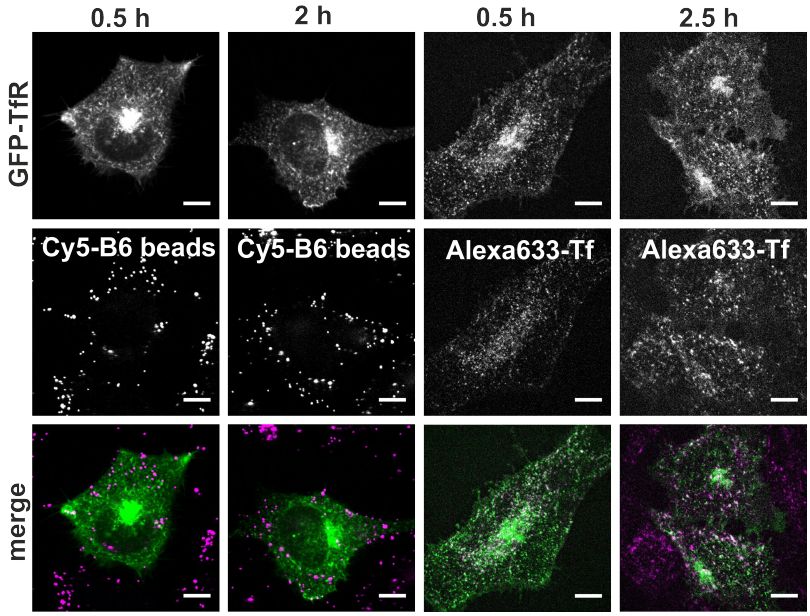

Figure 6.6: Colocalization with GFP labeled TfR. GFP-TfR transfected HeLa cells (1^{st} row) were incubated with Cy5 labeled TfR targeted B6 beads for 0.5 and 2 h or with Alexa633 labeled transferrin (2^{nd} row) for 0.5 and 2.5 h and the fluorescence was imaged alternatingly by excitation with 488 nm and 639 nm lasers with spinning disk microscopy. Representative images of one plane of single cells are shown. In the third row merged images are represented where co-localization can only clearly be detected for Tf and GFP-TfR. Scale bar = 10 µm.

6.1.2.5 Competition with free ligand

Before, it was shown that free Tf binds to GFP-labeled TfR, but mainly does not co-localize with B6 beads on target cells. The amount of free Tf was very low to avoid competition of the natural ligand for binding to the TfR. On contrary to these studies, we intended to block the surface TfRs on the target cells in an additional experiment. Two effects were expected: first, that binding of TfR targeted beads is reduced by free Tf and second, that beads which bind specifically to the TfR on target cells show less binding compared to control beads which bind non-specifically.

HuH7 cells were pretreated with non-labeled holo-Tf for 45 min. Afterwards, model beads were coincubated with an excess of holo-transferrin (5 mg/mL) with the HuH7 cells for 1 h. As a control, model beads were incubated with HuH7 cells without Tf treatment. The fluorescence of all beads on single cells was measured by spinning disk microscopy and the integrated density was calculated. The determined mean values are depicted in Fig. 6.7. Beads with the peptide B6 and the two scrambled versions (B6scr1 and B6scr2) bound in similar high amounts to the cells whereas the adhesion of beads with reduced surface charge (B6mod and hydroxylated) was very low. This result is consistent with the flow experiments. Treatment with free transferrin reduced the binding

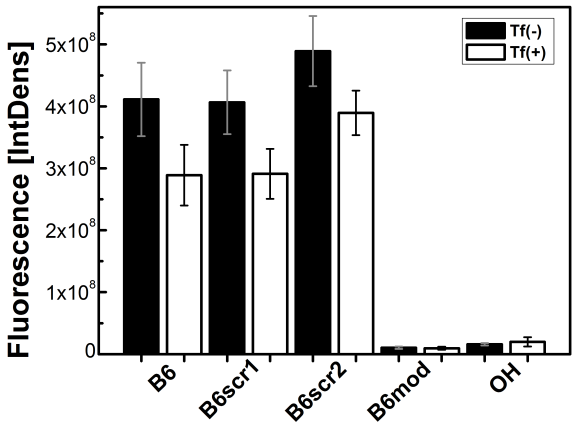

Figure 6.7: Competition with free transferrin. Adhesion of functionalized polystyrene beads (B6, B6 scrambled, B6 scrambled 2, B6 modified and hydroxylated) on TfR overexpressing HuH7 cells after 1 h of incubation in cell medium without transferrin (Tf(-), black column) and with free transferrin (Tf(+), 5 mg/mL, 45 min preincubation, white column). The mean values of the fluorescence integrated density (IntDens) of all beads on a single cell are shown. n=20.

of B6, B6scr1 and B6scr2 to the same low degree, but did barely influence the binding of beads with modified peptide or hydroxyl surface groups. There are two possible explanations: first, all beads bind non-specifically to the HuH7 cells, but the highly positively charged are partially repulsed by the negatively charged transferrin molecules bound on TfRs at the cell surface. As second alternative, some of the beads with B6 or scrambled peptide bound to the TfR, but probably not at the Tf binding site. Nonetheless, the main fraction of the beads seem to adhere in a non-specific manner to alternative surface molecules. Thus, we assume that the binding of beads equipped with the peptide B6 on HuH7 cells is essentially not based on specific receptor-ligand interactions.

6.1.2.6 Binding to non-target endothelial cells

As described in the previous chapters, we found many indications that model nanoparticles equipped with the peptide ligand B6 do not bind specifically to target cells. The specificity to the receptor is the main benefit of targeting ligands. Nevertheless, the targeting approach should not involve considerable drawbacks such as enhancing undesired adhesion to non-target cells. In other words, therapeutic nanoparticles should bind to diseased cells with target receptor overexpression, but not to healthy cells.

Hence, we tested the adhesion of the B6 beads to noncancerous endothelial HMEC-1 cells. As described before, we performed flow experiments where the binding of TfR targeted B6 beads is compared to the adhesion of hydroxylated control beads. A suspension of both bead types with different fluorescent labels was perfused over a cell monolayer for 40 min at a low flow rate. After fixation of the cells, the samples were imaged by widefield microscopy. Finally, the number of fluorescent maxima was counted on single cells. In Fig. 6.8 A, representative images of the fluorescence of B6 and hydroxylated beads are shown on single cells. To compare the adhesion

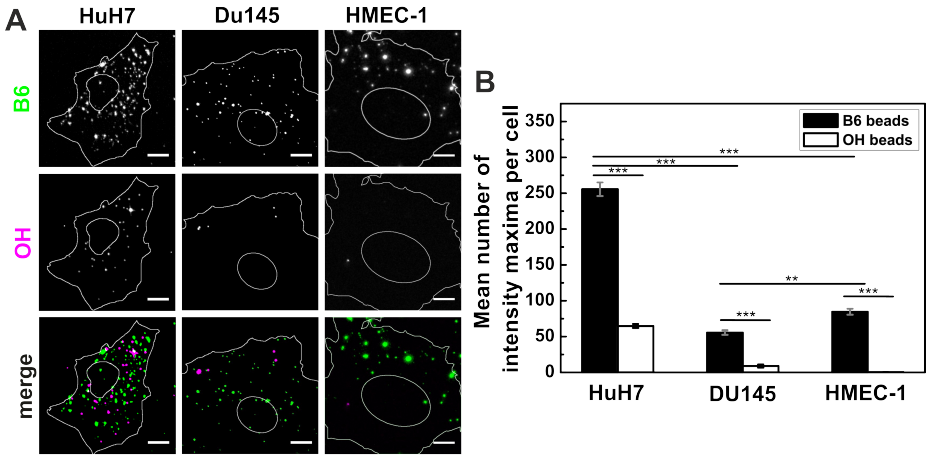

Figure 6.8: Binding to target epithelial cancer cells and non-target endothelial cells under shear conditions. Adhesion of beads with ligand (B6, dye 1) and hydroxylated control beads (OH, dye 2) on epithelial HuH7 and DU145 cells and endothelial HMEC-1 cells after 40 min under low shear conditions (26 s^{-1}). (A) Representative images of receptor targeted beads (with ligand B6; green) and control beads (hydroxylated; magenta) bound on single cells. The plasma membrane and the nucleus are depicted by white lines. Scale bar = 10 µm. (B) The mean numbers of beads, TfR targeted B6 beads (black columns) and hydroxylated control beads (white columns) on single cells are shown. ***p<0.0001, **p≤0.001; n = 40-121.

of the beads on the human microvascular endothelial cells (HMEC-1) with the binding on tumor cells, i.e. on hepatocellular carcinoma (HuH7) and prostate cancer (DU145) cells, the mean values of adhered beads on these cell lines are plotted in Fig. 6.8 B. The number of B6 beads on single endothelial cells (ca. 80) decreased significantly compared to the number on HuH7 target cells (ca. 250) , but was in a similar range as the number on DU145 target cells (ca. 65). This result implies that the affinity to HuH7 cells is higher, whereas the attraction to DU145 and HMEC-1 cells is almost equal. The lower binding to the endothelial cells is reasonable as they possess less surface TfR than HuH7 cells (see Appendix 5). The lower affinity to DU145 cells might result from a different composition of cell surface molecules and different cell surface charge. Thus, less unspecific interaction of the beads with the cell surface occur. Interestingly, almost no hydroxylated control beads bound to the HMEC-1 cells. This result suggests that HMEC-1 cells have a different membrane composition than the epithelial cancer cell lines. In addition, endothelial cells are very sensitive to shear forces. They can adapt to flow conditions by changing the morphology to a smooth surface [326] and rearrangement of actin [299]. Concluding, the number of bound B6 beads was still high on the non-target cells. Thus, nanoparticles equipped with the peptide B6 would probably also bind to other cells and tissues within the body.

6.2 Cellular adhesion of c-Met targeted cMBP2 beads

The peptide cMBP2 (KSLSRHDHIHHHK) which was found to bind the HGFR/c-Met [313] was investigated as a second potential ligand for receptor targeting. As described before for studies of B6, the peptide cMBP2 was linked to PEGylated polystyrene beads. Beads with hydroxy surface groups (OH) were used as control beads to analyze the electrostatic influences on cellular binding

of the beads. Additionally, a scrambled peptide (cMBP2scr, HHSIHRLHHKSDK) was coupled to the beads which is composed of the same amino acids, but in a different order. The obtained beads possessed similar surface charge compared to the cMBP2 beads and served as specificity control.

The binding studies were performed on HuH7 cells which have been tested positive for c-Met surface receptors by immunostaining analyzed by flow cytometry and fluorescence imaging (see Appendix 5 and 4). Interestingly, the images revealed bright fluorescent spots on the cell surfaces indicating that c-Met is clustered on the cell membrane. Furthermore, cells at different passage numbers were immunostained. Higher amounts of c-Met were observed at higher numbers of passaging (see Appendix 4).

Flow experiments with internal control allowed for assessing the potential of the cMBP2 peptide to be used as a targeting ligand. We analyzed the effect of this peptide in the same way as for the peptide B6. To apprise the binding capacity to non-targeting cells, we additionally tested the adhesion behavior also on endothelial HMEC-1 cells.

6.2.1 Qualification of cMBP2 as a targeting ligand

In order to assess the potential of the cMBP2 peptide to serve as a suitable targeting ligand, flow experiments were performed as described before. The adhesion of cMBP2 equipped beads was compared to the adhesion of control beads on c-Met expressing HuH7 target cells. Representative images of beads with ligand (green) and control beads (magenta) on single cells are illustrated in Fig. 6.9 A for each type of experiment. Predominantly, the beads were homogeneously distributed throughout the whole cell surface and did not attach to the bottom of the channel. The adjacent bars in Fig. 6.9 B show the mean number of beads with cMBP2 compared to the mean number of hydroxylated control beads per cell at low and moderate shear flow. Beads with cMBP2 ligand showed 4-5 times higher attachment to HuH7 cells than the neutrally charged, hydroxylated beads (electrostatic control) at low and moderate shear flow. The factor of the number of targeted divided by the number of control beads on single cells was calculated and depicted in a histogram (Fig. 6.9 C). The frequency of the factors corresponds to the number of single cells for which the respective factor was determined. The factor distributions shown in Fig. 6.9 C were similar for both flow velocities and ranged from factors of 2 until 20. Despite the high heterogeneity, all factors were above 1 indicating that the binding of beads with ligand was preferred on every cell. Experiments with the scrambled peptide (cMBP2scr) control beads (specificity control) resulted in similar average numbers of attached beads on the cells as the hydroxylated beads with lower surface charge (Fig. 6.9 D). The factor distribution at the low shear rate resembled the distribution at the moderate shear rate (Fig. 6.9 E). Thus, by comparing the binding of both control bead types, the adhesion is similar resulting in the assumption that the sequence of the cMBP2 peptide is crucial for binding to the c-Met expressing HuH7 cells. We expected to reduce cellular binding by increasing the shear force as observed by Sarfati *et al.* [303] for non-targeted particles and by Mennesson *et al.* [351] for polyplexes. On the contrary, cMBP2 beads showed enhanced binding at increased shear flow. A higher amount of adhered beads can be explained by the fact that the bead suspension passed the cells 10 times more often at moderate flow (forth and back flow) than at low flow (flow in one

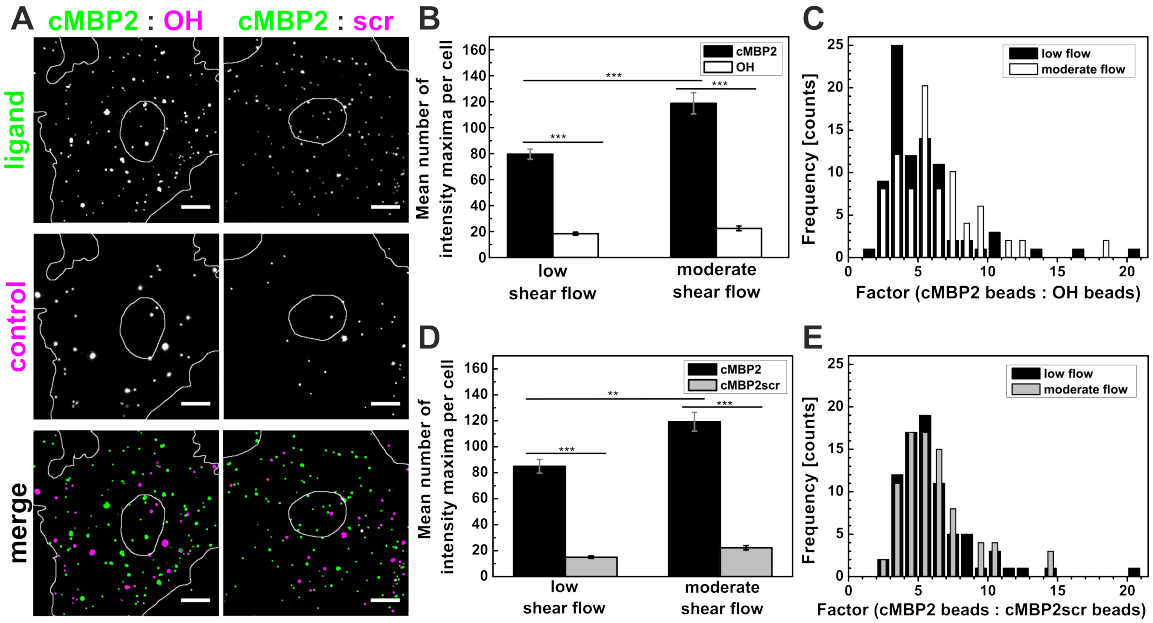

Figure 6.9: Effect of the ligand cMBP2 on cellular binding. Adhesion of beads with ligand (cMBP2, dye 1) and control beads (dye 2) on HuH7 cells after 40 min under low (26 s^{-1}) and moderate (263 s^{-1}) shear conditions. (A) Representative images of receptor targeted beads (with ligand: cMBP2; green) and control beads (hydroxylated or with scrambled peptide; magenta) on single cells after low shear flow. The plasma membrane and the nucleus are depicted by white lines. Scale bar = 10 μm. (B) The mean numbers of c-Met targeted cMBP2 beads (black column) and hydroxylated control beads (white column) on single cells after low (left) and moderate (right) shear flow are shown. ***p<0.0001; n =42-83. (C) The factor distributions of cMBP2 beads compared to hydroxylated control beads after low (black) and moderate (white) shear flow are depicted. (D) The mean numbers of c-Met targeted cMBP2 beads (black column) and control beads with scrambled peptide cMBP2scr (grey column) on single cells after low (left) and moderate (right) shear flow are shown. ***p<0.0001, **p≤0.001; n =80-81. (E) The factor distributions of cMBP2 beads compared to control beads with scrambled peptide cMBP2scr after low (black) and moderate (grey) shear flow are depicted.

direction), enhancing the probability for cell contacts. However, one should mention that changing the flow rate by the 10fold does not seem to dramatically change the factor distribution of the beads but only induces slight changes in bound bead numbers per cell. Thus, we consider that the results of the flow experiments are reasonable and independent in the regime of shear ranges we used.

6.2.2 Binding to endothelial cells

The adhesion of cMBP2 beads was also tested on microvascular endothelial cells (HMEC-1). Flow cytometry tests revealed that c-Met is exposed on the cell surface of HMEC-1 cells to the same extend as on HuH7 cells (see Appendix 5). However, with immunostaining and imaging by fluorescence microscopy different receptor levels were observed. While most HuH7 cells showed fluorescence of immunostained c-Met on their plasma membrane, some of the HMEC-1 cells did not show any fluorescence. Patel et al. [352] reported c-Met expression by HMEC-1 by western blot analysis. They found high levels of the β-subunit and low levels of the α-subunit. Our images from the immunostaining were obtained by using a primary antibody against c-Met with the antigen located at the first 100 amino acids (N-terminal). This region corresponds to a part of the α-subunit.

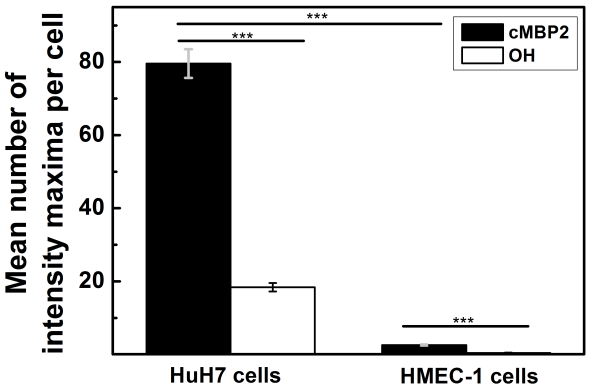

Figure 6.10: Binding of beads with cMBP2 ligand to non-targeted endothelial cells under shear conditions compared to the binding on HGFR/c-Met targeted epithelial cancer cells. Adhesion of HGFR/c-Met targeted cMBP2 beads (black column) compared to hydroxylated control beads (white column) on HuH7 target cells or endothelial HMEC-1 cells after 40 min of low (26 s^{-1}) shear flow. The mean numbers of bound beads on single cells are depicted. ***p<0.0001; n = 83-127.

Thus, a possible explanation of our finding could be the lack of matured c-Met (heterodimer) on the surface of some HMEC-1 cells, also taking into account that the number of passage was very low (3 passages). Eventually, the divers expression level of c-Met at the HMEC-1 surfaces suggest that the number of cMBP2 beads bound to single cells should vary highly on HMEC-1 cells.

Flow experiments with internal control were performed as described before. The mean numbers of cMBP2 (black) and hydroxylated (white) beads on single HuH7 and HMEC-1 cells are depicted in Fig. 6.10. Clearly, the binding of cMBP2 beads is significantly reduced on HMEC-1 cells. Only 3-4 beads adhered per HMEC-1 cell compared to around 80 per HuH7 cell. Almost no hydroxylated control bead bound to the HMEC-1 cell surfaces. This finding confirms the results obtained when comparing the adhesion of B6 beads to hydroxylated control beads on HMEC-1 cells. As expected, the number of cMBP2 beads on single cells varied (from 0 to 29). Nevertheless, this result can be interpreted by different levels of c-Met on single cells, but also might display biological heterogeneity. Likewise, the numbers of cMBP2 beads counted on HuH7 cells was within a broad range (18 to 169).

6.3 Summary and conclusion

In summary, we assessed the potential of peptide ligands to be a suitable targeting moiety. Therefore, cellular binding studies under flow conditions were performed. The binding of model nanoparticles (latex beads) equipped with targeting peptide was compared to the binding of internal control beads. The model beads were passed over a target cell monolayer for 40 min. First, beads with ligand were compared to hydroxylated beads. The receptor targeted beads exhibited a higher positive surface charge than the control beads which were considered as an electrostatic

control. A specificity control was performed by comparting beads with ligand to beads with a scrambled peptide, both exhibiting the same surface charge, but a different order of amino acids. The number of attached beads on single cells was counted and the ratio between the numbers of receptor targeted and control beads was calculated to yield factors. For a positive effect of the ligand on cellular binding, factors above 1 were expected. Especially factors above 2 were considered as significant. Factor mean values between 4-5 were obtained for the c-Met/HGFR targeting peptide cMBP2 for both controls at low and moderate shear flow. However, comparing B6 beads to beads equipped with a scrambled B6 peptide (B6scr1 or B6scr2), both bead types competed for binding to HuH7 cells and adhered with a ratio of about 1. Beads with either of the peptides B6, B6scr1 and B6scr2 have a highly positive surface charge (zeta potential = 24-30 mV) in contrast to the much lower surface charge of beads with B6mod peptide (zeta potential = -8 mV). Comparing the adhesion of B6 beads to the B6mod beads, mean factors between 4-6 were obtained. Considering the results of both types of control beads leads to the assumption that electrostatic interactions predominated during binding of B6 beads to HuH7 cells. Our findings revealed that beads with the peptide cMBP2 bind to target cells only when the amino acid sequence is in the correct order whereas beads with the peptide B6 bind also with similar affinity containing a different order of amino acids.

As all three peptides, B6, B6scr1 and B6scr2 showed similar effects on cellular binding of model beads, we assume that they have similar affinity to the target cells. Either all of them bind non-specific or all of them target the TfR in a similar manner. Xia *et al.* [309] found certain peptide motifs by phage display binding to the TfR. These short peptide motifs are "AKxxK/Rx", "KxKxPK/R" and "KxK". The peptide B6 which is composed of only 9 amino acids, but also the scrambled versions contain some of the motifs: the partial motif "KxPK" is included in the peptide B6scr1 and the motif "KxK" in the peptide B6scr2, the peptide B6 contains additionally all motifs. Thus, each of the scrambled peptides might represent another targeting ligand.

Increased shear flow did not significantly influence the factor distributions on single cells, but the total number of beads bound per cell. The total amount of attached B6 beads decreased whereas the number of cMBP2 beads increased. This can be explained by two facts occurring at enhanced shear flow: the number of beads passing the cell monolayer is increased as the suspension is perfused back and forth several times instead of passing once at low shear flow. Thus, more beads with high affinity bind. On the other hand, the number of bound beads with lower affinity decreases due to the enhanced shear force. Thus, less non-specifically binding beads are flushed away. Concluding, our findings suggest that beads with the targeting ligand cMBP2 have a higher affinity to the HuH7 cell surface whereas at least some of the B6 beads bind with lower affinity or non-specific.

The binding of model beads was investigated also on a non-targeted cell line, i.e. human microvascular endothelial cells (HMEC-1). The results revealed that beads with and without ligand bound in reduced amounts. The number of cMBP2 beads was around 3 per HMEC-1 cell whereas the number of B6 beads was around 80 per cell. Almost no hydroxylated control beads bound to the cells. Concerning the c-Met targeted beads, this was an interesting finding as the amount of c-Met on the cell surface detected by flow cytometry was in the same range for HuH7 and HMEC-1 cells.

Thus, similar amounts of bound cMBP2 beads were expected. We checked the receptor levels under both, static and flow conditions, but did not detect significant differences (see Appendix Fig.6). It should be noted that the statistics of the flow cytometry data were low as it was very difficult to extract the immunostained living cells from the flow channels. As the cMBP2 beads attached in significant differing numbers to two cell lines (HuH7 and HMEC-1), we assume that the cell lines have different surface characteristics under the experimental conditions. The possibility that new c-Met receptors are recruited to the HuH7 cell surface is very unlikely within the short time of the experiment (40 min). Furthermore, the findings of Kos *et al.* [166] show that the short peptide ligand does not induce signal transduction. More likely explanations are the following arguments: endothelial cells adapt to shear conditions [353] for instance by smoothening of the cell surface [326] and are deformed by the shear strain [354]. This would explain why less beads bound to the endothelial cells. Moreover, the cell surfaces of cancer cells exhibit a different composition of surface molecules such as integral proteins [355] like receptors and ion channels. In addition, the glycosylation pattern thereof can be very different in cancer cells compared to noncancerous cells [118, 356, 357]. This means that the binding sites of the beads are surrounded by different molecules which enable better or worse attachment. The number of bound beads varied also significantly on two different cell lines. Not only the TfR targeted B6 beads adhered in higher numbers to hepatocellular carcinoma (HuH7) than prostate cancer cells (DU145), but also the hydroxylated control beads. An elaborate method to verify unspecific binding on target cells would be using a cell line which does not express the target receptor. As the TfR is ubiquitously expressed [342], a comparison of cell lines with different receptor levels is considered as reasonable. Furthermore, TfR expression could be knocked down by gene silencing, but suitable controls would be very difficult for measuring single cells by fluorescence microscopy. All in all, the low amount of cMBP2 beads bound to endothelial cells is favorable whereas the high amount of TfR targeted B6 beads on the endothelial HMEC-1 cells is not favorable for the targeting approach. As assumed before, the B6 beads are presumably attached by unspecific interactions such as electrostatics. This means that the beads would also bind to non-target tissues *in vivo* which would be undesirable.

To support our hypothesis of the unspecific binding of B6 beads, some additional experiments were performed. As first approach, we investigated the uptake of the beads. The cellular internalization should be faster for receptor-meditated processes. We found similar uptake time ranges and efficiencies for both, B6 and B6scr beads. These findings suggest that both bead types were internalized by the same mechanisms. Incubation of the beads with free ligand revealed almost no co-localization of internalized B6 and B6scr beads with labeled Tf in a central plane of single cells after 1 h. This suggests that no or only few beads were internalized by receptor-mediated endocytosis. While high co-localization of free labeled Tf with TfR-GFP was observed, B6 beads were mainly not detected at the accumulation sites of the tagged TfR close to the nuclei. Thus, the labeled Tf attached clearly to the TfR whereas the B6 beads mainly did not. It has to be mentioned that also endogenous receptors were expressed in the cells during the experiment, but nevertheless a higher degree of co-localization was expected in case of a specific attachment and uptake mechanism via the TfR. Furthermore, experiments were performed where TfR targeted beads should compete for binding with free ligand. However, the binding of B6 and B6scr1/2 beads was only little affected by

a high amount of free Tf in the medium. There was no effect for B6mod and hydroxylated beads. The latter two types of control beads bound to a much lower extend so that a small effect could also disappear. There are two possible explanations of these findings. First, the B6 beads bound nonspecifically and the Tf on the TfR blocked binding sites on the cell surfaces (e.g. sterically) or second, only some of the B6 and B6scr beads bound "specifically" to the TfRs and they bind mainly due to other effects such as electrostatic interactions. This second argument is supported by the results of Xia *et al.*[309] which have shown that free Tf reduces B6 peptide binding. This means that the coupling on the model beads diminished the targeting potential of B6. Furthermore, there is the possibility that the small peptides do not bind at the same site as the Tf. Another aspect which should be considered to interpret the findings correctly is the fact that the number of ligands per bead also might play a role. Uptake experiments of Tf coated polystyrene particles by Tsuji *et al.*[350] revealed a dependency of the uptake efficiency on the number of ligands and the number of TfR expressed in the target cell line.

In conclusion, our binding studies under flow conditions show that the peptide cMBP2 is a potential targeting molecule for c-Met whereas we do not recommend the peptide B6 for TfR targeting due to its presumably unspecific binding characteristics.

7 Proof of principle: Development of flow experiments for screening of polyplex adhesion to different surfaces

Binding studies of model nanoparticles under flow conditions to assess the potential of peptide ligands were described in the previous chapter. Can we also quantify the binding capacity of actual therapeutic nanodevices? This is a challenging task because it is not always possible to synthesize delivery systems which are exactly reproducible. They may vary concerning their size, defined PEGylation, surface coating, amount of ligands and effective number of particles. For example, some delivery systems such as polyplexes are formed by condensation, and different numbers of polyplexes can be obtained for different approaches due to experimental deviations (e.g. pipetting and mixing of very small volumes). As a result, polyplexes containing higher or lower amounts of polymer and nucleic acids can affect the total number of formed particles. Thus, it is not reasonable to compare the adhesion of different types of polyplexes by performing individual experiments. Instead, in order to quantify the binding capacity of actual therapeutic nanodevices, the binding of polyplexes of the same type and preparation should be compared on different surfaces in parallel. This approach enables to study specific and non-specific interactions of the nanocarriers to various relevant biological surfaces.

After intravenous administration of therapeutic delivery systems, these nanoferries come into contact with blood, blood components and vessel walls. Then they enter the interstitial space through fenestrations of leaky tumor tissue and encounter components of the stroma like extracellular matrix or fibroblasts before they reach their actual target, the tumor cells. By performing animal experiments, the potential of therapeutics is assessed regarding its suitability for clinical studies. The accumulation of therapeutics at the diseased target site, but also in different organs is monitored to analyze specificity and toxicity. Here, we present an *in vitro* approach to test the binding of nanocarriers to different surfaces of relevance. More specifically, materials were used to which the delivery systems could potentially bind *in vivo* or which reveal information about surface properties, such as attraction or repulsion of nanocarriers by surface charge and hydrophobicity.

This chapter deals with the extension of our flow system from an one-channel system with internal control to a four-channels-in-parallel platform (Fig. 7.1). With this setup the adhesion of non-viral gene vectors on different surfaces was investigated as a proof of principle. These gene delivery systems, polyplexes, were formed by condensation of polymers with nucleic acids. Both, polymers and nucleic acids (plasmid DNA and labeled siRNA) were kindly provided by the group of Prof. Ernst Wagner (LMU Munich, especially by Dr. Christian Dohmen and Dr. Ulrich Lächelt).

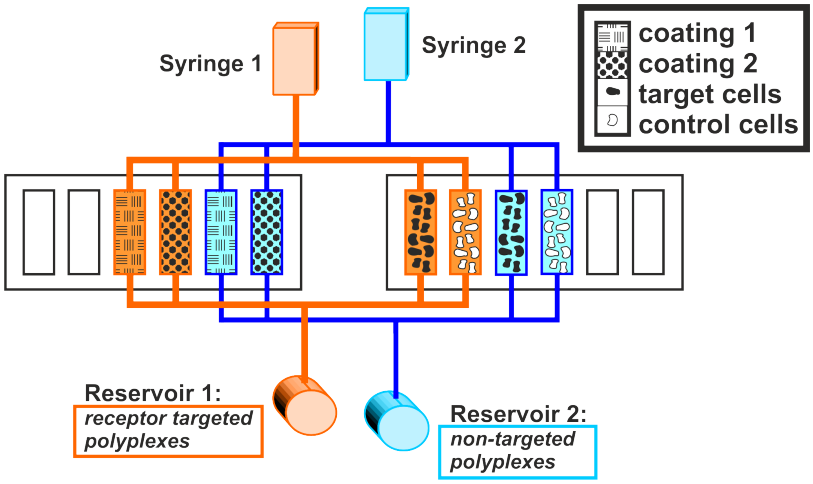

Figure 7.1: Scheme of two flow systems with four parallel channels. Two different polyplex suspensions in two separate reservoirs (bottom) can simultaneously be passed over four different surfaces in the flow channels (middle), for example two different surface coatings (left) and two different cell lines (right) via a syringe pump.

Flow experiments with siRNA polyplexes and LPEI polyplexes as well as channel characterization experiments were performed by the bachelor student Sebastian Siegl under my guidance. This chapter gives insights into the possibilities provided by the extension of the flow system. Furthermore, it shows how the adhesion of therapeutic nanoparticles can be studied in a quantitative manner, and how the flow experiments can be used as a selection tool for suitable drug delivery systems.

7.1 Development of a four-channel flow system

First studies on the interaction of nanocarriers with their biological environment are commonly performed in cell culture assays [292]. To gain more detailed insights, animal experiments are performed, mainly using mouse models. They exemplify the complex reality of multicellular organisms and biological heterogeneity and enable the analysis of biodistribution, accumulation sites and clearance of the delivery systems. However, in the past few years, the gap between simple cell culture and *in vivo* experiments is narrowing with the development of a variety of *in vitro* models, including 3D cell cultures, tissue engineering and microfluidics [358]. Despite the lower physiological relevance, such models permit control of experimental variables and quantitative evaluation. In this context, we developed a simple microfluidic system designed to investigate the specific and non-specific interaction of nano-therapeutics. Reduced gravitational sedimentation and homogeneous particle concentration were provided by the microfluidic approach and a hydrodynamic microenvironment was introduced. In addition, with this flow setup it is possible to simulate shear forces of vascular blood flow. On this basis, non-specific attachment to endothelial cells or targeting thereof can be investigated.

In the following, the design of our expanded flow setup and the implementation of different surface

coatings are described. In Fig. 7.1, the scheme of a parallelized flow setup is illustrated. From one reservoir filled with a homogeneous particle suspension, particles are floated over four surfaces in parallel channels on two different slides by the force of a syringe pump. In the channels of one slide, cells are seeded (for example target and control cells). In the channels on the other slide, the hydrophobic surface is coated, e.g. with blood components, extracellular matrix or interstitial space components. Two or more four-channel systems can be installed for parallel experiments. Parallelization of the flow channels allows for the simultaneous observation of particle adhesion, hence comparing their affinity towards multiple surfaces.

Interesting cell coatings include target cells which overexpress specific receptors, but also endothelial cells which intravenously administered delivery systems certainly encounter. Furthermore, different surface coatings like artificial extracellular matrix or single components thereof, as well as serum were deposited in the channels. While the cell monolayers were seeded according to standard protocols, the individual surface coatings were established for the flow experiments regarding their appearance, layer thickness and autofluorescence characteristics.

An artificial gel, containing human extracellular matrix (ECM) components including collagens, laminin, fibronectin, tenascin, elastin and a number of proteoglycans and glycosaminoglycans, was diluted in cell culture medium on ice and further in cold buffer to prepare mixtures of different densities. The gel was incubated at room temperature which induced polymerization. The network formation was observed by transmission light widefield microscopy and the images are displayed in Fig. 7.2 A. A dense mesh was obtained for high concentrations of ECM gel mixture, while small holes could be observed at higher dilutions. To ensure that particles were not trapped in the network structure during flow experiments, model nanoparticles were passed over different dilutions of ECM gel under low shear conditions (see Fig. 7.2 B). Therefore, Cy5-labeled PEGylated polystyrene beads with a terminal hydroxyl group were floated over 1:20, 1:50 and 1:100 dilutions of ECM gel. The particles' fluorescence was monitored by widefield microscopy with a short exposure time (50 ms) and a movie was recorded for 16 s. Time projections are depicted in pseudo-color displaying the intensity range from 0-6000 pixel values. Particles interacting with the ECM gel moved slower as they were retained and appeared on more frames of the movie. Thus, in the time projections, they had higher intensity values (red) whereas fast moving particles were dimmer (blue) and appeared as straight line. At higher concentration of ECM gel (1:20 dilution), the particles were observed as bright spots caused by interaction with the matrix components. At higher concentration of the gel (1:100), the particles appeared as long lines resulting from lower interaction with the surface coating. ECM gel with diluted 1:50 was chosen for further experiments because it provided a low retention of the particles.

To clearly distinguish the particles from the coating, the autofluorescence was analyzed. ECM gel, poly-L-lysine and collagen did not show significant autofluorescence when excited with a 633 nm laser at the respective laser power used for the experiments. On the contrary, pseudo-color images of the autofluorescence of fetal bovine serum (FBS) in flow channels are illustrated in Fig. 7.2 C. The fluorescence varied with concentration and excitation. Higher autofluorescence correlated with

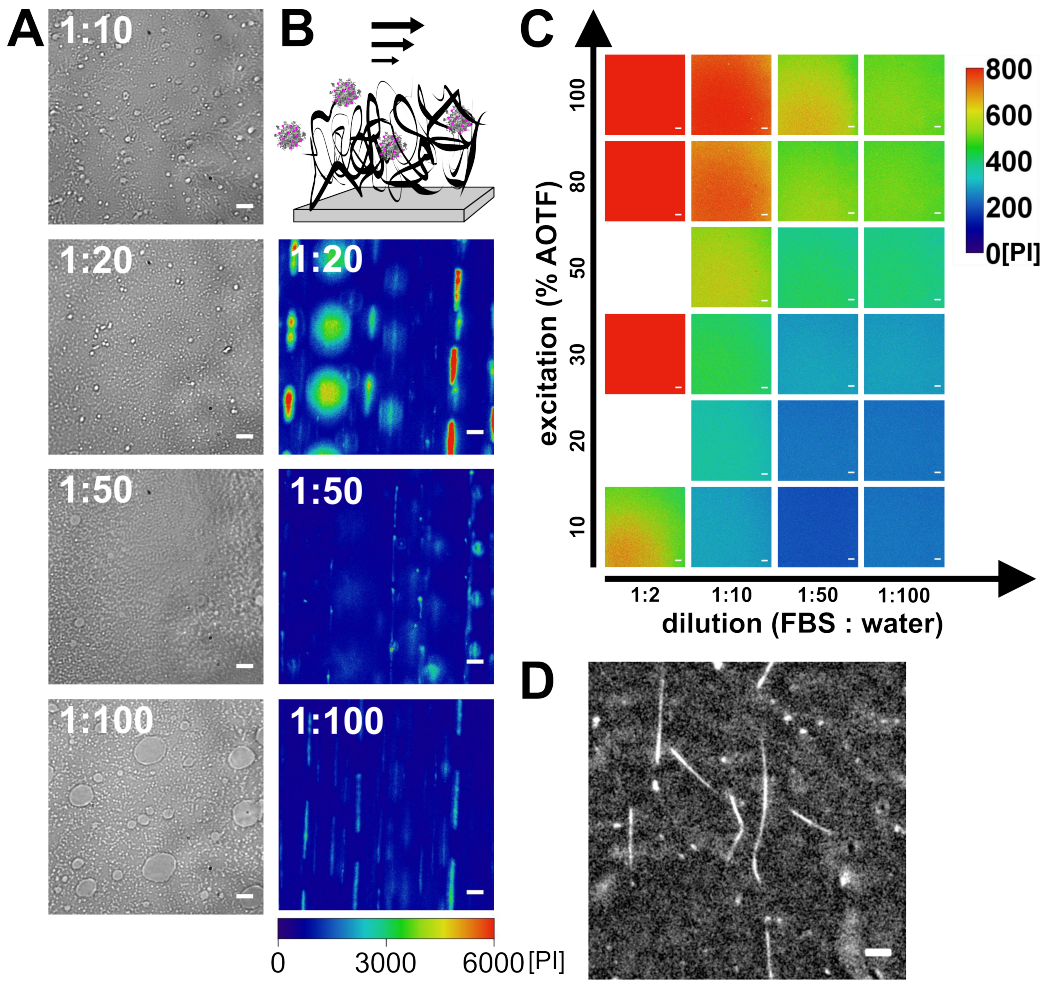

Figure 7.2: Characterization of surface coatings for flow channels. (A) Transmission light images of ECM gel coated on hydrophobic flow channels at different dilutions (1:10-1:100). At higher concentration, the matrix shows a higher density surface coverage. (B) Non-adhesive model beads (Cy5-labeled A200-PEG5-OH beads) were floated over ECM layers (diluted 1:20, 1:50 and 1:100) under shear conditions (17.6 s^{-1}) to investigate the flow profile. Movies of beads passing the surface were recorded (exposure time: 50 ms) for 16 s. Time-projections are depicted as pseudo-color images with pixel intensities between 0-6000 (blue-red). (C) Autofluorescent background of flow channels coated with FBS was recorded depending on FBS concentration and laser power. Pseudo-color images of single field of views (63.7x63.7 μm^2) are depicted for different FBS dilutions (1:2-1:100) and excitation power (10-100 % AOTF). The autofluorescence was in a reasonable range only at low concentration and low excitation power. (D) A hydrophobic flow channel was coated with collagen A which was stained with ATTO 488. A fluorescence image after excitation with 488 nm is displayed. Scale bars = 5 µm.

lower dilution of the serum and higher excitation power. For flow experiments, FBS concentrations were chosen with low autofluorescence, such that polyplexes could still be discriminated properly from the background. Furthermore, the FBS-coated surface was colored with Bradford reagent after flow application to confirm that it was not washed away during the experiment. Successful collagen coating was verified by incubation of the coated channel with ATTO 488 dye overnight. After several washing steps, the stained collagen fibers were observed with widefield microscopy and a representative image is displayed in Fig. 7.2 D. The image shows loose collagen fibers.

The viability of cells within the flow channels was monitored by transmission light widefield microscopy. All together, we expanded our flow setup to a four-channel-in-parallel system designed to compare the different affinities of gene vectors on cell lines and surface coatings.

7.2 Selection of suitable polyplexes

For adhesion experiments, non-viral gene delivery systems were used which are self-assembled nanostructures consisting of polymers and nucleic acids. Three different types were considered for the analysis. They varied in the polymer type and nucleic acid composition: polyplexes with (linear) polyethylene imine ((L)PEI), which is a standard transfection agent [64, 359], and polyplexes with succinoyl tetraethylene pentamine building blocks (STP), which have been developed for nucleic acid complexation in the past few years [360–363] contained either plasmid DNA or siRNA, respectively. All polyplexes were shielded with polyethylene glycol (PEG) for improvement of the biocompatibility and different targeting ligands were coupled to the individual polymers. The polyplexes with siRNA have been designed and successfully tested for gene silencing on folate receptor (FR) expressing cells [324]. Using LPEI as carrier polymer for pDNA, polyplexes have been effectively applied for gene transfer on epidermal growth factor receptor (EGFR) expressing target cells when equipped with the short synthetic peptide GE11 [364]. Sequence-defined STP-polymers have been developed for nucleic acid delivery [361] and demonstrated enhanced transfection efficiency equipped with either the peptide B6 or c(RGDfK) in a ligand-dependent manner in combination with endosomolytic agents [365]. All together, the selected polyplexes have been successfully applied for gene delivery and hence chosen for studies of their specific and non-specific binding behavior to relevant surfaces.

For quantification purposes some requirements have to be met, not only with respect to the detection system, but also concerning the particle properties. In order to quantify the adhesion of labeled polyplexes on different surfaces, it is necessary that they can be detected on each of the surfaces with similar quality. This means in particular that they should be bright enough to be visualized even on the surface with the highest background fluorescence.

The fluorescence characteristics of the siRNA polyplexes were investigated by widefield microscopy. Freshly prepared FA-PEG-STP polyplexes were diluted in water and spin coated on cover glass. In Fig. 7.3 A, the fluorescence of Cy5-labeled siRNA FA-PEG-STP polyplexes is depicted at the beginning of the laser excitation (t = 0 s) and after 66 s. Three fluorescent spots are

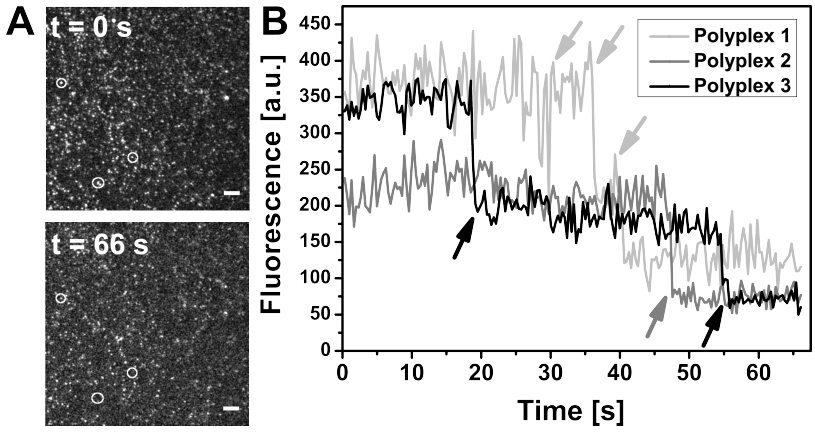

Figure 7.3: Blinking and bleaching of small siRNA polyplexes. Cy5-labled FA-PEG$_{24}$-STP siRNA polyplexes were diluted 1:40 in water and spin coated on cover glass. A movie was recorded with widefield microscopy exciting with a 633 nm laser (1.5 mW) for 66 s. (A) The fluorescence images of the first (t = 0 s) frame and after 66 s are shown. Scale bar = 5 µm. (B) The fluorescence intensity profiles of three polyplexes selected in A are displayed. The first polyplex shows one blinking and two bleaching steps (light grey arrows), the second polyplex shows one bleaching step (dark gray arrow) and the third polyplex shows two bleaching steps (black arrows).

encircled corresponding to three formed polyplexes. The fluorescence intensities of these polyplexes over the excitation time range are displayed in Fig. 7.3 B. Blinking and bleaching events are indicated by arrows. One polyplex (light gray) showed blinking after 30 s, a steep bleaching step after 35 s and a smaller bleaching step after almost 40 s. Being able to observe single bleaching steps points to the fact that only very few fluorophores are attached on the siRNA of the polyplex. The fluorescence of a second polyplex (dark gray) bleached completely in one step. This step was in the same range of magnitude as the small bleaching step of the first polyplex. This finding assumes that only one dye was bound to the polyplex. The third encircled polyplex (black) showed two small distinct bleaching steps. Again, these steps were in the same range as the small bleaching steps. Therefore, the latter polyplexes were labeled with approximately 2-3 dyes. Summarizing these results, and taking into account that each siRNA molecule was labeled with only one fluorophore, the resulting conclusion is that only few dyes were attached to single polyplexes.

When excited with UV/Vis light, cells auto-fluoresce in the blue and green range of visible light. The fluorescence arises from endogenous fluorophores such as aromatic amino acids in proteins, flavins, NAD(P)H and collagen [366]. Thus, the detectability of the siRNA polyplexes on cells and surface coatings was tested. Freshly prepared siRNA polyplexes (FA-PEG-STP and Ala-PEG-STP) were passed over KB cells, HMEC-1 cells, extracellular matrix (ECM) gel and fetal bovine serum (FBS) coating in parallel flow channels for one hour. Fluorescence images of the Cy5-labeled polyplexes on the cells and surface coatings are depicted in Fig. 7.4. The folate receptor (FR) targeted polyplexes were mainly found on KB cells and only a few attached to the ECM gel. Only a very low amount of non-targeted polyplexes adhered to KB cells and almost none of them on the endothelial cells and the surface coatings. Single polyplexes could not be spotted. They appeared mainly aggregated or clustered. This implies that detection with particle counting is not possible.

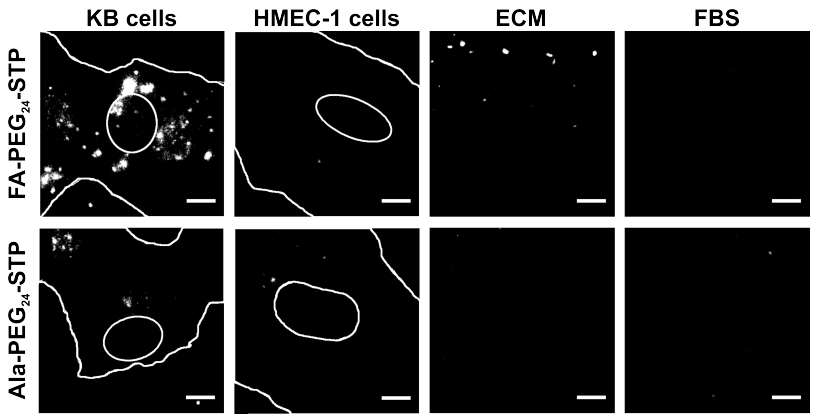

Figure 7.4: Small siRNA polyplexes on different surfaces. Cy5-labeled FA-PEG_{24}-STP (upper row) and Ala-PEG_{24}-STP (lower row) siRNA polyplexes were floated simultaneously over KB cells, HMEC-1 cells, an ECM layer and a FBS layer in parallel flow channels for 1 h under low shear conditions (4.4 s^{-1}). After fixation of the cells, the fluorescence was measured with widefield microscopy by excitation at 633 nm. Representative fluorescence images of single field of views (63.7x63.7 μm^2) are depcited. Scale bars = 10 μm.

A fluorescence intensity based approach should be used which in turn would correspond to a bulk measurement because determination of the mean fluorescence intensity of single polyplexes would be a very vague and presumably incorrect estimation. Hence, these polyplexes were not suitable for detection with widefield microscopy. In addition, measurements with confocal microscopy could not exclude that some of these small polyplexes would not be detected due to the autofluorescence of the cells and surface coatings.

In a next step, we investigated polyplexes with a higher number of labeling dyes to ensure proper detectability. Larger polyplexes are formed by condensation of a polymer with plasmid DNA (pDNA). Two kinds of polymers were used: linear polyethylene imine (LPEI) and succinoyl tetraethylene pentamine (STP). Single plasmids were labeled with around 50 or more fluorophores. Much brighter polyplexes were obtained compared to siRNA polyplexes, even by mixing with unlabeled copies of pDNA. In the upper row of Fig. 7.5, the fluorescence of pDNA polyplexes spin coated on cover glass is illustrated. The LPEI polyplexes appeared as fluorescent spots. The cRGD-PEG-LPEI polyplexes resulted in bigger polyplexes arising from condensation of a higher number of plasmids (and polymer) than GE11-PEG-LPEI and Cys-PEG-LPEI polyplexes. The size distribution of STP polyplexes (cRGD/GE11/Ala-PEG-STP) was broad as illustrated in the lower row of Fig. 7.5. Thus, both types of pDNA polyplexes were bright enough and did not bleach significantly during laser illumination. Single fluorescence maxima could be detected.

The uptake capability of the selected polyplexes into HuH7 cells was monitored to test their functionality. For both types of polyplexes, two ligands were chosen. The cRGD peptide is selectively recognized by $\alpha_V\beta_3$ and $\alpha_5\beta_1$ integrins [367] and GE11 is bound by the epidermal growth factor receptor (EGFR) [368]. Successful targeting involves faster uptake of polyplexes with ligand compared to polyplexes without ligand by receptor-mediated endocytosis. HuH7 cells express both receptors, EGFR in high [369] and $\alpha_V\beta_3$ integrins in low [370] amounts. Freshly prepared polyplexes

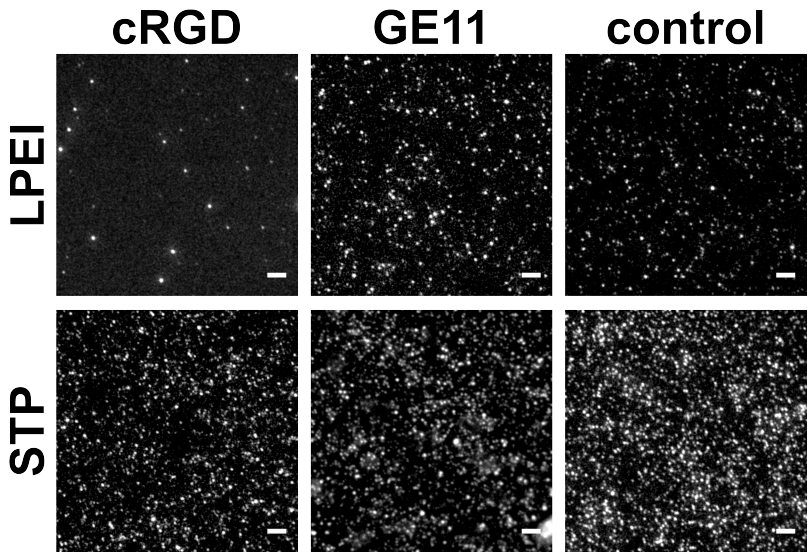

Figure 7.5: Fluorescence of pDNA polyplexes. Cy5-labeled pDNA polyplexes were diluted 1:50 in HBG buffer and coated on coverglass. The fluorescence was measured with widefield microscopy by excitation with a 633 nm laser. The images of the following poyplexes are depcited: cRGD-PEG2-LPEI, GE11-PEG2-LPEI, Cys-PEG2-LPEI, cRGD-PEG2-STP, GE11-PEG2-STP and Ala-PEG2-STP. Scale bars = 5 µm.

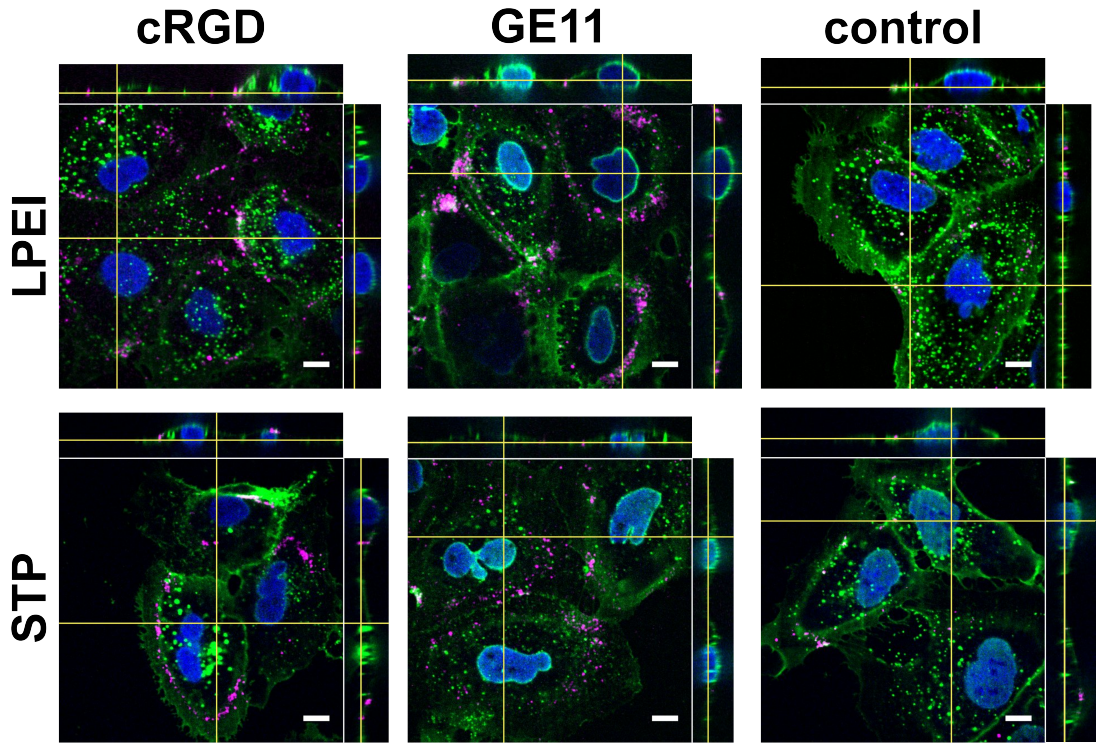

Figure 7.6: Association of pDNA polyplexes with HuH7 cells. Cy5-labeled pDNA polyplexes (cRGD/GE11/Cys-PEG2-LPEI or cRGD/GE11/Ala-PEG2-STP) were incubated with HuH7 cells for 1.5 h under static conditions. The cell membranes were stained with WGA-Alexa488 (green) and the nuclei with DAPI (blue). The fluorescence was recorded using spinning disk microscopy by excitation at 405 nm (DAPI), 488 nm (Alexa488) and 639 nm (Cy5). Images of polyplexes (magenta) in one central plane of several cells are shown. Orthogonal views are displayed on top (xz) and on the right (yz). Scale bars = 10 µm.

were incubated with HuH7 cells for 1.5 h under static conditions. The cell membranes were stained with WGA-488 (green), the nuclei with DAPI (blue) and the polyplexes on the cells were imaged by spinning disk microscopy. In Fig. 7.6, the fluorescence of Cy5-labeled polyplexes (magenta) is depicted in a representative the HuH7 cells. Orthogonal views of the xz-plane (on top) and of the yz-plane (left) are additionally shown. As can be observed, the cRGD- and GE11 polyplexes of both polymer types clearly accumulated on and within the cells. Only few control polyplexes bound to the cells. In flow experiments lasting 1 h, internalization of a low number of polyplexes is expected according to the previous findings. As a consequence, the merge of their fluorescence in endosomes is considered as negligible and thus the detection of fluorescence maxima is reasonable. Certainly, we were aware of the fact that some polyplexes aggregated, but polyplexes of the same polymer type showed similar aggregation tendencies.

7.3 Differential binding of polyplexes to multiple surfaces

We intended to provide an *in vitro* experiment suitable to pre-select delivery devices by testing their adhesion to biologically relevant surfaces under shear conditions. With our parallelized channel approach, not only the binding efficiency is examined, but also the unspecific adhesion to essential surfaces. Typically, polyplexes in cell medium were passed over four different parallelized surfaces for 1 h under very low shear conditions. After fixation, the fluorescence of adhered polyplexes, labeled with Cy5, was measured in each flow channel and the mean numbers were plotted in a diagram. To compare the binding capacities of different polyplexes, relative values calculated by normalization to the maximum number of bound polyplexes in every experiment were used. Binding profiles were obtained, for example: 100 % on cell line 1, x % on cell line 2, y % on surface coating 1, z % on surface coating 2. By evaluation of the binding profiles, one can to estimate potential binding sites of the delivery systems and the ratio of affinities to them.

In the following it is described as a proof of principle how polyplexes of different compositions bind to various surfaces in the channels of the parallelized flow setup. The experiments are not restricted to the parameters we used and can be performed with modified settings to answer further research questions. Herein, we investigated the binding profiles of LPEI and STP pDNA polyplexes to selected cell lines and surface coatings. We picked three examples: in a first approach, the binding profiles of receptor-targeted polyplexes were compared to those of polyplexes without ligand (section 7.3.1); in a second experiment, different surface combinations were tested (section 7.3.2) and as third exemplification, the effect of different polymer types forming the polyplexes and the influence of serum content are shown (section 7.3.3).

7.3.1 Receptor targeting

Binding profiles of EGFR-targeted GE11 and control polyplexes were recorded to approximate the effect of the targeting ligand on binding. As described before, a four-channel-in-parallel flow experiment was performed. EGFR-targeted GE11-PEG2-LPEI polyplexes and Cys-PEG2-LEPI poly-

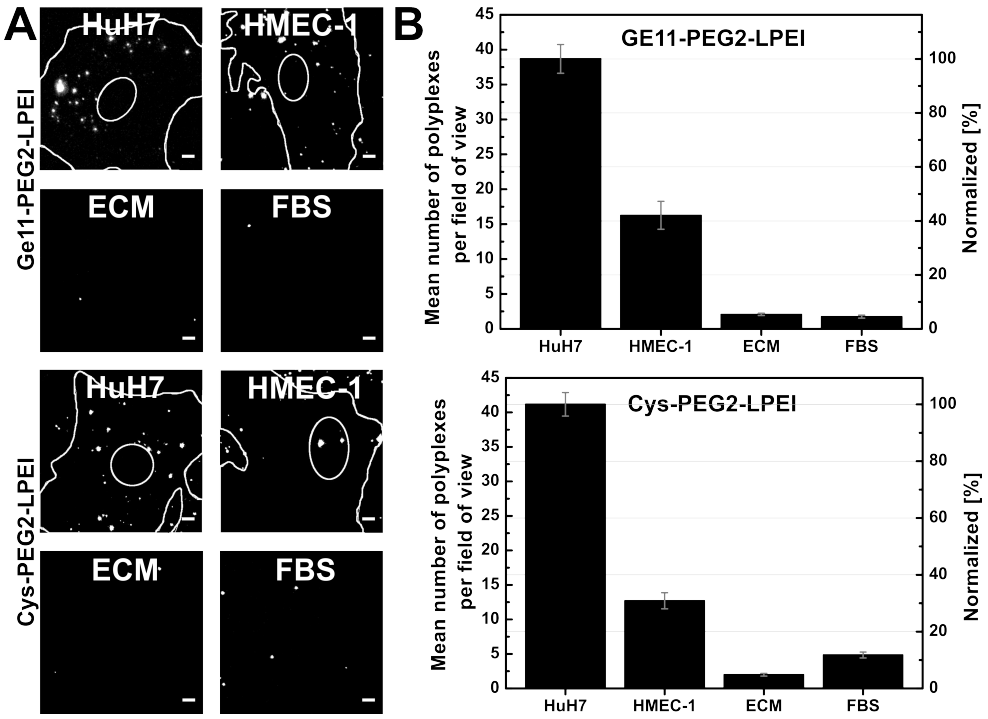

Figure 7.7: Binding profiles of EGFR targeted and control polyplexes on four different surfaces. Adhesion of Cy5-labeled polyplexes with ligand (GE11-PEG2-LPEI) and without (Cys-PEG2-LPEI) were perfused over four different surfaces (HuH7 target cells, HMEC-1 cells, ECM and FBS) in parallel for 1 h at very low shear conditions (4.4 s^{-1}). The fluorescence was recorded by widefield microscopy exciting with a 633 nm laser, adjusting the focus over single cells or on the surface, respectively. (A) Representative fluorescence images of the polyplexes per field of view. Scale bars = 5 µm. (B) The mean number of polyplexes per field of view are shown (right scale) and normalized to the maximum number of bound polyplexes in one channel (left scale). n = 40 (field of views/channel).

plexes were passed over hepatocellular carcinoma cells (HuH7), microvascular endothelial cells (HMEC-1), extracellular matrix (ECM) gel and fetal bovine serum (FBS) coating in four parallel flow channels. In Fig. 7.7 A, representative images of the two types of polyplexes on the different surfaces are shown. The mean numbers of adhered polyplexes are depicted in the diagram in Fig. 7.7 B (left scale) and are normalized to the maximum amount of bound polyplexes (right scale). In particular, the maximum number of adhered GE11-PEG2-LPEI polyplexes was 38 on HuH7 cell, thus this value was set to 100 %. Accordingly, values for polyplexes bound to the other surfaces were determined with respect to this maximum value. For the GE11-PEG2-LPEI polyplexes following binding profile was obtained: 100 % on HuH7 cells, 40 % on HMEC-1, 5 % on ECM, 5 % on FBS. This profile can be interpreted by a high attraction of the polyplexes to EGFR overexpressing HuH7 cells, lower attraction to HMEC-1 cell which also express EGFR [371] and only low unspecific attraction to ECM and FBS. For the control polyplexes (Cys-PEG2-LPEI) a similar binding profile was determined with slightly lower binding affinities to HMEC-1 cells, but higher numbers on matrix gel. These findings indicate that the targeting ligand GE11 did not have an effect on binding to the target cells as higher numbers were expected on the HuH7 cells for the receptor-targeted polyplexes. Hence, the carrier polymer LPEI with its positive charges contributed mainly to the affinity of the polyplexes to the negatively charged cell surfaces.

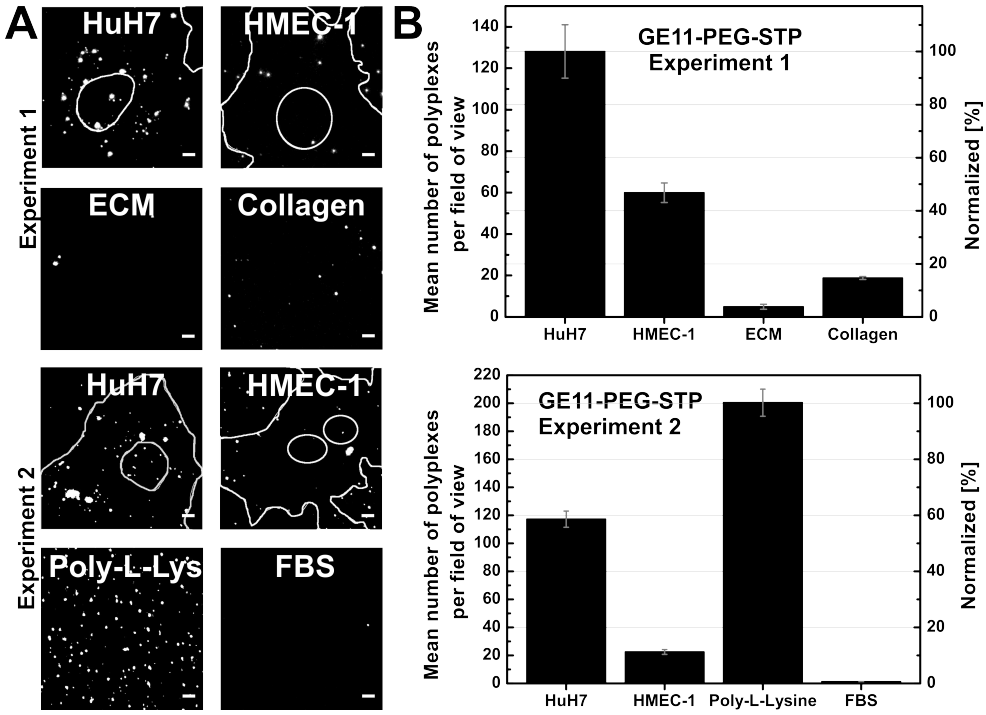

Figure 7.8: Binding profiles of EGFR-targeted polyplexes with different combination of surfaces. Cy5-labeled GE11-PEG-STP polyplexes were perfused over four different surfaces in parallel for 1 h at very low shear conditions (4.4 s^{-1}). The fluorescence of the polyplexes was recorded by widefield microscopy excited by a 633 nm laser. The number of polyplexes was counted per field of view (63.7x63.7 μm^2) based on the intensity maxima. (A) Representative fluorescence images per field of view are shown on HuH7 cells, HMEC-1 cells, ECM and collagen (Experiment 1) or on HuH7 cells, HMEC-1 cells, Poly-L-lysine and FBS (Experiment 2). Scale bars = 5 μm. (B) The mean numbers of polyplexes per field of view are illustrated (right scale) and normalized to the maximum number of bound polyplexes in one channel (left scale). n = 32 (field of views/channel).

7.3.2 Binding profile on different surfaces

In a second approach, binding profiles with different combinations of surface coatings were investigated. The same cell lines were used in both experiments, while the surface coatings were changed. As described before, EGFR-targeted GE11-PEG-STP polyplexes were passed through four different flow channels with HuH7 cells, HMEC-1 cells and different surface coatings for 1 h under very low shear conditions. In Fig. 7.8 A, representative images of the Cy5-labeled polyplexes on the cells and coatings are displayed for experiment 1 and 2. The mean values and normalized values with respect to the maximum number of bound polyplexes are shown in Fig. 7.8 B. In experiment 1, the following binding profile was obtained: 100 % on HuH7 cells, 50 % on HMEC-1, 5 % on ECM and 15 % on collagen. This distribution resembles the binding profile described in the previous section (see 7.3.1) for GE11-PEG2-LPEI polyplexes with the difference that collagen was coated in one channel instead of FBS. In experiment 2, similar numbers of GE11-PEG-STP polyplexes were counted on HuH7 cells (ca. 120-130) as in experiment 1, whereas the number of polyplexes on HMEC-1 cells was lower (instead of 50 %, ca. 20 % compared to HuH7). This observation could be explained by biological or experimental variance, but could also result from different polyplex

aggregation in the two separate experiments. Moreover, it can be observed in the images that polyplexes also attach non-specifically to the channel bottom, especially in the case of HMEC-1 cells. Hence, another reason could be that more polyplexes bound to the channel bottom in the second experiment. To exclude such causes, a cell layer confluence of 100 % will be used in further experiments.

The binding profile of experiment 2 differed strongly. The maximum number of polyplexes was counted on poly-L-lysine coating. This polyamino acid is positively charged at physiological pH and used to promote attachment of cells or proteins to surfaces by electrostatic interactions. The GE11-PEG-STP polyplexes contain polymer with neutral building blocks (STP) and posses a low, slightly positive zeta potential [365]. Thus, electrostatic attraction would mainly involve the negatively charged phosphate backbone of the pDNA. This explanation would include a disassembly of the polyplexes at least to some extent. Interestingly, the fluorescent spots detected on poly-L-lysine were more uniform and smaller than those observed on cells. Hence, the polyplexes were more aggregated on the cells. This would support the afore mentioned hypothesis that polyplexes aggregate in cell medium and bound to cells in an aggregated state. Another explanation would be that the polyplexes mainly aggregate on the cell either after or during cellular binding, or in endosomes.

7.3.3 Effect of polymer type and serum content on polyplex binding

In a third approach, the binding profiles of two types of polyplexes composed of two different polymer types were compared. In contrast to the previous experiments, FBS was not coated on the bottom of the channel, but its content in the fluid medium was increased to study the influence of the formation of a protein corona around the nanoparticles. This is relevant as blood contains much higher levels of serum than the 10 % usually used in cell culture experiments. Salvati *et al.* showed that transferrin-coated nanoparticles lost their targeting capability when serum biomolecules adsorbed on their surface [372]. The buffer was supplemented with 55 % FBS. In our demonstrations we adapted this parameter and supplemented the cell medium with 55 % FBS to show the interaction in presence of high serum content.

The binding experiments under flow conditions were conducted with integrin-targeted cRGD-PEG2-LPEI and cRGD-PEG2-STP polyplexes, first in cell medium with low serum (10 % FBS) and then with high serum (55 % FBS) content. In Fig. 7.9 A, representative images of polyplexes are illustrated. The mean values of bound polyplexes are displayed in Fig. 7.9 B on the left scale and normalized to the number of maximum bound polyplexes on the right scale. The integrin-targeted LPEI polyplexes showed maximal adhesion on collagen and bound in similarly high amounts to HuH7 and HMEC-1 cells, and they basically did not show attachment on ECM gel. As expected, the number of polyplexes on HMEC-1 cells was increased as this cell line expresses a manifold of integrins [373]. The high affinity of the LPEI polyplexes presumably originates from the nature of the polymer carrier, as STP polyplexes showed almost no unspecific binding to the scleroprotein. Comparing the binding profiles of the LPEI polyplexes of low and high serum content, it is obvious that the binding profile did not change significantly. Fewer polyplexes were counted on the cells.

However, the number of polyplexes in solution was expected to be similar. Thus, a meaningful conclusion was not possible. In the case of the STP polyplexes, the same effect of overall reduced polyplex binding was observed with increased serum content. Here, the binding profile changed, and the percentage of polyplexes bound to endothelial cells doubled, whereas it almost vanished on ECM gel. For further conclusions, additional experiments and more statistics are required to reliably elucidate the binding behavior of these polyplexes.

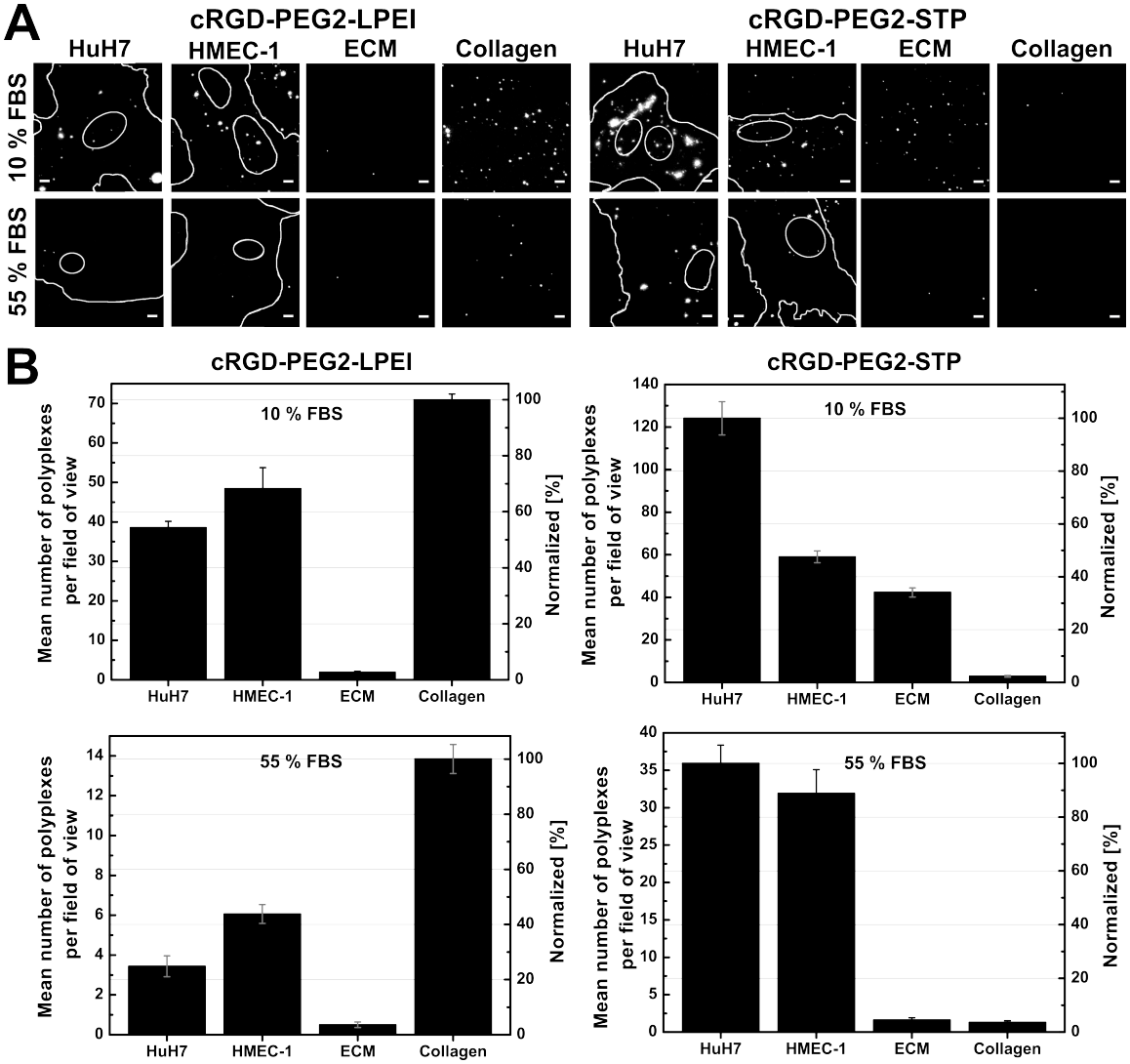

Figure 7.9: Influence of the polymer type and the serum content on the binding profiles of integrin targeted polyplexes. Cy5-labeled cRGD-PEG2-LPEI and cRGD-PEG-STP polyplexes were passed over four different surfaces (HuH7 cells, HMEC-1 cells, ECM and collagen) in parallel for 1 h at low shear conditions (4.4 s^{-1}). The fluorescence of the polyplexes was recorded by widefield microscopy excited by a 633 nm laser. The number of polyplexes was counted per field of view (63.7x63.7 μm^2) based on the intensity maxima. (A) Representative fluorescence images of the polyplexes are shown. The cell medium during the experiment was supplemented either with 10 % FBS (upper row) or with 55 % FBS (lower row). Scale bars = 5 μm. (B) The mean numbers of LPEI (left) and STP (right) polyplexes on different surfaces per field of view are shown (right scale) and normalized to the maximum number of bound polyplexes in one channel (left scale). The cell medium during the experiment was supplemented with 10 % FBS (upper diagrams) and with 55 % FBS (lower diagrams). n = 32 (field of views/channel).

7.4 summary and conclusion

In summary, we expanded our flow system (described in chapter 5) to a four-channel-in-parallel setup to perform binding studies of actual therapeutic nanoparticles. In particular, a solution with nanoparticles was passed through four parallel flow channels containing different cell monolayers and surface coatings. In principle, these surfaces were either targets of the polyplexes or surfaces which they would encounter *in vivo*. They included epithelial hepatocellular carcinoma cells, microvascular endothelial cells, extracellular matrix gel, fetal bovine serum and collagen. As therapeutic nanoparticles polyplexes were chosen, i.e. non-viral gene delivery particles formed by condensation of nucleic acids with cationic polymers. More specifically, pDNA polyplexes were selected as they provided the requirements for quantitative analysis, such as good detectability and stability in cell medium. The described binding experiments of these polyplexes on different surfaces were performed as a proof of concept. The assessed binding profiles revealed some interesting conclusions about polyplex binding. Similar amounts of LPEI polyplexes with and without the peptide ligand GE11 (targeted to the EGFR) were observed on all surfaces. This implies that the binding was primary mediated by the carrier polymer. High amounts of LPEI polyplexes with the peptide ligand cRGD were found on the scleroprotein collagen indicating high affinity to it. Another observation was that the binding of polyplexes varied most on HMEC-1 cells suggesting high sensitivity of this cell line to already little ambient or experimental changes. As discussed in literature [374], serum molecules in cell media influence the binding of nanoparticles. The binding of polyplexes of both types of polymers, LPEI and STP, was significantly reduced at increased serum content (from 10 to 55 %) in the cell medium. The STP polyplexes showed barely unspecific binding to extracellular matrix gel and collagen at high serum content. This is highly favorable for *in vivo* applications.

In addition to these findings, it is important to point out that the flow setup with parallel channels is not restricted to the investigations shown herein. Many variations can be implemented including the change of cell lines and surface coatings, the tuning of flow generating very low until high shear forces. Furthermore, different particle types can be analyzed and additional soluble components introduced. The variables ultimately depend on the research question.

In the following, some examples of applications will be elucidated. The flow provides many opportunities to either determine the magnitude of particle affinity to respective surfaces or mimic the shear forces of blood flow. The latter can hence provide useful information of specific and unspecific binding to endothelial cells. Thus, aspects of the toxicity of certain nanocarriers can be obtained or the (tumor) vasculature can be targeted [375]. Active targeting strategies to cancer endothelium can be pursued by coupling targeting ligands to therapeutic nanoparticles which address overexpressed receptors like various integrins [192] or vascular endothelial growth factor receptors (VEGFR) [376]. A further application of the flow system with parallelized channels could be the testing of binding to different components of the extracellular matrix, thus determining the main interactions with this gel. By blocking surface receptors with free ligand or antibodies, targeting studies could be performed. This is especially practicable for cheap ligands like folic acid

as high amounts of it are needed to saturate the cell medium in the whole flow system. To explore the effect of a ligand on the binding of the particles, the adhesion to cell lines with and without targeting receptor could be simultaneously observed. In this case, it would be important to test the receptor status on the cell lines by western blot or flow cytometry. The variation of perfusion time could disclose binding kinetics of the nanoparticles.

Additionally, the parallelization of flow channels allows for screening multiple surfaces. An internal standard could be incorporated in the flow experiments. For example, LPEI polyplexes without PEG shielding could be used as a particle type with maximum affinity and PEGylated model beads as particles with minimal binding affinity. Moreover, a surface coating could be used as an internal standard of the system to which the particles have high affinity. Based on our preliminary findings, collagen could serve as control surface for LPEI polyplexes and poly-L-lyisine for STP polyplexes. In conclusion, the flow setup with parallel channels offers many possibilities to answer a multitude of research questions.

8 Experimental materials and methods

8.1 Materials

DMEM/F-12, DMEM (low glucose, GlutaMAX and pyruvate), MCDB-131, RPMI 164 (with glutamine) and CO_2-independent medium, GlutaMAX^{TM}, HEPES buffer, human epidermal growth factor (hEGF), fetal bovine serum (FBS), phosphate buffered saline (PBS), transferrin (Tf) -Alexa Fluor®647 conjugate, WGA-Alexa Fluor®488 conjugate, DAPI and aliphatic amine latex beads (71.8 µEq NH_2/g, 2 % w/v, 0.2 µm) were purchased from Life Technologies AG (Carlsbad, CA, USA). Hydrocortisone, anhydrous dimethylsulfoxide (DMSO), ethylenediaminetetraacetic acid (EDTA), 2-mercaptoethanol, dithiothreitol (DTT), citric acid monohydrate, 4-(2-hydroxyethly)- 1-piperazine ethanesulfonic acid (HEPES), ultra filtrated water, poly-L-lysine, MaxGel ECM and human apo-Tf were obtained from Sigma-Aldrich Corp. (St. Louis, MO, USA). Sterile ibiTreat µ – Slides, 8-well and sterile ibiTreat µ – Slides $I^{0.4}$ Luer and $VI^{0.4}$ Luer were purchased from ibidi GmbH (Martinsried, Germany), *para*-formaldehyde (PFA) from Science Services GmbH (Munich, Germany), ATTO 488-NHS from ATTO-TEC GmbH (Siegen, Germany), Cy5-NHS from GE Healthcare (Freiburg, Germany), *ortho*-pyridyldisulfide-polyethylene glycol-N-hydroxysuccinimide (OPSS-PEG(5 kDa)-NHS) from Rapp Polymere GmbH (Tübingen, Germany), X-tremeGENE 9 DNA transfection reagent from F.Hoffmann-La Roche AG (Basel, Swiss), collagen A from Merck KGaA (Darmstadt, Germany) and iron(III) chloride from Grüssing GmbH (Filsum, Germany). Cy5 label IT was purchased from Mirus Bio LLC (Madison, WI, USA) and Secure-Seal Imaging spacers (ϕÂ 9 mmx0.12 mm) from Grace Bio-labs, Inc. (Bend, OR, USA). The plasmid pCMVLuc from plasmidfactory GmbH& Co. KG (Bielefeld, Germany) was kindly provided by the group of Prof. Ernst Wagner (LMU Munich). The plasmid pBa.TfR.GFP (Addgene 45060) was received from Gary Banker (Oregon Health & Science University). Peptide-cysteine derivatives were kindly provided by Dr. Ulrich Lächelt and Stephan Morys. B6-cysteine (B6-Cys, CGHKAKGPRK), cMBP2-cysteine (cMBP2-Cys, KSLSRHDHIHHHK(C)) were synthesized under standard Fmoc chemistry conditions using an ABI 431A peptide synthesizer (Applied Biosystems, Foster City, CA, USA). B6scr1-Cys (CAGKHGKRPK), B6mod-Cys (CGHGAGGPGG) and cMBP2scr-Cys (HHSIHRLHHKSDK(C)) were synthesized under standard Fmoc chemistry conditions using a Syro Wave peptide synthesizer (Biotage AB, Uppsala, Sweden). The site-specific coupling of cysteine at the ε-amine of the C-terminal lysine of cMBP2 and cMBP2scr was achieved with orthogonally protected Fmoc-Lys(ivDde)-OH. Peptide identity was verified by MALDI-TOF (Matrix-assisted laser desorption/ionization- time-of-flight) mass spectrometry, carried out using an Autoflex II mass spectrometer (Bruker Daltonics, Bremen, Germany) and a 2,5-dihydroxybenzoic acid (DHB) matrix. Folic acid-cysteine (FA-Cys) and PEGylated constructs (FA-PEG2-Cys and FA-PEG_{24}-Cys), transferrin-iminothiolane [Tf(it)] and transferrin-pyridyldithiol propionate [Tf(pdp)] were kindly provided by Dr. Ulrich Lächelt. The transferrin constructs were loaded with iron(III) (1.25 µL/mg

Tf; 1 Eq Fe^{3+}/mg Tf) by incubation with iron(III) buffer (1 mM $FeCl_3 6\dot{H}_2$ O; 200 mM citric acid monohydrate, pH 7.8, sterile-filtered) for 30 min at room temperature.

8.2 Particle synthesis, preparation and characterization

8.2.1 Polystyrene beads

Synthesis, DLS and zeta potential

Functionalized and labeled model beads, A110/200-(dye)-PEG5-(ligand/modification) were prepared according to the following procedure. Aliphatic amine latex beads (100 µL; 0.155 µmol NH_2, mean diameter: 0.11 µm; or 0.158 µmol NH_2, mean diameter: 0.2 µm) were centrifuged at 13 400 rpm (Microcentrifuge 5417R, Eppendorf AG, Hamburg, Germany) for 15 min and the supernatant was removed. The beads were resuspended in PBS (0.1 mL), shortly sonicated (Sonorex RK31, Bandelin electronic GmbH & Co. KG, Berlin, Germany), and ATTO 488-NHS (7.4 µL, 12.6 nmol) or Cy5-NHS (9.4 µL, 7.9 nmol) dissolved in anhydrous DMSO, was added. The suspension was shaken at 1000 rpm (Thermomixer comfort, Eppendorf) protected from light at room temperature for 2 h. Then, the reaction mixture was centrifuged for 20 min, the supernatant removed, the beads washed with PBS (3 x 0.5 mL) and resuspended in PBS (0.1 mL). To the labeled beads A110/200-(dye) (100 µL, 0.155 or 0.158 µmol NH_2) OPSS-PEG (2 or 5 kDa)-NHS (78 µL, 1.55 or 1.58 µmol), dissolved in anhydrous DMSO, and PBS (80 µL) were added. The reaction mixture was shaken (1000 rpm) at room temperature for 2 h. The suspension was washed as described above and the beads finally resuspended in PBS (200 µL) with EDTA (2.5 mM) to prevent oxidation. An assay with DTT was performed to estimate the yield of PEG-OPSS on the beads. The procedure which was used to estimate the coupling efficiency of OPSS-PEG(2 or 5 kDa)-NHS to the amine latex beads was previously described in literature [377, 378]. In brief, to a suspension of PEGylated A110/200-(dye)-PEG2/5-OPSS beads (10 µL) in PBS (9.2 µL) containing EDTA (2.5 mM), DTT (0.8 µL, 1 M) was added and the reaction mixture was shaken at 500 rpm for 1 h at room temperature. The disulfide bridge within the OPSS residue was reduced to yield 2-thiopyridone (2-TP), which was released into the supernatant after centrifuging at 13 400 rpm for 15 min. The absorption at 343 nm A_{343} of 2-TP was measured five times (Nanodrop ND-1000, PEQLAB Biotechnology GmbH, Erlangen, Germany) and the molar concentration of 2-TP was calculated by using its molar extinction coefficient ε_{343} = 8.08 x 10^3 $M^{-1}cm^{-1}$. The obtained concentration corresponds to the concentration of PEG-OPSS on the latex beads in the assay. For coupling with Tf(pdp), the beads were pretreated with DTT (at an excess of 100 Eq over PEG-OPSS, 10 mM) for 2 h at room temperature to provide a free thiol group. To a suspension of A110/200-(dye)-PEG2/5-OPSS (100 µL), peptide ligand (B6-Cys, cMBP2-Cys), modified peptide (B6scr1/2-Cys, B6mod-Cys, cMBP2scr-Cys), folate ligand (FA-Cys, FA-PEG2-Cys or FA-PEG_{24}-Cys), natural ligand [Tf(it) or Tf(pdp)] or 2-mercaptoethanol (HS-CH_2CH_2-OH) (each at an excess of 20 Eq over PEG-OPSS) and PBS were added to a total volume of 200 µL. The reaction mixture was shaken at 1000 rpm at 23 °C for 2 h. Then, the suspension was centrifuged for 20 min, the beads were washed with PBS (3x400 µL) and resuspended in PBS (50 µL). The average hydrodynamic diameter of the functionalized beads (1.5 µL) was measured in water (800 µL, 1 mM NaCl, pH 6.8 and 7.4) as a triplicate in 10 sub-runs of 10 s in a folded capillary cell (DTS1061) by

dynamic light scattering (DLS, Zetasizer Nano ZS, Malvern Instruments Ltd., Worcestershire, UK). The employed settings were an equilibrating time of 0 min, a temperature of 25 °C, a refractive index of 1.330, a dispersant dielectric constant of 78.5 and a viscosity of 0.8872 mPa · s. The Z-average and the polydispersity index (PdI) were determined by fitting of single exponentials to the correlation function. The same samples were used to determine the zeta potentials as triplicates in 10-30 sub-runs of 10 s at 25 °C. Data was analyzed by the Smoluchowski equation.

Fluorescence characterization on cover glass

For comparison experiments of different PEG linkers, beads (A110/200-PEG2/5-B6/OH) labeled with Cy5 or ATTO 488 were shortly vortexed, diluted 1:300 in PBS buffer, sonicated for 15 min, pipetted on a cover glass (5 µL) and coated by a spin coater 1001 (Convac GmbH, Vaihingen, Germany) at 2000 rpm. To compare different preparation methods including dilution and sonication, beads (A200-PEG2-OH/PEG_{24}-FA) were sonicated for 10 min, diluted (1:10 or 1:100) and again sonicated (for 0, 5 or 15 min), pipetted on cover glass (5 µL) and spin coated at 2000 rpm. Snap shots of the beads' fluorescence were recorded by widefield microscopy focusing on the surface of the cover glass.

External controls

Two external controls were performed as schematically depicted in Fig. 8.1. In both control experiments, the remnant of the mixture (5 µL) of beads with ligand (dye 1) and control beads (dye 2) which was used for the flow experiments was investigated. In the first test, the mixture (5 µL) was pipetted on a cover glass and spin coated at 3000 rpm.

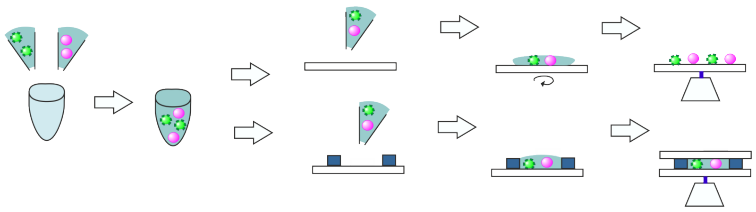

Figure 8.1: External control. Schematic drawing of two different external control experiments. For one external control, a mixture of beads with ligand and control beads was spin coated; for the other, the mixture was pipetted into an image spacer chamber.

In the second test, the mixture (9 µL) was pipetted into a imaging spacer chamber (9 mm diameter, 0.12 mm height) on a cover slide which was pre-coated with collagen A (10 % solution, 10 µL) for 30 min. The chamber was sealed by another cover glass. In both experiments, snapshots of the beads' fluorescence were recorded of multiple field of views (63.7x63.7 μm^2). The fluorescent maxima were counted and the mean values ± standard error (SE) calculated. By dividing the number of beads with ligand by the number of control beads per field of view, the correction factor was obtained.

Integrated fluorescence Density (IntDens)

To obtain the integrated fluorescence density (IntDens) of single beads, ATTO 488 labeled A200-PEG5-B6/B6scr/B6mod/cMBP2/cMBP2scr/OH beads were diluted in PBS buffer (1:100), sonicated

for 15 min and added to CO_2-independend medium supplemented with 10 % FBS in chamber slides. The fluorescence was measured by spinning disk microscopy.

Light absorption
The absorption of polystyrene beads (2 µL, 1:200 dilution in PBS buffer) was measured at 225-231 nm (Nanodrop ND-1000, PEQLAB Biotechnology GmbH, Erlangen, Germany) as quintuplicates. To calculate the concentration of amino groups in the suspension, a calibration curve was used. Therefore, serial dilution of unmodified beads was prepared and the absorption measured (see Appendix 1).

8.2.2 Polyplexes

Polyplexes are formed by condensation of nucleic acids with polymers. Cy5 labeled siRNA and polymer for siRNA polyplexes, and polymers and plasmid DNA for pDNA polyplexes were kindly provided by the group of Prof. Ernst Wagner (LMU Munich).

Labeling of plasmid DNA
Plasmid DNA (pCMVLuc, encoding for luciferase under control of the promotor CMV, 6400 bp, 4550 kDa) was labeled with Cy5 by covalent alkylation of reactive heteroatoms of the pDNA with the labeling reagent of the Label IT μArray, Cy5 Labeling kit (Mirus Bio LLC, MAdison, WI, USA) using the manufacturer's protocol. The Cy5-labeled pCMVLuc was purified by precipitation with sodium acetate (0.14 M, pH 5.2) in absolute ethanol at -20 °C overnight. After centrifugation at maximum speed with a microcentrifuge at 4 °C, the pellet was washed with cold ethanol (70 %, 3x), dried and resuspended in ultra filtrated sterile water to yield Cy5 labeled pCMVLuc (40 µg/mL). The concentrations of the label and the pDNA were determined with Nanodrop ND-1000 (PEQLAB Biotechnology GmbH, Erlangen, Germany).

8.2.2.1 siRNA polyplexes

Polymers and siRNA were kindly provided by Dr. Christian Dohmen (group of Prof. Ernst Wagner, LMU Munich). The oligomers were synthesized by standard peptide synthesis strategy using Fmoc-protection and solid phase support [67]. The sequence-defined polymers consist of 2x4 succinoyl tetraethylene pentamine (STP) building blocks, polyethylene glycol (PEG) with a defined length of 24 units ethylene glycol as shielding, and folic acid for receptor targeting or alanine as control. The identity was verified by MALDI-MS (matrix-assisted laser desorption/ionization mass spectrometry) and the purity was analyzed by RP-HPLC (reversed phase high performance/pressure liquid chromatography). The obtained oligomers are FA-PEG_{24}-K-$(STP_4$-$C)_2$ (referred as FA-PEG-STP, 4076 g/mol, 25 amines) and Ala-PEG_{24}-K-$(STP_4$-$C)_2$ (referred as Ala-PEG-STP). The siRNA was provided according to Dohmen *et al.* [324], and it is a siRNA against the house keeping gene AHA1, each molecule was labeled with one Cy5 dye (siANA1, sense sequence: Hexynyl-C_6-ss-C_6-5'-GGAuGAAGuGGAGAuuAGudTsdT-3'; antisense sequence: (Cy5-NH-C_6-5'-ACuAAUCUCcACUUcAUCCdTsdT-3'; 21 bp, 13500 Da).

The siRNA polyplexes (20 μg/mL siRNA) were freshly prepared for each experiment. Stock solutions of polymer and nucleic acid were mixed in HEPES buffered glucose (HBG buffer, 20 mM HEPES, pH 7.1, 5 % w/v glucose) with a molar ratio of polymer nitrogens to siRNA phosphates, N/P = 16. After incubation for 30 min at room temperature the formed polyplexes were used for experiments.

8.2.2.2 LPEI-pDNA polyplexes

Receptor targeted (cRGD-PEG2-LPEI22 and GE11-PEG2-LPEI22) and control (Cys-PEG2-LPEI22) polymers were synthesized by members of the group of Prof. Ernst Wagner (LMU Munich) by a standard peptide synthesis strategy using Fmoc-protection and solid phase support according to the literature [364, 379]. They consist of linear polyethylene imine (LPEI, 22 kDa), a PEG linker (2 kDa) and cRGD or GE11 for targeting or cysteine as a control. The cRGD peptide (H-βA-$C_1DC_2RGDC_3FC_4$-NH_2, C_1C_4/C_2C_3-bicyclo, 955 Da) was obtained form IRIS Biotech (Marktredwitz, Germany) and GE11 (CYHWYGYTPQNVI) from Biosyntan (Berlin, Germany).

The pDNA LPEI-polyplexes (20 μg/mL pDNA) were freshly prepared for each experiment. Stock solutions of polymer and nucleic acid (20-40 % Cy5 labeled mixed with non-labeled pCMVLuc) were mixed in HBG buffer with a molar ratio of polymer nitrogens to pDNA phosphates, N/P = 6 and incubated for 30 min at room temperature to form LPEI-polyplexes.

8.2.2.3 STP-pDNA polyplexes

Polymers (c(RGDfK)-PEG_{24}-K[Stp_4-C]$_2$, GE11-PEG_{24}-K[Stp_4-C]$_2$ and A-PEG_{24}-K[Stp_4-C]$_2$) were kindly provided by Dr. Ulrich Lächelt (group of Prof. Ernst Wagner, LMU Munich). The oligomers were synthesized by standard peptide synthesis strategy using Fmoc-protection and solid phase support according to the literature [361]. They consist of succinoyl tetraethylene pentamine (STP) building blocks, PEG spacer (24 units ethylene glycol) and targeting ligands (cRGD or GE11) or alanine as a control. The polymers were purified by size exclusion chromatography.

The pDNA STP-polyplexes (20 μg/mL pDNA) were freshly prepared for each experiment. Stock solutions of polymer and nucleic acid (20-40 % Cy5 labeled mixed with non-labeled pCMVLuc) were mixed in HBG buffer with a molar ratio of polymer nitrogens to pDNA phosphates, N/P = 12 on ice and incubated for 45 min at room temperature to form STP-polyplexes.

8.2.2.4 Polyplexes on cover glass

To investigate the fluorescence intensity of Cy5 labeled siRNA polyplexes, freshly prepared polyplexes (FA-PEG-STP) were diluted in water (1:40) and coated on cover glass at 3000 rpm. Movies (200 frames) of the polyplexes' fluorescence were recorded with widefield microscopy.

LPEI- and STP-polyplexes (20 μg/mL pDNA, 5 μL) labeled with Cy5 were diluted in HBG buffer (1:50) prior to coating on cover glass. The fluorescence was observed with widefield microscopy.

8.3 Cell culture

Human hepatocellular carcinoma cells (HuH7) were cultivated in DMEM/F-12, human cervical cancer cells (HeLa) in DMEM (low glucose), human prostate cancer cells (DU145) in RPMI 1640 (with glutamine), human nasopharyngeal epidermoid carcinoma cells (KB) in RPMI 1640 (without folic acid) and human dermal microvascular endothelial cells (HMEC-1) in MCDB-131 medium supplemented with 1 % Glutamax, 10 ng/mL hEGF and 1 µg/mL hydrocortisone. All media were prepared with addition of 10 % FBS. Cells were cultivated at 37 °C in a 5 % CO_2 containing, humidified atmosphere. For static experiments, cells were seeded into sterile ibiTreat µ – Slides, 8-well with a cell density of 2x10^4 (1x10^4) per well and incubated for 24 or48 h prior to the measurement. For live cell-imaging and experiments under static conditions, the medium was replaced by CO_2-independent medium supplemented with 10 % FBS prior to imaging. For experiments under flow conditions, cells were seeded into sterile ibiTreat µ – Slide $I^{0.4}$ Luer or $VI^{0.4}$ Luer flow chambers with a cell density of 4-4.5x10^5 per channel and incubated for 48 or 72 h. Before measuring, the medium was removed and replaced by CO_2-independent medium supplemented with 10 % FBS. Fixed cells were obtained by rinsing the cells twice with PBS, treatment with 4 % of PFA for 15 min followed by two final washing steps with PBS.

8.4 Cell experiments under static conditions

Experiments under static conditions were performed with cells cultivated in ibiTreat µ – Slides, 8-well chambers.

8.4.1 Uptake

8.4.1.1 Uptake of functionalized polystyrene beads

Two types of uptake experiments of functionalized polystyrene beads were performed. In the first one, Cy5 labeled latex beads (A200-PEG5-B6/B6scr1/B6scr2/B6mod/cMBP2/cMBP2scr/OH) were sonicated for 10 min, diluted in PBS buffer (1:25), again sonicated for 15 min. The beads (10 µL) were added to HuH7 cells in 8-well chambers (300 µL) and incubated for 2 h. After fixation, z-stacks of the labeled beads on the cells and of the cell membrane stained with WGA-Alexa Fluor488 (3.3 µg/mL for 2 min) were acquired with spinning disk microscopy. For the second uptake experiment, latex beads (ATTO 488 labeled A200-PEG5-B6 and Cy5 labeled A200-PEG5-B6scr/B6mod/OH) were incubated with DU145 cells for 6 h in presence of free Tf (1.25 mg/mL). Movies (500 frames) of the labeled beads in plane of the cells were recorded by live-cell imaging with spinning disk microscopy.

8.4.1.2 Uptake of polyplexes

Freshly prepared polyplexes (3 µL, see Section 8.2.2) were incubated with HuH7 cells in DMEM/F12 at 37 °C under 5% CO_2 atmosphere for 1.5 h. The cells were fixated afterwards. Next, cell membranes were stained with WGA-Alexa Fluor488 (3.3 µg/mL for 2 min) and nuclei with DAPI (300 µL, 300 nM for 5 min). Uptake was measured with spinning disk microscopy.

8.4.2 Folate receptor targeting

To target the folic acid receptor, Cy5 labeled A200-PEG5-FA/PEG2-FA/PEG_{24}-FA were sonicated for 5 min, diluted in PBS buffer (1:25) and again sonicated for 15 min. The particle suspensions (10 µL) were separately incubated with KB cells for 45 min at 37 °C and 5 % CO_2 atmosphere in folic acid free medium supplemented with 10 % FBS. After fixation with PFA, cell membranes were stained with WGA-Alexa Fluor488 (3.3 µg/mL for 2 min) and the cells were measured with spinning disk microscopy.

8.4.3 Competition with free ligand

Competitive adhesion experiments of A200-PEG5 beads with free Tf were performed on HuH7 cells. The concentration of the different bead suspensions was adjusted according to light absorption measurements at 230 nm. Cy5 labeled A200-PEG5-B6/B6scr1/B6scr2/B6mod/OH beads (49 µM NH_2, 1.5 x 10^{11} beads/mL) were incubated with HuH7 cells for 1 h at 37 °C in a 5 % CO_2 atmosphere with and without preincubation of holo-Tf (5 mg/mL) for 45 min. The cells were washed with PBS buffer (3x 300 µL) and fixated with PFA. Cell membranes were stained with WGA-Alexa Fluor488 (3.3 µg/mL for 2 min) and the integrated fluorescence density (IntDens) of the beads was measured with spinning disk microscopy.

8.4.4 Co-incubation with labeled, free ligand

The localization of TfR targeted and control beads in relation to free ligand was tested. HuH7 cells were preincubated with Tf-Alexa Fluor647 (3.3 µg/mL) for 45 min. Next, ATTO 488 labeled A200-PEG5-B6/B6scr/B6mod/OH beads (0.2 µL, sonicated for 5 min) were added and the cells incubated for another 1.5 h. Afterwards, the cells were washed with PBS buffer (3x 300 µL) and fixated with PFA. The beads and the Tf were imaged with spinning disk fluorescence microscopy.

8.4.5 TfR-GFP co-localization

For co-localization experiments of TfR and B6 beads or free Tf, HeLa cells were transfected with pBa.TfR.GFP (44 ng/µL, 9.5 µL with transfection reagent Xtreme GENE9 according to standard procedure) which was expressed in E.coli Top10 and purified with a QIAprep Spin Miniprep Kit (Quiagen N. V., Venlo, Netherlands). Sonicated, Cy5 labeled B6 beads or Alexa Fluor633 labeled Tf (3.3 µg/mL) were incubated on the GFP-TfR expressing HeLa cells in CO_2-independent medium for 0.5 and 2/2.5 h and their localization was analyzed by live-cell imaging.

8.5 Flow experiments

8.5.1 Experimental setup

Flow experiments were performed using a custom-built flow setup consisting of three main parts: a reservoir (15 mL falcon tube), a flow chamber (sterile ibiTreat µ − Slide $I^{0.4}$ or $VI^{0.4}$) and a syringe pump (KDS Legato 210P Infuse/Withdraw Programmable, KD Scientific Inc., Hollison, MA, USA),

all connected by flexible tubing (inner diameter: 1.6 mm; Tygon®). The reservoir was warmed in a heat bath to keep the temperature constant at 37 °C and the particle suspension was stirred to maintain a constant concentration within the whole volume. The flexible tubing, syringe and flow chambers were pre-filled with cell medium and assembled in such a way that no air bubbles were contained within the flow system. For experiments with parallel flow channels, the tubings were connected by Y-pieces. In Table 8.1, the typical parameter settings of the flow experiments are displayed if not otherwise stated.

Table 8.1: Parameter settings for flow experiments. Parameters of the flow channels, syringe, pump settings, volumes of fluid and duration of the experiments are listed.

Parameter	One channel (μ-slide I$^{0.4}$)	Four channels (μ-slide VI$^{0.4}$)
Channel dimensions	50x5x0.4 mm	17x3.8x0.4 mm
Channel volume	100 µL	30 µL
Syringe volume	10 mL	10 mL
Syringe diameter	15.8 mm	15.8 mm
Target volume	8 mL	6 mL
Flow rate	0.2 and 2 mL/min	0.1 mL/min
Pump mode	withdraw and withdraw/infuse	withdraw
Reservoir filling	9 mL	7 mL
Total fluid volume	13 mL	11 mL
Duration	40 min	60 min

8.5.2 Shear rate and shear stress

During flow experiments, shear stress is exerted on the cells on the channel bottom which refers to the force per cross-section area deforming the cells. Depending on the flow rate (ϕ) which is set at the syringe pump, the shear stress (τ) and the shear rate (γ) vary. Both parameters were calculated according to the technical report by ibidi GmbH [380]. They are based on the dynamical viscosity of water at 22 (η = 0.01 dyn · s/cm^2).

Shear stress:

$$\gamma = A \cdot \phi[\frac{dyn}{cm^2}] \tag{8.5.1}$$

where A is a factor depending on the respective chamber slide (A = 1.316 for µ − Slide I$^{0.4}$ Luer and A = 1.761 for µ − Slide VI$^{0.4}$ Luer).

Shear rate:

$$\gamma = B \cdot \phi[s^{-1}] \tag{8.5.2}$$

where B is a factor depending on the respective chamber slide (B = 131.6 for μ − Slide $I^{0.4}$ Luer and B = μ − Slide $VI^{0.4}$ Luer).

In the flow experiments with internal control, the shear stress was 0.263 dyn/cm^2 or 2.632 dyn/cm^2 and the shear rate was 26.3 s^{-1} or 263.2 s^{-1} at a low (0.2 mL/min) or a moderate (2 mL/min) flow rate, respectively. For flow experiments screening different surfaces, the shear stress was 0.044 dyn/cm^2 and the shear rate 4.4 s^{-1} at a very low flow rate (0.1 mL/min).

8.5.3 Cellular adhesion with internal control

Stock solutions of beads with ligand as well as control beads were sonicated for 10 min. The bead solutions (2 µL) were diluted in PBS buffer (800 µL) and sonicated again for 15 min. These dilutions of beads with ligand (dye 1, ca. 10^{10} /mL, 750 µL) and control beads (dye 2, ca. 10^{10} /mL, 750 µL) were added to the reservoir filled with CO_2-independent medium (7.5 mL) and magnetically stirred for 3 min to provide a homogenized suspension. The reservoir was surrounded by a warming bath to maintain a constant temperature (T = 37 °C). A continuous flow of particle suspension from the reservoir through the flow channel into the syringe (10 mL, Terumo®) was generated at a low flow rate of 200 µL/min (shear rate = 26.3 s^{-1}) and back and forth at a moderate flow rate of 2 mL/min (shear rate = 263.2 s^{-1}) by the syringe pump. The flow channel containing the cell monolayer at which the beads could bind during the experiment was mounted on a warming stage (T = 37 °C). After 40 min of flow, the flow channel was rinsed with warm PBS buffer at the same flow rate to remove unbound beads from the chamber. Afterwards, the cells were fixed. Experiments were performed as duplicates or triplicates.

8.5.4 Adhesion kinetics

To measure cellular adhesion kinetics, ATTO 488 labeled A110-PEG5-B6 and Cy5 labeled A110-PEG5-OH beads were sonicated for 10 min, diluted (1:300) in PBS buffer, again sonicated for 15 min and added to the reservoir (750 µL each) of the flow system. The cellular adhesion of the beads was observed by live-cell imaging. Thereafter, snapshots of single cells were taken with transmission light and movies (50 frames, 272 ms exposure time) of the same field of view were recorded by fluorescence widefield microscopy.

8.5.5 Characterization of different surfaces

Different methods were used to characterize the coatings within the flow channels (ibidi μ − Slide $VI^{0.4}$):

MaxGel ECM was diluted 1:10 in DMEM/F12 according to the manufacturer's protocol and further diluted in PBS (final ratios: 1:20, 1:50, 1:100). The formed network structure was air-dried and observed with transmission light widefield microscopy. Additionally, Cy5 labeled model beads (A200-PEG5-OH, 500 µL), sonicated and diluted (1:300) were passed over the ECM structures (1:20, 1:50 and 1:100 dilutions) at low shear flow (shear rate = 4.4 s^{-1}) [**?**]. Movies (200 frames) of the

beads' movement were recorded by widefield microscopy.

The autofluorescence of different dilutions of FBS was investigated by exposing the coated channel bottom to different laser intensities (10-100 % AOTF) and recording snapshots with widefield microscopy.

To image the collagen fibers within the flow channels, coated chambers (10 % collagen A, 2 h) were incubated with ATTO 488 overnight at 37 °C at 5 % CO_2 atmosphere. After washing with PBS buffer, the fluorescence of the fibers was measured with widefield microscopy.

8.5.6 Parallel adhesion experiments on different surfaces

One slide of flow channels (ibiTreated μ – Slide VI$^{0.4}$) was coated with cells (HuH7 and HMEC-1) and another one (hydrophobic μ – Slide VI$^{0.4}$) with different coatings (FBS, ECM, poly-L-lysine or collagen). FBS was diluted in water (1:5), poly-L-lysine (0.01 % solution) or collagen A (10 % solution) was pipetted into the channel, incubated for 2 h and dried on air. MaxGel ECM was diluted in water (1:50), pipetted into the channels on ice and incubated at 37 °C and 5 % CO_2 atmosphere for 2 h.

Polyplexes were freshly prepared as described above (see Section 8.2.2). They were added (10 μL, 20 μgDNA/mL) to the reservoir filled with CO_2-independent medium (6 mL), stirred for 3 min and a low flow rate (100 μL/min) was applied for 1 h using the syringe pump. The polyplex suspension was passed over the four surfaces in parallel through branched tubing. After the experiment, the channels were washed with PBS buffer and fixed with PFA.

8.6 Fluorescence microscopy

The fluorophores used in this work are listed in Table.

Table 8.2: Fluorescent dyes. The absorption (λ_{abs}) and emission (λ_{fl}) maxima, and the applied excitation wavelength (λ_{exc}) of fluorophores used in this work are listed below.

Fluorescent dye	λ_{abs} **[nm]**	λ_{fl} **[nm]**	λ_{exc} **[nm]**
Alexa Fluor 488	495	519	488
Alexa Fluor 633	632	647	633
Alexa Fluor 647	650	668	633/639
ATTO 488	501	523	488
Cy5	649	670	633/639
DAPI	358	461	405
FITC	493	528	488
GFP	488	509	488

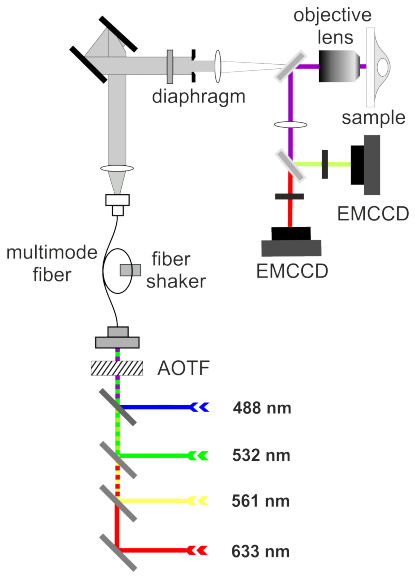

Figure 8.2: Widefield fluorescence microscope setup. Four different lasers (488 nm, 532 nm, 561 nm and 633 nm) are directed onto an AOTF. The selected wavelengths are passed through a multimode fiber and focused on the back focal plane of an objective illuminating the sample. Emitted fluorescent light is separated from the excitation beam by a dichroic mirror and split into two ranges of wavelengths. After passing appropriate emission filters, the fluorescent light is detected by two separated EMCCD cameras.

8.6.1 Widefield microscope

Particle characterization and cancer cell targeting experiments were imaged with a custom-built widefield fluorescence microscope based on a Nikon Eclipse Ti microscope corpus (Nikon Corp., Chiyoda, Tokyo, Japan). ATTO 488 and Cy5 dyes were excited alternately with 488 nm (Sapphire, Coherent Inc., Santa Clara, CA, USA) and 633 nm (gas laser, Nec Corp., Minato, Tokyo, Japan) laser lights, using a Plan Apo TIRF 60x, 1.45 NA oil immersion objective (Nikon). The fluorescence light was collected in epifluorescent mode, splitted into two beams by a dichroic mirror (565 DCXR, Chroma Technology Corp., Bellows Falls, VT, USA), passed through emission filters (GFP 526/50 and Cy5 720/149, Semrock Inc., Lake Forest, IL, USA) and directed onto two electron multiplying charge coupled devices (EMCCD, DU-897 iXon+, Andor Technology Ldt., Belfast, UK). The individual settings for each experiment are listed in Table 8.3. The laser light output was chosen such that an optimized signal-to-noise ratio and minimal autofluorescence were obtained. The camera gain was set to 300. Movies (25 or 50 frames) of single cells (ca. 40/flow channel) were recorded capturing the fluorescence of all particles on the cell within the field of view. To locate cell membranes and nuclei, transmission light images were recorded. Fluorescence of particles on cover glass was captured with one snapshot. Bleaching and blinking of siRNA polyplexes and beads passing ECM were observed by recording movies (200 frames). The images were visualized by applying the software Andor IQ.

Table 8.3: Widefield microscope settings.

Experiment (section)	Lasers [nm]	Dyes	AOTF [%]	Exposure time [ms]	Frame rate [Hz]
Fluorescence of beads (8.2.1)	488/633	ATTO 488/ Cy5	20/10	300	3.01
External control I (8.2.1)	488/633	ATTO 488/ Cy5	30/20	272/300	3.29/3.03
External control II (8.2.1)	488/633	ATTO 488/ Cy5	20/15	272/300	3.29/3.03
Internal control (8.5.3)	488/633	ATTO 488/ Cy5	20/15	272/300	3.29/3.03
Adhesion kinetics (8.5.4)	488/633	ATTO 488/ Cy5	30/20	272/300	3.29/3.03
siRNA pp (8.2.2)	633	Cy5	100	300	3.03
Surfaces screening (8.5.6)	633	Cy5	20	300	3.03
pp on cover glass (8.2.2)	633	Cy5	20	300	3.03
ECM, flow (8.5.5)	633	Cy5	20	50	12.45
FBS autofluorescence (8.5.5)	633	Cy5	10-100	300	3.03
collagen A (8.5.5)	488	ATTO 488	30	273	3.30

8.6.2 Spinning disk microscope

Confocal imaging was performed with a spinning disk microscope (Zeiss Cell Observer SD) containing a Yokogawa spinning disk unit CSU-X1. The fluorophores were excited by 405 nm, 488 nm and 639 nm laser light, passing through a quad-edge dichroic beamsplitter (FF410/504/582/669-Di01-25x36, Semrock) and a Plan apochromat 63x or 100x, 1.40 NA oil immersion objective (Zeiss, Oberkochen, Germany). The emitted light was collected in epifluorescent mode, split at a dichroic mirror (560 nm or 660 nm, Semrock, Rochester, NY, USA), passed through emission filters (525/50 and 690/60, Semrock) and directed onto two separate EMCCD cameras (PhotometricsEvolve). The fluorescence was measured by recording z-stacks (Δz = 200 nm). All excitation wavelength were alternated in one plane before the next plane was measured. The excitation power was adjusted individually for every experiment (405 nm laser: 72 µW, 488 nm laser: 168-416 µW and 639 nm laser: 27-309 µW), such that the signal was clearly detected and low autofluorescence recorded. The camera gain was set to 800. The settings for the different experiments are listed in Table 8.4. The images were visualized by applying the software ZEN, blue edition (Zeiss).

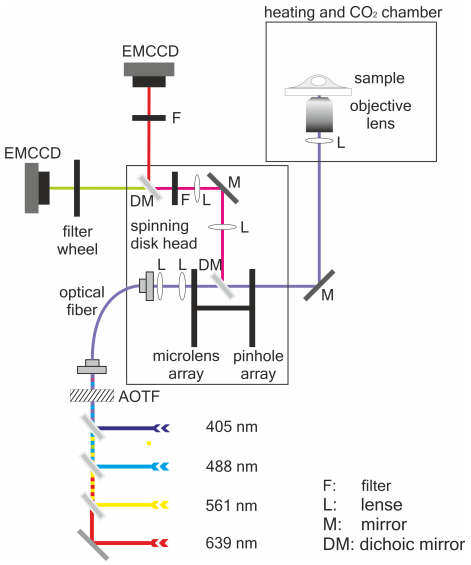

Figure 8.3: Spinning disk microscope setup. Four lasers (405 nm, 488 nm, 561 nm and 639 nm) are directed on an AOTF and are coupled into an optical fiber. In the spinning disk unit, the light is directed onto microlenses which focus it onto pinholes on a second disk from where it is directed into the objective illuminating the sample. Emitted fluorescent light is collected by the objective, guided back through the pinholes to a dichroic mirror separating it from the excitation light. The fluorescence is split by a second dichroic mirror into two ranges of wavelengths, passed through appropriate filters and recorded by two separated EMCCD cameras. The illustration was kindly provided by Dr. Veronika Weiß.

Table 8.4: Spinning disk microscope settings.

Experiment (section)	Lasers [nm]	Dyes	AOTF [%]	Exposure time [ms]	Objective
IntDens of beads (8.2.1)	488	ATTO 488	20	200	100x
Uptake of beads I (8.4.1.1)	488/639	Alexa488/ Cy5	25/10	100	63x
Uptake of beads II (8.4.1.1)	488/639	ATTO 488/ Cy5	50	100	63x
FR targeting (8.4.2)	488/639	Alexa488/ Cy5	25/10	100	63x
Competition of Tf (8.4.3)	488/639	Alexa488/ Cy5	25/10	100	100x
Co-localization of Tf (8.4.4)	488/639	ATTO 488/ Alexa647	10/100	100	100x
TfR-GFP (8.4.5)	488/639	GFP/ Cy5	25/20	100	100x
Uptake of polyplexes (8.4.1.2)	405/488/ 639	DAPI/ Alexa488/ Cy5	20/25/40	200	63x

8.7 Qualitative data analysis

8.7.1 Image visualization

Images for qualitative analysis were edited with Fiji [381]. The background was subtracted (rolling ball alogrithm r = 0.3 or 0.5 pixels) and a convolution Gaussian filter was applied (r = 1.0 pixel). The contrast and brightness of the fluorescence images were adjusted to obtain optimal visibility of labeled components.

8.7.2 Localization of particles on cover glass or cells

In order to localize particles on cells, two different procedures were used. With widefield microscopy, transmission light images were recorded from which the cell membrane and the areas of the nuclei were transferred to the fluorescence images. For confocal cell images obtained by spinning disk microscopy, the cell membranes (and the nuclei) were stained and the particles localized by merging the images of each fluorescence channels for every recorded plane.

Co-localization of ATTO 488 labeled B6/B6scr/B6mod/OH beads with Alexa Fluor647 labeled Tf was studied by merging the images of both fluorescence channels (green and red) of recorded z-stacks. In one central plane of the cell, co-localization was observed when the maximum fluorescence in both channels overlaid accurately.

To analyze the co-localization of GFP-TfR and Cy5-B6 beads/Alexa Fluor633-Tf, one central plane of single cells was displayed for each fluorescence channel and the merged image was evaluated qualitatively. Co-localization was obtained at the fluorescence maxima overlaying in both channels.

Bleaching and blinking of the fluorescence of siRNA polyplexes was analyzed by creating a time profile of single polyplexes. Using Fiji [381], single fluorescent spots (polyplexes) were encircled in movies of 200 frames, and the intensity/time profile was plotted.

The flow profile of model beads over ECM was evaluated by creating time projections of recorded movies (16 s) with Fiji. The obtained images were pseudo-color coded.

The autofluorescence of FBS dilutions within flow channels was depicted by coloring the recorded snapshots with pseudo-colors. Low autofluorescence was indicated by low intensity values (blue) and high background fluorescence by high intensity values (red).

8.8 Quantitative data analysis

8.8.1 Particle counting

Recorded movies of single cells were projected to one image using Fiji. The intensity maxima were selected and automatically counted with a Fiji macro (see Appendix 10). The accuracy of

this procedure was verified by manual counting of particles in parallel evaluations. The mean numbers of adhered beads per cell were calculated and presented as mean±standard error (SE), n = 79-140. To compare two groups, the unpaired student's *t*-test was performed. The results were considered as highly significantly different when $p<0.0001$. Transmission light images of the cells were recorded in differential interference contrast (DIC) mode. The regions of nucleus and plasma membrane were thus transferred to overlay images created with Fiji.

8.8.2 Particle in Cell 3D

The fluorescence integrated density (IntDens) of particles was obtained by using the ImageJ based macro Particle_in_Cell-3D described by Torrano *et al.* [276]. Several routines can be chosen. The IntDens of single particles was obtained by using the calibration routine 4. In brief, stacks of labeled particles on cover glass or on a chamber bottom were analyzed by integrating the fluorescence of each particle in every z-plane. The fluorescence of single particles can be plotted in a histogram, fitted and the maximum can be selected as mean IntDens of a particle type. The IntDens of particles on single cells was determined by the semi-/quantification routine 2 and 3. In brief, stacks of cells obtained by alternating excitation of Cy5 labeled nanoparticles and cell membrane stained with WGA-Alexa Fluor488 were split into separate channels. The macro creates a mask of the cell in every plane and background subtraction as well as an intensity threshold for the particle fluorescence have to be set. The macro measures the fluorescence intensity (IntDens) of each object (particle or agglomerate). Furthermore, the cell is reconstructed in 3D, and detected particles are alighned to three different regions: intracellular, enlarged membrane region and extracellular. Additionally, a color-coded image of the cell is displayed.

List of abbreviations

abbreviation	explanation
AAV	adeno-associated virus
Ala	alanine
AOTF	acousto-optical tunable filter
Arf6	ADP-ribosylation factor 6
ATP	adensoine triphosphate
BPEI	branched PEI
CAF	cancer-associated fibroblast
Cbl	Casitas B-lineage lymphoma
CD	cyclodextrin
CDC42	cell devision control 42
cMBP2	c-Met binding peptide 2
CME	clathrin-mediated endocytosis
cRGD	cyclic RGD
Cys	cysteine
DAPI	4′,6-diamidino-2-phenylindole
DHB	2,5-dihydroxybenzoic acid
DIC	differential interference contrast
DLS	dynamic light scattering
DMEM	dulbecco's modified eagle's medium
DMSO	dimethyl sulfoxide
DNA	deoxyribonucleic acid
DTT	dithiothreitol
DU145	human prostate cancer cell line
ECM	extracellular matrix
EDTA	ethylenediaminetetraacetic acid
EGF(R)	epidermal growth factor (receptor)
(EM)CCD	(electron multiplying) charge coupled device
EPR	enhanced permeability and retention effect
Eq	equivalents
ER	endoplasmic reticulum
ERC	endocytic recycling compartment

abbreviation	explanation
FA	folic acid
FBS	fetal bovine serum
Fc	fragment, crystallizable
FGF	fibroblast growth factor
FITC	fluorescein isothiocyanate
Fmoc	fluorenylmethyloxycarbonyl
FR	folate receptor
FRAP	fluorescence recovery after photobleaching
FRET	Förster resonance energy transfer
GFP	green fluorescent protein
GPCR	G-protein coupled recpeptor
GPI	gylcosyl phosphatidyl-inositol
GTP	guanosine triphosphate
HBG	HEPES buffered glucose
hEGF	human EGF
HeLa	human cervix adenocarcinoma cell line
HEPES	4-(2-hydroxyethly)-1-piperazineethanesulfonic acid
HGF(R)	hepatocyte growth factor (receptor)
HIV	human immunodeficiency virus
HMEC-1	human microvascular endothelial cell line
HPLC	high performance/pressure liquid chromatography
HuH7	human hepato cellular carcinoma cell line
IFP	interstitial fluid pressure
IgG/M	immunoglobulin G/M
IntDens	integrated fluorescence density
IPT	Ig-like, plexins, transcription factors
it	iminothiolane
ivDde	N^{ε}-1-(4,4-dimethyl-2,6-dioxocyclohex-1-ylidene)-3-methylbutyl
KB	human nasopharyngeal epidermoid carcinoma cell line
LDL	low density lipoprotein
LPEI	linear PEI
LSM	laser scanning microscopy
LV	lentivirus
Lys	lysine

abbreviation	explanation
MALDI	matrix-assisted laser desorption/ionization
MCDB-131	(Molecular, Cellular, and Developmental Biology): cell culture medium
miRNA	micro RNA
mod	modified
MPS	mononuclear phagocytic system
MTOC	microtubule-organizin center
MSC	mesenchymal stem cell
MVB	multivesicular bodies
NA	numerical aperture
NAD(P)	nicotinamideadenine dinucleotide (phosphate)
NHS	*N*-hydroxysuccinimide
NLS	nuclear localization sequence
NSOM	near-field scanning optical microscopy
OH	hydroxyl
OPSS	*ortho*-pyridyldisulfide
PAA	polyacrylic acid
PALM	photo-activated localization microscopy
(D)PBS	(Dulbecco's) phosphate buffered saline
PCFT	proton-coupled folate transporter
PCI	photochemical internalization
PDGF	platelet-derived growth factor
PDI	polydispersity index
pDNA	plasmid DNA
pdp	pyridyldithiol propionate
PEG	polyethylene glycol
PEI	polyethyleneimine
PEO	polyethylene oxide
PFA	*para*-formaldehyde
PI	particle intensity
PLL	poly-L-lysine
PSF	point spread function
PSI	plexin, semaphorin, integrin
PTP1B	protein-tyrosine phosphatase 1B
RFC	reduced folate carrier

abbreviation	explanation
RGD	(cyclic) arginine-glycine-aspartic acid
RhoA	Ras homolog gene family, member A
RNA	ribonucleic acid
ROI	region of interest
ROS	reactive oxygen species
RPMI 1640	(Roswell Park MEmorial Insitiute): cell culture medium
scr	scrambled
SD	spinning disk
SE	standard error
SF	scatter factor
SH	Src homology
SIM	structured illumination microscopy
siRNA	small interfering ribonucleic acid
STED	stimulated emission depletion
STORM	stochastical optical reconstruction microscopy
STP	succinoyl tetraethylene pentamine
Tf(R)	transferrin (receptor)
TGFα	transformation factor α
THF	tetrahydrofolate
TIRF(M)	total internal reflection fluorescence (microscopy)
TOF	time-of-flight
2-TP	2-thiopyridone
Tyr	tyrosine
UV/Vis	ultraviolet-visible
VEGF(R)	vascular endothelial growth factor
vWF	von Willebrand factor
WGA	wheat germ agglutinin

Bibliography

[1] F. Schmidt. Deutsche welle online article: German cancer congress: Fighting disease with personalized medicine, 05.04.2016 http://dw.com/p/1I1TX.

[2] World Health Organization. Cancer fact sheet n 297, February 2015 http://www.who.int/mediacentre/factsheets/fs297/en/.

[3] A. Marusyk, V. Almendro, and K. Polyak. Intra-tumour heterogeneity: a looking glass for cancer? *Nat Rev Cancer*, 12(5):323–34, 2012.

[4] A. Albanese, A. K. Lam, E. A. Sykes, J. V. Rocheleau, and W. C. Chan. Tumour-on-a-chip provides an optical window into nanoparticle tissue transport. *Nat Commun*, 4:2718, 2013.

[5] D. Loessner, C. Meinert, E. Kaemmerer, L. C. Martine, K. Yue, P. A. Levett, T. J. Klein, F. P. Melchels, A. Khademhosseini, and D. W. Hutmacher. Functionalization, preparation and use of cell-laden gelatin methacryloyl-based hydrogels as modular tissue culture platforms. *Nat Protoc*, 11(4):727–46, 2016.

[6] I. Brigger, C. Dubernet, and P. Couvreur. Nanoparticles in cancer therapy and diagnosis. *Adv Drug Deliv Rev*, 54(5):631–51, 2002.

[7] M. L. Adams, A. Lavasanifar, and G. S. Kwon. Amphiphilic block copolymers for drug delivery. *J Pharm Sci*, 92(7):1343–55, 2003.

[8] W. Gao, R. Langer, and O. C. Farokhzad. Poly(ethylene glycol) with observable shedding. *Angew Chem Int Ed Engl*, 49(37):6567–71, 2010.

[9] Z. X. Xiao, E. Levy-Nissenbaum, F. Alexis, A. Luptak, B. A. Teply, J. M. Chan, J. Shi, E. Digga, J. Cheng, R. Langer, and O. C. Farokhzad. Engineering of targeted nanoparticles for cancer therapy using internalizing aptamers isolated by cell-uptake selection. *ACS Nano*, 6(1):696–704, 2012.

[10] A. Gianella, P. A. Jarzyna, V. Mani, S. Ramachandran, C. Calcagno, J. Tang, B. Kann, W. J. Dijk, V. L. Thijssen, A. W. Griffioen, G. Storm, Z. A. Fayad, and W. J. Mulder. Multifunctional nanoemulsion platform for imaging guided therapy evaluated in experimental cancer. *ACS Nano*, 5(6):4422–33, 2011.

[11] F. Danhier, O. Feron, and V. Preat. To exploit the tumor microenvironment: Passive and active tumor targeting of nanocarriers for anti-cancer drug delivery. *J Control Release*, 148(2):135–46, 2010.

[12] K. K. Jain. *Drug Delivery Systems - An Overview*, pages 1–50. Humana Press, Totowa, NJ, 2008.

[13] L. Tao, W. Hu, Y. Liu, G. Huang, B. D. Sumer, and J. Gao. Shape-specific polymeric nanomedicine: emerging opportunities and challenges. *Exp Biol Med (Maywood)*, 236(1):20–9, 2011.

[14] A. Wicki, D. Witzigmann, V. Balasubramanian, and J. Huwyler. Nanomedicine in cancer therapy: challenges, opportunities, and clinical applications. *J Control Release*, 200:138–57, 2015.

[15] B. Atmaja, B. H. Lui, Y. Hu, S. E. Beck, C. W. Frank, and J. R. Cochran. Targeting of Cancer Cells Using Quantum Dot-Polypeptide Hybrid Assemblies that Function as Molecular Imaging Agents and Carrier Systems. *Adv Funct Mater*, 20(23):4091–7, 2010.

[16] M. R. Ali, S. R. Panikkanvalappil, and M. A. El-Sayed. Enhancing the efficiency of gold nanoparticles treatment of cancer by increasing their rate of endocytosis and cell accumulation using rifampicin. *J Am Chem Soc*, 136(12):4464–7, 2014.

[17] C. Argyo, V. Weiss, C. Bräuchle, and T. Bein. Multifunctional Mesoporous Silica Nanoparticles as a Universal Platform for Drug Delivery. *Chemistry of Materials*, 26(1):435–51, 2014.

[18] S. Merino, C. Martin, K. Kostarelos, M. Prato, and E. Vazquez. Nanocomposite Hydrogels: 3D Polymer-Nanoparticle Synergies for On-Demand Drug Delivery. *ACS Nano*, 9(5):4686–97, 2015.

[19] N. K. Mehra and S. Palakurthi. Interactions between carbon nanotubes and bioactives: a drug delivery perspective. *Drug Discov Today*, doi:10.1016/j.drudis.2015.11.011, 2015.

[20] H. Yang. Targeted nanosystems: Advances in targeted dendrimers for cancer therapy. *nanomedicine*, 12(2):309–16, 2016.

[21] J. Ezzati Nazhad Dolatabadi, H. Valizadeh, and H. Hamishehkar. Solid Lipid Nanoparticles as Efficient Drug and Gene Delivery Systems: Recent Breakthroughs. *Adv Pharm Bull*, 5(2):151–9, 2015.

[22] R. H. Prabhu, V. B. Patravale, and M. D. Joshi. Polymeric nanoparticles for targeted treatment in oncology: current insights. *Int J Nanomedicine*, 10(1):1001–18, 2015.

[23] P. P. Deshpande, S. Biswas, and V. P. Torchilin. Current trends in the use of liposomes for tumor targeting. *Nanomedicine*, 8(9):1509–28, 2013.

[24] E. G. Kim and K. M. Kim. Strategies and Advancement in Antibody-Drug Conjugate Optimization for Targeted Cancer Therapeutics. *Biomol Ther (Seoul)*, 23(6):493–509, 2015.

[25] C. J. Buchholz, T. Friedel, and H. Buning. Surface-Engineered Viral Vectors for Selective and Cell Type-Specific Gene Delivery. *Trends Biotechnol*, 33(12):777–90, 2015.

[26] C. S. Kue, A. Kamkaew, K. Burgess, L. V. Kiew, L. Y. Chung, and H. B. Lee. Small Molecules for Active Targeting in Cancer. *Med Res Rev*, doi: 10.1002/med.21387, 2016.

[27] C. Dufes, M. Al Robaian, and S. Somani. Transferrin and the transferrin receptor for the targeted delivery of therapeutic agents to the brain and cancer cells. *Ther Deliv*, 4(5):629–40, 2013.

[28] S. Valetti, F. Maione, S. Mura, B. Stella, D. Desmaele, M. Noiray, J. Vergnaud, C. Vauthier, L. Cattel, E. Giraudo, and P. Couvreur. Peptide-functionalized nanoparticles for selective targeting of pancreatic tumor. *J Control Release*, 192C:29–39, 2014.

[29] R. V. Chari, M. L. Miller, and W. C. Widdison. Antibody-drug conjugates: an emerging concept in cancer therapy. *Angew Chem Int Ed Engl*, 53(15):3796–827, 2014.

[30] J. L. Yang, D. X. Liu, S. J. Zhen, Y. G. Zhou, D. J. Zhang, L. Y. Yang, H. B. Chen, and Q. Feng. A novel anti-p21Ras scFv antibody reacting specifically with human tumour cell lines and primary tumour tissues. *BMC Cancer*, 16(1):131, 2016.

[31] M. Kijanka, B. Dorresteijn, S. Oliveira, and P. M. van Bergen en Henegouwen. Nanobody-based cancer therapy of solid tumors. *Nanomedicine (Lond)*, 10(1):161–74, 2015.

[32] M. Hu and K. Zhang. The application of aptamers in cancer research: an up-to-date review. *Future Oncol*, 9(3):369–76, 2013.

[33] S. Naahidi, M. Jafari, F. Edalat, K. Raymond, A. Khademhosseini, and P. Chen. Biocompatibility of engineered nanoparticles for drug delivery. *J Control Release*, 166(2):182–94, 2013.

[34] T. Sun, Y. S. Zhang, B. Pang, D. C. Hyun, M. Yang, and Y. Xia. Engineered nanoparticles for drug delivery in cancer therapy. *Angew Chem Int Ed Engl*, 53(46):12320–64, 2014.

[35] Y. Matsumura and H. Maeda. A new concept for macromolecular therapeutics in cancer chemotherapy: mechanism of tumoritropic accumulation of proteins and the antitumor agent Smacs. *Cancer Res.*, 46:6387–92, 1986.

[36] R. S. Langer and N. A. Peppas. Present and future applications of biomaterials in controlled drug delivery systems. *Biomaterials*, 2(4):201–14, 1981.

[37] S. Mura, J. Nicolas, and P. Couvreur. Stimuli-responsive nanocarriers for drug delivery. *Nat Mater*, 12(11):991–1003, 2013.

[38] S. Payne and D. Miles. *Mechanisms of anticancer drugs*. CRC press, 2008.

[39] Z. H. Siddik. Cisplatin: mode of cytotoxic action and molecular basis of resistance. *Oncogene*, 22(47):7265–79, 2003.

[40] A. J. Montero, B. Adams, C. M. Diaz-Montero, and S. Gluck. Nab-paclitaxel in the treatment of metastatic breast cancer: a comprehensive review. *Expert Rev Clin Pharmacol*, 4(3):329–34, 2011.

[41] C. Oerlemans, W. Bult, M. Bos, G. Storm, J. F. Nijsen, and W. E. Hennink. Polymeric micelles in anticancer therapy: targeting, imaging and triggered release. *Pharm Res*, 27(12):2569–89, 2010.

[42] Y. Barenholz. Doxil(R)–the first FDA-approved nano-drug: lessons learned. *J Control Release*, 160(2):117–34, 2012.

[43] K. S. Lee, H. C. Chung, S. A. Im, Y. H. Park, C. S. Kim, S. B. Kim, S. Y. Rha, M. Y. Lee, and J. Ro. Multicenter phase II trial of Genexol-PM, a Cremophor-free, polymeric micelle formulation of paclitaxel, in patients with metastatic breast cancer. *Breast Cancer Res Treat*, 108(2):241–50, 2008.

[44] R. Pieters, S. P. Hunger, J. Boos, C. Rizzari, L. Silverman, A. Baruchel, N. Goekbuget, M. Schrappe, and C. H. Pui. L-asparaginase treatment in acute lymphoblastic leukemia: a focus on Erwinia asparaginase. *Cancer*, 117(2):238–49, 2011.

[45] O. C. Farokhzad and R. Langer. Nanomedicine: developing smarter therapeutic and diagnostic modalities. *Adv Drug Deliv Rev*, 58(14):1456–9, 2006.

[46] H. C. Kang, K. M. Huh, and Y. H. Bae. Polymeric nucleic acid carriers: current issues and novel design approaches. *J Control Release*, 164(3):256–64, 2012.

[47] M. K. Joo, J. Y. Yhee, S. H. Kim, and K. Kim. The potential and advances in RNAi therapy: chemical and structural modifications of siRNA molecules and use of biocompatible nanocarriers. *J Control Release*, 193:113–21, 2014.

[48] Y. Shu, F. Pi, A. Sharma, M. Rajabi, F. Haque, D. Shu, M. Leggas, B. M. Evers, and P. Guo. Stable RNA nanoparticles as potential new generation drugs for cancer therapy. *Adv Drug Deliv Rev*, 66:74–89, 2014.

[49] M. Ogris and E. Wagner. Targeting tumors with non-viral gene delivery systems. *Drug Discov Today*, 7(8):479–85, 2002.

[50] L. M. Bryant, D. M. Christopher, A. R. Giles, C. Hinderer, J. L. Rodriguez, J. B. Smith, E. A. Traxler, J. Tycko, A. P. Wojno, and J. M. Wilson. Lessons learned from the clinical development and market authorization of Glybera. *Hum Gene Ther Clin Dev*, 24(2):55–64, 2013.

[51] S. Pearson, H. Jia, and K. Kandachi. China approves first gene therapy. *Nat Biotechnol*, 22(1):3–4, 2004.

[52] M. A. Islam, T. E. Park, B. Singh, S. Maharjan, J. Firdous, M. H. Cho, S. K. Kang, C. H. Yun, Y. J. Choi, and C. S. Cho. Major degradable polycations as carriers for DNA and siRNA. *J Control Release*, 193:74–89, 2014.

[53] M. C. Pedroso de Lima, S. Simoes, P. Pires, H. Faneca, and N. Duzgunes. Cationic lipid-DNA complexes in gene delivery: from biophysics to biological applications. *Adv Drug Deliv Rev*, 47(2-3):277–94, 2001.

[54] U. Lachelt and E. Wagner. Nucleic Acid Therapeutics Using Polyplexes: A Journey of 50 Years (and Beyond). *Chem Rev*, 115(19):11043–78, 2015.

[55] K. A. Mislick and J. D. Baldeschwieler. Evidence for the role of proteoglycans in cation-mediated gene transfer. *Proc Natl Acad Sci U S A*, 93(22):12349–54, 1996.

[56] S. V. Zaitsev, A. Haberland, A. Otto, V. I. Vorob'ev, H. Haller, and M. Bottger. H1 and HMG17 extracted from calf thymus nuclei are efficient DNA carriers in gene transfer. *Gene Ther*, 4(6):586–92, 1997.

[57] G. W. Bos, D. J. A. Crommelin, and W. E. Hennink. *Water-Soluble Cationic Methacrylate Polymers for Nonviral Gene Delivery*, pages 35–60. Humana Press, Totowa, NJ, 2001.

[58] C. Pfeifer, G. Hasenpusch, S. Uezguen, M. K. Aneja, D. Reinhardt, J. Kirch, M. Schneider, S. Claus, W. Friess, and C. Rudolph. Dry powder aerosols of polyethylenimine (PEI)-based gene vectors mediate efficient gene delivery to the lung. *J Control Release*, 154(1):69–76, 2011.

[59] T. Thuy le, S. Mallick, and J. S. Choi. Polyamidoamine (PAMAM) dendrimers modified with short oligopeptides for early endosomal escape and enhanced gene delivery. *Int J Pharm*, 492(1-2):233–43, 2015.

[60] S. Bauhuber, R. Liebl, L. Tomasetti, R. Rachel, A. Goepferich, and M. Breunig. A library of strictly linear poly(ethylene glycol)-poly(ethylene imine) diblock copolymers to perform structure-function relationship of non-viral gene carriers. *J Control Release*, 162(2):446–55, 2012.

[61] Y. Z. Du, L. L. Cai, J. Li, M. D. Zhao, F. Y. Chen, H. Yuan, and F. Q. Hu. Receptor-mediated gene delivery by folic acid-modified stearic acid-grafted chitosan micelles. *Int J Nanomedicine*, 6:1559–68, 2011.

[62] J. D. Heidel. In vivo transfection using cyclodextrin-containing polycations. *Cold Spring Harb Protoc*, 2011(11):1392–3, 2011.

[63] C. Scholz, P. Kos, L. Leclercq, X. Jin, H. Cottet, and E. Wagner. Correlation of length of linear oligo(ethanamino) amides with gene transfer and cytotoxicity. *ChemMedChem*, 9(9):2104–10, 2014.

[64] O. Boussif, F. Lezoualc'h, M. A. Zanta, M. D. Mergny, D. Scherman, B. Demeneix, and J. P. Behr. A versatile vector for gene and oligonucleotide transfer into cells in culture and in vivo: polyethylenimine. *Proc Natl Acad Sci U S A*, 92(16):7297–301, 1995.

[65] S. Brunner, T. Sauer, S. Carotta, M. Cotten, M. Saltik, and E. Wagner. Cell cycle dependence of gene transfer by lipoplex, polyplex and recombinant adenovirus. *Gene Ther*, 7(5):401–7, 2000.

[66] S. Brunner, E. Furtbauer, T. Sauer, M. Kursa, and E. Wagner. Overcoming the nuclear barrier: cell cycle independent nonviral gene transfer with linear polyethylenimine or electroporation. *Mol Ther*, 5(1):80–6, 2002.

[67] C. Dohmen, D. Edinger, T. Frohlich, L. Schreiner, U. Lachelt, C. Troiber, J. Radler, P. Hadwiger, H. P. Vornlocher, and E. Wagner. Nanosized Multifunctional Polyplexes for Receptor-Mediated SiRNA Delivery. *ACS Nano*, 6(6):5198–208, 2012.

[68] T. Blessing, J. S. Remy, and J. P. Behr. Monomolecular collapse of plasmid DNA into stable virus-like particles. *Proc Natl Acad Sci U S A*, 95(4):1427–31, 1998.

[69] T. Blessing, J.-S. Remy, and J.-P. Behr. Template oligomerization of DNA-bound cations produces calibrated nanometric particles. *J Am Chem Soc*, 120(33):8519–20, 1998.

[70] R. S. Burke and S. H. Pun. Extracellular barriers to in Vivo PEI and PEGylated PEI polyplex-mediated gene delivery to the liver. *Bioconjug Chem*, 19(3):693–704, 2008.

[71] Z. Yang, Z. Jiang, Z. Cao, C. Zhang, D. Gao, X. Luo, X. Zhang, H. Luo, Q. Jiang, and J. Liu. Multifunctional non-viral gene vectors with enhanced stability, improved cellular and nuclear uptake capability, and increased transfection efficiency. *Nanoscale*, 6(17):10193–206, 2014.

[72] G. Stingl, E. B. Brocker, R. Mertelsmann, K. Wolff, S. Schreiber, E. Kampgen, A. Schneeberger, W. Dummer, U. Brennscheid, H. Veelken, M. L. Birnstiel, K. Zatloukal, W. Schmidt, G. Maass, E. Wagner, M. Baschle, M. Giese, E. R. Kempe, H. A. Weber, and T. Voigt. Phase I study to the immunotherapy of metastatic malignant melanoma by a cancer vaccine consisting of autologous cancer cells transfected with the human IL-2 gene. *Hum Gene Ther*, 7(4):551–63, 1996.

[73] A. A. Sidi, P. Ohana, S. Benjamin, M. Shalev, J. H. Ransom, D. Lamm, A. Hochberg, and I. Leibovitch. Phase I/II marker lesion study of intravesical BC-819 DNA plasmid in H19 over expressing superficial bladder cancer refractory to bacillus Calmette-Guerin. *J Urol*, 180(6):2379–83, 2008.

[74] K. Anwer, M. N. Barnes, J. Fewell, D. H. Lewis, and R. D. Alvarez. Phase-I clinical trial of IL-12 plasmid/lipopolymer complexes for the treatment of recurrent ovarian cancer. *Gene Ther*, 17(3):360–9, 2010.

[75] M. E. Davis, J. E. Zuckerman, C. H. Choi, D. Seligson, A. Tolcher, C. A. Alabi, Y. Yen, J. D. Heidel, and A. Ribas. Evidence of RNAi in humans from systemically administered siRNA via targeted nanoparticles. *Nature*, 464(7291):1067–70, 2010.

[76] A. E. Nel, L. Madler, D. Velegol, T. Xia, E. M. V. Hoek, P. Somasundaran, F. Klaessig, V. Castranova, and M. Thompson. Understanding biophysicochemical interactions at the nano-bio interface. *Nature Materials*, 8(7):543–57, 2009.

[77] M. P. Monopoli, C. Aberg, A. Salvati, and K. A. Dawson. Biomolecular coronas provide the biological identity of nanosized materials. *Nat Nanotechnol*, 7(12):779–86, 2012.

[78] R. Gref, M. Luck, P. Quellec, M. Marchand, E. Dellacherie, S. Harnisch, T. Blunk, and R. H. Muller. 'Stealth' corona-core nanoparticles surface modified by polyethylene glycol (PEG): influences of the corona (PEG chain length and surface density) and of the core composition on phagocytic uptake and plasma protein adsorption. *Colloids Surf B Biointerfaces*, 18(3-4):301–13, 2000.

[79] A. Aderem and D. M. Underhill. Mechanisms of phagocytosis in macrophages. *Annu Rev Immunol*, 17:593–623, 1999.

[80] M. Longmire, P. L. Choyke, and H. Kobayashi. Clearance properties of nano-sized particles and molecules as imaging agents: considerations and caveats. *Nanomedicine (Lond)*, 3(5):703–17, 2008.

[81] E. Kuntz and H.-D. Kuntz. *Hepatology, Principles and practice: history, morphology, biochemistry, diagnostics, clinic, therapy*. Springer Science & Business Media, 2006.

[82] S. M. Moghimi, A. C. Hunter, and J. C. Murray. Long-circulating and target-specific nanoparticles: theory to practice. *Pharmacol Rev*, 53(2):283–318, 2001.

[83] W. M. Deen, M. J. Lazzara, and B. D. Myers. Structural determinants of glomerular permeability. *Am J Physiol Renal Physiol*, 281:F579–F596, 2001.

[84] H. S. Choi, W. Liu, P. Misra, E. Tanaka, J. P. Zimmer, B. Itty Ipe, M. G. Bawendi, and J. V. Frangioni. Renal clearance of quantum dots. *Nat Biotechnol*, 25(10):1165–70, 2007.

[85] W. C. Zamboni, V. Torchilin, A. K. Patri, J. Hrkach, S. Stern, R. Lee, A. Nel, N. J. Panaro, and P. Grodzinski. Best practices in cancer nanotechnology: perspective from NCI nanotechnology alliance. *Clin Cancer Res*, 18(12):3229–41, 2012.

[86] L. Sun, Q. Wu, F. Peng, L. Liu, and C. Gong. Strategies of polymeric nanoparticles for enhanced internalization in cancer therapy. *Colloids Surf B Biointerfaces*, 135:56–72, 2015.

[87] R. Duncan. The dawning era of polymer therapeutics. *Nat Rev Drug Discov*, 2(5):347–60, 2003.

[88] T. Miller, A. Hill, S. Uezguen, M. Weigandt, and A. Goepferich. Analysis of immediate stress mechanisms upon injection of polymeric micelles and related colloidal drug carriers: implications on drug targeting. *Biomacromolecules*, 13(6):1707–18, 2012.

[89] J. M. Rabanel, P. Hildgen, and X. Banquy. Assessment of PEG on polymeric particles surface, a key step in drug carrier translation. *J Control Release*, 185:71–87, 2014.

[90] R. K. Jain, J. D. Martin, and T. Stylianopoulos. The role of mechanical forces in tumor growth and therapy. *Annu Rev Biomed Eng*, 16:321–46, 2014.

[91] I. A. Khawar, J. H. Kim, and H. J. Kuh. Improving drug delivery to solid tumors: priming the tumor microenvironment. *J Control Release*, 201:78–89, 2015.

[92] A. S. Narang and S. Varia. Role of tumor vascular architecture in drug delivery. *Adv Drug Deliv Rev*, 63(8):640–58, 2011.

[93] M. Egeblad, E. S. Nakasone, and Z. Werb. Tumors as organs: complex tissues that interface with the entire organism. *Dev Cell*, 18(6):884–901, 2010.

[94] P. Vaupel and A. Mayer. Hypoxia in cancer: significance and impact on clinical outcome. *Cancer Metastasis Rev*, 26(2):225–39, 2007.

[95] E. Ruoslahti. Specialization of tumour vasculature. *Nat Rev Cancer*, 2(2):83–90, 2002.

[96] R. van Sluis, Z. M. Bhujwalla, N. Raghunand, P. Ballesteros, J. Alvarez, S. Cerdan, J. P. Galons, and R. J. Gillies. In vivo imaging of extracellular pH using 1H MRSI. *Magnetic Resonance in Medicine*, 41:743–50, 1999.

[97] S. J. Turley, V. Cremasco, and J. L. Astarita. Immunological hallmarks of stromal cells in the tumour microenvironment. *Nat Rev Immunol*, 15(11):669–82, 2015.

[98] N. A. Bhowmick, E. G. Neilson, and H. L. Moses. Stromal fibroblasts in cancer initiation and progression. *Nature*, 432(7015):332–7, 2004.

[99] Q. Li, A. Hata, C. Kosugi, N. Kataoka, and M. Funaki. The density of extracellular matrix proteins regulates inflammation and insulin signaling in adipocytes. *FEBS Lett*, 584(19):4145–50, 2010.

[100] P. Lu, V. M. Weaver, and Z. Werb. The extracellular matrix: a dynamic niche in cancer progression. *J Cell Biol*, 196(4):395–406, 2012.

[101] F. X. Maquart, G. Bellon, S. Pasco, and J. C. Monboisse. Matrikines in the regulation of extracellular matrix degradation. *Biochimie*, 87(3-4):353–60, 2005.

[102] A. Marusyk and K. Polyak. Tumor heterogeneity: causes and consequences. *Biochim Biophys Acta*, 1805(1):105–17, 2010.

[103] M. A. Swartz and A. W. Lund. Lymphatic and interstitial flow in the tumour microenvironment: linking mechanobiology with immunity. *Nat Rev Cancer*, 12(3):210–9, 2012.

[104] R. K. Jain. Normalizing tumor microenvironment to treat cancer: bench to bedside to biomarkers. *J Clin Oncol*, 31(17):2205–18, 2013.

[105] E. S. Nakasone, H. A. Askautrud, T. Kees, J. H. Park, V. Plaks, A. J. Ewald, M. Fein, M. G. Rasch, Y. X. Tan, J. Qiu, J. Park, P. Sinha, M. J. Bissell, E. Frengen, Z. Werb, and M. Egeblad. Imaging tumor-stroma interactions during chemotherapy reveals contributions of the microenvironment to resistance. *Cancer Cell*, 21(4):488–503, 2012.

[106] B. M. Lopes-Bastos, W. G. Jiang, and J. Cai. Tumour-Endothelial Cell Communications: Important and Indispensable Mediators of Tumour Angiogenesis. *Anticancer Res.*, 36(3):1119–26, 2016.

[107] M. Kanapathipillai, A. Brock, and D. E. Ingber. Nanoparticle targeting of anti-cancer drugs that alter intracellular signaling or influence the tumor microenvironment. *Adv Drug Deliv Rev*, 79-80:107–18, 2014.

[108] H. Sarin. Physiologic upper limits of pore size of different blood capillary types and another perspective on the dual pore theory of microvascular permeability. *J Angiogenes Res*, 2(1):1–19, 2010.

[109] S. D. Perrault and W. C. W. Chan. In vivo assembly of nanoparticle components to improve targeted cancer imaging. *PNAS*, 107(25):11194–9, 2010.

[110] H. Maeda. Macromolecular therapeutics in cancer treatment: The EPR effect and beyond. *J Control Release*, 164(2):138–44, 2012.

[111] B. Haley and E. Frenkel. Nanoparticles for drug delivery in cancer treatment. *Urol Oncol*, 26(1):57–64, 2008.

[112] H. Hashizume, P. Baluk, S. Morikawa, J. W. McLean, G. Thurston, S. Roberge, R. K. Jain, and D. M. McDonald. Openings between Defective Endothelial Cells Explain Tumor Vessel Leakiness. *American Journal of Pathology*, 156(4):1363–80, 2000.

[113] F. Yuan, M. Dellian, D. Fukumura, M. Leunig, D. A. Berk, V. P. Torchilin, and R. K. Jain. Vascular permeability in a human tumor xenograft: molecular size dependence and cutoff size. *Cancer Res.*, 55(17):3752–6, 1995.

[114] R. K. Jain and T. Stylianopoulos. Delivering nanomedicine to solid tumors. *Nat Rev Clin Oncol*, 7(11):653–64, 2010.

[115] P. Decuzzi, S. Lee, B. Bhushan, and M. Ferrari. A Theoretical Model for the Margination of Particles within Blood Vessels. *Ann Biomed Eng*, 33(2):179–90, 2005.

[116] Y. Geng, P. Dalhaimer, S. Cai, R. Tsai, M. Tewari, T. Minko, and D. E. Discher. Shape effects of filaments versus spherical particles in flow and drug delivery. *Nat Nanotechnol*, 2(4):249–55, 2007.

[117] P. Decuzzi, R. Pasqualini, W. Arap, and M. Ferrari. Intravascular delivery of particulate systems: does geometry really matter? *Pharm Res*, 26(1):235–43, 2009.

[118] M. N. Christiansen, J. Chik, L. Lee, M. Anugraham, J. L. Abrahams, and N. H. Packer. Cell surface protein glycosylation in cancer. *Proteomics*, 14(4-5):525–46, 2014.

[119] M. J. Akhtar, M. Ahamed, H. A. Alhadlaq, S. A. Alrokayan, and S. Kumar. Targeted anticancer therapy: overexpressed receptors and nanotechnology. *Clin Chim Acta*, 436:78–92, 2014.

[120] A. Accardo, R. Mansi, A. Morisco, G. Mangiapia, L. Paduano, D. Tesauro, A. Radulescu, M. Aurilio, L. Aloj, C. Arra, and G. Morelli. Peptide modified nanocarriers for selective targeting of bombesin receptors. *Mol Biosyst*, 6(5):878–87, 2010.

[121] J. Asundi, C. Reed, J. Arca, K. McCutcheon, R. Ferrando, S. Clark, E. Luis, J. Tien, R. Firestein, and P. Polakis. An antibody-drug conjugate targeting the endothelin B receptor for the treatment of melanoma. *Clin Cancer Res*, 17(5):965–75, 2011.

[122] D. Arosio and C. Casagrande. Advancement in integrin facilitated drug delivery. *Adv Drug Deliv Rev*, 97:111–43, 2016.

[123] B. Bahrami, M. Mohammadnia-Afrouzi, P. Bakhshaei, Y. Yazdani, G. Ghalamfarsa, M. Yousefi, S. Sadreddini, F. Jadidi-Niaragh, and M. Hojjat-Farsangi. Folate-conjugated nanoparticles as a potent therapeutic approach in targeted cancer therapy. *Tumour Biol*, 36(8):5727–42, 2015.

[124] C. Yewale, D. Baradia, I. Vhora, S. Patil, and A. Misra. Epidermal growth factor receptor targeting in cancer: a review of trends and strategies. *Biomaterials*, 34(34):8690–707, 2013.

[125] L. Cai, N. Qiu, X. Li, K. Luo, X. Chen, L. Yang, G. He, Y. Wei, and L. Chen. A novel truncated basic fibroblast growth factor fragment-conjugated poly (ethylene glycol)-cholesterol amphiphilic polymeric drug delivery system for targeting to the FGFR-overexpressing tumor cells. *Int J Pharm*, 408(1-2):173–82, 2011.

[126] Y. Wang, J. Xu, X. Xia, M. Yang, S. Vangveravong, J. Chen, R. H. Mach, and Y. Xia. SV119-gold nanocage conjugates: a new platform for targeting cancer cells via sigma-2 receptors. *Nanoscale*, 4(2):421–4, 2012.

[127] K. Hida, N. Maishi, Y. Sakurai, Y. Hida, and H. Harashima. Heterogeneity of tumor endothelial cells and drug delivery. *Adv Drug Deliv Rev*, 99(Pt B):140–7, 2016.

[128] T. C. Johannessen, M. Wagner, O. Straume, R. Bjerkvig, and H. P. Eikesdal. Tumor vasculature: the Achilles' heel of cancer? *Expert Opin Ther Targets*, 17(1):7–20, 2013.

[129] Y. Zhong, F. Meng, C. Deng, and Z. Zhong. Ligand-directed active tumor-targeting polymeric nanoparticles for cancer chemotherapy. *Biomacromolecules*, 15(6):1955–69, 2014.

[130] O. C. Farokhzad and R. Langer. Impact of nanotechnology on drug delivery. *ACS Nano*, 3(1):16–20, 2009.

[131] K. F. Pirollo and E. H. Chang. Does a targeting ligand influence nanoparticle tumor localization or uptake? *Trends Biotechnol*, 26(10):552–8, 2008.

[132] S. Nie. Understanding and overcoming major barriers in cancer nanomedicine. *Nanomedicine (Lond)*, 5(4):523–8, 2010.

[133] T. A. Denison and Y. H. Bae. Tumor heterogeneity and its implication for drug delivery. *J Control Release*, 164(2):187–91, 2012.

[134] J. M. El Hage Chahine, M. Hemadi, and N. T. Ha-Duong. Uptake and release of metal ions by transferrin and interaction with receptor 1. *Biochim Biophys Acta*, 1820(3):334–47, 2012.

[135] A. McClelland, L. C. Kuhn, and F. H. Ruddle. The human transferrin receptor gene: genomic organization, and the complete primary structure of the receptor deduced from a cDNA sequence. *Cell*, 39(2 Pt 1):267–74, 1984.

[136] T. R. Daniels, T. Delgado, J. A. Rodriguez, G. Helguera, and M. L. Penichet. The transferrin receptor part I: Biology and targeting with cytotoxic antibodies for the treatment of cancer. *Clin Immunol*, 121(2):144–58, 2006.

[137] W. A. Jefferies, M. R. Brandon, S. V. Hunt, A. F. Williams, K. C. Gatter, and D. Y. Mason. Transferrin receptor on endothelium of brain capillaries. *Nature*, 312(5990):162–3, 1984.

[138] A. Calzolari, I. Oliviero, S. Deaglio, G. Mariani, M. Biffoni, N. M. Sposi, F. Malavasi, C. Peschle, and U. Testa. Transferrin receptor 2 is frequently expressed in human cancer cell lines. *Blood Cells Mol Dis*, 39(1):82–91, 2007.

[139] D. Trinder and E. Baker. Transferrin receptor 2: a new molecule in iron metabolism. *Int J Biochem Cell Biol*, 35(3):292–6, 2003.

[140] M. E. Brandsma, A. M. Jevnikar, and S. Ma. Recombinant human transferrin: beyond iron binding and transport. *Biotechnol Adv*, 29(2):230–8, 2011.

[141] P. Aisen, A. Leibman, and J. Zweier. Stoichiometric and site characteristics of the binding of iron to human transferrin. *J Biol Chem*, 253(6):1930–7, 1978.

[142] J. G. Grossmann, J. B. Crawley, R. W. Strange, K. J. Patel, L. M. Murphy, M. Neu, R. W. Evans, and S. S. Hasnain. The nature of ligand-induced conformational change in transferrin in solution. An investigation using X-ray scattering, XAFS and site-directed mutants. *J Mol Biol*, 279(2):461–72, 1998.

[143] R. J. Ward, Y. Zhang, and R. R. Crichton. Aluminium toxicity and iron homeostasis. *J Inorg Biochem*, 87(1-2):9–14, 2001.

[144] K. M. Mayle, A. M. Le, and D. T. Kamei. The intracellular trafficking pathway of transferrin. *Biochim Biophys Acta*, 1820(3):264–81, 2012.

[145] B. S. Stein and H. H. Sussman. Demonstration of two distinct transferrin receptor recycling pathways and transferrin-independent receptor internalization in K562 cells. *J Biol Chem*, 261(22):10319–31, 1986.

[146] A. Dautry-Versat, A. Ciechanover, and H. F. Lodish. pH and the recycling of transferrin during receptor-mediated endocytosis. *Proc Natl Acad Sci U S A*, 80:2258–62, 1983.

[147] R. D. Klausner, G. Ashwell, J. van Renswoude, J. B. Harford, and K. R. Bridges. Binding of apotransferrin to K562 cells: explanation of the transferrin cycle. *Proc Natl Acad Sci U S A*, 80(8):2263–6, 1983.

[148] J. C. Dewan, B. Mikami, M. Hirose, and J. C. Sacchettini. Structural evidence for a pH-sensitive dilysine trigger in the hen ovotransferrin N-lobe: implications for transferrin iron release. *Biochemistry*, 32(45):11963–8, 1993.

[149] S. Tortorella and T. C. Karagiannis. Transferrin receptor-mediated endocytosis: a useful target for cancer therapy. *J Membr Biol*, 247(4):291–307, 2014.

[150] M. Singh, K. Mugler, D. W. Hailoo, S. Burke, B. Nemesure, K. Torkko, and K. R. Shroyer. Differential expression of transferrin receptor (TfR) in a spectrum of normal to malignant breast tissues: implications for in situ and invasive carcinoma. *Appl Immunohistochem Mol Morphol*, 19(5):417–23, 2011.

[151] C. R. Hopkins and I. S. Trowbridge. Internalization and processing of transferrin and the transferrin receptor in human carcinoma A431 cells. *J Cell Biol*, 97(2):508–21, 1983.

[152] H. Li and Z. M. Qian. Transferrin/transferrin receptor-mediated drug delivery. *Med Res Rev*, 22(3):225–50, 2002.

[153] T. R. Daniels, E. Bernabeu, J. A. Rodriguez, S. Patel, M. Kozman, D. A. Chiappetta, E. Holler, J. Y. Ljubimova, G. Helguera, and M. L. Penichet. The transferrin receptor and the targeted delivery of therapeutic agents against cancer. *Biochim Biophys Acta*, 1820(3):291–317, 2012.

[154] I. Garajova, E. Giovannetti, G. Biasco, and G. J. Peters. c-Met as a Target for Personalized Therapy. *Transl Oncogenomics*, 7(Suppl 1):13–31, 2015.

[155] S. L. Organ and M. S. Tsao. An overview of the c-MET signaling pathway. *Ther Adv Med Oncol*, 3(1 Suppl):S7–S19, 2011.

[156] L. Trusolino, A. Bertotti, and P. M. Comoglio. MET signalling: principles and functions in development, organ regeneration and cancer. *Nat Rev Mol Cell Biol*, 11(12):834–48, 2010.

[157] C. Basilico, A. Arnesano, M. Galluzzo, P. M. Comoglio, and P. Michieli. A high affinity hepatocyte growth factor-binding site in the immunoglobulin-like region of Met. *J Biol Chem*, 283(30):21267–77, 2008.

[158] T. Ueki, Y. Kaneda, H. Tsutsui, K. Nakanishi, Y. Sawa, R. Morishita, K. Matsumoto, T. Nakamura, H. Takahashi, E. Okamoto, and J. Fujimoto. Hepatocyte growth factor gene therapy of liver cirrhosis in rats. *Nat Med*, 5(2):226–30, 1999.

[159] M. Watanabe, M. Ebina, F. M. Orson, A. Nakamura, K. Kubota, D. Koinuma, K. Akiyama, M. Maemondo, S. Okouchi, M. Tahara, K. Matsumoto, T. Nakamura, and T. Nukiwa. Hepatocyte growth factor gene transfer to alveolar septa for effective suppression of lung fibrosis. *Mol Ther*, 12(1):58–67, 2005.

[160] R. Barrow-McGee and S. Kermorgant. Met endosomal signalling: in the right place, at the right time. *Int J Biochem Cell Biol*, 49:69–74, 2014.

[161] V. Sangwan, G. N. Paliouras, J. V. Abella, N. Dube, A. Monast, M. L. Tremblay, and M. Park. Regulation of the Met receptor-tyrosine kinase by the protein-tyrosine phosphatase 1B and T-cell phosphatase. *J Biol Chem*, 283(49):34374–83, 2008.

[162] P. M. Comoglio, S. Giordano, and L. Trusolino. Drug development of MET inhibitors: targeting oncogene addiction and expedience. *Nat Rev Drug Discov*, 7(6):504–16, 2008.

[163] D. S. Krause and R. A. Van Etten. Tyrosine kinases as targets for cancer therapy. *N Engl J Med*, 353(2):172–87, 2005.

[164] E. Ghiso and S. Giordano. Targeting MET: why, where and how? *Curr Opin Pharmacol*, 13(4):511–8, 2013.

[165] R. M. Lu, Y. L. Chang, M. S. Chen, and H. C. Wu. Single chain anti-c-Met antibody conjugated nanoparticles for in vivo tumor-targeted imaging and drug delivery. *Biomaterials*, 32(12):3265–74, 2011.

[166] P. Kos, U. Lachelt, A. Herrmann, F. M. Mickler, M. Doblinger, D. He, A. Krhac Levacic, S. Morys, C. Brauchle, and E. Wagner. Histidine-rich stabilized polyplexes for cMet-directed tumor-targeted gene transfer. *Nanoscale*, 7(12):5350–62, 2015.

[167] R. D. Cummings, A. M. Soderquist, and G. Carpenter. The oligosaccharide moieties of the epidermal growth factor receptor in A-431 cells. Presence of complex-type N-linked chains that contain terminal N-acetylgalactosamine residues. *J Biol Chem*, 260(22):11944–52, 1985.

[168] I. Lax, R. Fischer, C. Ng, J. Segre, A. Ullrich, D. Givol, and J. Schlessinger. Noncontiguous regions in the extracellular domain of EGF receptor define ligand-binding specificity. *Cell Regul*, 2(5):337–45, 1991.

[169] M. A. Lemmon, Z. Bu, J. E. Ladbury, M. Zhou, D. Pinchasi, I. Lax, D. M. Engelman, and J. Schlessinger. Two EGF molecules contribute additively to stabilization of the EGFR dimer. *EMBO J*, 16(2):281–94, 1997.

[170] C. W. Ward, P. A. Hoyne, and R. H. Flegg. Insulin and epidermal growth factor receptors contain the cysteine repeat motif found in the tumor necrosis factor receptor. *Proteins: Structure, Function, and Bioinformatics*, 22(2):141–53, 1995.

[171] K. M. Ferguson, M. B. Berger, J. M. Mendrola, H.-S. Cho, D. J. Leahy, and M. A. Lemmon. EGF Activates Its Receptor by Removing Interactions that Autoinhibit Ectodomain Dimerization. *Molecular Cell*, 11(2):507–17, 2003.

[172] A. Zaczek, B. Brandt, and K. P. Bielawski. The diverse signaling network of EGFR, HER2, HER3 and HER4 tyrosine kinase receptors and the consequences for therapeutic approaches. *Histol Histopathol*, 20(3):1005–15, 2005.

[173] N. E. Hynes and H. A. Lane. ERBB receptors and cancer: the complexity of targeted inhibitors. *Nat Rev Cancer*, 5(5):341–54, 2005.

[174] C. P. Mill, J. A. Chester, and D. J. Riese. EGFR may couple moderate alcohol consumption to increased breast cancer risk. *Breast Cancer : Targets and Therapy*, 1:31–8, 2009.

[175] N. Gotoh, A. Tojo, M. Hino, Y. Yazaki, and M. Shibuya. A highly conserved tyrosine residue at codon 845 within the kinase domain is not required for the transforming activity of human epidermal growth factor receptor. *Biochem Biophys Res Commun*, 186(2):768–74, 1992.

[176] W. X. Schulze, L. Deng, and M. Mann. Phosphotyrosine interactome of the ErbB-receptor kinase family. *Mol Syst Biol*, 1(1):n/a, 2005.

[177] R. Bianco, D. Melisi, F. Ciardiello, and G. Tortora. Key cancer cell signal transduction pathways as therapeutic targets. *Eur J Cancer*, 42(3):290–4, 2006.

[178] K. J. Wilson, J. L. Gilmore, J. Foley, M. A. Lemmon, and 2nd Riese, D. J. Functional selectivity of EGF family peptide growth factors: implications for cancer. *Pharmacol Ther*, 122(1):1–8, 2009.

[179] A. Sorkin, M. Mazzotti, T. Sorkina, L. Scotto, and L. Beguinot. Epidermal Growth Factor Receptor Interaction with Clathrin Adaptors Is Mediated by the Tyr974-containing Internalization Motif. *J Biol Chem*, 271(23):13377–84, 1996.

[180] J. D. Orth, E. W. Krueger, S. G. Weller, and M. A. McNiven. A novel endocytic mechanism of epidermal growth factor receptor sequestration and internalization. *Cancer Res.*, 66(7):3603–10, 2006.

[181] M. Sundvall, K. Iljin, S. Kilpinen, H. Sara, O. P. Kallioniemi, and K. Elenius. Role of ErbB4 in breast cancer. *J Mammary Gland Biol Neoplasia*, 13(2):259–68, 2008.

[182] Y. Yarden and M. X. Sliwkowski. Untangling the ErbB signalling network. *Nat Rev Mol Cell Biol*, 2(2):127–37, 2001.

[183] J. H. van Krieken, A. Jung, T. Kirchner, F. Carneiro, R. Seruca, F. T. Bosman, P. Quirke, J. F. Flejou, T. Plato Hansen, G. de Hertogh, P. Jares, C. Langner, G. Hoefler, M. Ligtenberg, D. Tiniakos, S. Tejpar, G. Bevilacqua, and A. Ensari. KRAS mutation testing for predicting response to anti-EGFR therapy for colorectal carcinoma: proposal for an European quality assurance program. *Virchows Arch*, 453(5):417–31, 2008.

[184] R. O. Hynes. The emergence of integrins: a personal and historical perspective. *Matrix Biol.*, 23(6):333–40, 2004.

[185] I. D. Campbell and M. J. Humphries. Integrin structure, activation, and interactions. *Cold Spring Harb Perspect Biol*, 3(3):a004994, 2011.

[186] J. A. Askari, P. A. Buckley, A. P. Mould, and M. J. Humphries. Linking integrin conformation to function. *J Cell Sci*, 122(Pt 2):165–70, 2009.

[187] A. Kren, V. Baeriswyl, F. Lehembre, C. Wunderlin, K. Strittmatter, H. Antoniadis, R. Fassler, U. Cavallaro, and G. Christofori. Increased tumor cell dissemination and cellular senescence in the absence of beta1-integrin function. *EMBO J*, 26(12):2832–42, 2007.

[188] A. L. Berrier and K. M. Yamada. Cell-matrix adhesion. *J Cell Physiol*, 213(3):565–73, 2007.

[189] W. Guo and F. G. Giancotti. Integrin signalling during tumour progression. *Nat Rev Mol Cell Biol*, 5(10):816–26, 2004.

[190] N. De Franceschi, H. Hamidi, J. Alanko, P. Sahgal, and J. Ivaska. Integrin traffic - the update. *J Cell Sci*, 128(5):839–52, 2015.

[191] R. E. Bridgewater, J. C. Norman, and P. T. Caswell. Integrin trafficking at a glance. *J Cell Sci*, 125(Pt 16):3695–701, 2012.

[192] J. S. Desgrosellier and D. A. Cheresh. Integrins in cancer: biological implications and therapeutic opportunities. *Nat Rev Cancer*, 10(1):9–22, 2010.

[193] X. Wang, S. Li, Y. Shi, X. Chuan, J. Li, T. Zhong, H. Zhang, W. Dai, B. He, and Q. Zhang. The development of site-specific drug delivery nanocarriers based on receptor mediation. *J Control Release*, 193:139–53, 2014.

[194] C. Chen, J. Ke, X. E. Zhou, W. Yi, J. S. Brunzelle, J. Li, E. L. Yong, H. E. Xu, and K. Melcher. Structural basis for molecular recognition of folic acid by folate receptors. *Nature*, 500(7463):486–9, 2013.

[195] I. Ifergan and Y. G. Assaraf. *Chapter 4: Molecular Mechanisms of Adaptation to Folate Deficiency*, volume 79, pages 99–143. Academic Press, 2008.

[196] N. Gonen and Y. G. Assaraf. Antifolates in cancer therapy: structure, activity and mechanisms of drug resistance. *Drug Resist Updat*, 15(4):183–210, 2012.

[197] R. Zhao and I. D. Goldman. The proton-coupled folate transporter: physiological and pharmocological roles. *Curr Opin Pharmacol*, 13(6):875–80, 2013.

[198] I. Lasry, B. Berman, R. Straussberg, Y. Sofer, H. Bessler, M. Sharkia, F. Glaser, G. Jansen, S. Drori, and Y. G. Assaraf. A novel loss-of-function mutation in the proton-coupled folate transporter from a patient with hereditary folate malabsorption reveals that Arg 113 is crucial for function. *Blood*, 112(5):2055–61, 2008.

[199] L. H. Matherly, M. R. Wilson, and Z. Hou. The major facilitative folate transporters solute carrier 19A1 and solute carrier 46A1: biology and role in antifolate chemotherapy of cancer. *Drug Metab Dispos*, 42(4):632–49, 2014.

[200] N. Parker, M. J. Turk, E. Westrick, J. D. Lewis, P. S. Low, and C. P. Leamon. Folate receptor expression in carcinomas and normal tissues determined by a quantitative radioligand binding assay. *Anal Biochem*, 338(2):284–93, 2005.

[201] S. Sabharanjak and S. Mayor. Folate receptor endocytosis and trafficking. *Adv Drug Deliv Rev*, 56(8):1099–109, 2004.

[202] S. Mayor, K. G. Rothberg, and F. R. Maxfield. Sequestration of GPI-anchored proteins in caveolae triggered by cross-linking. *Science*, 264(5167):1948–51, 1994.

[203] S. Chatterjee, E. R. Smith, K. Hanada, V. L. Stevens, and S. Mayor. GPI anchoring leads to sphingolipid-dependent retention of endocytosed proteins in the recycling endosomal compartment. *EMBO J*, 20(7):1583–92, 2001.

[204] L. E. Kelemen. The role of folate receptor alpha in cancer development, progression and treatment: cause, consequence or innocent bystander? *Int J Cancer*, 119(2):243–50, 2006.

[205] M. K. Siu, D. S. Kong, H. Y. Chan, E. S. Wong, P. P. Ip, L. Jiang, H. Y. Ngan, X. F. Le, and A. N. Cheung. Paradoxical impact of two folate receptors, FRalpha and RFC, in ovarian cancer: effect on cell proliferation, invasion and clinical outcome. *PLoS One*, 7(11):e47201, 2012.

[206] L. Teng, J. Xie, L. Teng, and R. J. Lee. Clinical translation of folate receptor-targeted therapeutics. *Expert Opin Drug Deliv*, 9(8):901–8, 2012.

[207] N. K. Mehra, V. Mishra, and N. K. Jain. Receptor-based targeting of therapeutics. *Ther Deliv*, 4(3):369–94, 2013.

[208] W. Xia and P. S. Low. Folate-targeted therapies for cancer. *J Med Chem*, 53(19):6811–24, 2010.

[209] R. A. Bamford, Z. Y. Zhao, N. A. Hotchin, I. B. Styles, G. B. Nash, J. H. Tucker, and R. Bicknell. Electroporation and microinjection successfully deliver single-stranded and duplex DNA into live cells as detected by FRET measurements. *PLoS One*, 9(4):e95097, 2014.

[210] J. Kulbacka, A. Pucek, M. Kotulska, M. Dubinska-Magiera, J. Rossowska, M. P. Rols, and K. A. Wilk. Electroporation and lipid nanoparticles with cyanine IR-780 and flavonoids as efficient vectors to enhanced drug delivery in colon cancer. *Bioelectrochemistry*, 110:19–31, 2016.

[211] J. Zhen, Y. Choi, S. Y. Ko, J. O. Park, and S. Park. Experimental and simulation studies on focused ultrasound triggered drug delivery. *Biotechnol Appl Biochem*, doi: 10.1002/bab.1453, 2015.

[212] S. D. Conner and S. L. Schmidt. Regulated portals of entry into the cell. *Nature*, 422:37–44, 2003.

[213] L. Y. Chou, K. Ming, and W. C. Chan. Strategies for the intracellular delivery of nanoparticles. *Chem Soc Rev*, 40(1):233–45, 2011.

[214] J. Mercer and A. Helenius. Virus entry by macropinocytosis. *Nat Cell Biol*, 11(5):510–20, 2009.

[215] G. J. Doherty and H. T. McMahon. Mechanisms of endocytosis. *Annu Rev Biochem*, 78(1):857–902, 2009.

[216] T. J. Pucadyil and S. L. Schmid. Conserved functions of membrane active GTPases in coated vesicle formation. *Science*, 325(5945):1217–20, 2009.

[217] J. Z. Rappoport. Focusing on clathrin-mediated endocytosis. *Biochem J*, 412(3):415–23, 2008.

[218] R. G. Anderson. The caveolae membrane system. *Annu Rev Biochem*, 67(1):199–225, 1998.

[219] L. A. Carver and J. E. Schnitzer. Caveolae: mining little caves for new cancer targets. *Nat Rev Cancer*, 3(8):571–81, 2003.

[220] G. Sahay, D. Y. Alakhova, and A. V. Kabanov. Endocytosis of nanomedicines. *J Control Release*, 145(3):182–95, 2010.

[221] R. G. Parton and K. Simons. The multiple faces of caveolae. *Nat Rev Mol Cell Biol*, 8(3):185–94, 2007.

[222] J. Fleddermann, E. Diamanti, S. Azinas, M. Kosutic, L. Dahne, I. Estrela-Lopis, M. Amacker, E. Donath, and S. E. Moya. Virosome engineering of colloidal particles and surfaces: bioinspired fusion to supported lipid layers. *Nanoscale*, 10.1039/c5nr08169f, 2016.

[223] A. Verma, O. Uzun, Y. Hu, Y. Hu, H. S. Han, N. Watson, S. Chen, D. J. Irvine, and F. Stellacci. Surface-structure-regulated cell-membrane penetration by monolayer-protected nanoparticles. *Nat Mater*, 7(7):588–95, 2008.

[224] J. Lin and A. Alexander-Katz. Cell Membranes Open "Doors" for Cationic Nanoparticles/Biomolecules: Insights into Uptake Kinetics. *ACS Nano*, 7(12):10799–808, 2013.

[225] L. N. Patel, J. L. Zaro, and W. C. Shen. Cell penetrating peptides: intracellular pathways and pharmaceutical perspectives. *Pharm Res*, 24(11):1977–92, 2007.

[226] J. Rejman, A. Bragonzi, and M. Conese. Role of clathrin- and caveolae-mediated endocytosis in gene transfer mediated by lipo- and polyplexes. *Mol Ther*, 12(3):468–74, 2005.

[227] G. Sahay, J. O. Kim, A. V. Kabanov, and T. K. Bronich. The exploitation of differential endocytic pathways in normal and tumor cells in the selective targeting of nanoparticulate chemotherapeutic agents. *Biomaterials*, 31(5):923–33, 2010.

[228] H. Herd, N. Daum, A. T. Jones, H. Huwer, H. Ghandehari, and C. M. Lehr. Nanoparticle geometry and surface orientation influence mode of cellular uptake. *ACS Nano*, 7(3):1961–73, 2013.

[229] B. D. Grant and J. G. Donaldson. Pathways and mechanisms of endocytic recycling. *Nat Rev Mol Cell Biol*, 10(9):597–608, 2009.

[230] A. K. Varkouhi, M. Scholte, G. Storm, and H. J. Haisma. Endosomal escape pathways for delivery of biologicals. *J Control Release*, 151(3):220–8, 2011.

[231] M. Mandal and K. D. Lee. Listeriolysin O-liposome-mediated cytosolic delivery of macromolecule antigen in vivo: enhancement of antigen-specific cytotoxic T lymphocyte frequency, activity, and tumor protection. *Biochim Biophys Acta*, 1563(1-2):7–17, 2002.

[232] W. Liang and J. K.W. Lam. *Endosomal Escape Pathways for Non-Viral Nucleic Acid Delivery Systems*. Molecular Regulation of Endocytosis. 2012.

[233] M. Horth, B. Lambrecht, M. C. Khim, F. Bex, C. Thiriart, J. M. Ruysschaert, A. Burny, and R. Brasseur. Theoretical and functional analysis of the SIV fusion peptide. *EMBO J*, 10(10):2747–55, 1991.

[234] P. J. Lou, P. S. Lai, M. J. Shieh, A. J. Macrobert, K. Berg, and S. G. Bown. Reversal of doxorubicin resistance in breast cancer cells by photochemical internalization. *Int J Cancer*, 119(11):2692–8, 2006.

[235] K. Nienhaus and G. U. Nienhaus. Where Do We Stand with Super-Resolution Optical Microscopy? *J Mol Biol*, 428(2 Pt A):308–22, 2016.

[236] K. de Bruin, N. Ruthardt, K. von Gersdorff, R. Bausinger, E. Wagner, M. Ogris, and C. Brauchle. Cellular dynamics of EGF receptor-targeted synthetic viruses. *Mol Ther*, 15(7):1297–305, 2007.

[237] A. A. Torrano and C. Brauchle. Precise quantification of silica and ceria nanoparticle uptake revealed by 3D fluorescence microscopy. *Beilstein J Nanotechnol*, 5:1616–24, 2014.

[238] J. Blechinger, A. T. Bauer, A. A. Torrano, C. Gorzelanny, C. Brauchle, and S. W. Schneider. Uptake kinetics and nanotoxicity of silica nanoparticles are cell type dependent. *Small*, 9(23):3970–80, 2013.

[239] F. M. Mickler, Y. Vachutinsky, M. Oba, K. Miyata, N. Nishiyama, K. Kataoka, C. Brauchle, and N. Ruthardt. Effect of integrin targeting and PEG shielding on polyplex micelle internalization studied by live-cell imaging. *J Control Release*, 156(3):364–73, 2011.

[240] S. A. Mackowiak, A. Schmidt, V. Weiss, C. Argyo, C. von Schirnding, T. Bein, and C. Brauchle. Targeted drug delivery in cancer cells with red-light photoactivated mesoporous silica nanoparticles. *Nano Lett*, 13(6):2576–83, 2013.

[241] A. S. Stender, K. Marchuk, C. Liu, S. Sander, M. W. Meyer, E. A. Smith, B. Neupane, G. Wang, J. Li, J. X. Cheng, B. Huang, and N. Fang. Single cell optical imaging and spectroscopy. *Chem Rev*, 113(4):2469–527, 2013.

[242] D. Toomre and J. Bewersdorf. A new wave of cellular imaging. *Annu Rev Cell Dev Biol*, 26:285–314, 2010.

[243] D. Axelrod. Cell-substrate contacts illuminated by total internal reflection fluorescence. *J Cell Biol*, 89(1):141–5, 1981.

[244] D. Axelrod, D. E. Koppel, J. Schlessinger, E. Elson, and W. W. Webb. Mobility measurement by analysis of fluorescence photobleaching recovery kinetics. *Biophys J*, 16(9):1055–69, 1976.

[245] L. Stryer. Fluorescence energy transfer as a spectroscopic ruler. *Ann Rev Biochem*, 47:819–46, 1978.

[246] F. Brandl, F. Kastner, R. M. Gschwind, T. Blunk, J. Tessmar, and A. Gopferich. Hydrogel-based drug delivery systems: comparison of drug diffusivity and release kinetics. *J Control Release*, 142(2):221–8, 2010.

[247] J. Yin, A. J. Lin, P. D. Buckett, M. Wessling-Resnick, D. E. Golan, and C. T. Walsh. Single-cell FRET imaging of transferrin receptor trafficking dynamics by Sfp-catalyzed, site-specific protein labeling. *Chem Biol*, 12(9):999–1006, 2005.

[248] J. Yang, R. Zhang, D. C. Radford, and J. Kopecek. FRET-trackable biodegradable HPMA copolymer-epirubicin conjugates for ovarian carcinoma therapy. *J Control Release*, 218:36–44, 2015.

[249] M. G. L. Gustafsson. Surpassing the lateral resolution limit by a factor of two using structered illumination microscopy. *J Microsc*, 198(2):82–7, 2000.

[250] E. Betzig and R. J. Chichester. Single molecules observed by near-field scanning optical microscopy. *Science*, 262(5138):1422–5, 1993.

[251] S. W. Hell and E. H. K. Stelzer. Fundamental improvement of resolution with a 4Pi-confocal fluorescence microscope using two-photon excitation. *Opt Commun*, 93(5-6):277–82, 1992.

[252] M. G. L. Gustafsson. Extended resolution fluorescence microscopy. *Curr Opin Struct Biol*, 9(5):627–34, 1999.

[253] A. H. Voie, D. H. Burns, and F. A. Spelman. Orthogonal-plane fluorescence optical sectioning: three-dimensional imaging of macroscopic biological specimens. *J Microsc*, 170(Pt 3):229–36, 1993.

[254] L. Mockl, D. C. Lamb, and C. Brauchle. Super-resolved fluorescence microscopy: Nobel Prize in Chemistry 2014 for Eric Betzig, Stefan Hell, and William E. Moerner. *Angew Chem Int Ed Engl*, 53(51):13972–7, 2014.

[255] E. Betzig, G. H. Patterson, R. Sougrat, Lindwasser O. W., S. Olenych, J. S. Bonifacino, M. W. Davidson, J. Lippincott-Schwartz, and H. F. Hess. Imaging Intracellular Fluorescent Proteins at Nanometer Resolution. *Science*, 313:1642–5, 2006.

[256] S. T. Hess, T. P. Girirajan, and M. D. Mason. Ultra-high resolution imaging by fluorescence photoactivation localization microscopy. *Biophys J*, 91(11):4258–72, 2006.

[257] M. J. Rust, M. Bates, and X. Zhuang. Sub-diffraction-limit imaging by stochastic optical reconstruction microscopy (STORM). *Nat Methods*, 3(10):793–5, 2006.

[258] J. W. Lichtman and J. A. Conchello. Fluorescence microscopy. *Nat Methods*, 2(12):910–9, 2005.

[259] M. P. Backlund, M. D. Lew, A. S. Backer, S. J. Sahl, and W. E. Moerner. The role of molecular dipole orientation in single-molecule fluorescence microscopy and implications for super-resolution imaging. *Chemphyschem*, 15(4):587–99, 2014.

[260] ATTO-TEC GmbH. Data sheet: Atto488, https://www.atto-tec.com/attotecshop/product_info.php?info=p99_atto-488.html, 10.03.2016.

[261] Joseph R. Lakowicz. *Quenching of Fluorescence*, pages 257–301. Springer US, Boston, MA, 1983.

[262] R. M. Hoffman. The multiple uses of fluorescent proteins to visualize cancer in vivo. *Nat Rev Cancer*, 5(10):796–806, 2005.

[263] R. Y. Tsien. The green fluorescent protein. *Annu Rev Biochem*, 67:509–44, 1998.

[264] S. Inoue. *Foundations of Confocal Scanned Imaging in Light Microscopy*, pages 1–19. Springer US, Boston, MA, 2006.

[265] D. Toomre and J. B. Pawley. *Disk-Scanning Confocal Microscopy*, pages 221–38. Springer US, Boston, MA, 2006.

[266] C. E. Shannon. Communication in the Presence of Noise. *Proceedings of the IRE*, 37(1):10–21, 1949.

[267] D. Frank, C. Tyagi, L. Tomar, Y. E. Choonara, L. C. du Toit, P. Kumar, C. Penny, and V. Pillay. Overview of the role of nanotechnological innovations in the detection and treatment of solid tumors. *Int J Nanomedicine*, 9:589–613, 2014.

[268] E. Fernandes, J. A. Ferreira, P. Andreia, L. Luis, S. Barroso, B. Sarmento, and L. L. Santos. New trends in guided nanotherapies for digestive cancers: A systematic review. *J Control Release*, 209:288–307, 2015.

[269] R. van der Meel, L. J. Vehmeijer, R. J. Kok, G. Storm, and E. V. van Gaal. Ligand-targeted particulate nanomedicines undergoing clinical evaluation: current status. *Adv Drug Deliv Rev*, 65(10):1284–98, 2013.

[270] C. M. Dawidczyk, L. M. Russell, and P. C. Searson. Nanomedicines for cancer therapy: state-of-the-art and limitations to pre-clinical studies that hinder future developments. *Front Chem*, 2:69, 2014.

[271] S. T. Yang, Y. Liu, Y. W. Wang, and A. Cao. Biosafety and bioapplication of nanomaterials by designing protein-nanoparticle interactions. *Small*, 9(9-10):1635–53, 2013.

[272] S. Xu, B. Z. Olenyuk, C. T. Okamoto, and S. F. Hamm-Alvarez. Targeting receptor-mediated endocytotic pathways with nanoparticles: rationale and advances. *Adv Drug Deliv Rev*, 65(1):121–38, 2013.

[273] E. Broda, F. M. Mickler, U. Lachelt, S. Morys, E. Wagner, and C. Brauchle. Assessing potential peptide targeting ligands by quantification of cellular adhesion of model nanoparticles under flow conditions. *J Control Release*, 213:79–85, 2015.

[274] J. V. Jokerst, T. Lobovkina, R. N. Zare, and S. S. Gambhir. Nanoparticle PEGylation for imaging and therapy. *Nanomedicine (Lond)*, 6(4):715–28, 2011.

[275] M. Zhu, S. Perrett, and G. Nie. Understanding the particokinetics of engineered nanomaterials for safe and effective therapeutic applications. *Small*, 9(9-10):1619–34, 2013.

[276] A. A. Torrano, J. Blechinger, C. Osseforth, C. Argyo, A. Reller, T. Bein, J. Michaelis, and C. Brauchle. A fast analysis method to quantify nanoparticle uptake on a single cell level. *Nanomedicine (Lond)*, 8(11):1815–28, 2013.

[277] T. L. Doane, C. H. Chuang, R. J. Hill, and C. Burda. Nanoparticle zeta -potentials. *Acc Chem Res*, 45(3):317–26, 2012.

[278] S. K. Hobbs, W. L. Monsky, F. Yuan, W. G. Roberts, L. Griffith, V. P. Torchilin, and R. K. Jain. Regulation of transport pathways in tumor vessels: role of tumor type and microenvironment. *Proc Natl Acad Sci U S A*, 95(8):4607–12, 1998.

[279] T. Stylianopoulos and R. K. Jain. Design considerations for nanotherapeutics in oncology. *nanomedicine*, 11(8):1893–907, 2015.

[280] K. Knop, R. Hoogenboom, D. Fischer, and U. S. Schubert. Poly(ethylene glycol) in drug delivery: pros and cons as well as potential alternatives. *Angew Chem Int Ed Engl*, 49(36):6288–308, 2010.

[281] W. R. Gombotz, W. Guanghui, T. A. Horbett, and A. S. Hoffman. Protein adsorption to poly(ethylene oxide) surfaces. *J Biomed Mater Res A*, 25:1547–62, 1991.

[282] A. Kolate, D. Baradia, S. Patil, I. Vhora, G. Kore, and A. Misra. PEG - A versatile conjugating ligand for drugs and drug delivery systems. *J Control Release*, 192C:67–81, 2014.

[283] M. Wang and M. Thanou. Targeting nanoparticles to cancer. *Pharmacol Res*, 62(2):90–9, 2010.

[284] A. Ediriwickrema and W. M. Saltzman. Nanotherapy for Cancer: Targeting and Multifunctionality in the Future of Cancer Therapies. *ACS Biomater Sci Eng*, 1(2):64–78, 2015.

[285] H. H. Liu, S. Surawanvijit, R. Rallo, G. Orkoulas, and Y. Cohen. Analysis of nanoparticle agglomeration in aqueous suspensions via constant-number Monte Carlo simulation. *Environ Sci Technol*, 45(21):9284–92, 2011.

[286] A. Elsaesser, A. Taylor, G. S. de Yanes, G. McKerr, E. M. Kim, E. O'Hare, and C. V. Howard. Quantification of nanoparticle uptake by cells using microscopical and analytical techniques. *Nanomedicine (Lond)*, 5(9):1447–57, 2010.

[287] R. P. Friedrich, C. Janko, M. Poettler, P. Tripal, J. Zaloga, I. Cicha, S. Durr, J. Nowak, S. Odenbach, I. Slabu, M. Liebl, L. Trahms, M. Stapf, I. Hilger, S. Lyer, and C. Alexiou. Flow cytometry for intracellular SPION quantification: specificity and sensitivity in comparison with spectroscopic methods. *Int J Nanomedicine*, 10:4185–201, 2015.

[288] C. Gottstein, G. Wu, B. J. Wong, and J. A. Zasadzinski. Precise quantification of nanoparticle internalization. *ACS Nano*, 7(6):4933–45, 2013.

[289] J. C. Waters. Accuracy and precision in quantitative fluorescence microscopy. *J Cell Biol*, 185(7):1135–48, 2009.

[290] C. Leduc, S. Si, J. J. Gautier, Z. Gao, E. S. Shibu, A. Gautreau, G. Giannone, L. Cognet, and B. Lounis. Single-molecule imaging in live cell using gold nanoparticles. *Methods Cell Biol*, 125:13–27, 2015.

[291] C. H. Heldin, K. Rubin, K. Pietras, and A. Ostman. High interstitial fluid pressure - an obstacle in cancer therapy. *Nat Rev Cancer*, 4(10):806–13, 2004.

[292] M. A. Elsheikh, Y. S. Elnaggar, and O. Y. Abdallah. Rationale employment of cell culture versus conventional techniques in pharmaceutical appraisal of nanocarriers. *J Control Release*, 194:92–102, 2014.

[293] H. Hogenesch and A. Y. Nikitin. Challenges in pre-clinical testing of anti-cancer drugs in cell culture and in animal models. *J Control Release*, 164(2):183–6, 2012.

[294] E. C. Cho, Q. Zhang, and Y. Xia. The effect of sedimentation and diffusion on cellular uptake of gold nanoparticles. *Nat Nanotechnol*, 6(6):385–91, 2011.

[295] S. K. Mahto, T. H. Yoon, and S. W. Rhee. A new perspective on in vitro assessment method for evaluating quantum dot toxicity by using microfluidics technology. *Biomicrofluidics*, 4(3):034111, 2010.

[296] E. Frohlich. The role of surface charge in cellular uptake and cytotoxicity of medical nanoparticles. *Int J Nanomedicine*, 7:5577–91, 2012.

[297] A. C. Shieh and M. A. Swartz. Regulation of tumor invasion by interstitial fluid flow. *Phys Biol*, 8(1):015012, 2011.

[298] M. J. Mitchell and M. R. King. Computational and experimental models of cancer cell response to fluid shear stress. *Front Oncol*, 3(44):1–11, 2013.

[299] T. Bhowmick, E. Berk, X. Cui, V. R. Muzykantov, and S. Muro. Effect of flow on endothelial endocytosis of nanocarriers targeted to ICAM-1. *J Control Release*, 157(3):485–92, 2012.

[300] O. C. Farokhzad, A. Khademhosseini, S. Jon, A. Hermmann, J. Cheng, C. Chin, A. Kiselyuk, B. Teply, G. Eng, and R. Langer. Microfluidic system for studying the interaction of nanoparticles and microparticles with cells. *Anal Chem*, 77(17):5453–9, 2005.

[301] P. Charoenphol, R. B. Huang, and O. Eniola-Adefeso. Potential role of size and hemodynamics in the efficacy of vascular-targeted spherical drug carriers. *Biomaterials*, 31(6):1392–402, 2010.

[302] N. Doshi, B. Prabhakarpandian, A. Rea-Ramsey, K. Pant, S. Sundaram, and S. Mitragotri. Flow and adhesion of drug carriers in blood vessels depend on their shape: a study using model synthetic microvascular networks. *J Control Release*, 146(2):196–200, 2010.

[303] G. Sarfati, T. Dvir, M. Elkabets, R. N. Apte, and S. Cohen. Targeting of polymeric nanoparticles to lung metastases by surface-attachment of YIGSR peptide from laminin. *Biomaterials*, 32(1):152–61, 2011.

[304] A. Lin, A. Sabnis, S. Kona, S. Nattama, H. Patel, J. F. Dong, and K. T. Nguyen. Shear-regulated uptake of nanoparticles by endothelial cells and development of endothelial-targeting nanoparticles. *J Biomed Mater Res A*, 93(3):833–42, 2010.

[305] J. Kusunose, H. Zhang, M. K. Gagnon, T. Pan, S. I. Simon, and K. W. Ferrara. Microfluidic system for facilitated quantification of nanoparticle accumulation to cells under laminar flow. *Ann Biomed Eng*, 41(1):89–99, 2013.

[306] C. Fillafer, G. Ratzinger, J. Neumann, Z. Guttenberg, S. Dissauer, I. K. Lichtscheidl, M. Wirth, F. Gabor, and M. F. Schneider. An acoustically-driven biochip - impact of flow on the cell-association of targeted drug carriers. *Lab Chip*, 9(19):2782–8, 2009.

[307] J. Thundimadathil. Cancer treatment using peptides: current therapies and future prospects. *J Amino Acids*, 2012(967347):1–13, 2012.

[308] F. M. Mickler, L. Mockl, N. Ruthardt, M. Ogris, E. Wagner, and C. Brauchle. Tuning nanoparticle uptake: live-cell imaging reveals two distinct endocytosis mechanisms mediated by natural and artificial EGFR targeting ligand. *Nano Lett*, 12(7):3417–23, 2012.

[309] H. Xia, B. Anderson, Q. Mao, and B. L. Davidson. Recombinant human adenovirus: targeting to the human transferrin receptor improves gene transfer to brain microcapillary endothelium. *J Virol*, 74(23):11359–66, 2000.

[310] P. G. Cavanaugh, L. Jia, Y. Zou, and G. L. Nicolson. Transferrin receptor overexpression enhances transferrin responsiveness and the metastatic growth of a rat mammary adenocarcinoma cell line. *Breast Cancer Res Treat*, 56(3):203–17, 1999.

[311] Z. Liu, X. Gao, T. Kang, M. Jiang, D. Miao, G. Gu, Q. Hu, Q. Song, L. Yao, Y. Tu, H. Chen, X. Jiang, and J. Chen. B6 peptide-modified PEG-PLA nanoparticles for enhanced brain delivery of neuroprotective peptide. *Bioconjug Chem*, 24(6):997–1007, 2013.

[312] P. Kos, U. Lachelt, D. He, Y. Nie, Z. Gu, and E. Wagner. Dual-targeted polyplexes based on sequence-defined peptide-PEG-oligoamino amides. *J Pharm Sci*, 104(2):464–75, 2015.

[313] K. Kim, Y. Hur, E. K. Ryu, J. H. Rhim, C. Y. Choi, C. M. Baek, J. H. Lee, and J. Chung. A neutralizable epitope is induced on HGF upon its interaction with its receptor cMet. *Biochem Biophys Res Commun*, 354(1):115–21, 2007.

[314] C. P. Leamon and P. S. Low. Delivery of macromolecules into living cells: A method that exploits folate receptor endocytosis. *Proc Natl Acad Sci U S A*, 88:5572–6, 1991.

[315] S. Wang and P. S. Low. Folate-mediated targeting of antineoplastic drugs, imaging agents, and nucleic acids to cancer cells. *J Control Release*, 53(1-3):39–48, 1998.

[316] Y. G. Assaraf, C. P. Leamon, and J. A. Reddy. The folate receptor as a rational therapeutic target for personalized cancer treatment. *Drug Resist Updat*, 17(4-6):89–95, 2014.

[317] J. J. McGuire. Anticancer antifolates: current status and future directions. *Curr Pharm Des*, 9(31):2593–613, 2003.

[318] X. Zhao, H. Li, and R. J. Lee. Targeted drug delivery via folate receptors. *Expert Opin Drug Deliv*, 5(3):309–19, 2008.

[319] E. L. Matteson, V. J. Lowe, F. G. Prendergast, C. S. Crowson, K. G. Moder, D. E. Morgenstern, R. A. Messmann, and P. S. Low. Assessment of disease activity in rheumatoid arthritis using a novel folate targeted radiopharmaceutical Folatescan. *Clin Exp Rheumatol*, 27(2):253–59, 2009.

[320] J. A. Konner, K. M. Bell-McGuinn, P. Sabbatini, M. L. Hensley, W. P. Tew, N. Pandit-Taskar, N. Vander Els, M. D. Phillips, C. Schweizer, S. C. Weil, S. M. Larson, and L. J. Old. Farletuzumab, a humanized monoclonal antibody against folate receptor alpha, in epithelial ovarian cancer: a phase I study. *Clin Cancer Res*, 16(21):5288–95, 2010.

[321] Q. Tu, Y. Zhang, R. Liu, J. C. Wang, L. Li, N. Nie, A. Liu, L. Wang, W. Liu, L. Ren, X. Wang, and J. Wang. Active drug targeting of disease by nanoparticles functionalized with ligand to folate receptor. *Curr Med Chem*, 19(19):3152–62, 2012.

[322] F. Canal, M. J. Vicent, G. Pasut, and O. Schiavon. Relevance of folic acid/polymer ratio in targeted PEG-epirubicin conjugates. *J Control Release*, 146(3):388–99, 2010.

[323] S. Niedermayer, V. Weiss, A. Herrmann, A. Schmidt, S. Datz, K. Muller, E. Wagner, T. Bein, and C. Brauchle. Multifunctional polymer-capped mesoporous silica nanoparticles for pH-responsive targeted drug delivery. *Nanoscale*, 7(17):7953–64, 2015.

[324] C. Dohmen, T. Frohlich, U. Lachelt, I. Rohl, H. P. Vornlocher, P. Hadwiger, and E. Wagner. Defined Folate-PEG-siRNA Conjugates for Receptor-specific Gene Silencing. *Mol Ther Nucleic Acids*, 1:e7, 2012.

[325] B. Zhang, Y. Li, C. Y. Fang, C. C. Chang, C. S. Chen, Y. Y. Chen, and H. C. Chang. Receptor-mediated cellular uptake of folate-conjugated fluorescent nanodiamonds: a combined ensemble and single-particle study. *Small*, 5(23):2716–21, 2009.

[326] S. P. Samuel, N. Jain, F. O'Dowd, T. Paul, D. Kashanin, V. A. Gerard, Y. K. Gun'ko, A. Prina-Mello, and Y. Volkov. Multifactorial determinants that govern nanoparticle uptake by human endothelial cells under flow. *Int J Nanomedicine*, 7:2943–56, 2012.

[327] H. Yang, X. Xiong, L. Zhang, C. Wu, and Y. Liu. Adhesion of bio-functionalized ultrasound microbubbles to endothelial cells by targeting to vascular cell adhesion molecule-1 under shear flow. *Int J Nanomedicine*, 6:2043–51, 2011.

[328] L. E. Paulis, I. Jacobs, N. M. van den Akker, T. Geelen, D. G. Molin, L. W. Starmans, K. Nicolay, and G. J. Strijkers. Targeting of ICAM-1 on vascular endothelium under static and shear stress conditions using a liposomal Gd-based MRI contrast agent. *J Nanobiotechnology*, 10(1):1–12, 2012.

[329] P. J. Onyskiw and O. Eniola-Adefeso. Effect of PEGylation on ligand-based targeting of drug carriers to the vascular wall in blood flow. *Langmuir*, 29(35):11127–34, 2013.

[330] A. J. Ditto, K. N. Shah, N. K. Robishaw, M. J. Panzner, W. J. Youngs, and Y. H. Yun. The Interactions between L-tyrosine based nanoparticles decorated with folic acid and cervical cancer cells under physiological flow. *Mol Pharm*, 9(11):3089–98, 2012.

[331] C. Buchanan and M. N. Rylander. Microfluidic culture models to study the hydrodynamics of tumor progression and therapeutic response. *Biotechnol Bioeng*, 110(8):2063–72, 2013.

[332] Z. D. Shi and J. M. Tarbell. Fluid flow mechanotransduction in vascular smooth muscle cells and fibroblasts. *Ann Biomed Eng*, 39(6):1608–19, 2011.

[333] J. M. Tarbell and Z. D. Shi. Effect of the glycocalyx layer on transmission of interstitial flow shear stress to embedded cells. *Biomech Model Mechanobiol*, 12(1):111–21, 2013.

[334] D. Huh, B. D. Matthews, A. Mammoto, M. Montoya-Zavala, H. Y. Hsin, and D. E. Ingber. Reconstituting organ-level lung functions on a chip. *Science*, 328(5986):1662–8, 2010.

[335] D. Huh, Y. S. Torisawa, G. A. Hamilton, H. J. Kim, and D. E. Ingber. Microengineered physiological biomimicry: organs-on-chips. *Lab Chip*, 12(12):2156–64, 2012.

[336] M. Stadler, S. Walter, A. Walzl, N. Kramer, C. Unger, M. Scherzer, D. Unterleuthner, M. Hengstschlager, G. Krupitza, and H. Dolznig. Increased complexity in carcinomas: Analyzing and modeling the interaction of human cancer cells with their microenvironment. *Semin Cancer Biol*, 35:107–124, 2015.

[337] S. Taurin, H. Nehoff, and K. Greish. Anticancer nanomedicine and tumor vascular permeability; Where is the missing link? *J Control Release*, 164(3):265–75, 2012.

[338] M. H. Sung and J. G. McNally. Live cell imaging and systems biology. *Wiley Interdiscip Rev Syst Biol Med*, 3(2):167–82, 2011.

[339] J. M. Raser and E. K. O'Shea. Noise in gene expression: origins, consequences, and control. *Science*, 309(5743):2010–3, 2005.

[340] J. Nicolas, S. Mura, D. Brambilla, N. Mackiewicz, and P. Couvreur. Design, functionalization strategies and biomedical applications of targeted biodegradable/biocompatible polymer-based nanocarriers for drug delivery. *Chem Soc Rev*, 42(3):1147–235, 2013.

[341] Z. M. Qian, H. Li, H. Sun, and K. Ho. Targeted drug delivery via the transferrin receptor-mediated endocytosis pathway. *Pharmacol Rev*, 54(4):561–87, 2002.

[342] A. N. Luck and A. B. Mason. Transferrin-mediated cellular iron delivery. *Curr Top Membr*, 69:3–35, 2012.

[343] Leonard M. Neckers and J. B. Trepel. Transferrin Receptor Expression and the Control of Cell Growth. *Cancer Investigation*, 4(5):461–470, 1986.

[344] D. P. Bottaro, J. S. Rubin, D. L. Faletto, A. M.-L. Chan, T. E. Kmiecik, G. F. V. Woude, and S. A. Aaronson. Identification of the Hepathocyte Growth Factor Receptor as the c-met proto-oncogene product. *Science*, 251:802–804, 1991.

[345] J. J. Cui. Targeting receptor tyrosine kinase MET in cancer: small molecule inhibitors and clinical progress. *J Med Chem*, 57(11):4427–53, 2014.

[346] F. Cecchi, D. C. Rabe, and D. P. Bottaro. Targeting the HGF/Met signalling pathway in cancer. *Eur J Cancer*, 46(7):1260–70, 2010.

[347] Q. Lu, G.-J. Teng, Y. Zhang, H.-Z. Niu, G.-Y. Zhu, Y.-L. An, H. Yu, G.-Z. Li, D.-H. Qiu, and C.-G. Wu. Enhancement of p53 gene transfer efficiency in hepatic tumor mediated by transferrin receptor through trans-arterial delivery. *Cancer Biology and Therapy*, 7(2):218–224, 2008.

[348] D. Trinder, O. Zak, and P. Aisen. Transferrin receptor-independent uptake of differic transferrin by human hepatoma cells with antisense inhibition of receptor expression. *Hepatology*, 23(6):1512–20, 1996.

[349] Y. Nie, M. Gunther, Z. Gu, and E. Wagner. Pyridylhydrazone-based PEGylation for pH-reversible lipopolyplex shielding. *Biomaterials*, 32(3):858–69, 2011.

[350] T. Tsuji, H. Yoshitomi, and J. Usukura. Endocytic mechanism of transferrin-conjugated nanoparticles and the effects of their size and ligand number on the efficiency of drug delivery. *Microscopy (Oxf)*, 62(3):341–52, 2013.

[351] E. Mennesson, P. Erbacher, M. Kuzak, C. Kieda, P. Midoux, and C. Pichon. DNA/cationic polymer complex attachment on a human vascular endothelial cell monolayer exposed to a steady laminar flow. *J Control Release*, 114(3):389–97, 2006.

[352] M. B. Patel, S. P. Pothula, Z. Xu, A. K. Lee, D. Goldstein, R. C. Pirola, M. V. Apte, and J. S. Wilson. The role of the hepatocyte growth factor/c-MET pathway in pancreatic stellate cell-endothelial cell interactions: antiangiogenic implications in pancreatic cancer. *Carcinogenesis*, 35(8):1891–900, 2014.

[353] I. Rodriguez and M. Gonzalez. Physiological mechanisms of vascular response induced by shear stress and effect of exercise in systemic and placental circulation. *Front Pharmacol*, 5:209, 2014.

[354] Y. Ueki, N. Sakamoto, and M. Sato. Direct measurement of shear strain in adherent vascular endothelial cells exposed to fluid shear stress. *Biochem Biophys Res Commun*, 394(1):94–9, 2010.

[355] G. Varady, J. Cserepes, A. Nemeth, E. Szabo, and B. Sarkadi. Cell surface membrane proteins as personalized biomarkers: where we stand and where we are headed. *Biomarkers Med.*, 7(5):803–19, 2013.

[356] M. E. Watson, L. A. Diepeveen, K. A. Stubbs, and G. C. Yeoh. Glycosylation-related Diagnostic and Therapeutic Drug Target Markers in Hepatocellular Carcinoma. *J Gastrointestin Liver Dis*, 24(3):349–57, 2015.

[357] J. L. Daniotti, A. A. Vilcaes, V. Torres Demichelis, F. M. Ruggiero, and M. Rodriguez-Walker. Glycosylation of glycolipids in cancer: basis for development of novel therapeutic approaches. *Front Oncol*, 3:306, 2013.

[358] M. E. Katt, A. L. Placone, A. D. Wong, Z. S. Xu, and P. C. Searson. In Vitro Tumor Models: Advantages, Disadvantages, Variables, and Selecting the Right Platform. *Front Bioeng Biotechnol*, 4:12, 2016.

[359] S. M. Zou, P. Erbacher, J. S. Remy, and J. P. Behr. Systemic linear polyethylenimine (L-PEI)-mediated gene delivery in the mouse. *J Gene Med*, 2(2):128–34, 2000.

[360] D. Schaffert, N. Badgujar, and E. Wagner. Novel Fmoc-polyamino acids for solid-phase synthesis of defined polyamidoamines. *Org Lett*, 13(7):1586–9, 2011.

[361] D. Schaffert, C. Troiber, E. E. Salcher, T. Frohlich, I. Martin, N. Badgujar, C. Dohmen, D. Edinger, R. Klager, G. Maiwald, K. Farkasova, S. Seeber, K. Jahn-Hofmann, P. Hadwiger, and E. Wagner. Solid-Phase Synthesis of Sequence-Defined T-, i-, and U-Shape Polymers for pDNA and siRNA Delivery. *Angew Chem Int Ed Engl*, 50(38):8986–9, 2011.

[362] D. Schaffert, C. Troiber, and E. Wagner. New sequence-defined polyaminoamides with tailored endosomolytic properties for plasmid DNA delivery. *Bioconjug Chem*, 23(6):1157–65, 2012.

[363] E. E. Salcher, P. Kos, T. Frohlich, N. Badgujar, M. Scheible, and E. Wagner. Sequence-defined four-arm oligo(ethanamino)amides for pDNA and siRNA delivery: Impact of building blocks on efficacy. *J Control Release*, 164(3):380–6, 2012.

[364] A. Schafer, A. Pahnke, D. Schaffert, W. M. van Weerden, C. M. de Ridder, W. Rodl, A. Vetter, C. Spitzweg, R. Kraaij, E. Wagner, and M. Ogris. Disconnecting the yin and yang relation of epidermal growth factor receptor (EGFR)-mediated delivery: a fully synthetic, EGFR-targeted gene transfer system avoiding receptor activation. *Hum Gene Ther*, 22(12):1463–73, 2011.

[365] I. Martin, C. Dohmen, C. Mas-Moruno, C. Troiber, P. Kos, D. Schaffert, U. Lachelt, M. Teixido, M. Gunther, H. Kessler, E. Giralt, and E. Wagner. Solid-phase-assisted synthesis of targeting peptide-PEG-oligo(ethane amino)amides for receptor-mediated gene delivery. *Org Biomol Chem*, 10(16):3258–68, 2012.

[366] M. Monici. Cell and tissue autofluorescence research and diagnostic applications. *Biotechnol Annu Rev*, 11:227–56, 2005.

[367] M. Pfaff, K. Tangemann, B. Muller, M. Gurrath, G. Muller, H. Kessler, R. Timpl, and J. Engel. Selective recognition of cyclic RGD peptides of NMR defined conformation by alpha IIb beta 3, alpha V beta 3, and alpha 5 beta 1 integrins. *J Biol Chem*, 269(32):20233–8, 1994.

[368] Z. Li, R. Zhao, X. Wu, Y. Sun, M. Yao, J. Li, Y. Xu, and J. Gu. Identification and characterization of a novel peptide ligand of epidermal growth factor receptor for targeted delivery of therapeutics. *Faseb J*, 19(14):1978–85, 2005.

[369] J. Kloeckner, L. Prasmickaite, A. Hogset, K. Berg, and E. Wagner. Photochemically Enhanced Gene Delivery of EGF Receptor-targeted DNA Polyplexes. *Journal of drug targeting*, 12(4):205–13, 2004.

[370] P. Harvie, B. Dutzar, T. Galbraith, S. Cudmore, D. O'Mahony, P. Anklesaria, and R. Paul. Targeting of lipid-protamine-DNA (LPD) lipopolyplexes using RGD motifs. *J Liposome Res*, 13(3-4):231–47, 2003.

[371] Q.-M. Sun, Z.-H. Miao, L.-P. Lin, M. Gui, C.-H. Zhu, H. Xie, W.-H. Duan, and J. Ding. BB, a new EGFR inhibitor, exhibits prominent anti-angiogenesis and antitumor activities. *Cancer Biology & Therapy*, 8(17):1640–7, 2014.

[372] A. Salvati, A. S. Pitek, M. P. Monopoli, K. Prapainop, F. B. Bombelli, D. R. Hristov, P. M. Kelly, C. Aberg, E. Mahon, and K. A. Dawson. Transferrin-functionalized nanoparticles lose their targeting capabilities when a biomolecule corona adsorbs on the surface. *Nat Nano*, 8(2):137–43, 2013.

[373] Y. Xu, R. A. Swerlick, N. Sepp, D. Bosse, E. W. Ades, and T. J. Lawley. Characterization of expression and modulation of cell adhesion molecules on an immortalized human dermal microvascular endothelial cell line (HMEC-1). *TJ Invest Dermatol*, 102(6):833–7, 1994.

[374] M. P. Monopoli, D. Walczyk, A. Campbell, G. Elia, I. Lynch, F. B. Bombelli, and K. A. Dawson. Physical-chemical aspects of protein corona: relevance to in vitro and in vivo biological impacts of nanoparticles. *J Am Chem Soc*, 133(8):2525–34, 2011.

[375] B. L. Chung, M. J. Toth, N. Kamaly, Y. J. Sei, J. Becraft, W. J. Mulder, Z. A. Fayad, O. C. Farokhzad, Y. Kim, and R. Langer. Nanomedicines for Endothelial Disorders. *Nano Today*, 10(6):759–76, 2015.

[376] R. K. Jain. Normalization of tumor vasculature: an emerging concept in antiangiogenic therapy. *Science*, 307(5706):58–62, 2005.

[377] D. H. Na, B. H. Woo, and K. C. Lee. Quantitative analysis of derivatized proteins prepared with pyridyl disulfide-containing cross-linkers by high-performance liquid chromatography. *Bioconjug Chem*, 10(2):306–10, 1999.

[378] J. Carlsson, H. Drevin, and R. Axen. Protein thiolation and reversible protein-protein conjugation. N-Succinimidyl 3-(2-pyridyldithio)propionate, a new heterobifunctional reagent. *Biochem J*, 173(3):723–37, 1978.

[379] D. Schaffert, M. Kiss, W. Rodl, A. Shir, A. Levitzki, M. Ogris, and E. Wagner. Poly(I:C)-mediated tumor growth suppression in EGF-receptor overexpressing tumors using EGF-polyethylene glycol-linear polyethylenimine as carrier. *Pharm Res*, 28(4):731–41, 2011.

[380] Robert Zantl. Shear stress and shear rates for all channel μ-slides- based on numerical calculations (ibidi gmbh), 2010.

[381] J. Schindelin, I. Arganda-Carreras, E. Frise, V. Kaynig, M. Longair, T. Pietzsch, S. Preibisch, C. Rueden, S. Saalfeld, B. Schmid, J. Y. Tinevez, D. J. White, V. Hartenstein, K. Eliceiri, P. Tomancak, and A. Cardona. Fiji: an open-source platform for biological-image analysis. *Nat Methods*, 9(7):676–82, 2012.

[382] A. R. Nicholas, M. J. Scott, N. I. Kennedy, and M. N. Jones. Effect of grafted polyethylene glycol (PEG) on the size, encapsulation efficiency and permeability of vesicles. *Biochim Biophys Acta*, 1463(1):167–78, 2000.

[383] P. G. de Gennes. Polymers at an interface; a simplified view. *Adv Colloid Interface Sci*, 27(3-4):189–209, 1987.

[384] J. L. Perry, K. G. Reuter, M. P. Kai, K. P. Herlihy, S. W. Jones, J. C. Luft, M. Napier, J. E. Bear, and J. M. DeSimone. PEGylated PRINT nanoparticles: the impact of PEG density on protein binding, macrophage association, biodistribution, and pharmacokinetics. *Nano Lett*, 12(10):5304–10, 2012.

Appendix

1 Absorption calibration

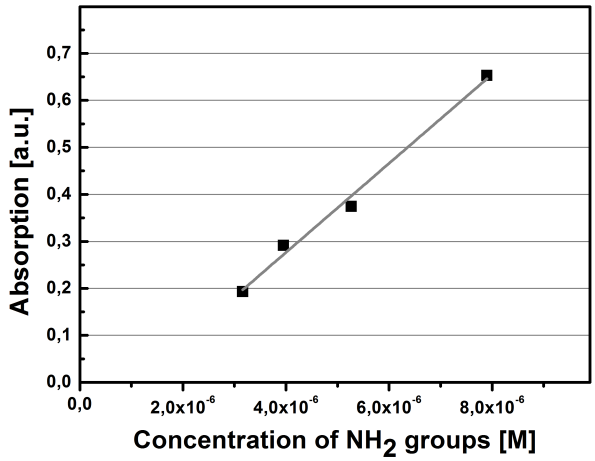

Figure 1: Calibration graph of the absorption of A200 polystyrene beads at 230 nm. The absorption is linearly proportional to the concentration of amino groups on the surface of the beads.

To calibrate the absorption of the latex beads at 230 nm, different concentrations of unmodified beads were measured as quintuplicate and fitted linearly. The attenuation coefficient ε* was calculated using the equation of the regression slope:

$$\varepsilon^* = \frac{a}{l} = \frac{94740\ M^{-1}}{0.1\ cm} = 947400\ M^{-1}cm^{-1} \tag{1.1}$$

where a is derived from the fitting curve and l is the length of the light pathway of the spectrophotometer.

2 PEGylation

The amount of PEGylated amino groups of the polystyrene beads was estimated by performing a small assay (DTT assay, see Chapter 8.2.1). For all batches, the degree of PEGylation was in the range of 5-10 % of the amino groups of the beads. According to the manufacturer's data, the surface area of a bead was calculated to equal 1.2566 $\cdot 10^{-13}$ m^2. This corresponds to an area of 65.74 Å^2/NH_2 group or 1.52 NH_2 groups/nm^2. If 5-10 % of the amino groups are PEGylated, the

distance D between the amino groups attached to a PEG molecule is 4.57-9.14 nm or the density of PEG molecules 0.08-0.15 PEG/nm^2.

To evaluate the conformation of the PEG chains on the surface of the beads, the Flory radius r_f was determined [382]:

$$r_F = a \cdot N^{\frac{3}{5}} = 0.35\ nm \cdot (5000/44)^{\frac{3}{5}} = 5.989\ nm \tag{2.1}$$

where a is the monomer size which is 0.35 nm for ethylene gylcol and N is the number of monomer units which is 5000/44≈ 114 for a 5 kDa PEG spacer.
The classification of the PEG chain conformation is defined in the literature. [283, 383, 384] If the distance D between the PEG chains is greater than the Flory radius r_f , the PEG chains are coiled into a "mushroom"-like conformation whereas if D is smaller than r_f , the PEG chains arrange into a "brush"-like structure.

For a PEGylation degree of 5 % with D = 9.14 nm a "mushroom"-like conformation is obtained, for 10 % PEGylation with D = 4.57 nm a "brush"-like conformation is expected.

3 Quantification of nanoparticles with fluorescence microscopy

The quantification of nanoparticles was performed by measuring the fluorescence of labeled particles by widefield or confocal microscopy and two different evaluation methods. One analysis involved the counting of intensity maxima with the program ImageJ, the other was based on integrating the fluorescence intensity. In Fig. 2, both methods were compared.

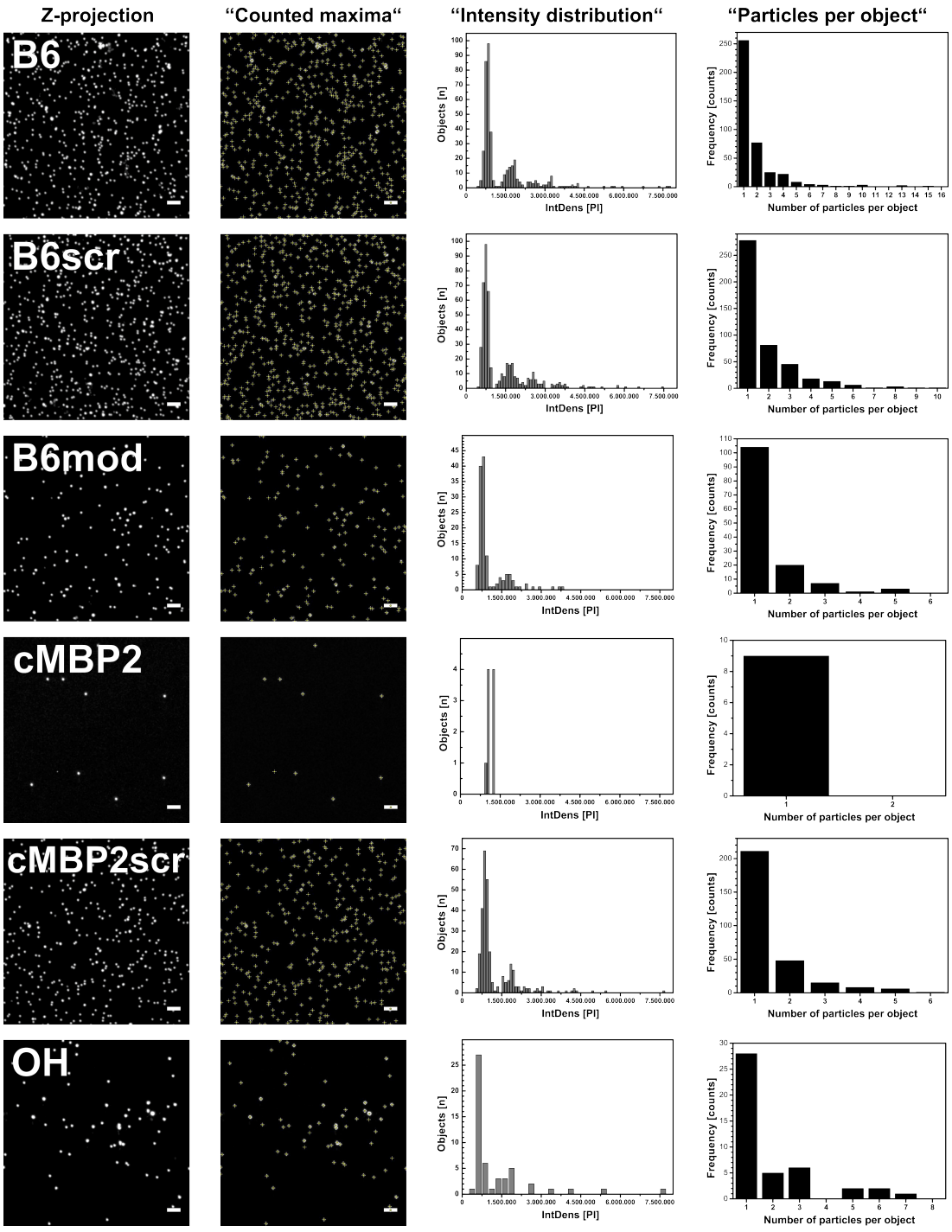

Figure 2: Particle analysis by counting fluorescent maxima and fluorescence integrated density (IntDens) based evaluation. In the first column, z-projections of fluorescence stacks of A200-PEG5-x (x = the peptide B6, B6scr, B6mod, cMBP2, cMBP2scr or hydroxylated) beads in CO_2 independent medium and 10 % FBS are shown. In the second column, the fluorescent maxima are selected by yellow crosses and counted as single beads. Scale bar = 5 μm. In the third column, the distribution of the IntDens of objects (corresponding to one or more beads) analyzed by Particle_i_Cell-3D. [276] are shown. The Nnumber of particles per object is depicted in the last column.

Table 1: External control II. Beads (A200-ATTO 488-PEG5-B6) with ligand and control beads (A200-Cy5-PEG5-OH/B6scr1/B6mod) from flow experiment preparations (1:400) were mixed 1:1 and pipetted into small imaging spacer chambers (9 mm diameter, 0.12 mm thickness) on a coverglass coated with collagen A. The beads were imaged with widefield microscopy, counted and the mean value obtained per field of view (63.7x63.7 μm^2) is shown. n = 40-51. The ratio was calculated and is displayed in the last column.

	B6 (ATTO 488)	**control (Cy5)**	**Ratio**
B6 : OH	58.4 ± 3.6	72.7 ± 16.8	0.87 ± 0.14
B6 : B6scr1	65.4 ± 9.5	41.6 ± 9.0	1.7 ± 0.40
B6 : B6mod	38.0 ± 14.9	37.9 ± 7.9	0.97 ± 0.36

4 External control

As the numbers of beads per cell were counted in our experiments, we assessed the initial numbers of beads added to the experiment in external control measurements. A suspension of beads with ligand (B6 beads) and control beads (Oh, B6scr1 or B6mod) as used in the flow experiments was pipetted into a imaging spacer chamber which was coated with collagen A. The chamber was closed by a second cover glass and the particles were imaged by widefield microscopy. In Table 1, the numbers of B6 beads compared to the number of control beads counted per field of view is shown. The ratio of both particle types is displayed in the last column. They ranged from 0.87 to 1.7. Thus, the factors of receptor targeted beads compared to control beads per single cell could be altered between 0.87 and 1.7. As we did not included these control factors into the resulting factors, only factors above 2 were considered to show a clear effect of the ligand.

5 Second scrambled peptide

Flow experiments were performed with a second scrambled peptide. In Fig. 3, the mean values of the number of B6scr2 beads on HuH7 cells compared to the number of hydroxylated beads and the factor distribution are shown.

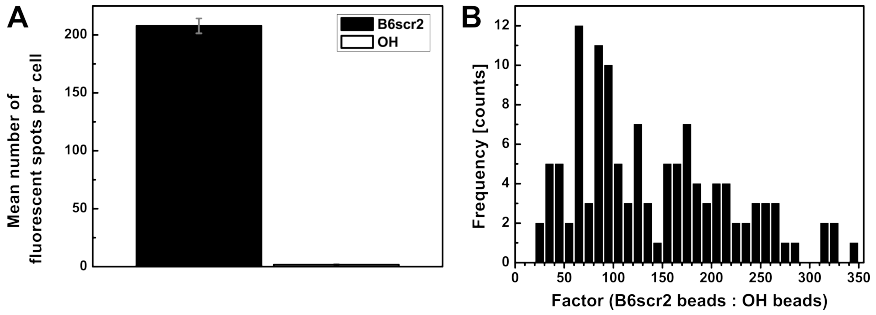

Figure 3: Effect of the scrambled peptide B6scr2 on binding to HuH7 cells. Adhesion of beads with scrambled peptide (B6scr2, labeled with Cy5) and hydroxylated control beads (labeled with ATTO 488) on HuH7 cells after 40 min under moderate (263 s^{-1}) shear conditions. (A) The mean numbers of B6scr2 (black column) and hydroxylated control beads (white column) on single cells are shown. n = 121. (B) The factor distribution of B6scr2 beads compared to hydroxylated control beads is depicted.

6 Immunostaining of surface receptors

Immunostaining and visualization by fluorescence microscopy

The presence of HGF receptors (c-Met) and transferrin receptors (TfR) on HuH7 cells was qualitatively assessed by immunostaining and visualization by fluorescence microscopy. Fixed cells were incubated with blocking buffer (10 % FBS in PBS) for 30 min, washed (4x, 5 min) and incubated with monoclonal rabbit anti-human c-Met primary antibody (3.9 µg/mL) or monoclonal mouse anti-human TfR primary antibody (10 µg/mL) for 50 min at room temperature. After washing with PBS (4x, 5 min), the treated cells and untreated cells for control were incubated with polyclonal donkey anti-rabbit Alexa647 secondary antibody (10 µg/mL) or monoclonal goat anti-mouse FITC secondary antibody (10 µg/mL), respectively. Finally, the cells were washed again with PBS (4x, 5 min). Images of the cells were obtained by spinning disk microscopy. The recorded z-stacks of single cells were transformed into z-projections with maximum intensity using Fiji imaging software and are displayed in Fig. 4. The images of the immunostained receptors and the respective IgG control images are illustrated with the same contrast settings.

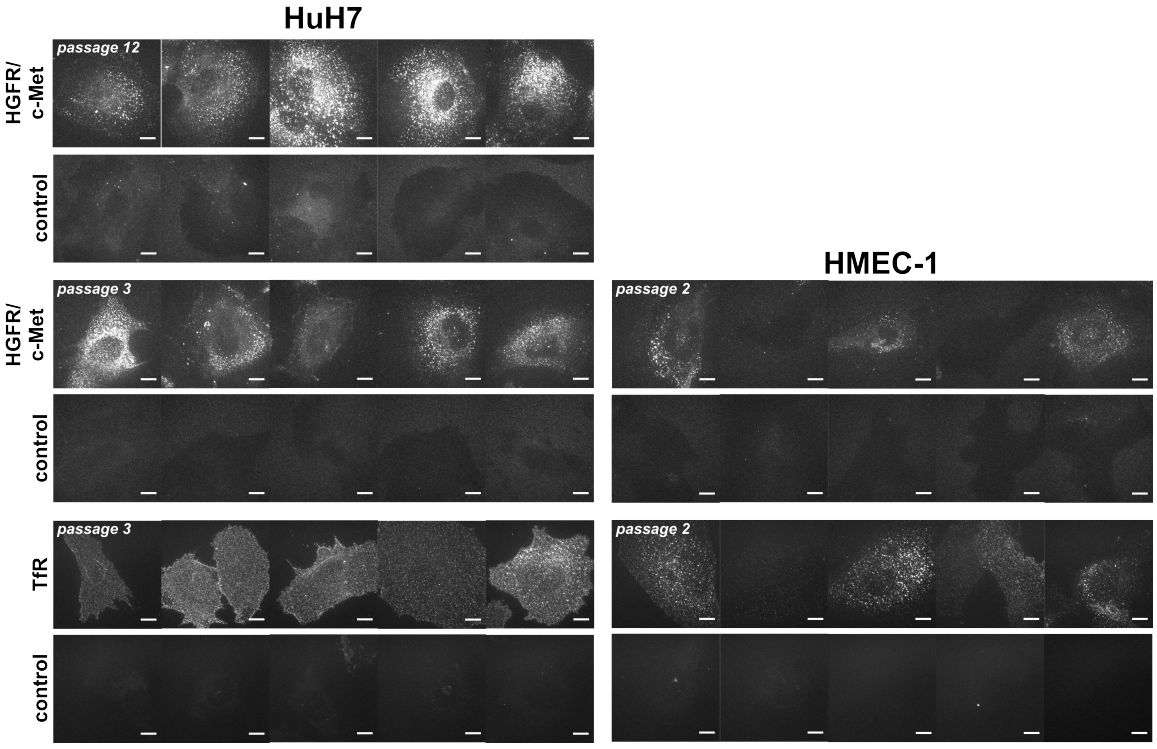

Figure 4: Immunostaining of HGFR/c-Met and TfR on HuH7 and HMEC-1 cells and visualization by fluorescence microscopy. HuH7 and HMEC-1 cells cultivated under static conditions were immunostained with monoclonal rabbit anti-human HGFR/c-Met and monoclonal mouse anti-human TfR. Surface receptor expression status was detected by using Alexa647 labeled donkey anti-rabbit and FITC labeled goat anti-mouse secondary antibodies. The fluorescence was imaged excitation with 639 nm and 488 nm lasers respectively by spinning disk microscopy. Representative z-projections of stacks over cells are shown. Scale bar = 10 μm.

Appendix

Immunostaining and flow cytometry analysis

The levels of HGF receptor (c-Met) and transferrin receptor (TfR) on HuH7 cells were determined by immunostaining and flow cytometry analysis. For each experiment, 300 000 cells in 100 μL blocking buffer (10 % FBS in PBS) were incubated with monoclonal mouse anti-human HGFR/c-met antibody, monoclonal mouse anti-human TfR or IgG control for mouse primary antibodies (1:100 dilution) for 1 h on ice and afterwards washed twice with blocking buffer. The cells were incubated with Alexa488- labeled goat anti-mouse (1:400 dilution) and FITC- labeled goat anti-mouse (1:100 dilution) secondary antibodies, respectively for 1 h on ice, washed twice and resuspended in 1 mL blocking buffer. After counterstaining with DAPI (1 μg/mL) the cells were analyzed on a CyanTM ADP flow Cytometer (Dako, Hamburg, Germany) using SummitTM acquisition software (Summit, Jamesville, NY, USA). The fluorophores were excited at 405 nm (DAPI) and 488 nm (Alexa488, FITC) and detected with a 450/50 nm bandpass filter and a 530/40 nm bandpass filter, respectively. In Fig. 5 and 6, the geometric mean fluorescence intensity (gMFI) of the plotted cell population is displayed.

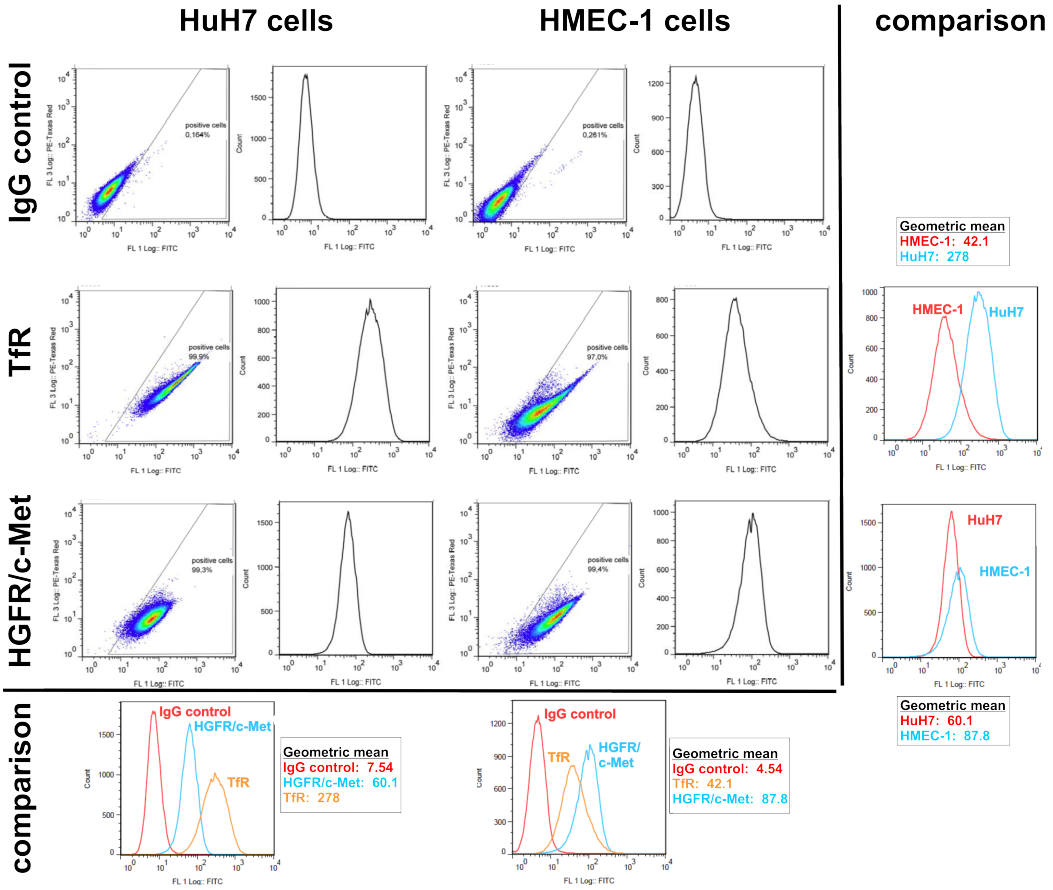

Figure 5: TfR and HGFR/c-Met receptor levels on HuH7 and HMEC-1 cells. HuH7 and HMEC-1 cells, cultivated under static conditions, were immunostained with monoclonal mouse anti-human HGFR/c-Met, anti-human TfR and IgG control. Surface receptor expression levels were detected by using Alexa488 and FITC labeled goat anti-mouse secondary antibodies and flow cytometry. The geometric mean values of the surface receptor levels on the different cell lines are depicted on the right and the different receptors on the same cell line at the bottom row.

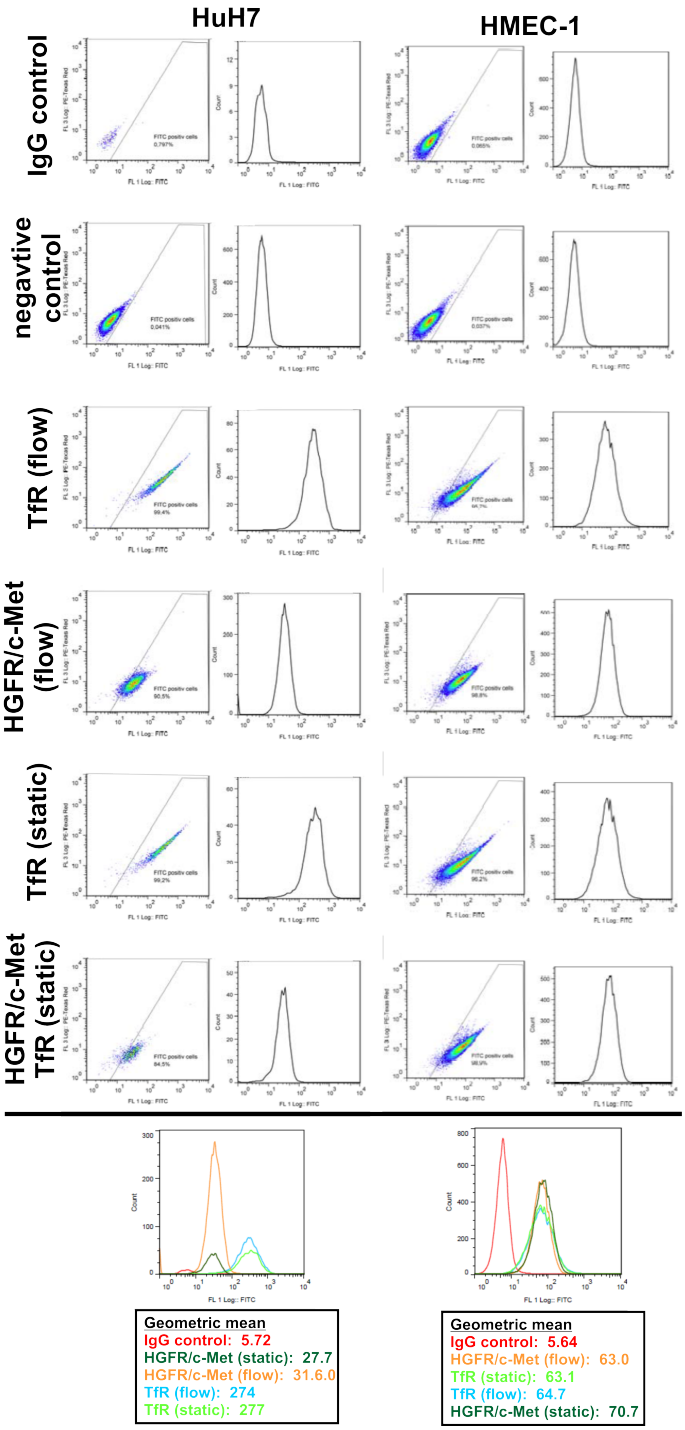

Figure 6: TfR and HGFR/c-Met receptor levels on HuH7 and HMEC-1 cells cultivated under static and flow conditions. HuH7 and HMEC-1 cells were cultivated under static conditions, seeded into flow channels and either remained under static conditions (static) or low shear flow (26 s^{-1}) was applied for 40 min (flow). The cells were immunostained with monoclonal mouse anti-human HGFR/c-Met, anti-human TfR and IgG control. Surface receptor expression levels were detected by using FITC labeled goat anti-mouse secondary antibody and flow cytometry. The geometric mean values of the different receptor levels on the two cell lines are depicted at the bottom.

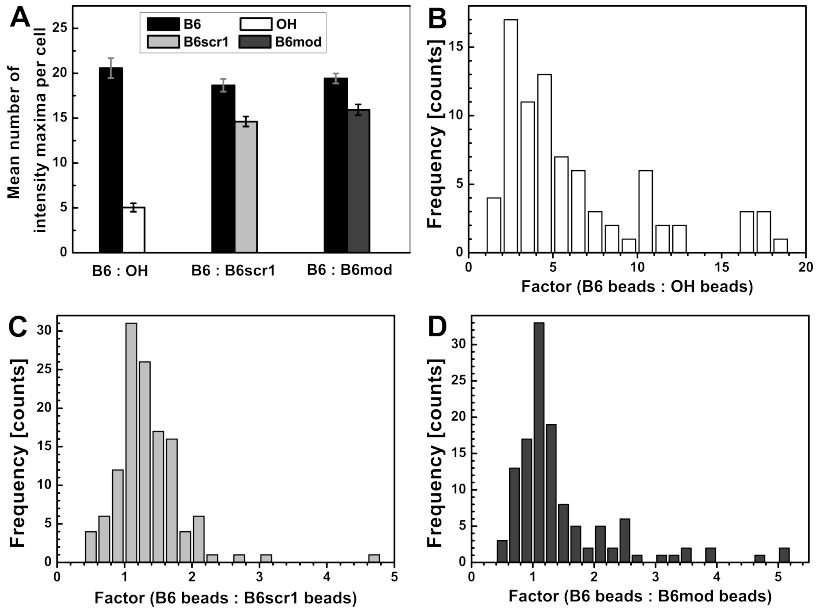

Figure 7: Binding of TfR targeted B6 beads compared to control beads without shear flow. Adhesion of beads with ligand (B6, dye 1) and control beads (dye 2) on HuH7 cells after 40 min incubation within a flow channel, but no shear flow (0 s^{-1}). (A) The mean numbers of B6 beads (black columns) and control beads (withe: hydroxylated, light gray: with scrambled peptide B6scr1 and dark gray column: modified peptide B6mod) on single cells are shown. n = 81-126. The factor distributions of B6 beads compared to (B) hydroxylated control beads, (C) with scrambled peptide B6scr1 or (D) with modified peptide B6mod are depicted.

7 Experiments with B6 beads in flow channels under static conditions

Experiments studying the adhesion of B6 beads with internal control were performed under static conditions with the same bead concentration as under flow conditions and within flow channels.

Model beads with the ligand B6 were mixed separately with differently labeled control beads: with hydroxylated beads (OH), with scrambled peptide (B6scr1) and with modified peptide (B6mod). The mixture was incubated with target HuH7 cells within flow channels for 40 min. After washing and fixation, the samples were imaged by widefield microscopy. In Fig. 7 A, the mean numbers of B6 beads (black) were compared to hydroxylated (white), B6scr1 (light gray) and B6mod (dark gray). In general, the total number of beads per cell was much smaller (between 25-35) compared to the numbers counted on cells exposed to shear flow (between 150-300). This result can be explained by the higher number of beads passing the cell surfaces under flow conditions. Diffusion and sedimentation are the main process by which particles appraoch the cell surfaces in static experiments. On average, around 20 B6 beads bound per cell in each experiment. The number of control beads differed strongly. While only a quarter of hydroxylated beads bound compared to the TfR targeted beads, the number of scrambled and modified peptide beads was similar to the number of B6 beads. Thus, both control peptides showed a similar affinity to the target cells as the ligand B6. By dividing the number of B6 beads by the number of control beads on single cells,

factors were calculated. The distributions of the factors are shown in Figures 7 B-D. The factor distribution of B6 compared to hydroxylated beads is conform with the distribution under flow conditions. Interestingly, the ratios of B6 to B6mod beads on single cells is close to 1 and assimilates the distribution of B6 to B6scr1. This means that the B6mod peptide has a higher affinity to the HuH7 cells under static conditions despite the lack of basic amino acids. Whether this increased attraction is due to specific receptor-ligand recognition or due to non-specific interactions cannot be concluded from the experiment.

Discussion:
It was found that replacing the basic amino acids within the peptide chain of B6 by glycines revealed that beads with either B6 or B6mod bound similarly under static conditions.This finding leads to the assumption that the initial binding step could be driven thermodynamically. It has to be mentioned that the experiments under static and flow conditions cannot be compared reasonably even tough they were conducted in the same flow channels with the same particle concentration, because the number of beads passing the cell surfaces is drastically increased under flow conditions. This fact implies that a multi-fold volume passes the cells, depending on the flow rate. The growth area of the cells in the channels is 2.5 fold higher than in the well chambers and thus the cell densities vary between 40.000 cells/cm^2 in a well and 360.000 cells/cm^2 in a channel. In addition, the number of bound beads was relatively low in the flow channels of the static experiment. Thus, the statistics are low and the binding could have been unspecific. Comparing the flow experiments to static experiments in well chambers is even more critical as the height of the medium in the channels is much lower than in the well chambers (0.4 mm compared to 3 mm). Moreover, the bead concentration was lower in flow experiments, up to the factor of 6.4 (1:48000 dilution compared to 1:750 for uptake experiments and 1:2000 for Tf competition).

8 Reproduction of experiments with cMBP2 beads

The experiments described in Chapter 6.2.1 were reproduced with another batch of HuH7 cells and the results are displayed in Fig. 8.

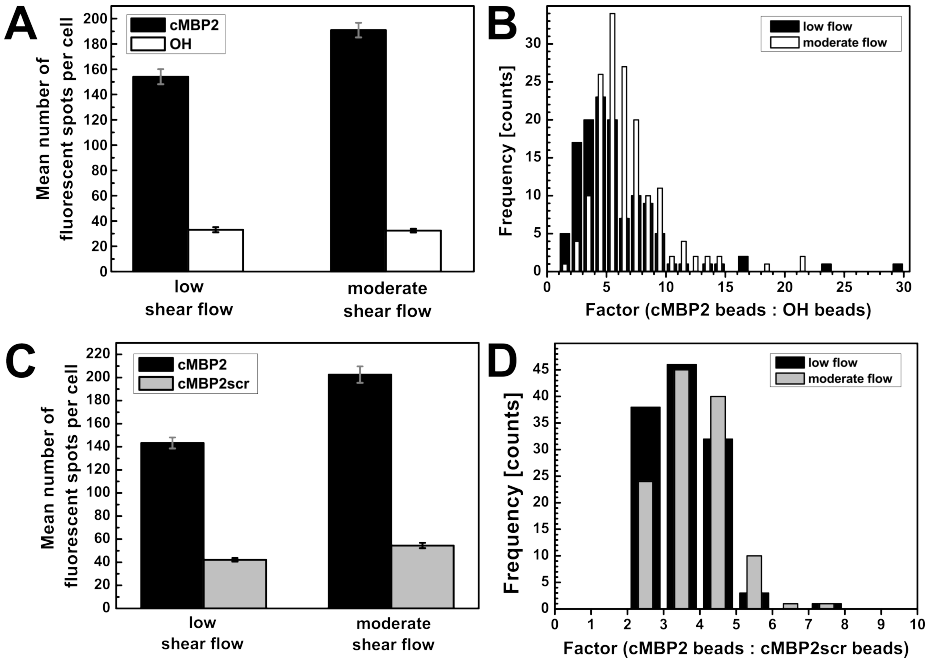

Figure 8: Reproduction of cMBP2 binding studies under flow conditions. The graphs show the experiments from Fig. 6.9 reproduced with another batch of HuH7 cells: Adhesion of beads with ligand (cMBP2, dye 1) and control beads (dye 2) on HuH7 cells after 40 min under low (26 s^{-1}) and moderate (263 s^{-1}) shear conditions. (A) The mean numbers of c-Met targeted cMBP2 beads (black column) and hydroxylated control beads (white column) on single cells after low (left) and moderate (right) shear flow are shown. n =124-160. (C) The factor distributions of cMBP2 beads compared to hydroxylated control beads after low (black) and moderate (white) shear flow are depicted. (D) The mean numbers of c-Met targeted cMBP2 beads (black column) and control beads with scrambled peptide cMBP2scr (grey column) on single cells after low (left) and moderate (right) shear flow are shown. n =120-121. (E) The factor distributions of cMBP2 beads compared to control beads with scrambled peptide cMBP2scr after low (black) and moderate (grey) shear flow are depicted.

9 Surface functionality of polystyrene beads

The beads used as model nanoparticles (see Chapter 4, 5 and 6) were commercially available polystyrene beads (Aliphatic Amine latex, 2 % w/v 0.2 μm) with surface amino groups. The manufacturer's data claim a diameter of 0.20 ± 0.05 μm, a density of 1.055 g/cm^3 for polystyrene at 20 °C and an amine content of 71.8 μEq/g. Subsequent, some parameters of interest were calculated by using the information above.

The volume of one bead V_{bead} is:

$$V_{bead} = \frac{4}{3} \cdot r^3 \cdot \pi = 4.189 \cdot 10^{-21}\ m^3 = 4.189 \cdot 10^{-12}\ \mu L \tag{9.1}$$

where r is the radius of the bead. The volume of all beads in 1 mL suspension is:

$$V = \frac{m}{\rho} = \frac{0,022g}{1,055\ g/cm^3} = 0,02085\ mL \tag{9.2}$$

where m is the mass of the solids (beads) and ρ is the density of the beads. Thus, the concentration

c of the beads is:

$$c = \frac{V}{V_{beads}(200\ nm)} = 4.978 \cdot 10^{12}\ beads/mL \tag{9.3}$$

The amine concentration $c(NH_2)$ is:

$$c(NH_2) = \frac{0,022\ g \cdot 71,8\ \mu mol/g}{1\ mL} = 1,5796\ \mu mol/mL \tag{9.4}$$

Thus, the amine content of one bead $n_{bead}(NH_2)$ is:

$$n_{bead}(NH_2) = \frac{1,5796\ \mu mol/mL}{4.978 \cdot 10^{12}\ beads/mL} = 3.173 \cdot 10^{-19}\ mol/bead \tag{9.5}$$

The number of amino groups per bead $n_{bead}(NH_2)$ is:

$$n_{bead}(NH_2) = 3.173 \cdot 10^{-19}\ mol/bead \cdot 6,022 \cdot 10^{23}\ mol^{-1} = 191088\ NH_2/bead \tag{9.6}$$

This means that beads labeled with 5 % Cy5 contain a maximum of 9554 dyes and labeled with 8 % ATTO488 contain a maximum of 15287 dyes, respectively. Furthermore, emanating from a PEGylation degree of 5-10 %, the maximum modification of one bead is in the range between 9554 - 19109 ligands/bead.

10 Macro for particle counting

To count fluorescent spots on cells a macro for Fiji (open source) was used. In principle, the fluorescent maxima of the labeled particles were counted. The macro is displayed below. The options "Subtract Background", "Gaussian Blur" and "Find maxima" were adjusted according to the signal to noise of the fluorescence images.

```
run("Close All");
dir1 = getDirectory("Select a nanoparticle image");
dir2 = getDirectory("Choose Destination Directory1: Z-Projections");
dir3 = getDirectory("Choose Destination Directory2: Results");

////////////////////////////////

list = getFileList(dir1);
setBatchMode(true);
for (i=0; i<list.length; i++) {
showProgress(i+1, list.length);
open(dir1+list[i]);
```

```
rename("z-Projection"+list[i]);
run("Z Project...", "start=1 stop=100 projection=[Max Intensity]");
saveAs("tiff", dir2+"z-pro_" + list[i]);
close();
}

run("Close All");
list = getFileList(dir2);
setBatchMode(true);
for (i=0; i<list.length; i++) {
showProgress(i+1, list.length);
open(dir2+list[i]);

rename("z-Projection"+list[i]);
run("Subtract Background...", "rolling=50");
run("Gaussian Blur...", "sigma=1.0");
run("Find Maxima...", "noise=80 output=[Point Selection]  exclude");
run("Create Mask");
saveAs("tiff", dir3+"Mask_" + list[i]);
run("Analyze Particles...", "size=1-Infinity circularity=0.00-1.00
show=Nothing display clear add");
roiManager("Show All with labels");
roiManager("Show All");
n = nResults;
print(n);
saveAs("Results", dir3+"Results" + list [i]);
}

selectWindow("Log");
saveAs("text", dir3 + "LogFile.txt");
```

Acknowledgments

I would like to sincerely thank my supervisor Prof. Christoph Bräuchle for his guidance and support during my PhD work. I appreciate the opportunities I had to study a very interesting research topic and contribute my own ideas. I am very grateful to Prof. Ernst Wagner for his advice and encouragement for our cooperation projects and the appraisal of my thesis. My thanks go to Prof. Don Lamb for the many discussion and suggestions during the group seminars and to Prof. Bettina Lotsch for the very interesting insights in a different research field. Furthermore, I would like to thank all reviewers of this thesis, including Prof. Achim Hartschuh and Prof. Regina de Vivie-Riedle.

My gratitude is extended to my collaboration partners, Dr. Ulrich Lächelt, Dr. Christian Dohmen and Stephan Morys as well as all people from AK Wagner helping me with little things: Dr. Petra Kos, Wolfgang Rödl, Miriam Höhn and Ruth Röder. Special thanks to Uli for the great ideas and discussions about my research projects. I would like to express my appreciation to Dr. Ida Pavlichenko for letting me participate in one of her research projects and for all the inspiring scientific discussions.

I had the chance to continue and advance a research project of Frauke as a successor, and benefit from her experience, thanks for that. Many thanks to Adriano who gave me insights into his evaluation skills and with whom I enjoyed discussing science very much. Special thanks also to Lena who listened to many issues and always proposed many good suggestions. I appreciated the experience of Giulia, Jelle and Stephan who gave me many good advices. Thanks to Dr. Hanna Engelke for all the interesting discussions in the cell culture lab. I appreciated the good atmosphere, many discussions and group events with the members of AK Bräuchle, AK Lamb and AK Michaelis. I would like to thank especially Vroni, Julia Blechinger, Waldi, Philipp, Viola, Doro, Bärbel, Fabian, Sushi and Anders as well as Meli, Leonhard, Jens, Alvaro, Aurelie, Maria, Bässem, Daniela, Ganesh, Nader, Ivo, Chen, Niko, Evelyn, Alex, Kira, Matthias, Korbi, Christian, Julia, Moni, Kasia, Jochen, Thilo, Wolfi, Vova, Sergey and Robert. I express my gratitude to Monika Franke who prepared cells for me, but also taught me cell culturing. Thanks to my students Sebastian, Johannes and Christian for participating in my research projects with much effort and interest. I would like to thank Silke Steger and Dr. Moritz Ehrl for all administrative support.

My acknowledgments are directed to the Center for NanoScience (CeNS), the Center for Integrated Protein Science Munich (CIPS^M) and especially the Nanosystems Initiative Munich (NIM) for the financial support, workshops, conferences, interesting events and networking opportunities.

I would like to express my sincere thanks to my family and my friends. It was always a pleasure to share lunch time with Claudi, Anna, Chris and Linus. Ganz besonders dankbar bin ich meinen El-

tern Ute und Lothar. Herzlichen Dank für euren unendlichen Glauben an mich und eure großartige Unterstützung. Meine Geschwister Benedikt, Esther und Felicitas, und meinen Opa Hans möchte ich in meinen herzlichen Dank mit einschließen!

List of publications

Publication related to the thesis

Peer reviewed journals

- Assessing potential peptide targeting ligands by quantification of cellular adhesion of model nanoparticles under flow conditions. Broda E., Mickler F. M., Lächelt, U., Morys S., Wagner E., Bräuchle C., *J. Control. Release* 2015, 213, 79-85.

Publications not related to the thesis

Peer reviewed journals

- Bringing one-dimensional photonic crystals to a new light: an electrophotonic platform for chemical mass transport visualisation and cell monitoring. Pavlichenko I., Broda E., Fukuda Y., Szendrei K., Hatz A. K., Scarpa G., Lugli P., Bräuchle C., Lotsch B. V.,*Mater. Horiz.* 2015, 2, 299.

- Directed ortho-metalation-cross-coupling strategies. One-pot Suzuki reaction to biaryl and heterobiaryl sulfonamides. Schneider C., Broda E., Snieckus V., *Org. Lett* 2011, 13, 3588-91.

Conferences and public talk

- PhD colloquium, Physical chemistry, LMU Munich, Faculty of Chemistry and Pharmacy. *Assessing potential peptide targeting ligands by quantification of cellular adhesion of model nanoparticles under flow conditions*, (talk). Munich, January 2016.

- International Meeting of Physics of Living Systems Network - iPoLS. Munich, Germany, July 2014.

- 58th annual meeting of the Biophysical Society. *Influences of cellular adhesion of nanoparticles under blood flow-like conditions*, (poster). San Francisco, CA, USA, February 2014.

- CeNS Workshop 2013: Great Adventures on Small Scales. *Therapeutical nanoparticles â€“ how specific do they bind to their target?*, (poster). Venice, Italy, September 2013

- NIM-GP Summer Retreat 2013. *Towards a better understanding of cellular nanoparticle binding*, (poster). Fall-Lenggries, Germany, July/August 2013

- NIM Winterschool 2013 in cooperation with iNANO. *Adhesion of therapeutical nanoparticles under flow conditions*, (poster). Kirchberg, Austria, March 2013.
- CeNS Workshop 2012: Soft, Solid, Alive and Kicking. *Adhesion of therapeutical nanoparticles under flow conditions*, (poster). Venice, Italy, September 2012.
- NIM Nanoday - Deutsches Museum München. *Nanopartikel in der Medizin*, (poster), Munich, Germany, September 2012.
- NIM Summer Retreat 2012. *Effects of targeting ligands on cellular binding of model particles*, (poster). Garmisch-Partenkirchen, Germany, June 2012.
- NIM Summer Retreat 2011. *Effects of targeting ligands on cellular binding of therapeutical devices*, (poster). Aschau im Chimgau, Germany, July 2011.

Award

- Publication Award 2015, Category: Best interdisciplinary publication, Center for Nano Science (CeNS) for J. Control. Release 213, 79-85 (2015).